Perovskite Monolithic Structures for Solar-Powered Thermochemical Redox Cycles

Monolithische Perowskitstrukturen zur Anwendung in solarbetriebenen thermochemischen Redoxzyklen

Von der Fakultät für Maschinenwesen der Rheinisch-Westfälischen Technischen Hochschule Aachen zur Erlangung des akademischen Grades eines Doktors der Naturwissenschaften genehmigte Dissertation

vorgelegt von

Mathias Pein

Berichter:	Univ.-Prof. Dr. rer. nat. Christian Sattler
	Prof. Dr. rer. nat. Gianaurelio Cuniberti
Tag der mündlichen Prüfung:	15. Februar 2024

Zusammenfassung

Die Nutzung von Sonnenwärme hat ein großes Potenzial im Kontext der Energieversorgung. Solare Wärme kann eine wesentliche Rolle bei der Bewältigung der Herausforderungen des industriellen Übergangs von fossilen Energiequellen hin zur Versorgung mit erneuerbarer Energiegewinnung spielen. Konzentrierte Sonnenwärme ist vielseitig einsetzbar. Sie kann zur Stromerzeugung, sowie zur Bereitstellung von Wärmeenergie in industriellen Prozessen oder zum Antrieb chemischer Reaktionen genutzt werden.
Thermochemische Redoxzyklen, die mit konzentrierter Sonnenwärme betrieben werden, haben in den letzten Jahren vielversprechende Ergebnisse in einer Reihe von Prozessen gezeigt, nicht nur im Zusammenhang mit der Wasser- und Kohlendioxidspaltung für die Synthesegaserzeugung, sondern auch für die (thermische) Energiespeicherung, das Pumpen von Sauerstoff und die Luftzerlegung. Perowskite in Form von ABO_3-Mischmetalloxiden sind eine vielseitige Materialklasse für solch thermochemische Redoxkreisläufe. Die große Anzahl möglicher Zusammensetzungen, die durch Bildung von festen Lösungen mit verschiedenen A- und B-Stellen-Kationen verfügbar sind, ermöglichen eine Feinabstimmung der thermodynamischen Eigenschaften des Materials auf die Anforderungen eines Prozesses. Darüber hinaus können Perowskite nichtstöchiometrisch reduziert und oxidiert werden, was bedeutet, dass sie bei der Reduktion und Oxidation keine substantiellen Veränderungen ihrer Kristallstruktur erfahren.
Insbesondere bei Anwendungen, welche dreidimensionale Strukturen nutzen, ist die strukturelle Stabilität von großer Bedeutung. Perovskite können dabei im Vergleich zu konkurrierenden Redoxsystemen, wie z. B. Mn_2O_3/Mn_3O_4 und Fe_2O_3/Fe_3O_4, aufgrund ihrer thermodynamischen, kinetischen und thermomechanischen Eigenschaften vorteilhaft sein.
Die vorliegende Arbeit konzentriert sich auf sogenannte Downstream-Prozesse, wie die thermische bzw. thermochemische Speicherung von Energie und das thermochemische Pumpen von Sauerstoff. Solche Prozesse finden abseits eines Solarreceivers statt und erfordern Temperaturen bis zu 1100 °C. Diese Arbeit deckt die gesamte Entwicklungskette vom Screening geeigneter Perowskit-Zusammensetzungen in kleinmaßstäblichen Versuchsaufbauten und Analysetechniken, über die Herstellung stabiler, offenporiger, monolithischer Strukturen identifizierter Zusammensetzungen, die Charakterisierung solcher Strukturen und die Demonstration ihrer Nutzung in einem Reaktor im Labormaßstab ab.
Die Ergebnisse zeigen, dass $CaMnO_3$ und seine A-Stellen Sr-substituierten Varianten ein großes Potenzial für die thermochemische Energiespeicherung und das thermochemische Pumpen von Sauerstoff aufweisen. In diesem Kontext, zeigte sich $Ca_{0.9}Sr_{0.1}MnO_{3-\delta}$ aufgrund der Ergebnisse als besonders vielversprechendes Material.

Abstract

The utilization of solar heat offers great potential in the context of energy supply. Solar heat can play an essential role overcoming challenges of the industrial transfer away from fossil energy sources. Concentrated solar heat is versatile and can be used to produce electricity, supply thermal energy in industrial processes or to drive chemical reactions. Thermochemical redox cycles, powered by concentrated solar heat, have shown promising results in a variety of processes within the past years. They can be utilized in the context of water and carbondioxide splitting for syngas production, energy storage, oxygen pumping and air separation. Perovskites in the form of ABO_3 mixed metal oxides are a versatile material class for such thermochemical redox cycles. The large number of possible compositions, available through the formation of solid solutions with various A- and B-site cations, allow fine tuning of thermodynamic characteristics of the material in order to fit the requirements of a desired process. Furthermore, perovskites can be reduced and oxidized non-stoichiometrically, meaning they do not undergo severe changes in their crystal structure upon reduction and oxidation. Especially in applications where threedimensional structures are utilized, structural stability is of utter importance. In this context, perovskites can be beneficial in comparison to competing redox systems, such as Mn_2O_3/Mn_3O_4 and Fe_2O_3/Fe_3O_4, due to their favorable thermodynamic, kinetic and thermomechanic characteristics.

The presented work focuses on so-called down-stream processes, such as thermal and thermochemical energy storage and thermochemical oxygen pumping. These processes are performed away from a solar receiver and require temperatures up to 1100 °C. This work covers the complete chain of development from screening of suitable perovskite compositions in small-scale test-setups and analysis techniques, over the production of stable, open porous, monolithic structures of identified compositions, the characterization of such structures and the demonstration of their utilization in a lab-scale reactor.

The results showed that open porous structures made from $CaMnO_3$ and its A-site Sr-substituted variants offer great potential for thermochemical energy storage and thermochemical oxygen pumping. In this context, $Ca_{0.9}Sr_{0.1}MnO_{3-\delta}$ was shown to be a particularly promising material composition for the utilization of monolithic open porous strucures.

Contents

List of Figures

List of Tables

Acronyms

BET N_2 gas-adsorption by Brunauer-Emmett-Teller model. 39

CDS carbon dioxide splitting. 7, 8, 12, 15

CSE concentrated solar energy. 7, 12, 14, 18, 19, VII

CSP concentrated solar power. 1–4, 11, 16, 26

DFT density functional theory. 32

DLR German Aerospace Center. 2

DNI direct normal irradiation. 2

DSC differential scanning calorimetry. 39, 49, 52, 53, 73–78, 85, 91–94, 96, 98–107, 110, 117, 146, VIII–XI, XIV

EDX electron dispersive x-ray spectroscopy. 110

HHI Herfindahl-Hirschmann-Index. 5

HT-XRD high temperature x-ray diffraction. 47, 92, 93, IX

HTF heat transfer fluid. 3, 4, 11, 14–17, 24, 26, 27

LCOE levelised cost of electricity. 2, 3

MCC microcrystalline cellulose. 44

PF pumping furnace. 57, 58, 62, 63, 79, 80

PM pumping material. 57, 58, 65–67, 79, 80, 82, 140, 142–144, 148, IX

ppi pores per inch. 43, 48, 110–113, 115, 118, 124, 128, 131, 147, VIII, X, XI

PSD particle size distribution. 43

PU polyurethane. 110, 111

PV photovoltaics. 1, 2, 4

PVP polyvinylpyrrolidone. 43

RPC reticulated porous ceramics. 27

SEM scanning electron microscopy. 39, 47, 110, 113–116, 132–135, XI, XII

SF splitting furnace. 57, 58, 62, 63, 66, 79

SM splitting material. 57, 65–67, 79, 80, 82, 140, 142–144, VIII, IX

STA simultaneous thermal analysis. 52

TCES thermochemical energy storage. 7, 8, 11, 19, 24, 26, 78, 146–148

TCOP thermochemical oxygen pumping. 7, 12, 146–148

TES thermal energy storage. 11

TGA thermogravimetric analysis. 39, 49, 50, 53, 57, 70, 71, 73, 74, 88, 101–104, 110, 117–121, 124, 128, 146, VIII–XI, XIV

WS water splitting. 7–9, 12, 15

XRD x-ray diffraction. 39, 47, 69, 93, 96, 113, 146

1. Introduction

In a world of growing energy demand, reliable supply of sustainable energy is among the biggest challenges of the 21st century. In order to reach the global goal of a net-zero greenhouse gas emission economy, rapid expansion of sustainable energy technologies is required. Researchers across scientific disciplines have relentlessly tried to further advance technology to provide solutions in order to overcome this challenge of sustainable energy supply. If captured and converted with todays technologies and even with only economically viable production sites considered, globally available wind and solar energy alone could meet the worlds energy demand by a factor of over 50 already today and a prospected factor of 100 by the year 2030.[1] However, one major drawback of renewable energy sources is their fluctuating nature. While solar and wind energy fluctuate in their availability influenced by daytime and season, a steel production factory is typically operated 24 hours on 7 days a week. The commonly used technique of continuous casting with yearly operating hours of 7000 and more siginificantly loses out on economic potential when interrupted by down-times.[2] The lack of widespread cost and energy efficient ways to store the energy from renewable sources and make them available on-demand is one of the biggest obstacles that keep renewable energy sources from dominating the market already. Fossil fuels like oil or gas can be shipped in large tanks or can be pumped through a pipelines in huge quantities and over long distances. That not only makes it easier to transport the energy carrier from its source to its point of demand, but also makes it easier to be traded on a global or interregional market.

Solar radiation is by far the biggest renewable energy source. Multiple ways exist to harvest this energy and make it available for use out of which photovoltaics (PV), concentrated solar power (CSP) and photocatalysis are most prominent. PV can directly convert solar radiation to electricity. It can utilize scattered radiation, but only makes use of certain wavelengths and not the full spectrum of solar radiation. CSP facilities, i.e. movable mirror assemblies that track the sun and reflect and concentrate its radiation, are able to provide high temperature heat even beyond 1000 °C, which can be used to drive a power generation cycle similar to conventional power plants to produce electricity.[3] The generated heat can also be used to drive (thermo-)chemical processes. These processes require high temperatures to produce gaseous energy carriers like hydrogen or syngas, a mixture of hydrogen and carbon monoxide. Syngas can be further refined to produce synthetic fuels, like kerosine.[4,5] If the required carbondioxide is captured from the atmosphere, these synthetic fuels are practically carbon neutral. Especially the transport sector, more specific the aviation and shipping industry, will largely depend on carbon neutral synthetic fuels as electrification is only hardly realizable in these sectors. Moreover, converting the harvested solar energy to a gas like hydrogen or liquid synthetic hy-

drocarbon fuels makes transportation of the actual energy carrier more accessible. Lastly there is photocatalysis, which is able to produce hydrogen at temperatures close to ambient from a catalytic reaction aided by non-concentrated solar radiation, but has not yet seen wide spread practical use.[6]

The two most advanced solar power generation technologies are PV and CSP, which operate most efficiently in regions with a sunny and generally dry climate. While CSP is non-feasible during cloudy or rainy days and requires high direct normal irradiation (DNI), PV is only affected by comparably small losses and can still operate under such non-optimal conditions. Countries with high DNI are located in southern Europe and around the mediterranean sea in northern Afrika as well as the middle east. To cover for the energy intensive industry of central european countries, energy will have to be imported from countries with high DNI. Between the two main approaches to produce electricity at utility-scale levels from solar radiation, PV and CSP, the former has rapidly decreased in costs in the last decade due to technological advances and the benefits of mass production and reached grid-parity in many electricity markets. The strong deployment and related technological development of PV have led to a technological shift from CSP to PV. However, simply adding PV (or wind) capacity to the grid without covering for invariance will increase the chances of grid instability and high levels of marginal curtailment. That means electricity generation has to be tuned down and installed plants do not operate at their full capacity in order to stabilize the electric grid.

CSP power plants with their straightforward, prolonged and cost-effective storage capabilities can supply green electricity around the clock at a constant level. They can cover the baseload demand and serve as a buffer in time of invariance of other green electricity sources. In this way, fossil power plants can be replaced by CSP and greenhouse gases can be reduced cost-effectively. The specific electricity production costs for CSP plants can be reduced considerably if such plants are combined with PV fields. PV modules can serve the peak loads in the grid more cost-effectively than CSP, which can cover the baseload. PV and CSP can also share the general utilities and infrastructure that a solar farm needs. Such hybrid co-located CSP and PV plants are already reaching levelised cost of electricity (LCOE) lower than that of natural gas plants.[7]

A comprehensive study, carried out by the German Aerospace Center (DLR) in the context of the ambitious DESERTEC project, layed out a scenario how energy demand in europe could be met by 2050.[8] The map in fig. 1.1 shows the distribution of wind parks along the coastlines and CSP facilities in southern Europe, north Africa and the middle east. Hydro- and geothermal power plants and spread out PV were considered as support

units where possible.

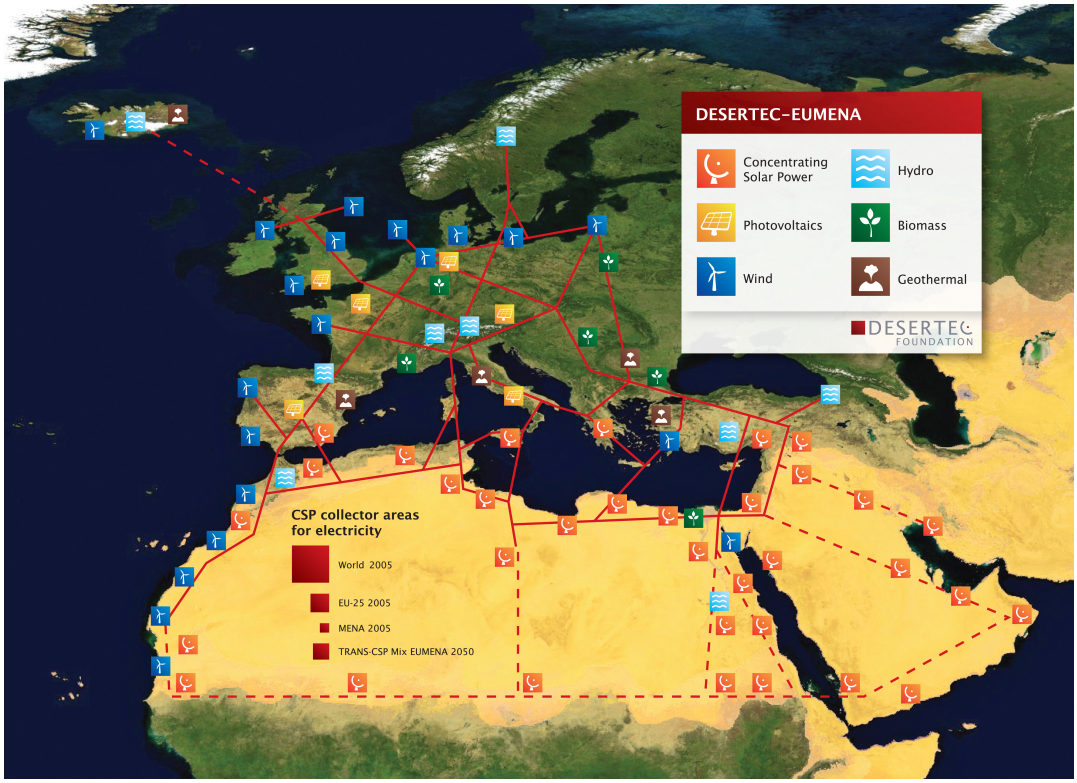

Fig. 1.1.: Outline of a possible infrastructure for sustainable power supply in Europe, the Middle East and North Africa (EU-MENA). Squares indicate required area for solar collectors to meet the energy demand as of 2005. The "TRANS-CSP Mix EUMENA 2050" is the prospected area (120x120km) to realize DESERTEC by 2050 according to the TRANS-CSP scenario developed by DLR, covering 17% of european electricity demand. Source: DESERTEC Foundation. CC BY-SA 2.5

The inherent intermittency of renewable energy sources like wind and solar still prevents even stronger market penetration. Still, renewable energy sources become more and more economically viable with LCOE ranging from 0.039 to 0.108 USD/kWh,[9] which are comparable to that of natural gas power plants.[7] CSP is one of the technologies with great potential to overcome this intermittency by employing thermal storage systems that are charged during times of high radiation during the day, and can be discharged during the night and morning hours when there is no sun light. The NOOR III CSP-plant in Morocco operates with a thermal storage, allowing to supply 150 MW for 7.5 hours after sunset.[10] Most such thermal storage systems operate with molten salts or thermal oils, which are also used as heat transfer fluid (HTF) and are currently limited to temperatures below 600 °C due to decomposition or corrosivity. These salts and oils mainly find

use in parabolic through CSP plants. In contrast, tower plants can utilize higher concentration ratios, reach higher temperatures and require thermal storage systems that can operate at such temperatures as well. Although research is ongoing for open absorber systems that facilitate air as the HTF, existing commercial solar tower plants, such as the PS10 in Spain and Ivanpah in USA, use steam at temperatures in the range of 250 °C and elevated pressures.

State-of-the-art thermal storage units for high temperatures beyond 600 °C are typically sensible thermal storage units, consisting of concrete or non-reactive ceramics.[11] Such storage units can operate with a variety of HTF and are not only considered for thermal storage of solar tower plants,[11] but also for industrial waste heat recovery[12] and electrically heated storage systems[13] in order to store energy of renewable power sources like PV or wind.

Due to the achievable high concentration ratios, tower plants such as the research facility Plataforma Solar de Almeria (PSA) depicted in fig. 1.2 are also utilized for high temperature applications beyond 700 °C. At such tower plants a field of mirrors, called heliostats, is located around a tower. The heliostats concentrate the solar radiation to a focal point at the top of the tower onto a receiver, thereby creating temperatures that can reach up to 1400 °C.[14]

Fig. 1.2.: Solar tower facility at the Plataforma Solar de Almeria, owned and operated by CIEMAT. Heliostats concentrate sunlight on a receiver, reaching high temperatures to drive a power cycle or thermochemical reactions. Source: DLR/Ernsting.

Such high temperatures can not only be utilized to run a turbine and produce electricity, but also to drive various chemical reactions. Among such reactions are two-step redox (reduction-oxidation) pair reactions based on metal oxides operating on the transition between the oxidized and the reduced state of an oxide. Most prominent is the production of hydrogen through water-splitting, but also nitrogen or carbon monoxide can be products of employed thermochemical processes. These processes are carried out in two steps. In a first step, a metal oxide is reduced, thereby releasing oxygen. In a second step, the metal oxide is re-oxized, absorbing oxygen again. Since the reduced metal oxide has a higher energy level than its oxidized counterpart, energy is stored in the reduction-oxidation, short redox, material in step one and can be utilized in step two. Depending on the source of oxygen during re-oxidation, different products are produced. Re-oxidation in step two can be performed with water (H_2O) to produce hydrogen (H_2), with carbon dioxide (CO_2 to produce carbon monoxide (CO) or atmospheric air to produce heat. The latter process can be used in thermal storage devices to increase thermal storage capacity and can also be utilized to separate oxygen and nitrogen from atmospheric air. A detailed overview of possible reactions that can be driven in solar thermal receiver reactor is provided in chapter 2.1 of this work.

For each of the described processes, materials need to meet certain criteria in order to be deemed suitable. Some of these criteria are rather fundamental chemical or physical properties, e.g. material need to have a certain reaction enthalpy to be able to split water or carbon dioxide, others are related economic and ecological factors, e.g. cost and health risks (toxicity). Additionally, also geopolitical considerations and market availability come into play when new materials are developed. In fig. 1.3 a periodic table of elements is depicted, indicating the abundance as well as the Herfindahl-Hirschmann-Index (HHI), an economic index representing market concentration. A high HHI thereby indicates that the market is heavily concentrated on only a few producers. Speaking in color schemes, new materials that are developed for large industrial processes across the globe in significant quantities should consist of elements in the blue, light blue or green range in fig. 1.3 with respect to abundance and market availability.

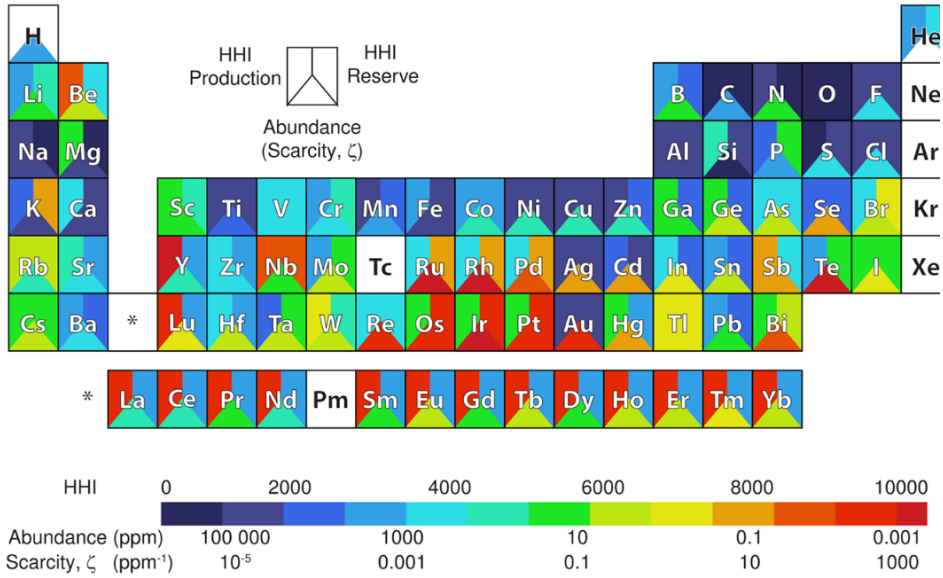

Fig. 1.3.: Periodic table indicating elemental scarcity and HHI indices for most elements (2011 data). Reprinted with permission from Gaultois et al..[15] Copyright 2013 American Chemical Society.

In this context, materials that consist of alkaline earth elements like Mg, Ca and Sr or transition metals like Ti, Cr, Mn, Fe, Ni become very attractive from an economic and, with some exceptions like Cr and Ni, ecological perspective. This factor should not be underestimated. Material compositions from the perovskite class in the form of ABO_3 with A = [Mg, Ca, Sr...] and B = [Ti, Cr, Mn, Fe, Ni...] are not only widely regarded as potent materials for thermochemical applications because they have suitable chemical and physical properties, but also because they can be made from abundant, low-cost and non-toxic elements.

In this work, perovskite compositions based on the Ca-Mn-O system are explored as reactive materials in thermochemical applications with a focus on thermochemical energy storage and oxygen gas atmosphere control, which includes thermochemical oxygen pumping and air separation processes. First of their kind reticulated porous structures, made entirely from reactive perovskite material, are produced and tested in lab-scale demonstration setups.

2. Theory and Background

In this chapter the theoretical foundation and technological background required to put the results of this work into context are introduced.It covers metal oxide redox reactions and their utilisation in solar powered thermochemical cycles, reactor concepts to harvest concetrated solar energy, an energetic analysis of redox thermochemical cycles, production routes of open porous ceramics and an introduction to the perovskite material class.

2.1. Solar Powered Thermochemical Cycles with Redox Oxides

Redox-oxide based two-step thermochemical cycles typically exist of a reduction reaction at higher temperatures and an oxidation reaction at lower temperatures. Combined, this pair of reactions is also referred to as a redox reaction and involves the release of oxygen during the reduction step and the incorporation of oxygen during the oxidation. In general, a multitude of thermally powered reactions can be run in this fashion. Solar applications, powered by means of CSE, include fuel production like water splitting (WS) and carbon dioxide splitting (CDS), thermochemical energy storage (TCES), thermochemical oxygen pumping (TCOP) and air separation. While industrial waste heat recovery is an option to supply the necessary energy, it typically delivers process heat in the lower temperature region <500 °C, favorable for TCES with hydroxides like $Mg(OH)_2$ and $Ca(OH)_2$.[21] However, CSE has the potential to deliver process heat up to >1400 °C, making metal oxides the predominant candidates for the above mentioned applications in the context of CSE.

The reduction of the metal oxide can occur either stoichiometric and in one single step,

This chapter is partially based on peer-reviewed publications authored and co-authored by the author of this work:

Christos Agrafiotis, Mathias Pein, Dimitra Giasafaki, Stefania Tescari, Martin Roeb, and Christian Sattler. "Redox Oxides-Based Solar Thermochemistry and Its Materialization to Reactor/Heat Exchanger Concepts for Efficient Solar Energy Harvesting, Transformation and Storage". In: *Journal of Solar Energy Engineering* 141.2 (2019). DOI: 10.1115/1.4042226

Mathias Pein, Christos Agrafiotis, Josua Vieten, Dimitra Giasafaki, Stefan Brendelberger, Martin Roeb, and Christian Sattler. "Redox thermochemistry of Ca-Mn-based perovskites for oxygen atmosphere control in solar-thermochemical processes". In: *Solar Energy* 198 (Mar. 2020), pp. 612–622. DOI: 10.1016/j.solener.2020.01.088

Mathias Pein, Nicole Carina Neumann, Luke J. Venstrom, Josua Vieten, Martin Roeb, and Christian Sattler. "Two-step thermochemical electrolysis: An approach for green hydrogen production". In: *International Journal of Hydrogen Energy* 46.49 (2021), pp. 24909–24918. ISSN: 0360-3199. DOI: https://doi.org/10.1016/j.ijhydene.2021.05.036

Mathias Pein, Luca Matzel, Lamark de Oliveira, Gözde Alkan, Alexander Francke, Peter Mechnich, Christos Agrafiotis, Martin Roeb, and Christian Sattler. "Reticulated Porous Perovskite Structures for Thermochemical Solar Energy Storage". In: *Advanced Energy Materials* 2102882 (2022). ISSN: 1614-6832. DOI: https://doi.org/10.1002/aenm.202102882

Lena Klaas, Mathias Pein, Peter Mechnich, Alexander Francke, Dimitra Giasafaki, Dorottya Kriechbaumer, Christos Agrafiotis, Martin Roeb, and Christian Sattler. "Controlling thermal expansion and phase transitions in Ca1−xSrxMnO3−δ by Sr-content". In: *Physical Chemistry Chemical Physics* 24 (45 2022), pp. 27976–27988. DOI: 10.1039/D2CP04332G

or non-stoichiometric and continously. Stoichiometric redox reactions are characterized by an uptake and release of a well-defined amount of oxygen and complete transition from one crystal phase to another throughout reduction and oxidation. An example is given for the reduction of cobalt(II,III)-oxide to cobalt(II)-oxide and its reverse reaction the oxidation in eq. 2.1 and eq. 2.2.

$$2\,Co_3O_4 \xrightarrow{+\Delta H} 6\,CoO + O_2 \qquad (\text{Reduction}) \tag{2.1}$$

$$6\,CoO + O_2 \xrightarrow{-\Delta H} 2\,Co_3O_4 \qquad (\text{Oxidation}) \tag{2.2}$$

At a given temperature and oxygen partial pressure, resulting in a Gibbs free energy below zero, the reaction takes place spontaneously until its completion. When the oxygen partial pressure is held constant (e.g. through continuous fresh air supply), reduction and oxidation take place in a small temperature window, making it ideal for TCES. Since the reduction is endothermal, thermal energy can be stored in the reduced oxide and be released again in the exothermal oxidation. For cobalt oxide, this has already been demonstrated in a 74 kW h reactor, containing 90 kg of Co_3O_4.[22–24] Other examples of stoichiometric oxides in solar-thermochemical applications are copper oxide,[25] barium oxide,[26] manganese oxide[27] and lead oxide[28] considered for TCES, as well as zinc oxide,[29–31] iron oxide[32–34] or tin oxide[35] that have been tested for thermochemical fuel production (WS/CDS).

Stoichiometric oxides undergo a complete change of the crystal structure throughout the conversion from their reduced to their oxidized state and vice versa. These crystal structures can be severely different. That is the case for cobalt(II,III)-oxide, which crystallizes in a spinell structure ($Fd\bar{3}m$) and converts to a cubic structure ($Fm\bar{3}m$) upon conversion to cobalt(II)-oxide. This change in the crystal structure leads to large expansion and contraction effects upon cycling,[19] increasing the chance of cracking and ultimately reducing the cyclic stability of solid oxide objects employed in solar reactor systems, like particles or granules. This cyclic expansion and contraction becomes even more important when reactor systems with non-moving monolithic solids, like honeycombs or foams, are utilized. Furthermore, this phase change results in slow reaction kinetics, as much more time is needed to reach equilibrium.[36]

Non-stoichiometric redox oxides on the other hand are characterized by the gradual generation of oxygen vacancies upon reduction without drastically altering the crystal structure. Quickly after being proposed as a potential candidate for thermochemical wa-

ter and carbon dioxide splitting,[37] Ceria (CeO_2) and its doped variants evolved to be recognized as the state-of-the-art material in the field.[38] Perovskites, named after the mineral $CaTiO_3$, of the general formula ABO_3 represent a whole group of non-stoichiometric redox materials. Therein A and B can be replaced by a multitude of metal cations. The perovskite material class, being in the focus of this work, is discussed more detailed in section 2.5. Both, Ceria and Perovskites can release a substantial amount of oxygen upon reduction and retake the oxygen upon oxidation, without drastic alteration of the crystal lattice. An indicator for the amount of existing oxygen vacancies, and therefore the reduction extent, in the material is δ, which ranges from 0 – fully oxidized – to 0.5 – fully reduced. The fully reduced perovskite in the form of $ABO_{2.5}$ (also described as $A_2B_2O_5$) is a known as brownmillerite, named after the mineral $Ca_2(Al_Fe)_2O_5$. However, many perovskites destabilize at large values of δ and decompose or dissociate before reaching complete reduction to the brownmillerite. The general redox reactions for Ceria and Perovskites are given in eq. 2.3 - 2.6.

$$CeO_2 \xrightarrow{+\Delta H} CeO_{2-\delta} + \frac{\delta}{2}O_2 \qquad (Reduction) \qquad (2.3)$$

$$CeO_{2-\delta} + \frac{\delta}{2}O_2 \xrightarrow{+\Delta H} CeO_2 \qquad (Oxidation) \qquad (2.4)$$

The redox reactions of Perovskites are given in eq. 2.5 and eq. 2.6.

$$ABO_3 \xrightarrow{+\Delta H} ABO_{3-\delta} + \frac{\delta}{2}O_2 \qquad (Reduction) \qquad (2.5)$$

$$ABO_{3-\delta} + \frac{\delta}{2}O_2 \xrightarrow{-\Delta H} ABO_3 \qquad (Oxidation) \qquad (2.6)$$

Perovskites are extremely versatile as their A-site and B-site cations can be chosen from a vast amount of different combinations. That includes multi-cation perovskites such as $La_{0.6}Ca_{0.4}Mn_{0.6}Al_{0.4}O_{3-\delta}$[39] and even double perovskites such as $Sr_2CoNb_{0.3}Ti_{0.7}O_{6-\delta}$[40] that are considered for WS. The versatility makes perovskites a very interesting material class for various thermochemical applications, which are introduced in the following sections.

Fuel Production via Thermochemical Water and Carbon Dioxide Splitting

In order to split water or carbon dioxide, the oxidation of the reduced oxide is not done with oxygen but with H_2O or CO_2 resulting in eq. 2.7 and eq. 2.8 and in the production of H_2 and CO in the overall process.

$$CeO_{2-\delta} + \delta H_2O \longrightarrow CeO_2 + \delta H_2O \qquad (Oxidation, WS) \qquad (2.7)$$

$$CeO_{2-\delta} + \delta CO_2 \longrightarrow CeO_2 + \delta CO \qquad (Oxidation, CDS) \qquad (2.8)$$

These reactions only take place when the Gibbs free energy ΔG of the oxidation reaction is below zero, typically requiring high enthalpy changes and resulting in the fact that suitable oxides are hard to reduce in the first place. While the solar thermal aided H_2 and CO production route offers high theoretical efficiency, it suffers from obvious drawbacks that could not be overcome so far. High temperatures above 1300 °C are needed to sufficiently reduce the oxides, creating huge challenges with respect to reactor design and cyclic stability. Although being scaled up and put into operation up to 750 kW_{th}[14,41] the process suffers from thermal losses and low conversion rates, limiting its economic viability so far. Besides ceria and perovskites, ferrites and aluminates have been considered, some of which show promising results in isothermal process conditions.[42]

Hydrogen may already serve as a fuel to power fuel cell vehicles[43] or in the steel industries,[44] but together with carbon monoxide it becomes appealing to produce alkanes through the Fischer-Tropsch process:[45,46]

$$nCO + 2\,nH_2 \longrightarrow (CH_2)_n + nH_2O \qquad (2.9)$$

With rapidly shrinking fossil resources and an increasing demand of green house gas reduction, the synthetic petrochemical production of alkanes from green H_2 and CO appears to be a viable option. Especially in sectors like aviation, where alternatives like fully electric aviation are not yet competitive,[47,48] this source of practically zero-emission fuels can be crucial to reduce green house gas emissions. Naturally, the zero-emission argument only holds true if all energy throughout the production process is provided by renewable sources and the CO is produced from air-captured CO_2.

Thermochemical Energy Storage

Reliable and high energy density thermal energy storage (TES) is a crucial factor to implement CSP-plants as suppliers for electricity baseload, as it allows the plant to operate over night on a continuous 24h-scale. Until today, commercial deployment of high-temperature TES in CSP plants has been limited to steam accumulators and molten nitrate salts.[49] Steam accumulators are lacking in energy density for large scale thermal power plants and nitrate salts are limited by chemical stability to temperatures below 550 °C.[50] While inert oxide particles, like natural rocks, sand or minerals[51,52] as well as manufactured particles of alumina and silica[53,54] offer a low cost alternative and have been tested as storage media, they are still limited to sensible heat only. Utilizing a reversible chemical reaction with large heat effects offer a great possibility to increase the energy storage density significantly.

In accordance to eq. 2.1 and eq. 2.2, as well as eq. 2.5 and eq. 2.6, redox oxide thermochemical cycles can be utilized to store energy in addition to the sensible heat. The total energy storage capacity hereby is the sum of sensible heat and the chemical energy released as heat during the oxidation. A detailed look at energy analyis of such storage media is provided in section 2.3 later on. As stoichiometric materials, besides single cation oxides,[23,25–27,55,56] also mixed (Fe,Mn)-oxides[57–59] have been considered. Stoichiometric and non-stoichiometric oxides differ, above all, by the temperature window in which chemical energy is released. While stoichiometric oxides have a distinct equilibrium temperature at which the oxidation is completed, non-stoichiometric oxides are reduced and oxidized gradually and continuously over a wide temperature range. The stored chemical energy is released in the very same fashion, which is why stoichiometric TCES-devices are only able to provide heat at $T_{eq.}$ in addition to their sensible heat. In contrast, non-stoichiometric oxides are viable to be operated (meaning reduced and re-oxidized) at various, especially lower, temperatures, and over a wide range starting as low as 400 °C for $La_{1-x}Sr_xCo_{1-y}(Mn_Fe)_yO_{3-\delta}$.[60] This makes them particularly viable for CSP-plants that operate with air as a HTF.

Cobalt oxide has long been regarded as the leading candidate with theoretical storage densities of approx. 844 $\frac{kJ}{kg}$, but fell out of favor due to its toxicity and poor cyclic stability.[61] Perovskites may prove to be superior, utilizing non-toxic, earth-abundant and thereby low-cost elements and materials that overcome the drawback of lower storage densities. Moreover, they provide additional degrees of freedom when it comes to material design,[36] which can be utilized to adjust TCES-systems to particular power cycles like supercritical or air Brayton cycles.

Thermochemical Oxygen Pumping and Air Separation

Especially in WS and CDS processes, it is important to reach low partial pressures of oxygen ($p(O_2)$) in order to sufficiently reduce the metal oxide at reasonable temperatures and increase conversion efficiency per cycle. The two common ways to achieve low $p(O_2)$ are inert gas purging and vacuum pumping. The provision of highly pure inert gas in vast amounts and subsequent regeneration/recycling is a challenge, as it can add up to a significant energy penalty and negatively effect the overall process efficiency.[62–64] Sufficient vacuum can in most cases only be reached by turbo pumps, which not only have a high energy demand, but are also very costly. Brendelberger et al. have shown in a theoretical study that thermochemical oxygen pumping can be energetically beneficial compared to turbo pumps reaching low $p(O_2)$.[65] The study has also revealed that cheap mechanical pumps are superior to non-selectively remove gases down to a total pressure of approx. 100 Pa to 1000 Pa with subsequent selective reduction of the $p(O_2)$ by a thermochemical pump. A comparison of pumping options is given in fig. 2.5 in section 2.3.

A lab-scale demonstration of such process has been done with $SrFeO_{3-\delta}$ particles as the oxygen pumping material.[66] Another recently proposed approach is thermally driven adsorption/desorption cycles, utilizing high surface area materials.[67] Although thermochemical air separation serves the cause of producing highly pure N_2, the process is very much comparable to TCOP, as both processes thrive to reach very low $p(O_2)$ in a gas stream or chamber atmosphere. In ammonia production processes using the Haber-Bosch process, even minor oxygen contents can lead to poisoning of the catalyst material.[68,69] Ammonia is not only used in vast amounts in fertilizer production, but could also be used directly as fuel, e.g. in the shipping sector.[70,71] Producing H_2 and N_2 from solar-powered thermochemical processes can reduce green house gas emissions ammonia production significantly. In 2008 presumably 1% of the world wide primary energy demand was consumed by ammonia production alone.[72] This process chain for solar-aided ammonia and fertilizer production is schematically shown in fig. 2.1.

Due to their versatility and fast reaction kinetics, perovskites are drawing attention as potential materials for TCOP and air separation. Theoretical and experimental studies have been carried out to evaluate and identify suitable compositions.[74–77] A rather sophisticated approach to define materials design principles for perovskites in such applications has been done by J. Vieten.[78]

An overview of relevant CSE-applications utilizing perovskites is given in fig. 2.2. Therein, partial oxidation of methane and hybridized electrolysis can also be found. The former, also known as methan reforming, can be performed with steam (steam re-

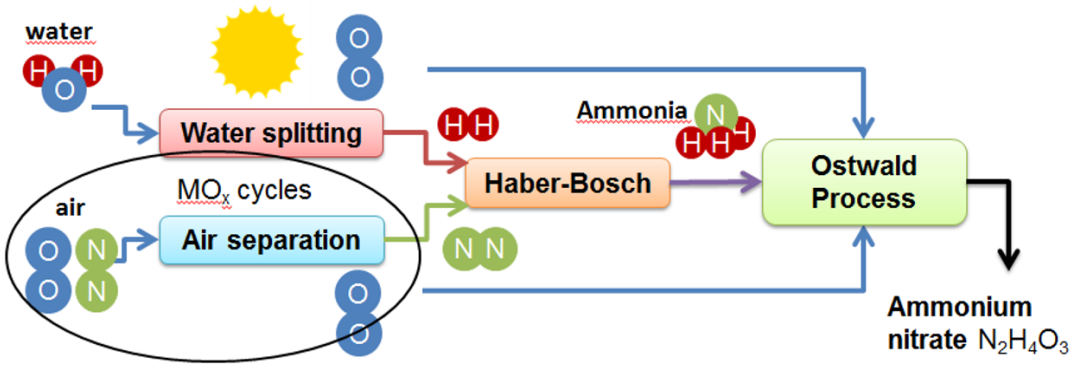

Fig. 2.1.: Schematic visualization of ammonia (Haber-Bosch process) and fertilizer (Ostwald process) production via solar-powered thermochemical production of H_2 and N_2. Taken with permission from Guban et al..[73]

forming), carbondioxide (dry reforming) or a mixture of both (mixed reforming). The reforming of methane is considered to be a bridge technology towards a hydrogen based energy supply and is, in general, a well known industrial process. If methane feedstock in this process is not supplied from natural gas, but from biogas it has the potential to contribute to the production of net-carbon-zero carbohydrate fuels for industrial sectors that still rely on such fuels, like the aviation sector. Hybridized electrolysis is a novel innovative process that has been developed at DLR's Institute of Future Fuels and combines high-temperature electrolysis with cyclic redox reactions as elucidated by Pein et al.[18] and the related filed patent.[79]

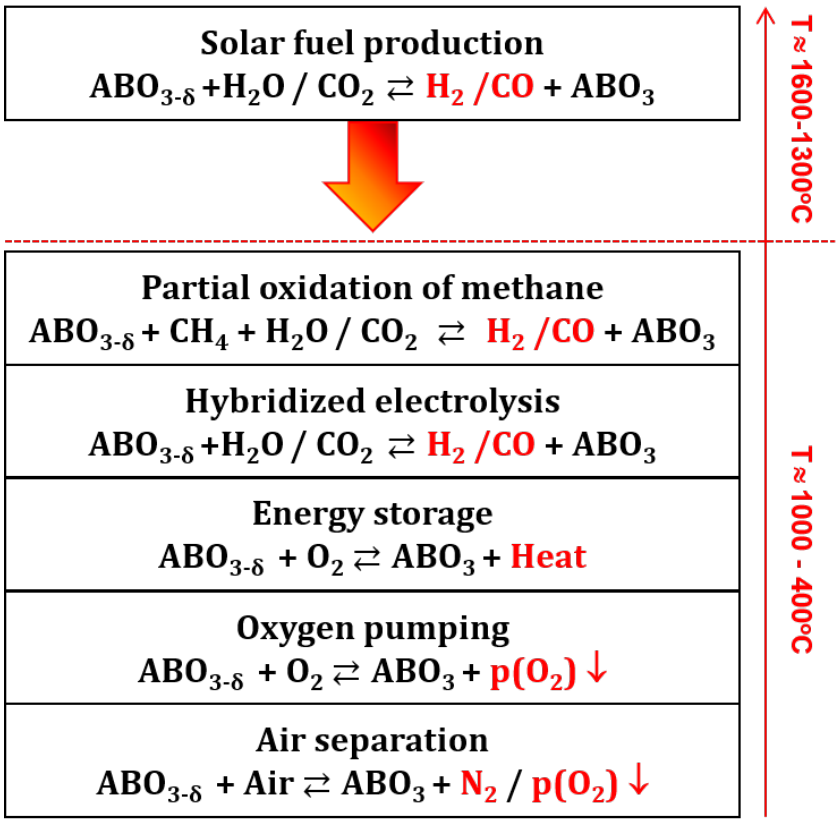

Fig. 2.2.: Potential thermochemical processes in a CSE-plant. Processes below the dashed red line can be powered down-stream with waste or excess heat from a main process above. Main processes include fuel production and power generation, but down-stream processes can also be run independent from a main process.

2.2. Reactor Concepts for Concentrated Solar Energy Harvesting

In principle the receiver of a CSE-plant is a heat exchanger, which is placed in the focal point of the heliostats. It captures high temperature heat from the concentrated solar irradiation. The resulting heat can be utilized in two ways. The heat is used within the receiver to drive a chemical reaction, like H_2O- or CO_2-splitting, or it is transferred by a HTF to power any reaction or process outside of the receiver. Utilising the heat inside the receiver is typically done in cavity receivers.[80–83] Transferring the heat away from the receiver through a HTF to a downstream-application is virtually independent of the receiver concept. However, the required temperature level of the desired application largely influences the choice of receiver, which has to be carefully adjusted to the

reached temperatures, heat amounts and the used HTF.

Although this work focuses on the actual downstream-applications, for now neglecting the way heat is exchanged with the solar receiver, a small overview on common receiver concepts is given in the following and a schematic depiction of commonly used receiver/reactor systems is shown at the end of this section in fig. 2.3.

Cavity Receivers and Reactors

In cavity receivers the absorber material is directly irradiated through a small aperture in a well-insulated enclosure. It is designed to reduce reradiation losses by allowing the absorber material to also absorb reflected sunlight and reradiated thermal radiation, ideally resulting in a blackbody-behavior. Additionally, cavity receivers allow to be operated in a fully clontrolled atmosphere by closing the aperture with a transparent, gas-tight window. That allows the receiver to be operated under pure inert-gas atmosphere or under vacuum during the reduction and under a defined steam-/CO_2-atmosphere during the oxidation. In addition to the very high temperatures that are possible, cavity receivers are a preferred choice for H_2O- and CO_2-splitting reactors. Cavity receivers such as rotatary kilns[84,85] or the Centrec receiver[86,87] typically involve moving particles as absorbers, while other concepts do not include any moving solid parts. Only gases are transported in and out of the cavity either as HTF or reactants. Open porous structures like foams or honeycombs are often used inside cavity receivers to further decrease reradiation losses, increase reactive surface area and control the gas-flow through the receiver. Such a cavity receiver-reactor concept that utilises open porous Ceria structures for WS/CDS has been developed, studied and optimised by a consortium lead by research groups from APTL and DLR in a series of projects developing a $750kW_{th}$-solar reactor.[14,81,88–91]

Particle Receivers

Directly irradiated particle receivers in its simplest form are free-falling particle receivers, where a curtain of falling particles is irradiated by concentrated sunlight through an aperture. Since its inception in the 1980's a multitude of studies have been performed.[92–95] However, free-falling particle receivers are not capable of reaching sufficiently high temperatures for H_2O- and CO_2-splitting and can only be operated in direct contact to atmospheric air. Novel design concepts have been investigated that include a dome or window to enclose the receiver and exlude contact to the outside atmosphere.[96]

Obstructed particle flow receivers, where particles are moved, for example with a cylindrical conveyor, ensure a longer residence time and are able tp reach higher temperatures and increased thermal efficiency, but cause issues with obstruction or blocking of the conveyor and discontinouos mass flow.

For thermochemical applications, the most promising particle receiver concept is that of the fluidized bed.[97] Therein, very small particles are fluidized by an external gas stream while being irradiated through an aperture. Temperatures over 1000 °C can be reached and operation can be done in enclosed atmospheres.[98–101] Additionally, particle receivers offer the possibility to use the particles not only as the absorber material, but also as the HTF and direct thermal storage medium. Naturally this requires additional engineering effort as hot particles need to be moved and handled. Attrition, cyclic stability, thermal insulation and heat transfer during discharge become even more relevant in that case.

Open Volumetric Receiver

Open volumetric receivers consist of solid, open porous shapes (honeycombs, foams, knit-wire packs etc.) that allow concentrated radiation to penetrate deep into the structure and therefore enable absorption in the depth of the receiver.[102] The concept of open volumetric receivers has been investigated and developed since the 1980's, mostly under the lead and involvement of DLR.[103–107] On that regard open volumetric receivers technically are cavity receivers and share some of their benefits as well. The irradiation and heat transfer approach however is much more straight-forward. Open volumetric receivers are often shaped in simple forms like rectangles and are open to atmosphere air. In fact open volumetric receivers use air as the working HTF, which is sucked into the receiver and heated up by forced convection through the receiver. Absorber materials may consist of metals or ceramics. Despite their relatively high costs, SiC-based ceramics are prevalent in open volumetric receivers due to their adequate absorptivity, high melting point, mechanical robustness and good thermal shock resistance. Additionally, high temperatures in the range of 1000 °C to 1500 °C are possible.

While commercial CSP-plants for electricity production are mainly equipped with tubular external receiver systems, utilizing steam of molten salts as HTF, the open volumetric receiver concept has been investigated not only for electricity production, but also to supply heat for industrial processes.[108–110] Given the high temperatures and air as the HTF, thermal storage units of such plants typically consist of low-cost inert solids like concrete or sand. Through heat exchangers the heat is used to power a steam-power

cycle for electricity generation. Allowing direct contact of the thermal storage medium to the HTF reduces the plants complexity and simplifies the handling of the storage unit. A similar receiver approach is the so-called external receiver, which typically exists of a tubular arrangement of non-moving absorber material. External receivers are irradiated from 360° and therefore find use almost exclusively in solar tower plants that operate with a circular heliostat field around the central receiver, which is irradiated from all sides.

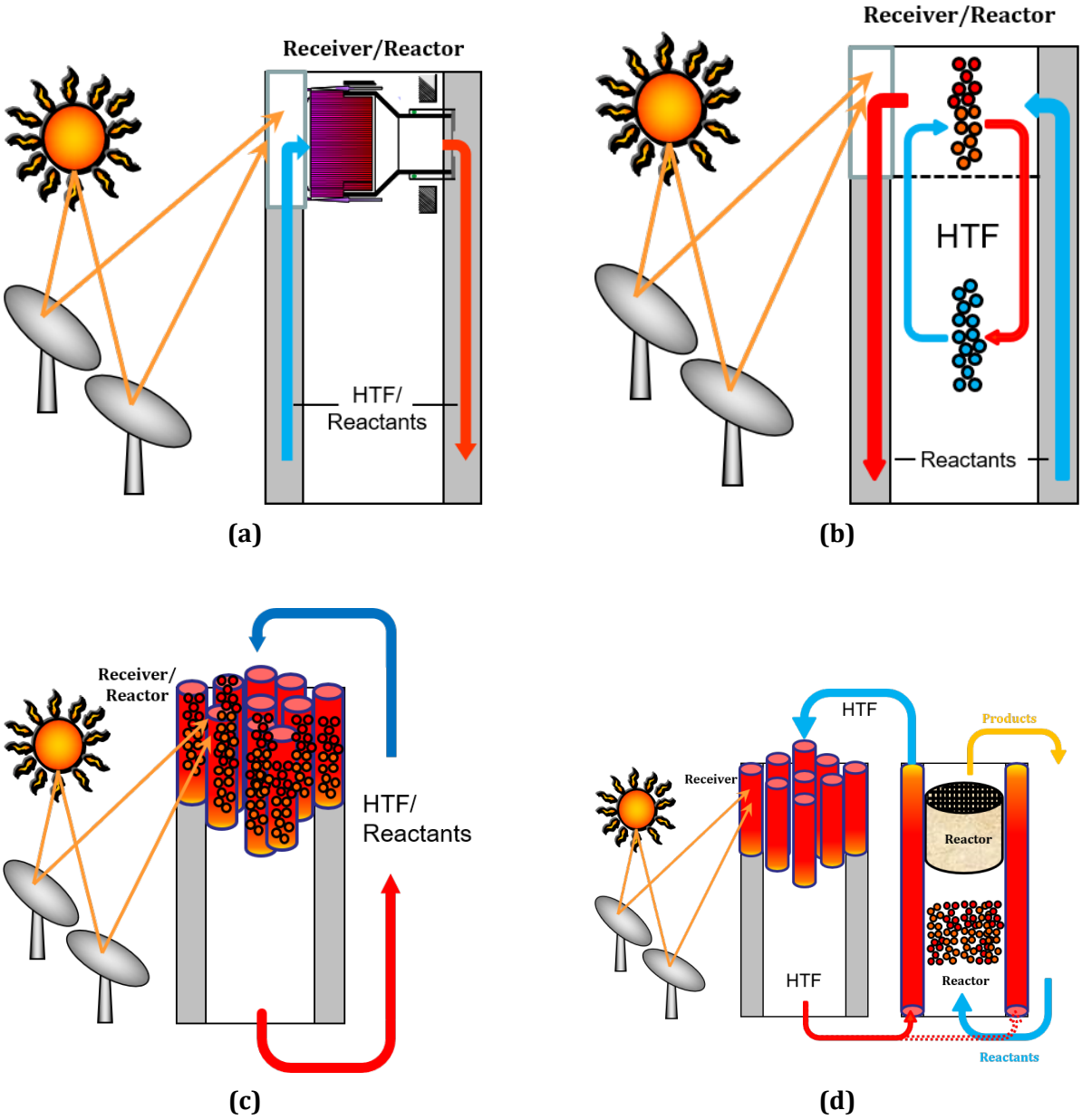

Fig. 2.3.: Schematic depiction of common receiver/reactor concepts in CSE. a) Open volumetric receiver/reactor; b) Direct particle receiver/reactor; c) Indirect particle receiver/reactor; d) Indirect receiver with separated reactor. Adapted from Lu et al.,[38] Copyright 2019, with permission from Elsevier.

2.3. Energy Analysis of Redox Cycles

In order to evaluate and compare different material compositions with respect to their energy demand to drive the redox reaction, it is crucial to implement a common basis for

energy analysis of such cyclic redox reactions. Since this work focuses on downstream applications, any reactions that involve fuel production (H_2O- and CO_2-splitting) are omitted here. Additionally any parasitic energy consumption, e.g. from pumping sweep gases, are neglected in the following as they are dependent on the exact receiver/reactor setup that is used and are not directly related to material properties. As long as identical conditions are assumed for every material composition, it is reasonable to exclude such non-material related factors from the analysis for comparison. In terms of concentrated solar energy plants, the total amount of energy needed to drive the redox reaction, and therefore has to be supplied by CSE, can be defined as:

$$Q_{CSE} = Q_{chem} + Q_{sens}(+Q_{losses}) \tag{2.10}$$

Q_{CSE} : Total energy supplied by CSE

Q_{chem} : Chemical energy to reduce the material

Q_{sens} : Sensible energy needed to heat the redox material from T_{ox} to T_{red}

Q_{losses} : Thermal losses

For stoichiometric oxides T_{ox} and T_{red} represent the lower and upper limit of the temperature range the material is cycled within. In the case of stoichiometric oxides the oxidation and reduction temperatures are only separated by a small hysteresis considering otherwise stable conditions. The thermal losses Q_{losses} are not considered any further as they are independent of material composition. It becomes clear that in the context of thermal energy storage, TCES can add additional storage capacity compared to sensible-only thermal energy storage systems through the chemical energy Q_{chem}. In the case of H_2O- and CO_2-splitting, Q_{chem} represents additional demand for the splitting reaction. For stoichiometric redox oxides Q_{chem} is quite simply given by the reaction enthalpy ΔH:

$$Q_{chem} = \Delta H_R \tag{2.11}$$

In contrast, non-stoichiometric redox oxides like perovskites are continously reduced and oxidized over a range of δ. Therefore exploitable Q_{chem} depends on the reduction extent δ. Additionally, ΔH_R is frequently not independent from δ. The chemical energy Q_{chem} of the perovskite can then be calculated by integrating $\Delta H_R(\delta)$ in the borders of the minimum and maximum reduction extents δ_{ox} and δ_{red}:

$$Q_{chem} = \int_{\delta_{ox}}^{\delta_{red}} \Delta H_R(\delta) \mathrm{d}\delta \tag{2.12}$$

In fact ΔH_R can also be dependent on the temperature. There are no reports pointing out that this is the case for perovskite materials, which is why temperature dependence of ΔH_R is neglected within this work. When fully oxidized and reduced states are considered, given at $\Delta\delta = \delta_{red} - \delta_{ox} = 0.5$, eq. 2.12 and eq. 2.11 are equivalent. At $\Delta\delta = 0.5$ the material is technically no longer considered a perovskite, but a brownmillerite with the chemical formula $ABO_{2.5}$ (or $A_2B_2O_5$) that crystallises in an orthorhombic structure (space group: Ibm2). Many perovskites however will dissociate or decompose before reaching a $\Delta\delta = 0.5$. Exact limitations are unique to each composition and need to be considered accordingly.

As described previously, some perovskite undergo phase transitions from the ideal cubic to distorted hexagonal, tetragonal or orthorhombic structures and vice versa depending on the temperature and the reduction extent. For Ca-Mn-based perovskites and its doped variants, such (reversible) phase transitions from orthorhombic to cubic have already been reported and linked to endo- and exothermal heat effects.[17,19,111–113] The intercorrelation of structure and heat effects, and how this can be exploited through materials design, will be discussed in the later chapters of this work. The exploitable amount of chemical energy from the redox reaction Q_{chem} needs to be extended by the possible contribution of a reversible phase transition in the crystal structure of the perovskite. Extending eq. 2.12 by the heat effect of a phase transition ΔH_{pt} results in:

$$Q_{chem} = \int_{\delta_{ox}}^{\delta_{red}} \Delta H_R(\delta) + \Delta H_{pt}(\delta, T) \mathrm{d}\delta \tag{2.13}$$

Depending on the range of temperature and δ, there might even be more than one reversible phase transition with significant heat effects resulting in multiple contributions ($\Delta H_{pt,1}$, $\Delta H_{pt,2}$ etc.). This property is not exclusive for perovskites, but can also be found in stoichiometric oxides and does not strictly have to involve changes in crystal structure.

For example, Co^{3+}-cations in Co_3O_4 have been reported to reversibly transition from a low-spin to a high-spin electronic state with considerable heat effects involved.[36,114,115] The sensible energy Q_{sens} originates from the materials heat capacity C. The heat capacity of a material represents the amount of thermal energy that is needed to raise its temperature by 1 K. Vice versa it is the amount of thermal energy released when cooling down the material by 1 K. It is typically given either for constant pressure, C_p, or constant volume, C_v. Since we are only considering solids, it is reasonable to assume $C_p \approx C_v = C$. Therefore, the value C is used in the following.

This sensible energy always has to be supplied to heat a material, and represents a main source of recuperated heat, especially in cyclic processes where redox material is heated and cooled repeatedly in a cyclic fashion. For perovskites, the Debye model can be used to determine heat capacities. The heat capacity C can then be described in dependency on the temperature T and the Debye temperature Θ_D:[116,117]

$$C(T) = 9R \left(\frac{T}{\Theta_D}\right)^3 \int_0^{\frac{\Theta_D}{T}} \frac{x^4 e^x}{(e^x - 1)^2} \mathrm{d}x \cdot n_a \tag{2.14}$$

n_a represents the amount of atoms per formula unit. For perovskites n_a varies between 5 for the fully oxidized state and 4.5 for the fully reduced brownmillerite. It has to be mentioned that the Debye temperature Θ_D is in fact also dependent on the reduction extent δ, represented by $\Theta_{D,\delta}$. Only few experimental values of Debye temperatures of perovskites are available and available theoretical values only cover fully reduced ($\delta = 0.5$) and fully oxidized ($\delta = 0$) formulas. For values of $0 < \delta < 0.5$, $\Theta_{D,\delta}$ can be estimated by linear interpolaration between $\Theta_{D,\delta=0.5}$ and $\Theta_{D,\delta=0}$. Thereby, linear interpolation between the extreme values of $C(T, \Theta_{D,\delta}$ for $\delta = 0$ and $\delta = 0.5$ is used, resulting in:[78]

$$C(T, \delta) = C(T, \delta = 0, \Theta_{D,\delta=0}) \cdot (1 - 2\delta) + C(T, \delta = 0.5, \Theta_{D,\delta=0.5}) \cdot 2\delta \tag{2.15}$$

This model to calculate heat capacities of perovskites has been successfully utilized by Vieten et al..[77,78] At $T >> \Theta_{D,\delta}$, we can describe the heat capacity of a perovskite in relation to the reduction extent δ, according to the Dulong-Petit law, as:

$$C(\delta) = 3 \cdot R \cdot n_a = 3 \cdot R \cdot (5 - \delta) \tag{2.16}$$

While this assumption is reasonable for some perovskites that show Debye temperatures below 600 K like $LaCoO_3$ and $LaFeO_3$,[118,119] it may not be correct for every per-

ovskite. However, if second-order phase transitions, such as magnetic order-disorder transitions, are ruled out or neglected, eq. 2.16 can serve as an upper threshold and good approximation of heat capacity values at $T > \Theta_{D,\delta}$ for all perovskites. Using eq. 2.16 instead of eq. 2.15, may lead to less accurate values, but rather overestimates the energy demand with respect to the sensible heat of a perovskite, making it still a viable option to quickly compare perovskites to one another or to other competitors qualitatively. As demonstrated in fig. 2.4, eq. 2.16 exhibits close proximity to calculated values from eq. 2.14 in the case of $CaMnO_{3-\delta}$ with only 2.6% and 4.8% deviation at 873 K for the reduced and oxidized state respectively. In first approximation, eq. 2.16 results in values between $\approx 112 \frac{J}{mol \cdot K}$ and $\approx 124 \frac{J}{mol \cdot K}$, which fits values reported for $SrFeO_3$ from theoretical calculations[77] and experiments.[120]

Other research groups reported values $> 150 \frac{J}{mol \cdot K}$[121,122] for La-Mn-based compounds, using different approaches such as the Neumann-Kopp rule,[123] which estimates the heat capacity of mixed oxides by the stoichiometric mixing of its compounds heat capacity. For stoichiometric oxides, like Co_3O_4 and Mn_3O_4, literature values are available by Barin[124] and are plotted together with values for $CaMnO_3$, which have been calculated via eq. 2.15, in fig. 2.4. Values of $\Theta_{D,\delta}$ were derived from available Data on *Materials Project*[77,125] and are given as $\Theta_{D,\delta=0} = 847.3K$ and $\Theta_{D,\delta=0.5} = 632.8K$.

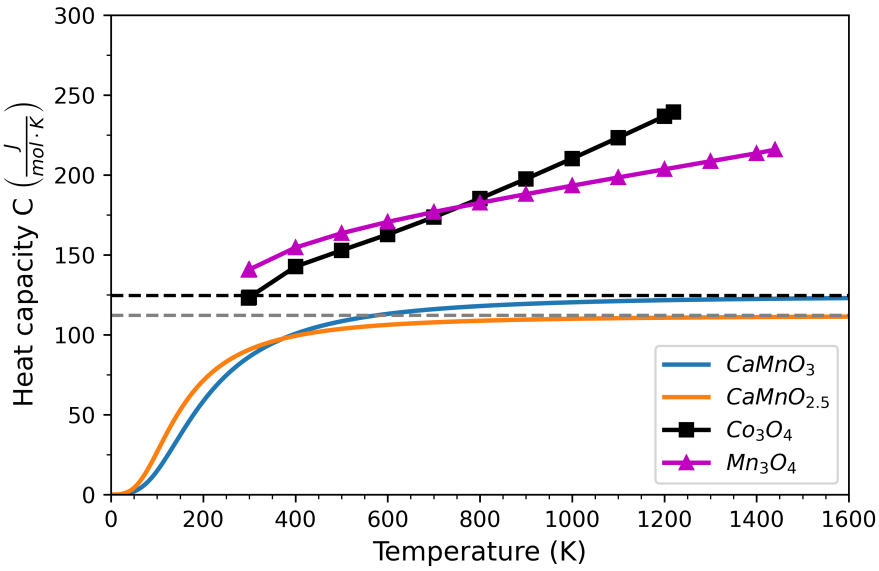

(a)

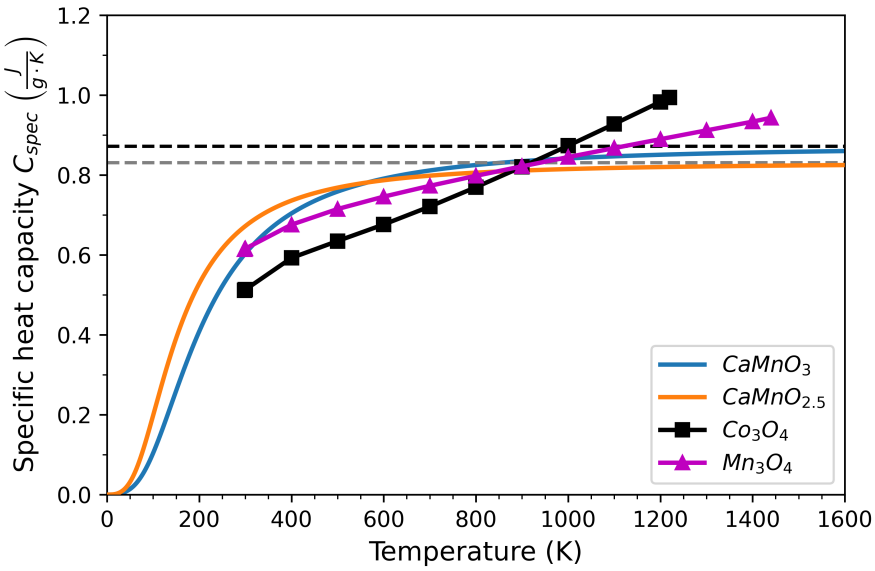

(b)

Fig. 2.4.: Heat capacities of $CaMnO_3$, $CaMnO_{2.5}$, Co_3O_4 and Mn_3O_4. a) Heat capacity per mol of oxide; b) Specific heat capacity per gram of oxide. Values of $CaMnO_3$ are calculated theoretically according to eq. 2.15. Values for Co_3O_4 and Mn_3O_4 are taken from Barin..[124] Approximations for heat capacities of the perovskite according to eq. 2.16 are given in black ($\delta = 0$) and grey ($\delta = 0.5$) dashed lines.

The stoichiometric redox oxides Co_3O_4 and Mn_3O_4 have substantially higher heat capacities per mol oxide compared to $CaMnO_{3-\delta}$ but using values per mole is rather uncommon in technical evaluation of such energy storage systems. Materials on the world market are typically traded in units of weight. Additionally, weight and volume are the most important factors to determine the costs of a storage unit. Therefore, the specific heat capacity C_{spec}, given in $\frac{J}{g \cdot K}$, is used in the scope of this work. Notably, $CaMnO_{3-\delta}$ has the lowest density of the three compared materials ($\rho_{CaMnO_{3-\delta}} = 4.35 \frac{g}{cm^3}$ vs. $\rho_{Co_3O_4} = 6.11 \frac{g}{cm^3}$ vs. $\rho_{Mn_3O_4} = 4.86 \frac{g}{cm^3}$) and thereby the smallest volume at identical weight amounts of material. As can be seen in fig. 2.4b, all three materials show comparable values for C_{spec}, especially in the temperature range of interest (873 K to 1273 K), which is in accordance to values reported in literature.[126]

In contrast to TCES units, which are typically designed to be operated with air as the HTF, additional care has to be taken if water or carbon dioxide are to be splitted in a thermochemical reactor. For a redox material to split H_2O during oxidation for example, its reaction enthalpy has to match at least that of the formation enthalpy of H_2O. The same applies for CO_2-splitting. In order to account for losses, reaction rates and conversion efficiency, ΔH_R of considered materials are required to be even higher. The reaction enthalpy of Ceria, widely considered as state-of-the-art for thermochemical water splitting, ranges from $\sim 475 \frac{kJ}{mol_O}$ to $\sim 400 \frac{kJ}{mol_O}$ depending on δ.[127–130] In comparison, the formation enthalpy of H_2O is substanially smaller with 241 $\frac{kJ}{mol_O}$.[131]

The high enthalpy of materials that are able to split water during oxidation comes at the price of less reducibility, meaning high temperatures in the range of 1300 °C to 1600 °C are needed to reach reduction extents that produce sufficient conversion rates in a cyclic redox process. In addition to the high temperatures, low $p(O_2)$ are needed, in accordance to eq. 2.21, to further increase the reduction extent δ. In order to achieve sufficiently low $p(O_2)$ the two main options that have been applied so far are inert gas sweeping and vacuum pumping. The utilization of sweep gas to reach low $p(O_2)$ has been shown to have lower overall process efficiences compared to mechanical vacuum pumping.[132] On top of that, recent studies by the same group revealed that thermochemical oxygen pumping has the potential to outperform mechanical pumping, especially at pressures below 100 Pa.[65,66] Fig. 2.5 depicts the comparison of a various mechanical pumping options, a mechanical envelope function and thermochemical oxygen pumping based on the Co_3O_4 redox cycle.[65] The underlying models of this study, have been reported by Brendelberger et al..[65,66]

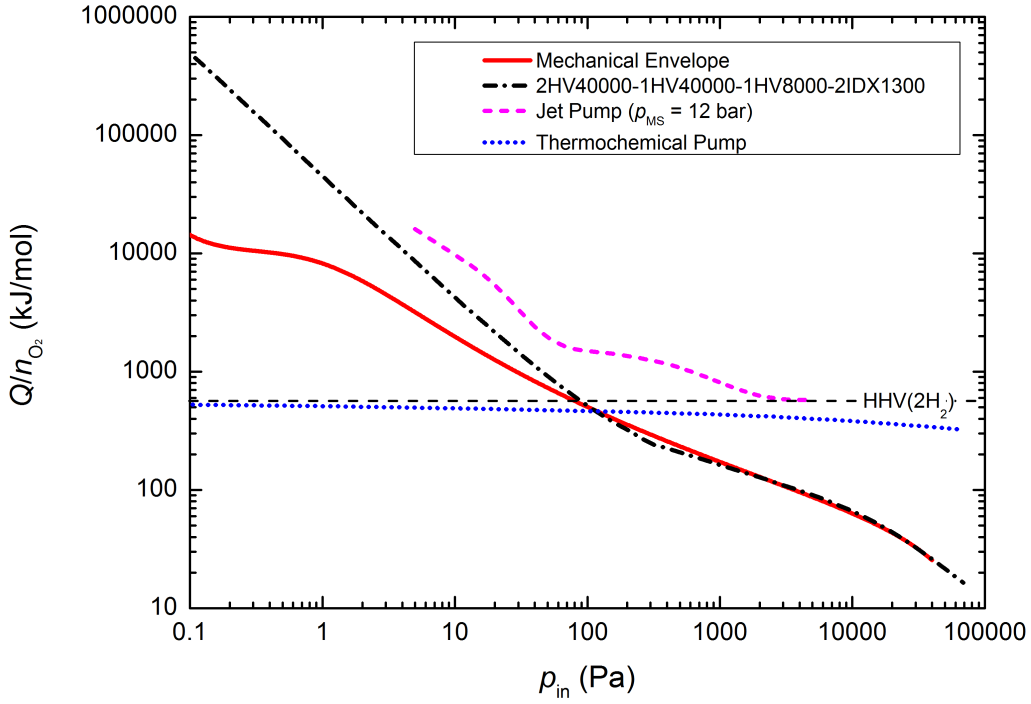

Fig. 2.5.: Comparison of different pumping systems based on a study of Brendelberger et al., showing thermochemical oxygen pumping may outperform mechanical vacuum pumping at low $p(O_2)$. Calculations for thermochemcial oxygen pump are based on Co_3O_4-redox cycle. Reprinted from Brendelberger et al.,[65] Copyright 2017, with permission from Elsevier.

In order to maximize system efficiency in any of the described thermochemical processes utilizing cyclic reduction and oxidation of a metal oxide, powered by concentrated solar irradiation, not only the material choice needs to be considered, but also the designated receiver/reactor design as well as the peripheral system has to be taken into account. This requires interdisciplinary collaboration in the fields of engineering, chemistry, physics and material science. It might be that a certain material would theoretically exhibit extraordinary performance, but cannot be implementend in the foreseen reactor concept due to practical limitations. Furthermore, the best performing reactor system might never find its use, because no material fulfills the necessary requirements for operation. Therefore, it is commong to either develop better performing materials for certain processes and build a reactor and operation concept around it or start from the reactor side and then try to identify materials that could work under the given op-

eration principles. Either way, both efforts need to be combined to further develop the technology as a whole.

In this work a generic approach from the perspective of materials development is chosen, which is designed to be flexibly implemented into existing reactor concepts. In order to reduce complexity of the framework wherein materials and components are investigated, reasonable limitations, e.g. only gaseous HTF and downstream/indirectly heated reactors, have been made.

2.4. Open Porous Ceramics for Thermochemical Cycles

Due to their beneficial characteristics like high thermal shock resistance, low density high permeability, mechanical rigidity and chemical resistance, open porous ceramic structures are widely used in various technical applications in the fields of engine exhaust filters, molten metal processing and catalyst support.[133–135]

Predominantly, SiC and SiSiC ceramics are also employed as absorber materials in receivers for CSP,[108,136] where typically air is used as HTF, reaching temperatures above 1000 °C to drive a downstream power cycle for electricity generation. If receiver materials are not only used as absorber material, but also as an active reactant in thermochemical applications, a lot more requirements, when it comes to material choice, have to be met. Specifically ensuring mechanical stability, cyclability, thermal shock resistance and stable conversion rates are challenging, due to increased thermal expansion during reduction and oxidation, sintering effects, thermal stresses and loss of reactivity. These requirements have sparked research to improve compositions and structures used in such applications.[82,137–139] In order to overcome some the above mentioned restraints, efforts have been made to coat reactive redox materials onto inert ceramic support structures. Commercially available open porous ceramic structures, like honeycombs or foams made from cordierite, can be dipped into a slurry mixture, containing fine powders of the redox material and subsequently dried and sintered. For TCES with Mn-, and Co-oxides, this has been extensively investigated in a series of research work by Agrafiotis et al.[55,56,140–143] after originally being considered for H_2O- and CO_2-splitting with Fe-based oxides[144] and La-Mn-based perovskites.[145,146]

However, coating active material onto inert ceramic supports does come at the drawback of a limited load of active material. The support material has to be heated without taking part or contributing to the thermochemical reaction, resulting in major energy penalties, especially when temperature swings are employed. Monolithic structures, en-

tirely made from redox material, raise interest due to the much higher load of active material per unit where all the bulk material, in theory, takes part in the reaction.

Addressing this issue, researchers from ETH Zurich have successfully produced monolithic structures from the state-of-the-art H_2O-splitting material Ceria and have tested them in lab-scale tests and small scale solar reactors.[4,138,147–151] The predominant technique to produce such monolithic open porous ceramic structures, also called reticulated porous ceramics (RPC), is the so-called replica-method, originally proposed by Schwarwalder and Somers.[152] Therein a previously manufactured polymeric sponge with a defined porosize-distribution is immersed in a viscous slurry that contains the redox material and an organic binder. The slurry sticks to the sponges surface, even after drying, resulting in the RPC green body. In a subsequent firing step the polymeric support structure and the organic binder are burned off and the ceramic particles are sintered, resulting in a ceramic replica of the original polymeric sponge.

The replica-method is a presumably easy process, but a lot of factors, like the ceramic powders particle size distribution, dispersant, type of binder, pH and rheological behavior of the slurry, drying and firing procedure, need to be considered to produce rigid and stable structures. Nonetheless, once a suitable recipe is defined, the replica method provides a reliable way to produce monolithic open porous ceramics, which is a desirable option for thermochemical applications. In addition to having higher loads of redox active material in the absorber/reactor compared to coated support structures, monolithic foams still offer all the benefits of rigid, stable and durable open porous structures. Compared to flow-through ceramic honeycombs usually made by extrusion, the foams' extremely high, yet interconnected porosity provides for a very low pressure drop, a feature that renders them suitable for use with pressurized gaseous HTFs. Foams also exhibit enhanced mass and heat transfer due to high convection in the winding open flow channel network and a considerable degree of radial mixing, which is advantageous in potentially heat transfer-limited processes.[153] Such foams can also be used in a modular fashion in non-moving systems utilizing pressurized gaseous HTF, while only exhibiting minor pressure changes.[136]

2.5. Perovskites

In the following, the chemical and structural characteristics of perovskite metal oxide material class are outlined. Thermodynamic and kinetic considerations are described and the suitability of perovskites for thermochemical redox processes is set forth.

Perovskite Chemistry

The material class of perovskites is named after a mineral containing $CaTiO_3$, which was first described by Gustav Rose in the early 19th century[154] and was named "Perowskit" in honor of the mineralogist Lew Perowski. Although the eponymous composition $CaTiO_3$ crystallizes in a distorted orthorhombic structure, perovskites of the general formula ABO_3, with A and B representing metal cations, are characterized by an ideal cubic crystal structure in space group $Pm\bar{3}m$. In alignment with $CaTiO_3$, distorted variants of the ideal cubic structure are generally described as perovskites as well. Additonally there exist hybrid mixed organic-metal-halide perovskites, which contain organic molecules and are used in solar cells[155,156] and lasers.[157]

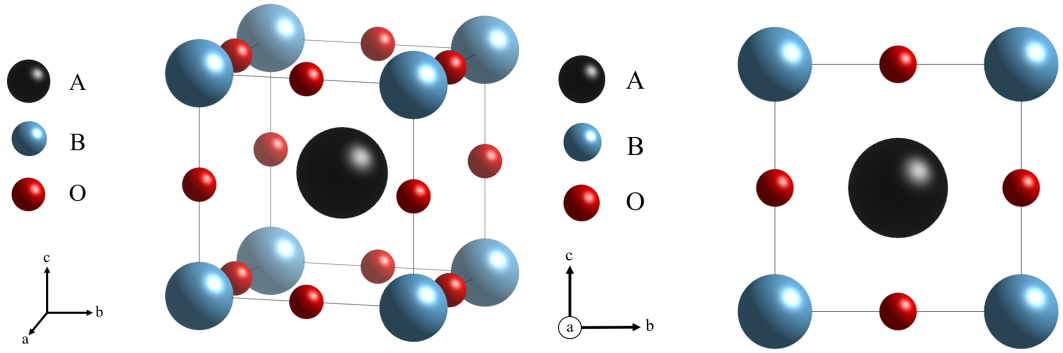

Fig. 2.6.: The ideal cubic perovskite structure. A and B represent metal cations in the composition ABO_3. Drawing of crystal structure made with *VESTA3*.[158]

A thorough description of perovskites and their crystal structure has been made by Goldschmidt in 1926.[159] From geometrical considerations, Goldschmidt defined a tolerance factor, that indicates if an ABO_3 oxide with a given combination of A- and B-site cations will crystallize in the perovskite crystal structure (see eq.2.17). The ionic radii r_A and r_B need to be within a certain ratio to be densely packed in the cubic structure. The Goldschmidt tolerance factor t equals exactly 1 if this condition is met.[159] Additionally, A- and B-sites can be occupied by more than one cation species if the ionic radii do not differ too much.

$$t = \frac{r_A + r_O}{\sqrt{2}(r_B + r_O)} \tag{2.17}$$

r_A : Ionic radius of A-site cation

r_B : Ionic radius of B-site cation

r_O : Ionic radius of Oxygen-ion

If the tolerance factor diverts from 1, the ideal cubic crystal structure is distorted to accomodate the ions. If it is greater than 1, hexagonal and rhombehedral distorted structures form, while values below 1 result in tetragonal and orthorhombic structures. However, the range of possible distortion is limited. If the deviation becomes too large, other structures can become more stable and lead to the formation of non-perovskite phases. Since reality is often much more complex than this simple geometric factor, it can only be considered as an indicator and no hard limits concerning phase stability can be derived. Other characteristics such as electronegativity and polarizability of involved species, bond strength and temperature influence the perovskite phase stability as well.[160–162] Various research groups have modified and expanded the definition of the tolerance factor to improve the precision of made predictions,[163–165] but the original Goldschmidt tolerance factor is still accurate for many perovskites and remains a valuable metric.

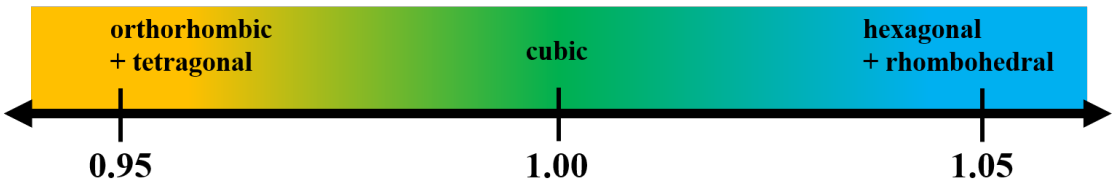

Fig. 2.7.: Tolerance factor ranges for stable perovskite phases. 0.95 and 1.05 are only soft boundaries and the transitions are fluid as illustrated by the color gradient.

In order to calculate the tolerance factor, the ionic radii of the involved species have to be known. The work of Shannon, published in 1976, contains an extensive list of ionic radii from many ionic species in various oxidation states and coordinations and has been cited over 50000 times since.[166] Values given by Shannon serve as a basis for tolerance factor calculations in this work. Within the scope of this work an adjusted coordination number (CN) of the A-site ion is used. The work of Vieten et al. has shown empirically for $SrMn_xFe_{1-x}O_{3-\delta}$ that assuming a mixture of coordination states with 80% CN 12 and 20% CN 10 of the A-site ion improves the crystal structure predictions made, based on the tolerance factor.[77,78] B-Site and Oxygen ions are coordinated in CN 6 forming octahedrals.

It has to be kept in mind that calculated values are primarily valid at 0K. The tempera-

ture increase however has a significant influence on the tolerance factor in two different ways. Firstly it leads to a reduction of the perovskite, resulting in the formation of oxygen vacancies and a reduced B-site ion species. These oxygen vacancies have a representative ionic radii of 131 pm as reported by Chatzichristodoulou et al.,[167] which is smaller than the nominal ionic radii of O^{2-}, which is 140 pm for CN 6 as given by Shannon.[166] However, the ionic radii of the reduced B-site species typically increase by a greater value (e.g. $r(Mn^{+IV}) = 53pm$ vs. $r(Mn^{+III}) = 64.5pm$), ultimately resulting in a decrease of the tolerance factor. Especially when multiple B-site species are present and take part in the reduction reaction, this correlation becomes significantly more complex. Secondly, increasing temperatures result in an expansion of the crystal lattice. Dabrowski et al. reported that the <A-O> and <B-O> atomic bonds do not increase in similar fashion, but the <A-O> bond increases by a greater margin than the <B-O> bond.[162] This leads to an increase of the tolerance factor with increasing temperature.

In fact the rise in temperature drives two counteracting mechanisms, one leading to a decrease, the other one leading to an increase of the tolerance factor. Additionally, as it is explained in section 2.5, temperature is not the only driving factor for the oxide's reduction. The reaction enthalpy as well as the surrounding atmosphere, more specifically the $p(O_2)$, have to be accounted for. In general, the magnitude of both effects is strictly related to the involved atomic species and therefore dependent on the exact composition of the perovskite.

Thermodynamics

A common thermodynamic function to describe the behavior of a closed system is the Gibbs free energy G,[168] which is given in eq. 2.18:

$$G = H - TS \tag{2.18}$$

G : Gibbs free Energy

H : Enthalpy

S : Entropy

For a chemical reaction at constant temperature and pressure the differential of eq.2.18 results in eq. 2.19:

$$\Delta G = \Delta H - T\Delta S \tag{2.19}$$

The system thrives to minimize G. Thereby, a chemical reaction proceeds spontaneously if ΔG is below zero. The change in enthalpy ΔH of a reaction can also be considered as the reaction enthalpy ΔH_R. In the case of the redox reaction of perovskites (see eq. 2.5 and 2.6) ΔH_R can also be interpretated as the heat the reaction consumes or releases. The entropy S is a measure for the extent of disorder in a system and ΔS for the reduction reaction of perovskites is exclusively positive, due to the fact that gaseous product is released from a solid reactant. The Gibbs free energy is temperature dependent, which means for the endothermal reduction reaction in air that the oxide is reduced at elevated temperatures. Reaction enthalpies of reversible oxide redox reactions are typically given in positive values, representing the change in enthalpy of the reduction reaction. Positive values hereby account for endothermal reactions, while negative values account for exothermal reactions. If fully reversible, the oxidation has identical values of ΔH with a negative sign.

Since the redox reaction releases and consumes oxygen, ΔG is also dependent on the partial pressure of oxygen. ΔG can be calculated at any given $p(O_2)$ with ΔG^0, the change in Gibbs free energy at standard conditions:

$$\Delta G = \Delta G^0 + \frac{1}{2} RT \cdot ln(\frac{p_{O_2}}{p^0}) \tag{2.20}$$

When combined with eq. 2.19, eq. 2.20 results in:

$$\Delta G = \Delta H_0 - T\Delta S_0 + \frac{1}{2} RT \cdot ln(\frac{p_{O_2}}{p^0}) \tag{2.21}$$

Herein the standard pressure p^0 is set to 1 bar and R is the ideal gas constant. The factor $\frac{1}{2}$ originates from the fact that values for ΔG, ΔH and ΔS are given per mol O, while the partial pressure is given per mol O_2 (originally the factor is an exponent inside the natural logarithm). Additionally, ΔH can also be dependent on the reduction extent δ. This correlation is especially true for perovskites containing multiple B-site elements, e.g. $SrFe_{0.5}Mn_{0.5}O_{3-\delta}$, but is considered negligible for single element B-site perovskites like $CaMnO_{3-\delta}$.[169] Based on a model derived for ceria,[130,170] the work of Vieten[77,78] pro-

vides an approach to model the δ-dependency of ΔH in multi-cation B-site substituted perovskites as a numerical derivative of $p(O_2)$ with respect to temperature. Within the scope of this work it is reasonable, for perovskite compositions with only one B-site element, to approximate ΔH as constant over the considered δ-range.

The change in entropy ΔS of the redox reaction can be described as the sum of the partial molar entropy of Oxygen $S^0_{O_2}(T)$, the change in vibrational entropy $\Delta s_{vib}(T)$ and the change of configurational entropy $\Delta s_{conf}(\delta, T)$:[77,130,169]

$$\Delta S(\delta, T) = \frac{1}{2} \cdot S^0_{O_2}(T) + \Delta s_{vib}(T) + \delta s_{conf}(\Delta, T) \tag{2.22}$$

The reduction reaction involves the release of oxygen into the gas phase from a bound state in the crystal lattice, resulting in large entropic contributions. In fact the molecular entropy of oxygen gas $S^0_{O_2}(T)$ is by far the biggest contributor to entropic changes for most perovskite compositions. $S^0_{O_2}(T)$ can be calculated using the Shomate equation and listed data from NIST-JANAF thermochemistry tables.[131,171] The change in vibrational entropy $\Delta s_{vib}(T)$ originates from excitation of vibrational phonon modes in the crystal lattice. With rising temperature, more phonon modes are excited, resulting in an increase of entropy, and is therefore closely related to the heat capacity of a solid, which is predominantly determined by the extent of phonon mode excitation. $s_{vib}(T)$ is accessible through the Debye model.[116] If the Debye temperature $\Theta_{D,\delta}$, the temperature where all phonon modes of a crystalline solid are occupied, for phases at given δ is known, $s_{vib}(T)$ can be calculated by:[116]

$$s_{vib,\delta}(T) = R \cdot [-3 \cdot ln(1 - e^{-(\frac{T}{\Theta_{D,\delta}})})] + 4 \cdot D(\frac{T}{\Theta_{D,\delta}}) \tag{2.23}$$

It becomes clear that the Debye temperature of all phases at any given non-stoichiometry δ has to be known in order to properly calculate $s_{vib,\delta}(T)$. Experimentally these values are very difficult to obtain. While theoretical calculations offer a pathway to obtain Debye temperatures, they require calculated elastic tensors of these phases. That can be done via density functional theory (DFT),[172,173] but is a lengthy and computationally expensive process. Some materials databases such as *Materials Project*[125] contain elastic tensors for some perovskite materials, but they are not complete and data therein is only added slowly.

For perovskites it has been shown that not only does the vibrational entropy repre-

sent only a small fraction of the overall change in entropy, but also only varies slightly in between perovskite compositions, making it possible to approximate $\Delta s_{vib}(T)$ by calculated values for a representative composition (e.g. $SrFeO_{3-\delta}$).[77,78] This approach has been followed within the scope of this work. Additionally, the materials discussed herein are designated to operate at high temperatures. At $T >> \Theta_D$ all vibrational modes are excited and the error introduced by this approach is becoming negligible for the most part.

The change in configurational entropy derives from possible locations in the crystal lattice, where oxygen vacancies can form. Compared to ceria, less possibilites are accounted for in perovskites, as only B-site atoms are actively reduced during the formation of oxygen vacancies, limiting the possible oxygen sites that can be vacated. While configurational entropy contributions are smaller compared to single cation non-stoichiometric redox oxides like ceria, perovskites offer great tunability of configurational entropy by introducing multiple B-site cations or inducing phase transitions and order-disorder transitions. Based on a dilute species model derived from previous work on ceria,[130] the change in configurational entropy with respect to the reduction extent δ can be described as:[169]

$$\Delta s_{conf} = 2 \cdot a \cdot R \cdot [ln(\frac{1}{2} - \delta) - ln\delta] \tag{2.24}$$

The factor 2 in eq. 2.24 accounts for the fact that 2 mol of perovskite are needed per 1 mol of monoatomic oxygen. The vacancy ordering is accounted for with the dimensionless constant a. A random distribution without any vacancy ordering is considered if $a = 2$ according to Bulfin et al.,[130,169] which is assumed throughout this work. If multiple B-site cations are present and the perovskite can be described as a combination of sub-lattices within the solid solution, Δs_{conf} consists of the weighted sums of each sub-lattice (described by the index 1 and 2):[78,130]

$$\Delta s_{conf}(\delta, T) = \Delta s_{conf,1}(\delta, \delta_1, T, \Delta H_1) + \Delta s_{conf,2}(\delta, \delta_2, T, \Delta H_2) \tag{2.25}$$

This model is very accurate to predict entropy changes in perovskite solid solutions and has been utilized for DFT-based material calculations previously.[77,78]

Kinetics

While thermodynamics deals with the direction in which a reaction or process takes place, it does not provide any information on the reaction on a timescale. Kinetics introduce time as a factor to evaluate chemical reactions, dealing with measurement and parametrization of reaction rates. In general the kinetics of solid state redox reactions can be parametrized by three major values: Temperature, T; extent of conversion, α; pressure, p resulting in a generic equation for the reaction rate:[174]

$$\frac{d\alpha}{dt} = k(T)f(\alpha)h(p) \tag{2.26}$$

Classic solid-state kinetic models do not include a term for the pressure dependence[175] and the majority of kinetic models in the field of thermal analysis and thermochemical reactions omit the pressure dependency $h(p)$ as well. This is reasonable if the condition $h(p) = const.$ holds true throughout the reaction. For redox reactions involving gaseous components, this is usually established by using sweep gases to either remove any gaseous reaction products or provide excessive amounts of gaseous reactants.

Instead of a generic pressure dependent function, the concentration of the gaseous reactants can be used as well. This was successfully done by Bulfin et al., who found the concentration dependence to follow a power law $\frac{d\alpha}{dt} \propto c_{O_2}^n$ with a value of $n = 0.695$ for $SrFeO_3$.[176] Additionally, they have shown that only little variation exists in values for n and that its impact on the determined activation energies were marginal.[176] The concentration c_{O_2} can be calculated from the partial pressure of oxygen $p(O_2)$ via the ideal gas law:

$$c_{O_2} = \frac{n}{V} = \frac{p(O_2)}{RT} \tag{2.27}$$

In order to describe the temperature dependence of the reaction rate, typically an Arrhenius equation is used:

$$k(T) = A \cdot exp\left(\frac{-E_a}{RT}\right) \tag{2.28}$$

Therein, A is a preexpotential factor and E_a the activation energy. This activation energy is often referred to as an apparent activation energy since it only describes the effect of temperature on the overall kinetic process and not the intermediate steps involved in the reaction. The function $f(\alpha)$, describing the dependence of the reaction rate on the extent of conversion α, can be represented by a multitude of functions. Regularly $f(\alpha)$ needs to be defined empirically, especially if the reaction model has not been defined in details. In its simple and most common form, $f(\alpha)$ takes the form of a reaction-order model:[174]

$$f(\alpha) = (1-\alpha)^m \tag{2.29}$$

The order or reaction is given by m. The complete reaction rate equation can be described by:

$$\frac{d\alpha}{dt} = (1-\alpha)^m \cdot c_{O_2}^n \cdot A \cdot exp\left(\frac{-E_a}{RT}\right) \tag{2.30}$$

The initial rate at $t = 0$ is defined as:

$$\left(\frac{d\alpha}{dt}\right)_{t=0} = c_{O_2}^n \cdot A \cdot exp\left(\frac{-E_a}{RT}\right) \tag{2.31}$$

Taking the logarithm of eq. 2.30 results in:

$$log\left(\frac{d\alpha}{dt}\right) = m \cdot log\left(1-\alpha\right) + log\left(\left(\frac{d\alpha}{dt}\right)_{t=0}\right) \tag{2.32}$$

Plotting $\frac{d\alpha}{dt}\ vs.\ (1-\alpha)$, m can be determined from the linear slope and $log\left(\left(\frac{d\alpha}{dt}\right)_{t=0}\right)$ from the y-axis intercept. Using these intercepts, plotting $c_{O_2}^{-n}\left(\frac{d\alpha}{dt}\right)_{t=0}\ vs.\ \frac{10^3}{RT}$ gives the activation energy E_a as the slope and the pre-exponential factor $log(A)$ as the intercept. This kinetic model is closely following the work of Bulfin et al.[176] and has been applied in the kinetic analysis within this work. Although the actual reaction mechanism can be more complex, the reduction and oxidation of perovskites can be broken down into three major steps, which are depicted schematically in Fig. 2.8:

- Diffusion of gaseous reactants (e.g. oxygen) in the surrounding atmosphere
- Adsorption/Desorption of gaseous reactants on the perovskite surface
- Diffusion of oxygen ions, oxygen vacancies and electrons within the perovskite crystal lattice

Typically one of these 3 steps is substantially slower, and thus considered the rate limiting factor. During the reaction a concentration gradient forms in the reactant atmosphere causing diffusion either away or towards the redox oxide. For a fast reaction it must be ensured that during the reduction, evolved oxygen is removed quickly, and during the oxidation a constant supply of oxidants (e.g. O_2, H_2O or CO_2) is given. A limitation by the diffusion of gaseous reactants can be ruled out by excessive sweep gas supply. During reduction, alternatively vacuum can be provided to ensure a sufficient mean free path and constant removal of gaseous products from the atmosphere.

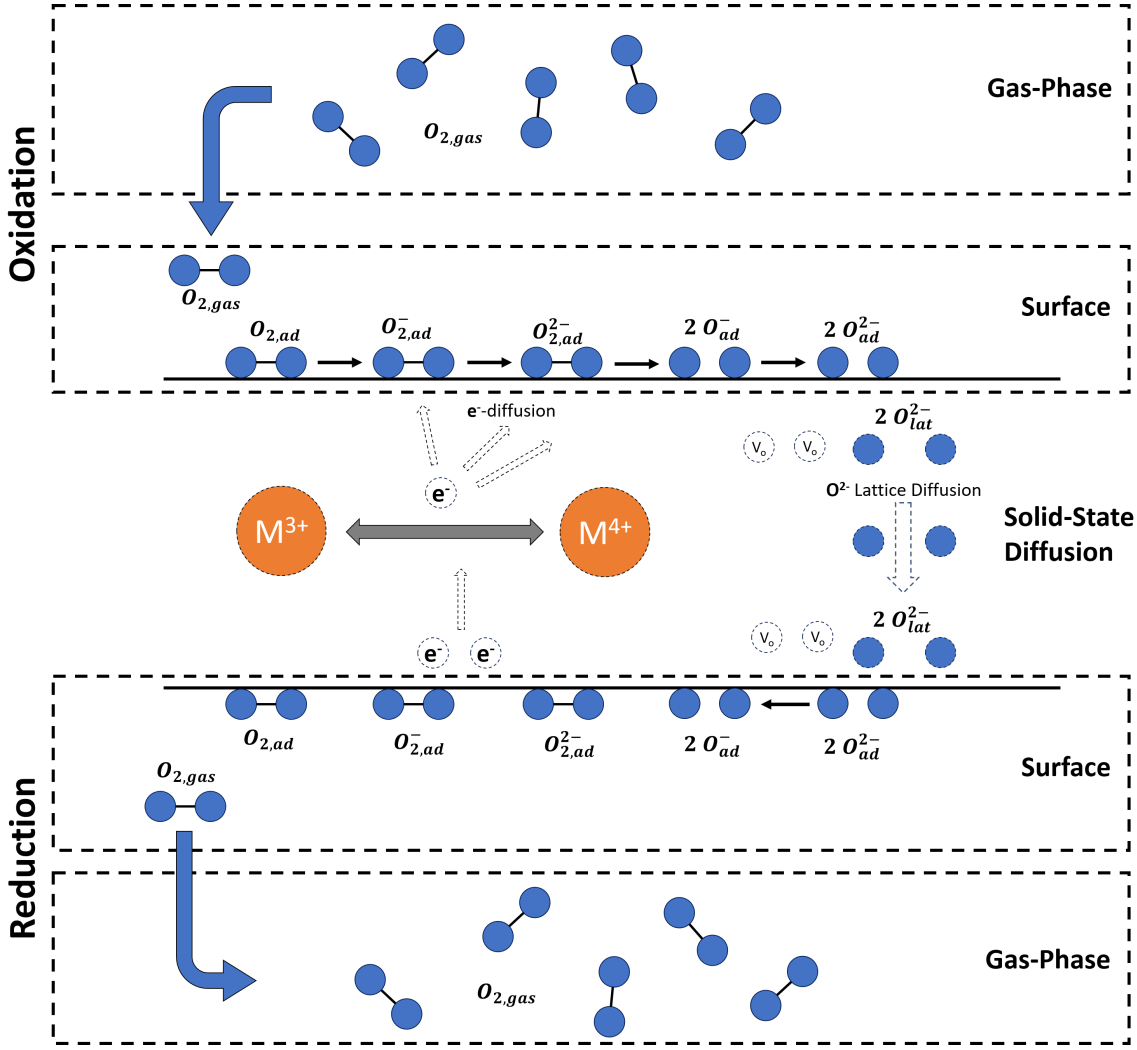

Fig. 2.8.: Schematic illustration of the 3 major steps of the perovskite redox reaction. M^{3+} and M^{4+} represent the reduced and oxidized B-site species respectively.

The adsorption and desorption of gaseous oxygen on the perovskite surface is also summarized as the surface exchange reaction, or simply surface reaction. During oxidation oxygen from the gas phase has to be adsorbed at the surface and incorporated into the crystal lattice. The reverse reaction is occuring during reduction. Literature suggests that this surface exchange reaction involves multiple intermediate oxygen species,[177–179] which are accounted for in the schematic depiction of the reaction mechanism in fig. 2.8. The electrons that are released or consumed during the conversion of $O_{2,gas}$ to O^{2-}-ions are related to the reduction and oxidation of transition metal species in the perovskite. Typically only the B-site species is changing its redox state. Some perovskites can form carbonates on the surface, especially when oxidized by CO_2.[180] It has been shown that

perovskites can be cured from such passivating surface phase by heating in oxygen rich atmospheres.[78,169]

Diffusion of oxygen ions and electrons also follows concentration gradients. It occurs from the surface into the bulk, from bulk to surface and within the bulk. Perovskites are considered as mixed ionic-electronic conductors, showing considerably high diffusion rates for both, electrons and oxygen ions.[181–184] That also renders them as possible candidates for anodes in fuel cells[185] and cathodes in Li-Air-batteries.[183]

The internal diffusion is influenced by the morphology of the perovskite as well. Particle and grain sizes, grain boundaries, crystal structure, secondary phases and phase transitions can all either enhance or hinder the diffusion of oxygen ions and electrons through the bulk. Additionally the surface exchange reaction is also influenced by the perovskite morphology, mainly by the available surface area. Different sample morphologies, such as powder, particle, pellets or monolithic structures can significantly vary in their kinetic properties. Exploring these properties theoretically proves to be difficult. However, utilizing experimental techniques like thermal analysis and the kinetic reaction model described in this section, activation energies can be determined. Different activation energies in certain regions of temperature and $p(O_2)$ indicate different rate-limiting factors for these regions. By closely observing the activation energies, regimes of dominant rate-limiting factors can be distinguished, and sample morphologies can be compared qualitatively.

3. Methods

Within this work, multi-cation perovskites with varying compositions are synthesized and characterized. A solid state synthesis approach has been utilized and a procedure to produce monolithic open porous structures from perovskites has been established. Characterization has been done by means of x-ray diffraction (XRD), SEM, TGA, DSC, dilatometry, N_2 gas-adsorption by Brunauer-Emmett-Teller model (BET), mercury porosimetry and mechanical force tests. An experimental test-rig has been used for the initial screening of perovskite compositions with respect to their oxygen pumping performance and the best performing composition has been chosen to produce monolithic RPC foams. An adjusted and expanded version of this test-rig has been rebuilt in a later stage to test produced RPC foams.

This chapter is partially based on peer-reviewed publications authored and co-authored by the author of this work:

Christos Agrafiotis, Mathias Pein, Dimitra Giasafaki, Stefania Tescari, Martin Roeb, and Christian Sattler. "Redox Oxides-Based Solar Thermochemistry and Its Materialization to Reactor/Heat Exchanger Concepts for Efficient Solar Energy Harvesting, Transformation and Storage". In: *Journal of Solar Energy Engineering* 141.2 (2019). DOI: 10.1115/1.4042226

Mathias Pein, Christos Agrafiotis, Josua Vieten, Dimitra Giasafaki, Stefan Brendelberger, Martin Roeb, and Christian Sattler. "Redox thermochemistry of Ca-Mn-based perovskites for oxygen atmosphere control in solar-thermochemical processes". In: *Solar Energy* 198 (Mar. 2020), pp. 612–622. DOI: 10.1016/j.solener.2020.01.088

Mathias Pein, Nicole Carina Neumann, Luke J. Venstrom, Josua Vieten, Martin Roeb, and Christian Sattler. "Two-step thermochemical electrolysis: An approach for green hydrogen production". In: *International Journal of Hydrogen Energy* 46.49 (2021), pp. 24909–24918. ISSN: 0360-3199. DOI: https://doi.org/10.1016/j.ijhydene.2021.05.036

Mathias Pein, Luca Matzel, Lamark de Oliveira, Gözde Alkan, Alexander Francke, Peter Mechnich, Christos Agrafiotis, Martin Roeb, and Christian Sattler. "Reticulated Porous Perovskite Structures for Thermochemical Solar Energy Storage". In: *Advanced Energy Materials* 2102882 (2022). ISSN: 1614-6832. DOI: https://doi.org/10.1002/aenm.202102882

Lena Klaas, Mathias Pein, Peter Mechnich, Alexander Francke, Dimitra Giasafaki, Dorottya Kriechbaumer, Christos Agrafiotis, Martin Roeb, and Christian Sattler. "Controlling thermal expansion and phase transitions in Ca1−xSrxMnO3−δ by Sr-content". In: *Physical Chemistry Chemical Physics* 24 (45 2022), pp. 27976–27988. DOI: 10.1039/D2CP04332G

3.1. Synthesis of Perovskite Solid Solutions

All perovskite compositions investigated within this work have been synthesized by solid-state-synthesis. Therein, two procedures have been used. While at first, a rather simplistic synthesis approach, in the following referred to as "simple synthesis", has been used to synthesize the compositions for the material screening (chapter 4), this procedure has been continuously refined and adjusted, ultimately leading to an "advanced synthesis" procedure, which has been utilized to synthesize perovskite compositions in larger quantities for foam and granule production in the later stages of this work (chapter 7.

However, identical precursor materials were used in both procedures. Stoichiometric oxides were used as-purchased: Co_3O_4 (Materion Advanced Chemicals, Milwaukee, WI, USA), (0.75)(Mn_2O_3)*(0.25)(Fe_2O_3) prepared as dry-mixture of Mn_2O_3 (Materion Advanced Chemicals, Milwaukee, WI, USA) and Fe_2O_3 (Alfa Aesar, Karlsruhe, Germany). All precursors were technical grade materials with a purity of >98%. Used presursors for A- and B-site elements, including their sources are listed in table 3.1.

Main reasons to choose solid state synthesis for this work are: it utilizes comparably cheap raw materials; easily scalable; easy to reproduce. All of these factors are enabling fast transfer from lab scale to industrial scale.

Table 3.1.: Used precursors for perovskite solid state synthesis and their sources.

Precursor, Source	
A-Site	B-Site
• $CaCO_3$, Merck (Darmstadt, Germany) • $SrCO_3$, Alfa Aesar (Karlsruhe, Germany)	• Mn_3O_4, ERACHEM (Saint-Ghislain, Belgium) • TiO_2, Evonik (Hanau, Germany) • α-Al_2O_3, SCFa-5, SASOL (Hamburg, Germany) • Cr_2O_3, Merck (Darmstadt, Germany)

Simple Synthesis

The stoichiometric amounts of metal oxides and carbonates were dry mixed and thoroughly grinded with mortar and pestle before firing in a Carbolite® RHF 14/35 muffle furnace. The firing schedule consisted of a 6-h isothermal step at 800 °C and a 10-h step at 1300 °C with heating rates of 10 °C min^{-1} in-between the steps. Grinding and firing has been repeated once, for each sample to ensure complete reaction and phase purity, which could not be achieved for all samples (see tab. 3.2). All compositions were ground once more after the final firing procedure.

Advanced Synthesis

In order to obtain single phase perovskites without firing and grinding the material multiple times, the simple synthesis procedure described above has been adjusted. Inhomogeneous mixing, resulting concentration gradients of the used A- and B-site ions, was identified as the main reason for the formation of non-perovskite side phases. Therefore, stoichiometric amounts of the precursors were mixed in a 1:2 wt.-ratio in isopropanol and vigorously stirred for 2 hours. The solids were filtered and dried of any residue liquid for 24h at room temperature and 24h at 80 °C. The dried powder mixture was then transferred to alumina crucibles and fired in a Carbolite RHF 14/35 muffle furnace for 24h at 1200 °C and heating rates of 5 °C min^{-1}. In principal, drying could also be done directly in the furnace, further reducing manual labor involved in the synthesis process. This advanced synthesis resulted in single phase perovskites after the first and only firing procedure.

An overview of all synthesized compositions, sorted by synthesis method, is provided in tab. 3.2 together with their respective tolerance factor.

Table 3.2.: Overview of all synthesized perovskite compositions.

Simple Synthesis			
Composition	Structure	Side Phases	t_0
$CaTi_{0.2}Mn_{0.8}O_{3-\delta}$	orthorhombic		0.9881
$CaAl_{0.2}Mn_{0.8}O_{3-\delta}$	orthorhombic		0.9952
$CaCr_{0.1}Mn_{0.9}O_{3-\delta}$	orthorhombic		0.9948
$CaCr_{0.05}Mn_{0.95}O_{3-\delta}$	orthorhombic		0.9953
$CaMnO_{3-\delta}$	orthorhombic	$CaCO_3$, $CaMn_2O_4$	0.9958
$Ca_{0.95}Sr_{0.05}MnO_{3-\delta}$	orthorhombic		0.9978
$Ca_{0.9}Sr_{0.1}MnO_{3-\delta}$	orthorhombic	$CaMn_2O_4$	0.9997
$Ca_{0.8}Sr_{0.2}MnO_{3-\delta}$	orthorhombic	$CaMn_2O_4$	1.0036
$SrFeO_{3-\delta}$	cubic	unidentified	1.0060
$SrFe_{0.67}Mn_{0.33}O_{3-\delta}$	cubic		1.0153
$SrFe_{0.5}Mn_{0.5}O_{3-\delta}$	cubic		1.0201
$SrMnO_{3-\delta}$	hexagonal		1.0346
Advanced Synthesis			
Composition	Structure	Side Phases	t_0
$CaMnO_{3-\delta}$	orthorhombic		0.9958
$Ca_{0.95}Sr_{0.05}MnO_{3-\delta}$	orthorhombic		0.9978
$Ca_{0.90}Sr_{0.10}MnO_{3-\delta}$	orthorhombic		0.9997
$Ca_{0.8}Sr_{0.2}MnO_{3-\delta}$	orthorhombic		1.0036

3.2. Perovskite Monolithic Structures

Within this work, four types of monolithic structures have been prepared for further analysis: Foams, granules, bars and pellets. Foams, granules and pellets have been solemnly produced from perovskites obtained by the described advanced synthesis method, while bars have been produced from perovskites obtained by both synthesis methods. By which method the used perovskite has been synthesized is indicated in the respective result sections.

Open Porous Perovskite Foams

The foams have been manufactured via the polyurethane (PU) foam replica method, which involves impregnation of sacrificial PU foam templates with slurries of the powder and subsequent drying and firing of the green body. Given this approach, the final particle size of the redox powder has to be sufficient to facilitate its formulation in stable slurries that do not settle under gravity. Therefore, the sintered powder was dry-milled in a Pulverisette 6 planetary ball mill (Fritsch, Germany) with zirconia spheres as the grinding media. Various milling conditions have been explored. The powders' particle size distribution (PSD) after milling was measured with a Mastersizer 2000 Low Angle Laser Light Scattering Analyzer (Malvern Panalytical, UK) and their specific surface area was determined with a Surfer Micro nitrogen porosimeter (ThermoFischer, Germany). An average particle size of 5 µm was targeted for slurry production. PSD and the chosen milling parameters of the powder used to manufacture foams within this work are shown in fig. 3.1. A synthetic polyelectrolyte with the commercial name DOLAPIX CE64 (supplied by Zschimmer & Schwarz GmbH & Co, Lahnstein, Germany) was employed as a dispersant to induce slurry stabilization. Slurries of the $CaMnO_{3-\delta}$ powder with 80%-wt. solid content, 17%-wt. water and 3%-wt. dispersing agent were prepared. Perovskite foam samples used in the oxygen pumping demonstration experiments were prepared with an adjusted slurry formula with the addition of 6.6%-wt. of polyvinylpyrrolidone (PVP) as a polymeric binder and a total solid wt.-ratio of 65.4%. PU foam specimens of 30 and 60 ppi were sectioned from larger samples with the commercial name Regicell 30 (FoamPartner GmbH, Leverkusen, Germany). Under stirring, the selected amount of powder was slowly added in the corresponding amount of deionized water, followed by the dispersant. After approximately ten minutes the temperature of the slurry was raised to 60 °C. Stirring at this temperature was continued for ten more minutes. If foaming occurred, several drops of the anti-foaming agent Kontraspum KWE (supplied

by Zschimmer & Schwarz GmbH & Co, Lahnstein, Germany) were added. Then, the PU specimens were impregnated in the slurries. The loaded specimens were withdrawn and excess slurry was removed by compression and a compressed air jet. The resulting green bodies were dried at ambient temperature overnight, placed on alumina tiles and fired at 1350 °C in a single-stage sintering schedule for 3 hours with a heating rate of 1 °C min^{-1} and subsequent cooling to ambient temperature with a cooling rate of 2 °C min^{-1}.

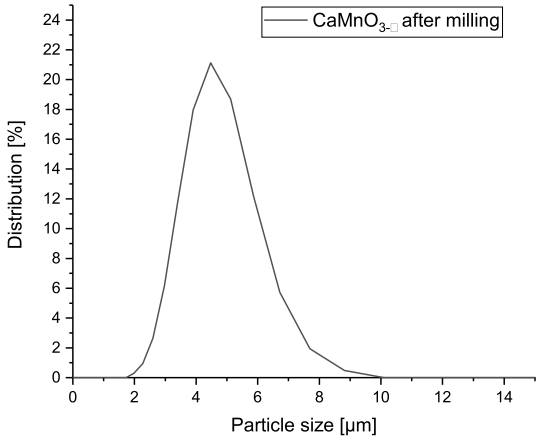

(a)

Milling Parameter	Value
Time	15 minutes
Rotation Speed	450 rpm
Wet or dry	dry
wt.-ratio sample:mil. balls	1:2
Type of milling balls	Zr, ⌀5 mm

(b)

Fig. 3.1.: a) Particle size distribution of $CaMnO_{3-\delta}$ powder after milling with parameters shown in b).

Perovskite Granules

Desired perovskite powders were granuled in an EL1 lab-mixer (Gustav Eirich GmbH & Co KG, Germany). Therefore, finely milled powder, identical to the foam production precursors in the prior section, was used. 100 g of powder was mixed with microcrystalline cellulose (MCC) in a 10:3 ratio (Perovskite:MCC) in the Eirich-mixer and initially mixed dry at 1500 rpm for about 10 min. Any residues of the mixture that stick to the mixer walls were scraped off manually with a spatula and the mixing was repeated for about 5 min.

Subsequently the mixing speed was set to 800 rpm and about 40 mL H_2O was added slowly. Mixing was continued for 10 min, residues on the wall were again scraped off manually before mixing for additional 10 min. At this second mixing step at 800 rpm, more H_2O was added very slowly (drop by drop) until particles of the desired shape and size form. At this step more H_2O added to the mixture will result in bigger particles, while the desired shape is always spherical. After finishing the granulation the particles

were transferred to an alumina crucible and sintered at 1300 °C for 24 h with intermediate isotherms during heat-up at 280 °C and 500 °C for 2 h each. A slow heating rate of 1 °C min^{-1} and a slightly faster cooling rate of 2 °C min^{-1} were employed during this sintering process. Sintered particles were then sieved through a metal mesh sieve stack with variable mesh sizes to further narrow down the particle size to the desired range. Utilizing the above described procedure, granules of $CaMnO_{3-\delta}$and $Ca_{0.95}Sr_{0.05}MnO_{3-\delta}$ with a particle size (diameter) range of 1 mm to 5 mm were produced and used for experimental tests on the oxygen pumping performance later on in chapter 7.

Perovskite Bars and Pellets

As-synthesized powders were used to prepare 50 cm long, rectangular (5x5 mm) bar-specimens of each sample. Bar-specimens were prepared by cold pressing the composite powders in a mold with a laboratory PERKIN-ELMER hydraulic press. A force of $9 \cdot 10^4$ N was applied and the green bodies were subsequently sintered at 1350 °C for 20 h under air with a heating rate of 5 °C min^{-1}. This process was used for powders obtained from simple synthesis and advanced synthesis alike. Additionally, pellets, using $CaMnO_{3-\delta}$ obtained by advanced synthesis, were prepared with the respective mold and identical firing parameters as described above. Exemplary photographs of all produced structured perovskite specimens are shown in fig. 3.2.

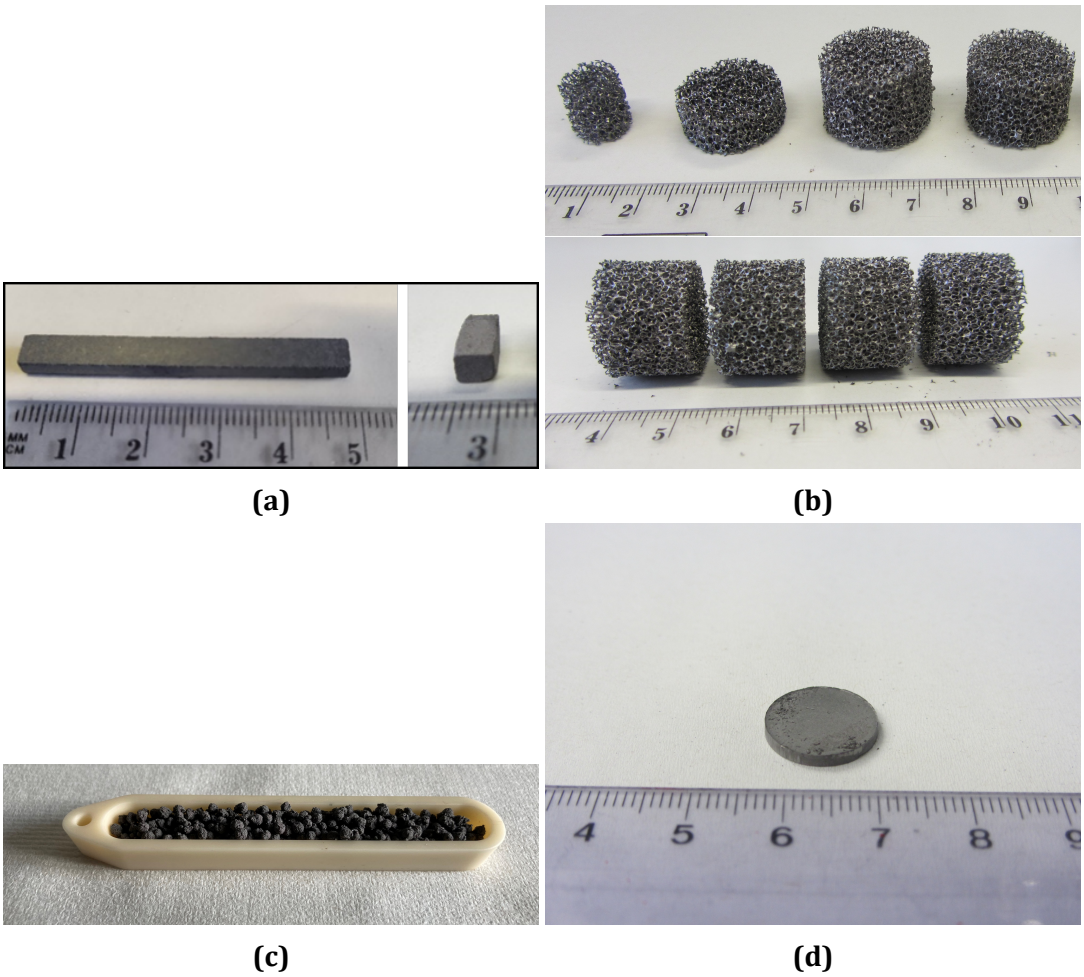

Fig. 3.2.: Photographs of all structured specimen. a) bar, b) foams, c) granules d) pellet. a) and b) taken from Pein et al..[19] CC-BY

3.3. Phase Analysis and Microscopy

Analysis of crystal structure and phases of prepared samples was performed by XRD and with three different instruments. Employed parameters were kept constant throughout measurements in each of the instruments. Samples were prepared as powders and were measured either as volumetric sample in a polymer mold or on an Si single crystal sample holder. The different setups are described in the following.

D-5000: The Siemens Kristalloflex D-5000 X-ray powder diffractometer is equipped with a Cu-K_α-radiation source. Scans were performed in a $\theta - 2\theta$-setup with diffraction angles (2θ) of 10° to 80°, a step size of 0.015° and 6 s per step.

D8-Co: This D8-Advance X-ray diffractometer by Bruker is equipped with a Co-X-ray radiation source and a Lynxe-EyeXET-Detector. Scans were performed in a $\theta - 2\theta$-setup with diffraction angles (2θ) of 10° to 100°, a step size of 0.02° and two seconds per step.

D8-Cu: A similar D8-Advance X-ray diffractometer by Bruker, equipped with a Cu-X-ray radiation source and a Lynxe-Eye XET detector, was employed for in-situ HT-XRD experiments, utilizing a high temperature chamber HTK 1200N by Anton-Paar and a Göbel Mirror. The samples were heated from ambient temperature to 1300 °C and cooled again to ambient temperature under air with a ramp rate of 5 °C min^{-1}. XRD spectra were obtained at 25, 500, 870, 900, 930 and 1100 °C during heat-up and cool-down in $\theta-2\theta$-scans with a diffraction angle (2θ) range of 22° to 85°. A step size of 0.02° with one second per step was applied. Heating and cooling took place with 5 °C min^{-1} and isothermal steps were included while performing the scans.

XRD spectra shown in later sections are labeled with *D-5000*, *D8-Co* and *D8-Cu* respectively to indicate which instrument has been used to obtain the spectrum. Microstructural observations of the specimens by SEM were performed with two instruments. On the one hand a ZEISS ULTRA 55 FEG instrument coupled with an INCA Pentafet x3 EDS X-ray microanalysis system from Oxford Instruments was used, for which samples have been sputtered with Pt to increase the electric conductivity of the surface. On the other hand a Hitachi SU3900 coupled with a Ulim Max 40 EDS X-ray analysis system from Oxford Instruments was utilized for SEM analysis.

3.4. Mechanical Strength Tests of Perovskite Foams

Mechanical strength tests of produced foam structures were carried out with a Dynamometer PCE-DFG N 50K (PCE, Meschede, Germany). The device is able to measure

tensile as well as compressive forces. Within this work, the dynamometer was used to determine the maximum compressive force that foam samples withstand without cracking or breaking, which marks the point of failure. Samples were place inbetween two aluminum plates, each weighing 49 g, to enhance uniform force entry on the topside area of the sample. Force was applied manually by moving the dynamometer in a fixed vertical plane by a screw handle. The force of 0.48 N added by the weight of the topside alumina plate was then added to the force measured by the dynamometer in the calculation of the applied pressure following eq. 3.1. Measuring accuracy of the dynamometer is 0.1N. An exemplary depiction of a foam sample before a strength test is shown in fig. 3.3.

$$p_{\mathrm{a}} = \frac{F_{\mathrm{c}} + 0.48N}{A_{\mathrm{f}}} \tag{3.1}$$

p_{a} : Pressure applied to foam

F_{c} : Compressive force applied by dynamometer

A_{f} : Topside area of the foam; calculated as the circular base with diameter d_{foam}

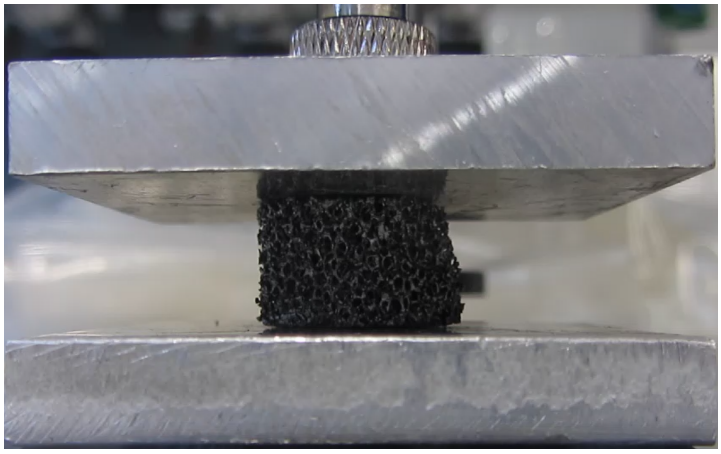

Fig. 3.3.: Example of a 30 ppi $CaMnO_{3-\delta}$-foam just before the mechanical strength test. Samples were placed between two alumina plates. Compressive force was applied from the top via the indenter of the dynamometer.

3.5. Thermal Analysis by TGA and DSC

In order to obtain information on the thermodynamic characteristics, as well as endothermal and exothermal effects of the redox reaction and phase transitions under various temperature and atmosphere conditions, TGA and DSC have been used. All TGA and DSC experiments were buoyancy corrected by means of blank measurements run under identical conditions.
Initial analysis of perovskite powder compositions were done with a SETARAM SETSYS Evolution 18 Analyzer obtaining thermogravimetric and calorimetric data simultaneously. 50 mg to 90 mg of sample were used for each composition and put in alumina crucibles. Measurements were cycled 5 times in the range of 300 °C to 1100 °C with 5 °C min^{-1} heating rate under synthetic air (Linde, 5.5) with ambient pressure and a purge gas flow rate of 16 mL min^{-1}. The final cooling step was performed at a rate of 50 °C min^{-1} Furthermore all DSC-data shown in this work was obtained with this device. DSC calibration was performed under argon atmosphere by using melting temperatures and enthalpies of a series of metals as references in the range of 120 °C to 1500 °C: Ni (1455 °C), Au (1064.18 °C), Ag (961.78 °C), Al (660.32 °C), Zn (419.53 °C), Pb (327.46 °C), Sn (231.93 °C) and In (156.6 °C), including the temperature range in which perovskites' redox reactions take place.

The cyclic redox behavior of the $CaMnO_{3-\delta}$-foam specimens was examined by TGA experiments, performed under air flow using the Netzsch STA 449 F3 Jupiter instrument. The experimental protocol adopted did not involve any dwell at specific temperature plateaus. All samples were cycled under synthetic air (Linde, 5.5) atmosphere, between an upper and a lower temperature limit of 1100 °C to 300 °C respectively, with 5 °C min^{-1} heating/cooling rate.

Extracting Enthalpy and Entropy of Reaction by the Van't Hoff Method

A common procedure to extract thermodynamic properties from thermogravimetric experiments is the Van't Hoff method,[77,78,169] which is based on the Van't Hoff equation (eq. 3.2):[186]

$$\ln\left(K_{eq}\right) = -\frac{\Delta H}{RT} + \frac{\Delta S}{R} \tag{3.2}$$

The equilibrium constant K_{eq} at $\Delta G = 0$ can also be described by the partial pressure of oxygen at constant $\Delta\delta$:

$$0.5 \cdot ln(\frac{p_{O_2}}{p^0})_{\Delta\delta=const.} = -\frac{\Delta H}{RT} + \frac{\Delta S}{R} \tag{3.3}$$

This allows to extract ΔH as the slope and ΔS as the y-axis intercept when plotting $0.5ln(p_{O_2})vs.\frac{1}{RT}$ in a Van't Hoff plot. However, weight loss and gain determined by TGA first need to be transposed into $\Delta\delta$-values:

$$\Delta\delta = \frac{\Delta m \cdot M_{Oxide}}{m \cdot M_O} \tag{3.4}$$

m : Mass of oxide sample

M_O : Molar mass of oxygen

M_{Oxide} : Molar mass of oxide

With an oxygen sensor (Setnag, France) at the outlet of the sample chamber the $p(O_2)$ is determined. The $p(O_2)$ is set to 0.8, 0.2, 0.1, 0.01, 0.05 and 0.002 by means of mixing appropriate amounts of purge gases from N_2, O_2 and synthetic air (80/20 N_2/O_2) with a total gas flow of 120 mL min^{-1}. The 20 mL min^{-1} Ar protective gas flow around the microscale was taken into account.

Samples were then cycled between 400 °C and 1200 °C with isothermal plateaus at various temperatures in between to establish equilibrium and extract data points to be fitted according to eq. 3.2. These measurements allow determination of ΔH and ΔS according to the described Van't Hoff method. Exemplary data is shown in fig. 3.4.

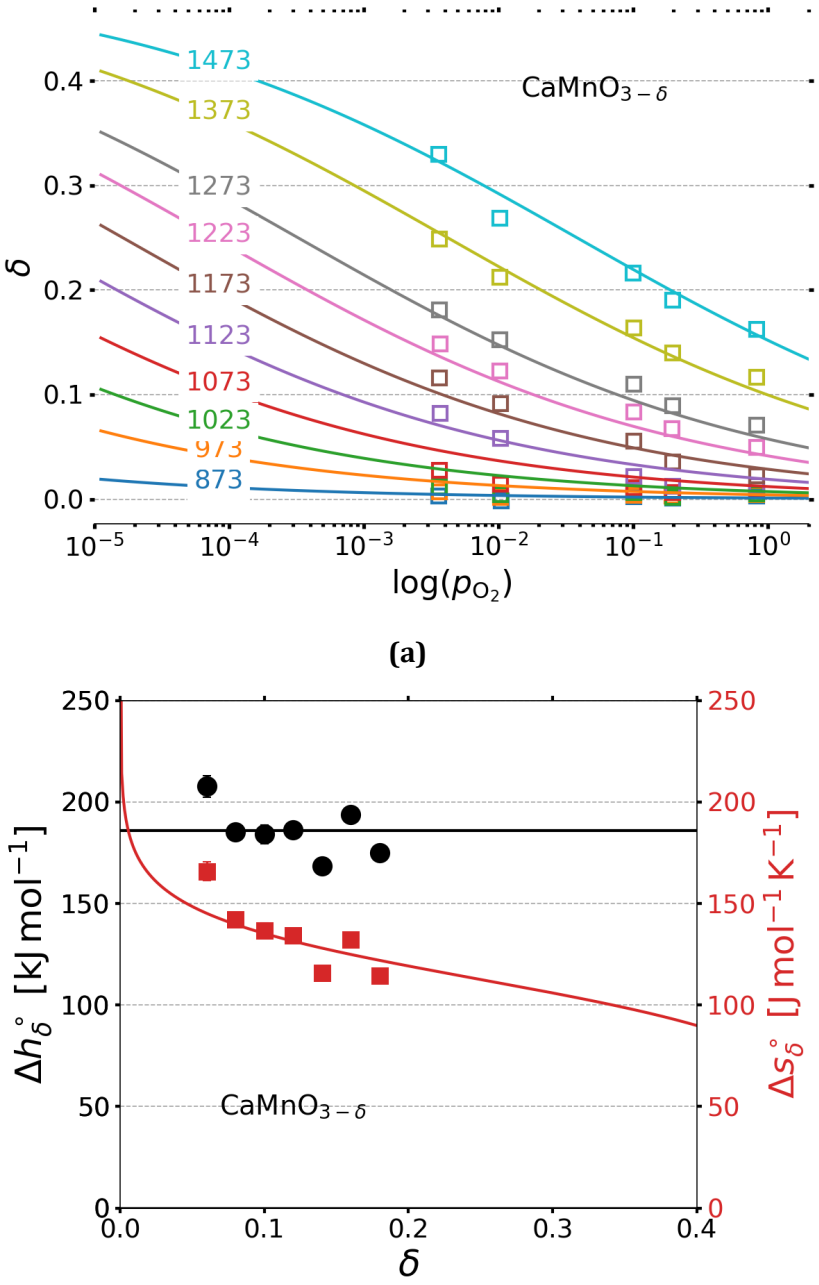

Fig. 3.4.: a) Van't Hoff plot for extracting ΔH and ΔS. Each color represents a different value of $\Delta\delta$ with linear fits through data points from experimental data. b) Extracted values of $\Delta H(\delta)$ and $\Delta S(\delta)$. Uncertainties are given by the covariance matrices of the linear fits from the Van't Hoff plot.

Identification of Phase Transitions by DSC

In most cases, phase transitions are accompanied by the release (exothermal) or consumption (endothermal) of energy in the form of heat, without changing the materials temperature. This heat, called latent heat or heat of transformation, is typically derived from a first-order phase transition and is most prominent in transitions that include a change in the state of aggregation, e.g. during the evaporation and condensation of water transitioning from liquid to gas.

While structural transitions of a crystal rarely get any attention with respect to their latent heat, these structural phase transitions can exhibit a unique heat signature, which enables DSC to detect and interpret occurring crystal phase transitions in metal oxides, such as the perovskites investigated in this work. Within the scope of this work, DSC is mainly used to determine temperature and atmosphere conditions at which phase transitions occur, as well as their reversibility over multiple cycles.

Phase transitions become evident in the DSC experiments by recognisable peaks in the heat signal, indicating a sudden uptake or release of heat. Experiments were carried out as described above with the SETARAM SETSYS Evolution 18 Analyzer, but in a temperature range of 400 °C to 1200 °C (heating/cooling rate of 5 °C min^{-1}) and with varying oxygen partial pressures, using mixed gas flows of oxygen (Linde, 5.0) and argon (Linde, 5.0) to create atmospheres with 20% O_2, 1% O_2 and pure Ar ($\approx$0.01% O_2). A final cycle at 20% O_2 was carried out to test reversibility and reoxidize the samples. Using an simultaneous thermal analysis (STA)-device, the weight signal is captured simultaneously and can be used for further analysis as well. The temperature was cycled twice for each atmosphere, resulting in 6 cycles total. The full measurement procedure is depicted in fig. 3.5.

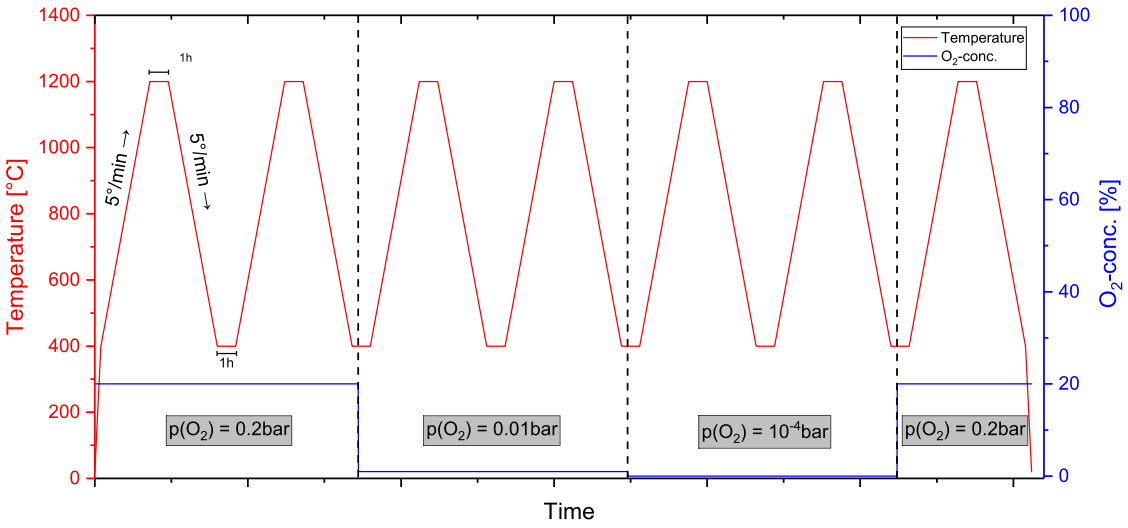

Fig. 3.5.: Exemplary measurement procedure of DSC experiments to determine phase transitions in perovskites. Three different regimes of $p(O_2)$ are indicated by dashed lines.

Kinetic Analysis

The reduction reaction of non-stoichiometric perovskites, such as $CaMnO_{3-\delta}$and the $Ca_{1-x}Sr_xMnO_{3-\delta}$ system investigated in this work, is considered very fast at elevated temperatures compared to the oxidation reaction as recently shown by Klaas et al..[187] The oxidation reaction is likely to be a limiting factor when it comes to thermal cycling and repeated reduction and oxidation. In this work, a straight forward measurement technique was employed, utilizing a TGA, wherein the samples were consecutively heated to a fixed reduction temperature and re-oxidation at varying selected temperatures. Reduction was performed at low $p(O_2)$, realized by pure Ar gas flow. Oxidation was carried out at 20% O_2 in a O_2/Ar gas mixture. The reduction temperature was fixed at 900 °C, whereas the oxidation temperature varied between 300 °C and 800 °C, using small temperature steps of 20 °C in the lower temperature region that were increased to 50 °C per step at higher temperatures. During cool-down between reduction and oxidation, Ar-flow was kept constant to prevent oxidation until the oxidation temperature is reached.

Subsequently, the gas flow was switched to an oxygen rich stream. Throughout the experiment the total gas flow was kept at a constant 120 mL min^{-1}. Before starting the measurement, each sample went through one cycle of heating and cooling in 20% O_2 atmosphere in order to get rid of any possible surface moisture, check for thermodynamic conformity of the samples and ensure identical starting points in each measurement. As previously described, the reduction extent $\Delta\delta$ can be calculated from the weight signal.

The extent of conversion, or re-oxidation, X is defined as the fraction of oxidation that occurs during time t:

$$\Delta\delta_{Ox}(t) = \Delta\delta_0 - \Delta\delta(t) \tag{3.5}$$

$$\Delta\delta_R Red = \Delta\delta_0 - \Delta\delta_\infty \tag{3.6}$$

$$X = \frac{\Delta\delta_{Ox}(t)}{\Delta\delta_R Red} \tag{3.7}$$

$\Delta\delta_0$ represents the reduction extent at $t = 0$ and $\Delta\delta_\infty$ is the value $\Delta\delta(t)$ is converging upon. If $X = 0$ the sample is fully reduced. If $X = 1$ the sample is fully re-oxidized and in chemical equilibrium. A quick check of reaction speed can be carried out by examining the time needed to complete 50% of the reaction, which is the halflife $t_{1/2}$ defined as:

$$X(t_{1/2}) = 0.5 \tag{3.8}$$

Closely following an approach reported by Bulfin et al.,[176] apparent activation energies can be calculated from the gained data. Therein it is assumed that the rate of reaction can be parametrized in terms of temperature T, the conversion extent X and the oxygen gas concentration c_{O_2}:

$$\frac{dX}{dt} = k(T) f(X) c_{O_2}^n \tag{3.9}$$

$\frac{dX}{dt}$ thereby depends on the rate constant $k(T)$, a generic function of the conversion extent $f(X)$ and the oxygen concentration $c_{O_2}^n$ including the order of oxygen concentration dependence n. Bulfin et al. have found that n does not vary significantly between perovskite compositions and determined an average value of $n = 0.695$, which was used in this study as well. $k(T)$ takes an Arrhenius form:

$$k(T) = k_0 exp\left(\frac{-E_a}{RT}\right) \tag{3.10}$$

Therein, E_a represents the apparent activation energy and k_0 is a pre-exponential factor. The activation energy in eq. 3.10 is only apparent, because this approach merely shows the effect of temperature on the overall kinetic processes It does not allow to distinguish between single steps within the process. With a fixed value of X, eq. 3.9 can be formulated as:

$$c_{O_2}^{-n}\left(\frac{dX}{dt}\right)_{X=const.} = k(T)f(X)_{X=const.} \tag{3.11}$$

Taking the logarithm of eq. 3.11 into account results in:

$$log\left(c_{O_2}^{-n}\left(\frac{dX}{dt}\right)_{X=const.}\right) = \frac{-E_a}{RT} + log(k_0 f(X)_{X=const.}) \tag{3.12}$$

From eq. 3.12 a logarithmic plot of $c_{O_2}^{-n}\left(\frac{dX}{dt}\right)_{X=const.} vs. \frac{10^3}{RT}$ gives the apparent activation energy as the slope and $log(k_0 f(X)_{X=const.})$ as the y-axis intercept. Without further knowledge on $f(X)$, only E_a can be extracted.

3.6. Thermal Expansion and Dilatometry

Determination of the thermal expansion of the various sample materials within this work was performed by dilatometry. Two different instruments, a contact dilatometer and a contactless optical dilatometer were used within this work. A depiction of exemplary samples are shown in fig. 3.6.

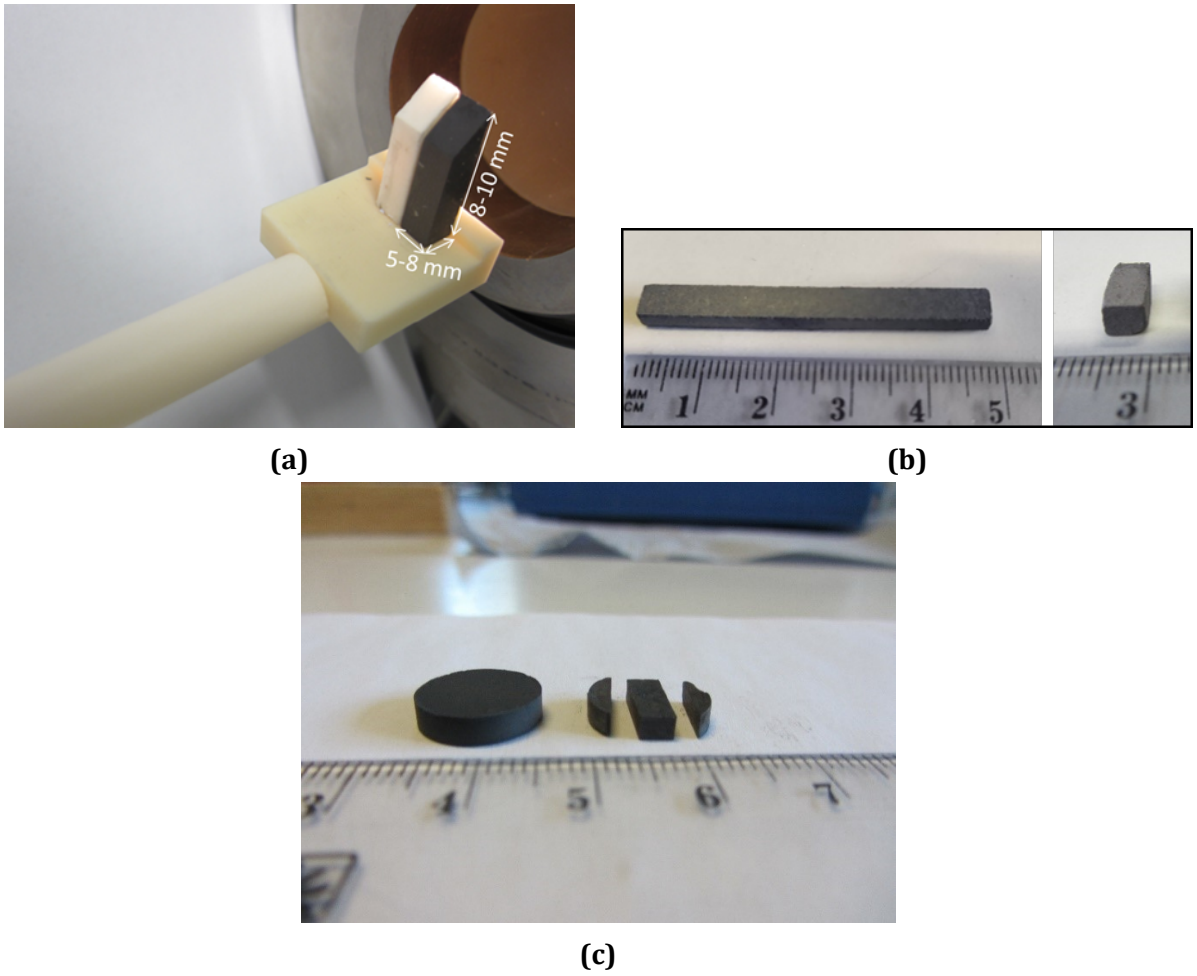

Fig. 3.6.: Exemplary depiction of dilatometry samples. a) Sample setup in the optical dilatometer with the white curundum reference sample. b) Original bar specimen. c) Pellet that has been used to prepare the Mn_2O_3 sample. Taken from Pein et al..[19] CC-BY.

Contact dilatometer: For the initial material screening, a horizontal contact dilatometer DIL 803 (TA Instruments, USA) was used. As samples, the approx. 5 cm long bar specimen, described in section 3.2, were placed onto the alumina sample holder and contacted by a pushing rod with minimal force. Over a sliding rail the tube furnace can be placed around the sample. A sapphire rod of similar length and shape was measured together with each sample to correct the systematic error of the instrument. Such systematic errors originate from thermal expansion of instrument parts. Measurements were carried out in air. Samples were heated up to 1200 °C with a subsequent isotherm for 1 h and cooled down to 200 °C with a heating rate of 5 °C min^{-1}.

Optical dilatometer: In order to additionally investigate the influence of the sur-

rounding atmosphere, namely the $p(O_2)$ on the thermal expansion, an optical dilatometer L74/HS/1600 (Linseis, Germany) was used. Out of the prepared 5 cm long bar specimens, a 1 cm long piece, with a diagonally tapering end on one side, was cut out with a wire saw. For Mn_2O_3 and Co_3O_4 samples, pellets that were sintered at 1450 °C and 1000 °C respectively were taken to cut out appropriate pieces. Mn_2O_3 and Co_3O_4 samples were chosen for better comparison with previously reported results on Mn_2O_3 and Co_3O_4.[143] The instrument uses a high resolution camera to measure the expansion of the sample. In order to correct the systematic error a reference sample of identical shape made from corundum was placed next to the sample and measured simultaneously. The temperature program involved five cycles between 300 °C to 1100 °C with a heating rate of 5 °C min^{-1} and was carried out twice. Once under air and once in 1% O_2 in N_2. The temperature vs. time profile resembled that of the TGA experiments, described in section 3.5.

The thermal expansion coefficient α can be obtained by linear fit from the relative length change

$$\frac{\Delta L}{L_0}$$

vs. the temperature:

$$\alpha = \frac{d\left(\frac{\Delta L}{L_0}\right)}{dT} \tag{3.13}$$

3.7. Oxygen Pumping Setup

For the initial material screening, an experimental setup based on an operating principle previously reported[66] was used. Central to the setup were two tube furnaces. One of the furnaces was the splitting furnace (SF) (CARBOLITE GERO STF 16/180 with a 301 PID controller), which contained the SM as a representative for a material that can split H_2O or CO_2 in a thermochemical cycle. In this work the SM is represented by 5 g of CeO_2 in spherical particles of 200 µm to 400 µm in diameter. The other furnace is referred to as the pumping furnace (PF) (GERO REST E230/3), containing the PM, which was tested with respect to its oxygen pumping capability. PMs are represented by 3 g of either the synthesized perovskite powders or of Co_3O_4 as a reference material. The two furnaces were interconnected via a gas-tight ceramic and metal tube system, which was in turn connected to a gas supply of Ar and O_2 with mass flow controllers (MKS Instruments) and a rotary vane vacuum pump (VACUUBRAND, RZ5). At the outlet of the tube system a

lambda sensor (MESA GmbH, Lprobe with MK) detected the oxygen concentration. The total mass flow at the outlet of the system was controlled with a calibrator (BIOS, Definer 220L) to be in the desired range of 450–460 sccm.

The experimental procedure, broken down into 5 steps, is given in tab. 3.3. All perovskite compositions tested as PMs were comparatively screened in two temperature modes, one isothermal case (ISO) and one temperature swing case (TS). For the isothermal case the PM was kept at 700 °C at all steps of the experiment. For the temperature swing case the PM was brought to 800 °C at step 1 and cooled down to 700 °C at step 3 during the heat-up/reduction of the SM. This way the actual process of oxygen removal did not consume any additional time since it was carried out simultaneously to the heat-up of the splitting material. Additionally, a high temperature swing case (HTS) was tested for Co_3O_4 in order to ensure reduction of the material and $SrFeO_{3-\delta}$ was used in this case as a representative perovskite for comparison. This high temperature swing case was carried out between 1000 °C to 800 °C as well as 900 °C to 700 °C for Co_3O_4 and between 1000 °C to 800 °C for $SrFeO_{3-\delta}$. The SM in all cases was CeO_2. The reduction temperature for the SM in step 3 was 1440 °C and the oxidation temperature was 980 °C at steps 1 and 4 in all experiments. The temperatures inside the PF and SF were measured with type K and type S thermocouples respectively. Thermocouples were placed between the protection tube of the furnace and the reaction tube containing the sample. Alumina foil was used at the openings of each furnace to function as a reflective heat shield and prevent convection inside the protective tube of the furnace. Leakage of the evacuated setup was determined to be $6 \cdot 10^{-5} \frac{mbar}{s}$. All experimental runs have been carried out at least three times for each setup (ISO / TS) and material, and the results are shown as averaged numbers over all runs with the error bars representing the standard deviation. A schematic drawing and a photograph of the setup are shown in fig. 3.7.

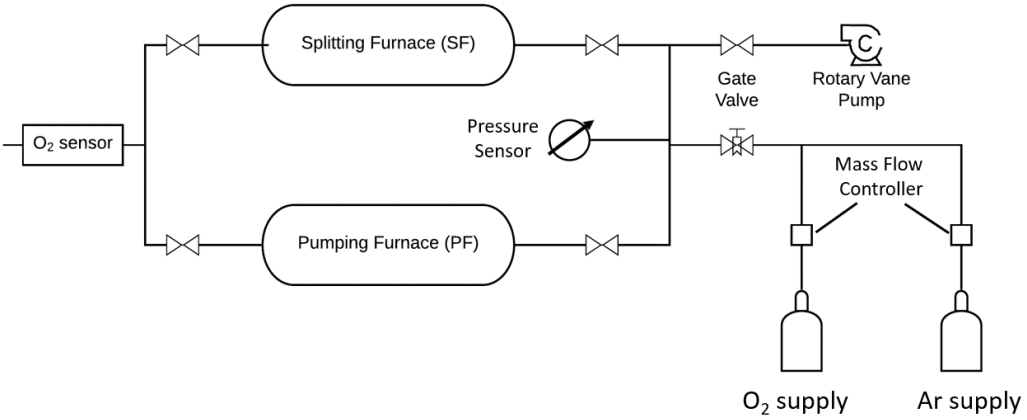

(a)

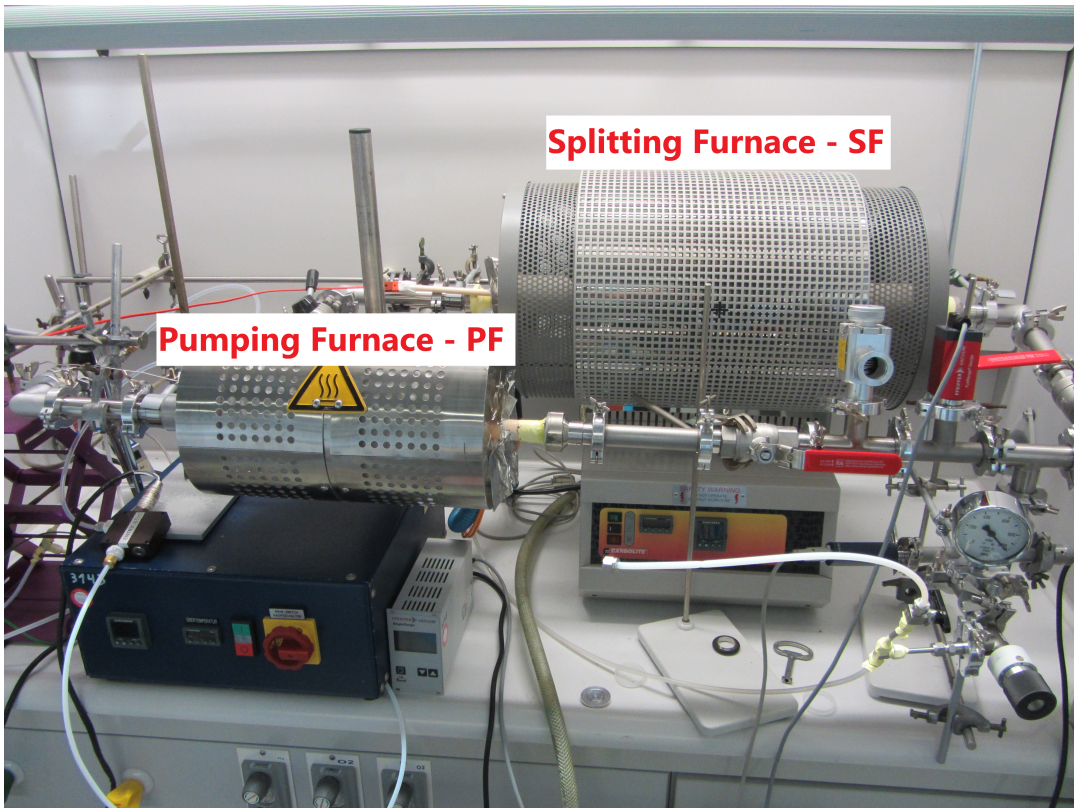

(b)

Fig. 3.7.: Experimental setup for thermochemical oxygen pumping tests, used for the material screening campaign. a) Schematic drawing of the test rig. Taken from Pein et al..[17] b) Photograph of the actual test rig.

Table 3.3.: Main steps of the experimental procedure used in the material screening campaign. Temperatures given as measured by thermocouples. Adapted from Pein et al..[17]

Step	Objective	Action	Temperature (°C)			
			Isothermal		Temp. swing[1]	
			SF	PF	SF	PF
1	Generate oxidized state	Oxidized state of samples is ensured at constant temperature and oxygen rich gas stream; 1h	980	700	980	800
2	Decrease p_{total}; reduce PM	Test rig evacuated down to approx. 1mbar; PM is reduced; reduction of SM negligible under these conditions; 5 min	980	700	980	800
3	Reduce SM	Disconnect vacuum pump; increase temperature of SF; in temperature swing case: simultaneously reduce temperature of PF; PF and SF stay connected; 30 min	1440	700	1440	700
4	Prepare SM for re-oxidation	Disconnect SF and PF; cool down SF to oxidation temperature; 30 min; flush SF with Argon, up to ambient pressure; 5 min	980	700	980	700
5	Re-oxidize SM	Send defined stream of O_2 through SF; 10 min	980	700	980	700

[1] Additional temperature swings applied for Co_3O_4 and $SrFeO_{3-\delta}$ with 1000 °C to 800 °C and 900 °C to 700 °C respectively.

The described experimental setup was dismantled after the completion of the material screening campaign. In a later stage of this work, the setup was rebuilt to analyze the thermochemical oxygen pumping performance of fabricated foams and granules. It was expanded by additional oxygen sensors, capable of measuring $p(O_2)$ under vacuum conditions. Due to leakage caused by one of the sensor types, only one sensor, the Nano-S (Setnag, France) could actually be operated in the evacuated part of the setup. The other sensors (A19 custom made, Metrotec, Germany) were placed outside the evacuated parts of the setup to function as additional observation devices to monitor the $p(O_2)$ at the outlet of each furnace. Due to its fast reaction time, the same lambda sensor (MESA GmbH, L-probe with MK) as in the previous setup was used to determine the oxygen concentration of the outlet gas. These values were used for further calculation later on. A schematic drawing is shown in fig. 3.8 and a photograph of the setup is depicted in fig. 3.9.

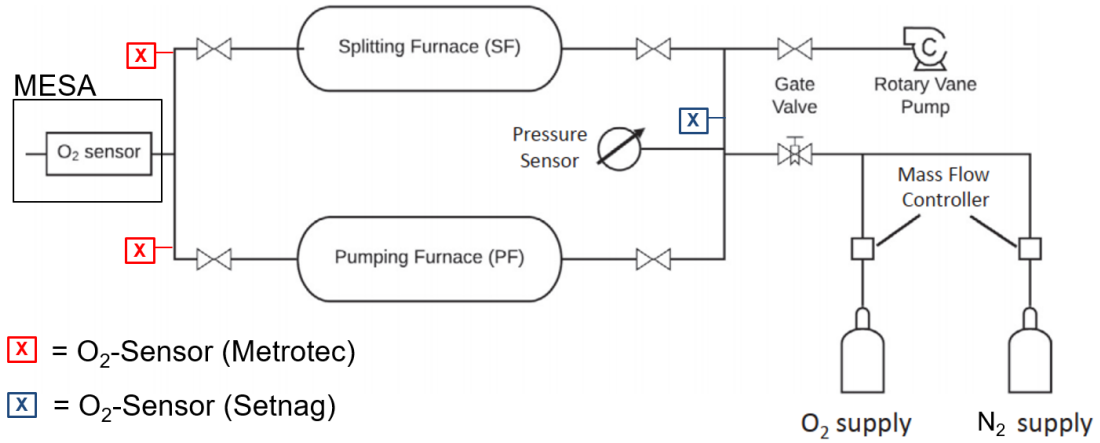

Fig. 3.8.: Schematic drawing of the test rig used to analyze structured specimens. Additional oxygen sensors compared to fig. 3.7 are highlighted. Adapted from Pein et al..[17]

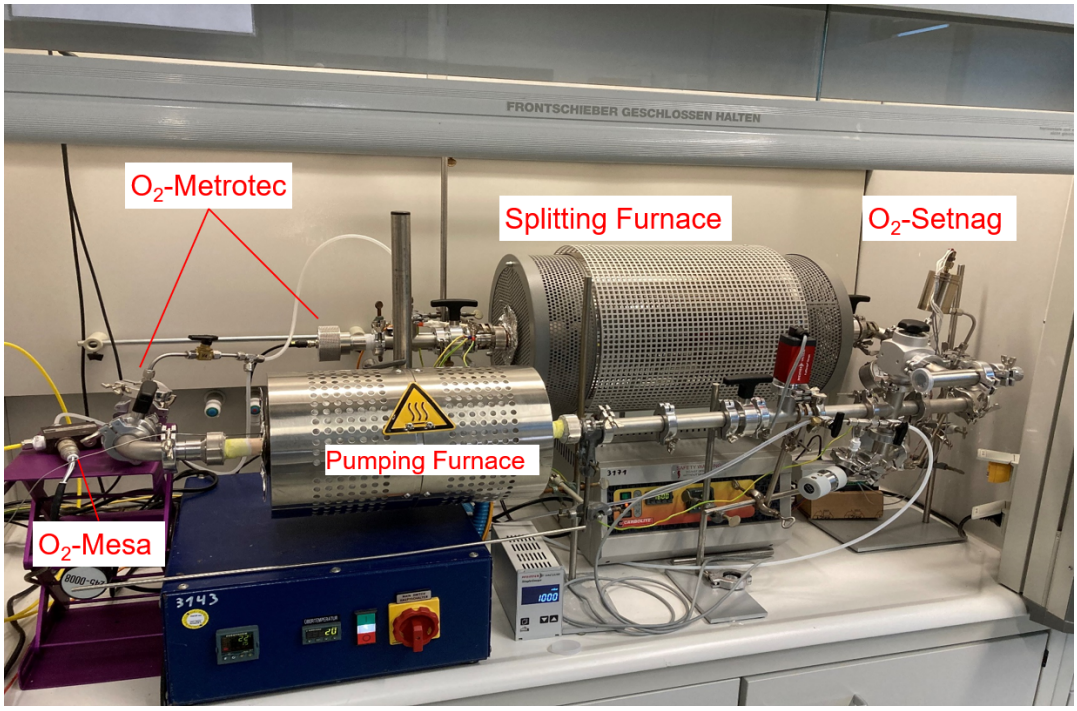

Fig. 3.9.: Photograph of the actual test rig, used to analyze structured specimen.

In contrast to the material screening campaign, only temperature swing operation was chosen in these tests and gas mixtures of O_2 (5.0) and N_2 (5.0) with mass flow controllers were used to define the oxygen concentration of the gas stream. Yet, a second operating principle was tested as well. These operating principles were named "Case 1" and "Case 2" in the following. Leakage of the evacuated setup was determined to be $7.5 \cdot 10^{-5} \frac{mbar}{s}$.

Case 1: Both furnaces, the SF and the PF were initially brought to their reduction temperature (T_{red}) (1500 °C and 800 °C) under a constant gas stream with 4.1% O_2 (Step 1). The furnaces were evacuated by a rotary vane pump over 20 min (Step 2). The SF is kept at T_{red}, while the PF is cooled down to its oxidation temperature (T_{ox}, 700 °C) (Step 3). SF and PF were disconnected and the SF cooled down to its T_{ox}(1000 °C) and flushed with N_2; at ambient pressure the outlet was opened to purge the gas outlet lines of residual O_2 (Step 4). After 5 minutes, a defined gas stream with 4.1% O_2 is fed into the SF to re-oxidize the sample.

Case 2: The SF was initially held T_{ox}. The PF was held at T_{red} under a constant gas stream with 4.1% O_2(Step 1). Both furnaces were evacuated over 20 min with a rotary vane pump (Step 2). Subsequently, the SF was heated up to T_{red} and the PF was cooled to T_{ox} simultaneously (Step 3). SF and PF were disconnected, the SF cooled down to T_{ox} and flushed with N_2; at ambient pressure, the gas outlet is opened to free the gas outlet

lines of residual O_2 (Step 4). After five minutes, a defined gas stream with 4.1% O_2 was fed into the SF to re-oxidize the sample.

In both cases, SF and PF stayed connected throughout steps 1 to 3 and were disconnected from each other at step 4. The total gas flow of 1748 mL min^{-1} was kept constant throughout the experiments. Each sample was measured three times for each case. The two implemented operating principles, broken down into five steps, are given in tab. 3.4.

Table 3.4.: Main steps of the experimental procedure used to test structured specimens.

Step	Objective	Action	Temperature (°C)[1]			
			Case 1[2]		Case 2[3]	
			SF	PF	SF	PF
1	Ensure equilibrium state	equilibrium of samples is ensured at constant temperature and oxygen rich gas stream; 30min	1500	800	1000	800
2	Decrease p_{total}; reduce PM(SM)	Test rig evacuated down to approx. $2 \cdot 10^{-2}$ mbar; PM(SM) is reduced; reduction of SM negligible in case 2; 20 min	1500	800	1000	800
3	(Further) Reduce SM; oxidize PM	Disconnect vacuum pump; Case 1: decrease temp. of PF; Case 2: decrease temp. of PF and increase temp. of SF; PF and SF stay connected; 30 min	1500	700	1500	700
4	Prepare SM for re-oxidation	Disconnect SF and PF; cool down SF to oxidation temperature; 30 min; flush SF with N_2, up to ambient pressure; 5 min	1000	700	1000	700
5	Re-oxidize SM	Send defined stream of O_2 through SF; 10 min	1000	700	1000	700

[1] Temperatures given are rounded for readability. Actual temperatures measured by thermocouples are given in chap. 7.
[2] Reduction of SM is done in step 1&2 separate from the oxidation of the PM in step 3.
[3] Reduction of SM and Oxidation of PM is done simultaneously in step 3.

Analyzing the Oxygen Pumping Effect from Experimental Data

Switching the gas stream from inert gas to a mixture of inert gas and O_2 with a defined O_2-concentration results in a near step function like behavior of the oxygen signal at the exit. With no SM and no PM present, the measurement is referred to as ”empty” and served as a baseline. When an SM is introduced, the absorption of oxygen during oxidation causes a shift in the oxygen step function depending on the amount of oxygen absorbed by the SM. In turn, that shift can be used to calculate the reduction extent of the SM before oxidation in step 5 (compare tab. 3.3 and tab. 3.4). This measurement is referred to as ”reference” and was used to determine the amount of additionally absorbed oxygen by the PM. The PM absorbs oxygen during the reduction of the SM thereby shifting the equilibrium towards the reduced state of the SM. That ultimately increases the reduction extent of the SM. As a result, the oxygen step function is further shifted, which is directly correlated to the reduction extent of the SM. This procedure is illustrated in fig. 3.10 exemplarily with $SrFeO_{3-\delta}$.

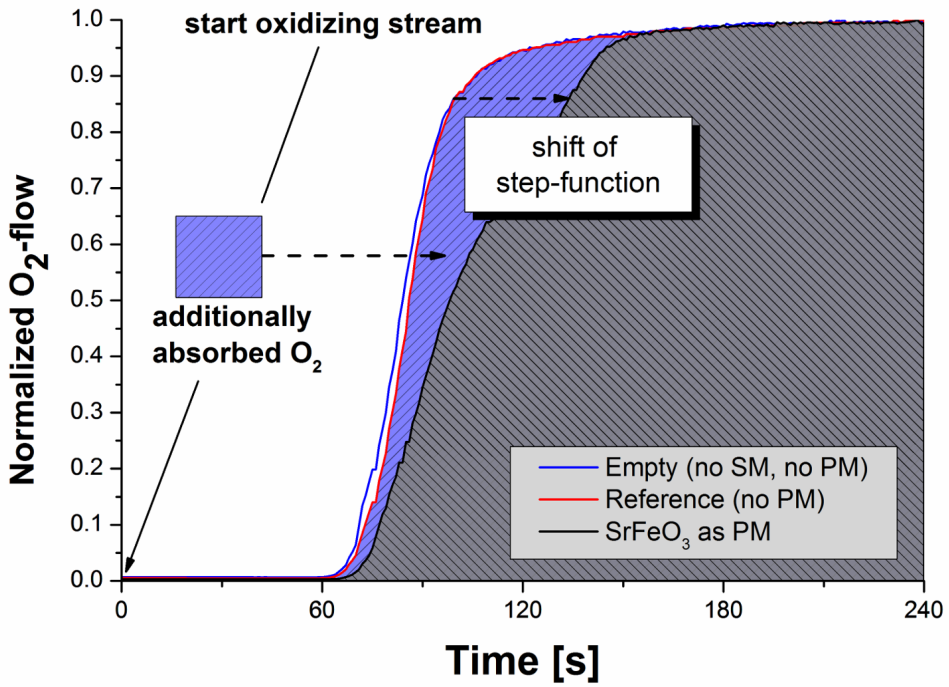

Fig. 3.10.: Illustration of the shift in the oxygen-signal step function during the oxidation step, caused by the increased reduction extent of the SM. Taken from Pein et al..[17]

In order to calculate the amount of oxygen absorbed by the SM, three general cases were defined:

- ”empty”: experiment carried out with neither SM nor PM present; serves as general baseline to calculate the absolute amount of oxygen absorbed by an SM.

- ”reference”: experiment carried out with **only** SM present; used to differentiate the influence of a PM and the systematic influence of the experimental setup and procedure.

- ”pump”: experiment carried out **with** SM and PM; main experiment reveals influence of PM on the reduction extent of SM.

The absolute amount of oxygen absorbed by an SM present in the SF was then calculated by the differences in the total amount of oxygen in the outlet stream during the re-oxidation phase:

$$n_{O_2,X} = \frac{1}{V_m} \int \dot{V_{ox}} \cdot c_{O_2,X} \mathrm{d}t \tag{3.14}$$

With V_m, the molar mass of an ideal gas (used here in approximation for the oxidzer gas stream), $\dot{V_{ox}}$ being the total mass flow of the oxidizer gas stream and $c_{O_2,X}$(X=empty, reference, pump) the oxygen concentration at the outlet during the re-oxidation phase as measured by the oxygen sensor for each of the cases. Using the calculated values from eq. 3.14 the amount of absorbed oxygen can be determined for the reference and pump cases:

Reference case:

$$n_{O_2,abs.} = n_{O_2,empty} - n_{O_2,reference} \tag{3.15}$$

Pump case:

$$n_{O_2,abs.} = n_{O_2,empty} - n_{O_2,pump} \tag{3.16}$$

Given the molar amount of SM, n_{SM}, the reduction extent $\Delta\delta$ can then be calculated by:

$$\Delta\delta = \frac{2 \cdot n_{O_2,abs.}}{n_{SM}} \tag{3.17}$$

Therein, the factor 2 accounts for the 2 mol O that are contained in 1 mol O_2. Furthermore, the absolute amount of *additionally* absorbed O_2, solemnly due to the PM, can also be used as a figure of merit in the comparison of oxygen pumping efficiency of each PM-material, excluding any systematic effects of the experimental procedure:

$$n_{O_2,add.} = n_{O_2,reference} - n_{O_2,pump} \tag{3.18}$$

4. Material Screening for Thermochemical Energy Storage and Oxygen Pumping

A pool of 12 different perovskite compositions were synthesized via the simple synthesis described in chapter 3.1, a solid state reaction approach. An overview of synthesized compositions has been given in tab. 3.2. The rationale to choose suitable compositions to be investigated followed the desired properties for the 3 main target applications within this work: Oxygen pumping, energy storage and air separation. Thus, it resembles a top-down design approach. In order to function in one of the target applications, chosen materials should exhibit significant reduction below 1000 °C and sufficiently high oxygen affinity at temperatures between 600 °C and 800 °C. Furthermore, compositions should consist predominantly of earth-abundant, low-cost materials. The synthesis process should be straight-forward and easily scalable. Choice of composition must account for the fact that a high performing material is in many cases not the first choice to realize such applications in a bigger industrial scale, considering all techno-economic factors such as costs or availability. A schematic illustration of the materials design approach applied in this work is given in fig. 4.1.

This chapter is partially based on peer-reviewed publications authored and co-authored by the author of this work:

Christos Agrafiotis, Mathias Pein, Dimitra Giasafaki, Stefania Tescari, Martin Roeb, and Christian Sattler. "Redox Oxides-Based Solar Thermochemistry and Its Materialization to Reactor/Heat Exchanger Concepts for Efficient Solar Energy Harvesting, Transformation and Storage". In: *Journal of Solar Energy Engineering* 141.2 (2019). DOI: 10.1115/1.4042226

Mathias Pein, Christos Agrafiotis, Josua Vieten, Dimitra Giasafaki, Stefan Brendelberger, Martin Roeb, and Christian Sattler. "Redox thermochemistry of Ca-Mn-based perovskites for oxygen atmosphere control in solar-thermochemical processes". In: *Solar Energy* 198 (Mar. 2020), pp. 612–622. DOI: 10.1016/j.solener.2020.01.088

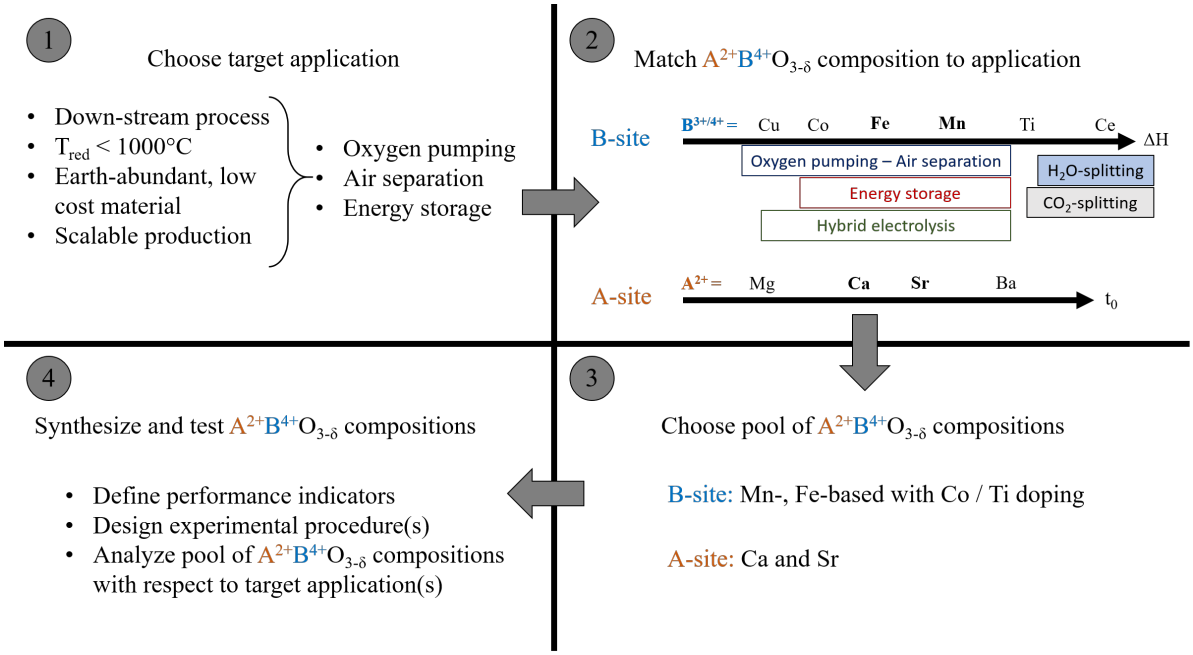

Fig. 4.1.: Schematic illustration of a top-down materials design approach for perovskites in thermochemical cycles, broken down into 4 elemental steps: 1) Choice of target application; 2) Define suitable compositions; 3) Define finite pool of compositions to be analyzed; 4) Synthesis and testing of compositions.

After synthesis of the 12 perovskite compositions, all samples were checked for phase purity by means of XRD. While most samples were identified as single phase, especially $CaMnO_{3-\delta}$ and its Sr-substituted variants showed very small amounts of residual side phases (compare tab. 3.2).

4.1. Thermal Analysis of Synthesized Perovskites

Before being tested in an application setup, all perovskite samples, as well as samples of Co_3O_4 and $(0.75)(Mn_2O_3)^*(0.25)(Fe_2O_3)$, were analyzed by TGA and DSC under air. All samples showed good cyclability with cyclic variation of less than 2% weight loss and gain per cycle over the applied five cycles. Some samples showed a small initial weight gain/loss during the first heating between RT and 400 °C, but stabilized after the first cycle. They showed reversible behavior at the downwards or upwards shifted weight level. While weight loss in this temperature region is likely related to the volatilization of surface adsorbates, e.g. H_2O, weight gain in the first heating phase is typically attributed to oxidation due to a metastable δ, which is higher than equilibrium after synthesis. Possible

reasons are fast cooling during synthesis and slow oxidation kinetics of the composition. Values of weight loss/gain and correlated $\Delta\delta$-values were calculated from the reversible cycle-to-cycle fraction, which neglects initial weight changes in the first heating phase. In fig. 4.2, the %-wt. change of the 14 samples as determined by TGA is shown.

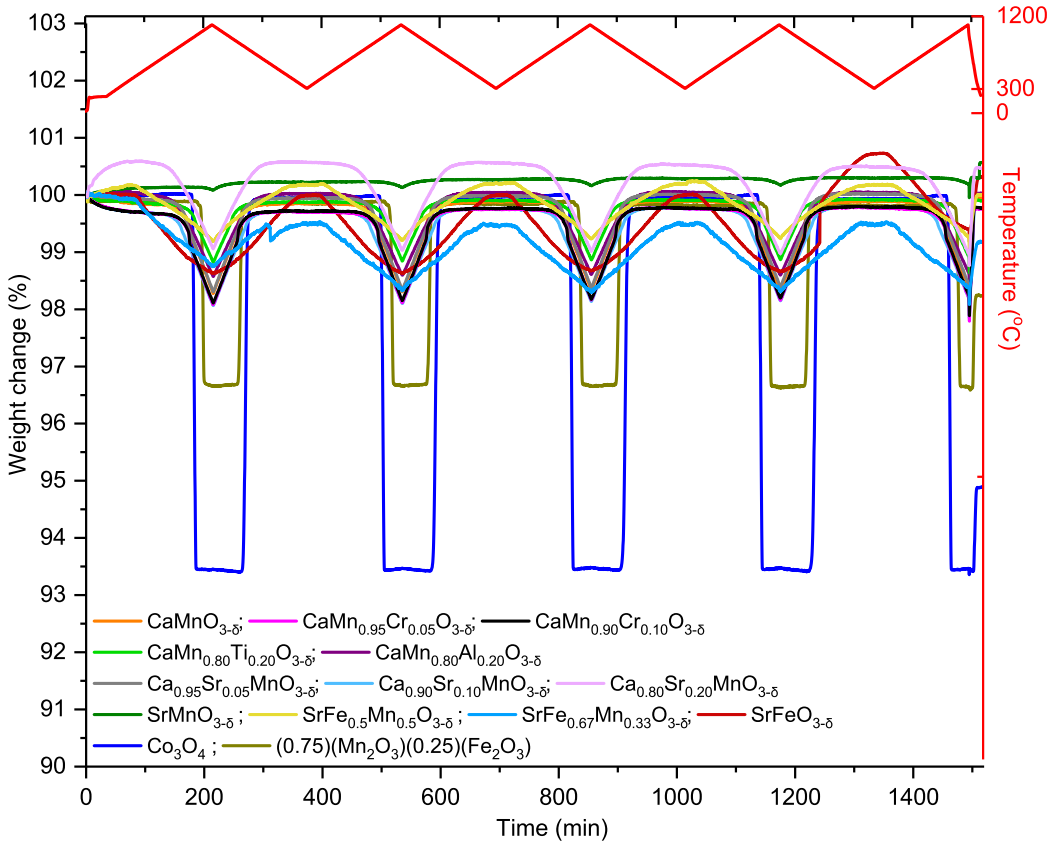

Fig. 4.2.: Weight change of all 12 perovskite samples and the 2 stoichiometric oxide reference samples Co_3O_4 and $(0.75)(Mn_2O_3)^*(0.25)(Fe_2O_3)$ cycled 5 times between 300 °C and 1100 °C. b) a).

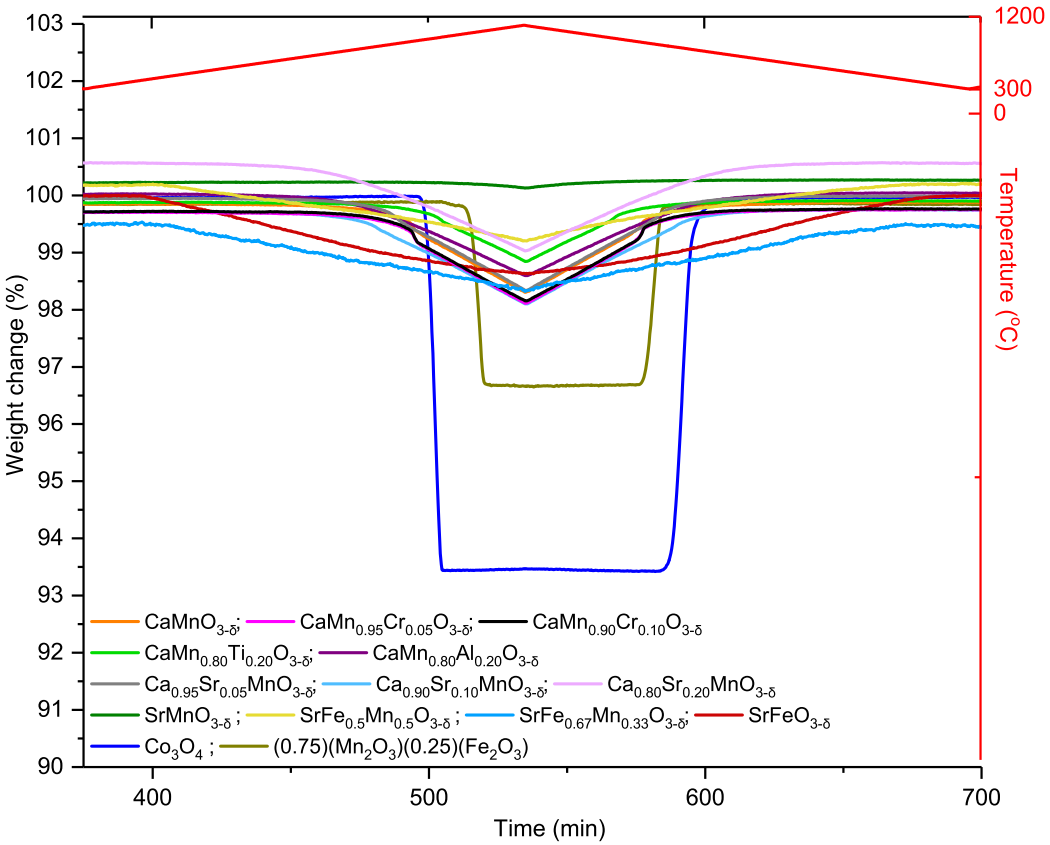

Fig. 4.3.: Zoomed in 2nd cycle of TGA experiments depicted in fig. 4.2.

Co_3O_4 and $(0.75)(Mn_2O_3)$*$(0.25)(Fe_2O_3)$ show a distinctively different behavior than perovskites. They are reduced and oxidized stoichiometrically at one specific temperature of 915 °C and 994 °C respectively instead of gradually over a wide temperature range. This fact is accompanied by significantly higher weight change throughout one cycle. Excluding $SrMnO_3$, which exhibited exceptionally poor redox-behavior compared to all other perovskites, the weight loss/gain of the stoichiometric oxides are higher by a factor of 2.03 % to 3.26 % in the case of $(0.75)(Mn_2O_3)$*$(0.25)(Fe_2O_3)$ and by a factor of 4.08 % to 6.54 % in the case of Co_3O_4. The determined weight changes are close to the theoretical maximum as per eq. 2.1 and 2.2 as well as the respective reduction and oxidation reaction of the mixed Fe-Mn-Oxide.

In the magnified section from the second cycle in fig. 4.3 the differences between the perovskite compositions are easier to distinguish. Besides $SrMnO_{3-\delta}$, all tested perovskites show comparable values of maximum reduction $\Delta\delta_{max}$ in the range of 0.09 to 0.16. $SrMnO_{3-\delta}$ is hardest to reduce under the applied conditions and only showed marginal weight loss and gain compared to the other compositions. It has to be kept in

Table 4.1.: Maximum reversible weight loss/gain of tested perovskite and stoichiometric samples. For perovskites corresponding values of $\Delta\delta$ and for stoichiometric oxides the theoretical weight loss/gain for stoichiometric reduction/oxidation are given. Obtained from 5 cycle measurement shown in fig. 4.2.

Perovskites		
Composition	Max. %-wt. loss/gain	$\Delta\delta_{max}$
$Ca_{0.8}Sr_{0.2}MnO_{3-\delta}$	1.52	0.14(5)
$Ca_{0.9}Sr_{0.1}MnO_{3-\delta}$	1.62	0.15(0)
$Ca_{0.95}Sr_{0.05}MnO_{3-\delta}$	1.62	0.14(7)
$CaMnO_{3-\delta}$	1.55	0.13(9)
$CaCr_{0.05}Mn_{0.95}O_{3-\delta}$	1.60	0.14(3)
$CaCr_{0.1}Mn_{0.9}O_{3-\delta}$	1.60	0.14(3)
$CaAl_{0.2}Mn_{0.8}O_{3-\delta}$	1.43	0.12(3)
$CaTi_{0.2}Mn_{0.8}O_{3-\delta}$	1.06	0.09(4)
$SrMnO_{3-\delta}$	0.13	0.01(5)
$SrFe_{0.5}Mn_{0.5}O_{3-\delta}$	1.01	0.12(1)
$SrFe_{0.67}Mn_{0.33}O_{3-\delta}$	1.23	0.14(7)
$SrFeO_{3-\delta}$	1.34	0.16(0)
Stoichiometric oxides		
Composition	Max. %-wt. loss/gain	stoichiometric
Co_3O_4	6.61	6.64
$(0.75)(Mn_2O_3)$*$(0.25)(Fe_2O_3)$	3.29	3.37

mind that the weight changes depicted in fig. 4.2 do not directly translate to $\Delta\delta$ of each composition, but are calculated by eq. 3.4. Determined values of $\Delta\delta_{max}$, the maximal reversible $\Delta\delta$ reached, and the corresponding weight loss/gain are also summarized in tab. 4.1.

Increasing Sr-content leads to a decrease of the reduction onset temperature. Higher Fe content in the $SrFe_{1-x}Mn_xO_{3-\delta}$ system decrease the reduction onset temperature as well. These compositions start to be reduced at temperatures as low as 400 °C, while Ca-Mn-based compositions do not exhibit any significant reduction until 700 °C. As Fe is easier to reduce than Mn, increasing Fe-content leads to a decrease of the overall redox enthalpy, making the reduced state more favorable at lower temperatures. That also causes higher reduction extents with increasing Fe content in the investigated temperature window. As has been reported previously, the redox enthalpy may also follow a step function where one elemental species, e.g. Fe^{4+}, is reduced completely before a second

species, e.g. Mn^{4+} starts being reduced.[78] Such observations have not been made in this work. This could either originate from simultaneous reduction and oxidation of both species, or from the fact that not all available Fe^{4+}-ions are reduced in the investigated $\Delta\delta$-range.

For B-site substituted $CaMnO_{3-\delta}$ Ti causes an increase of the reduction onset temperature originating from an increase in redox enthalpy. In contrast, substituting Mn with Cr or Al shifts the reduction onset temperature towards lower temperatures with increasing maximum reduction extents per cycle, apparently causing a decrease of the redox enthalpy. Similar results are obtained when A-site substituting $CaMnO_{3-\delta}$ with Sr, yet no significant changes with increasing Sr-content can be observed. Although not taking part in the redox reaction (Sr does not change its oxidation state) it has a significant influence on the thermodynamics of the composition. This can be correlated to another feature that is only observed for Ca-Mn-based compositions within this work: A steep increase of reduction extent in a narrow temperature window. All A-site and B-site substituted compositions except the one substituted with Al exhibits this behavior. While the obtained data from the TGA does not offer any more insight into this behavior of the Ca-Mn-perovskites, the DSC measurements carried out simultaneously can offer additional insight.

The isolated TGA and DSC curves from the second cycle of $CaMnO_{3-\delta}$ serve as an example of the compositions that exhibit such steep increase in $\Delta\delta$ and are shown in fig. 4.4.

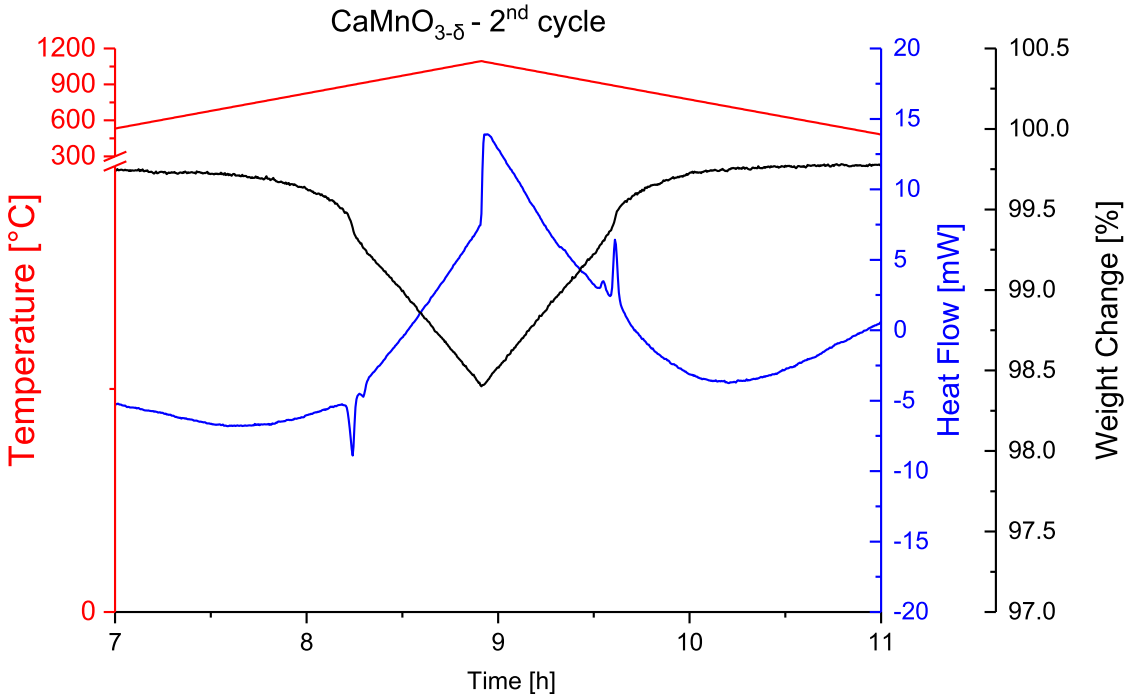

Fig. 4.4.: TGA and DSC curves of the $CaMnO_{3-\delta}$ extracted from the second measurement cycle.

The heat flow signal obtained from DSC not only reveals that the increase in reduction extent during heat-up is reversed during cool-down, but also that it coincides with an endothermal reaction during heat-up, which is reversed to exothermal during cool-down as well. A doublet of peaks can be identified with rather small thermal flows involved. This points at a phase transition of the crystal structure from orthorhombic to cubic with an intermediate tetragonal phase. Such phase transition has also been reported in literature[111,188] and appears to strongly influence the thermodynamics of the material. The presented results lead to the conclusion that Ca-Mn-based perovskites undergo a phase transition throughout the thermal cycling. Its influence on the compositions thermodynamics is discussed in chapter 5 within this work.

The rapid release of oxygen during the phase transition from orthorhombic to cubic leads to the conclusion that the oxygen vacancy formation energy is much lower in the cubic phase as compared to the orthorhombic phase, causing the material to release oxygen until the new equilibrium is reached. From there on, the speed of reduction with increasing temperature is slowing down a little, but remaining higher than that of the orthorhombic phase. It is remarkable that this whole process is fully reversible during cool-down and mirrors the behavior during heat-up. In order to take a closer look at the

on-set and completion temperatures of the observed phase transition, the peaks of the DSC signal have been isolated by baseline substraction and are shown in fig. 4.5.

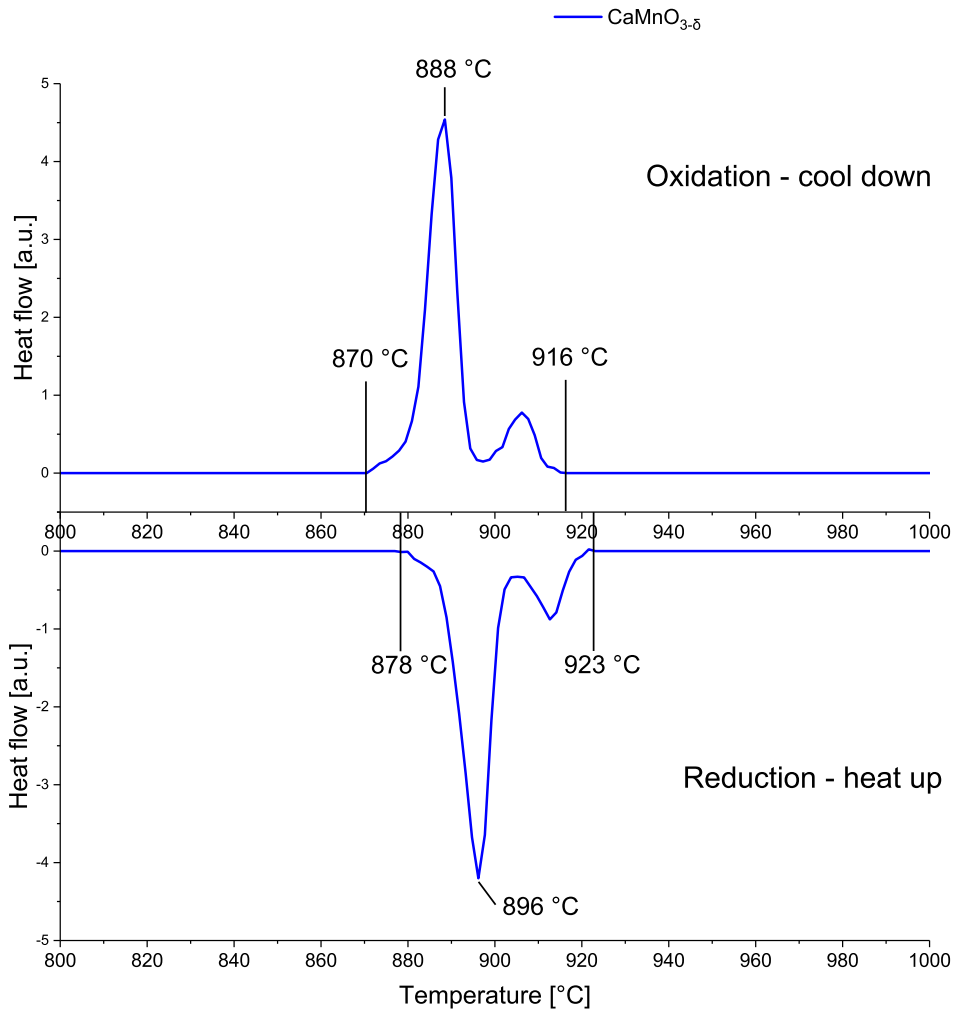

Fig. 4.5.: Isolated peaks from DSC-signal from the second cycle of $CaMnO_{3-\delta}$. Isolated via baseline subtraction.

The isolated and magnified DSC-peaks in fig. 4.5 reveal a small hysteresis of the phase transition during reduction and oxidation. The phase transition starts and finishes 8 °C higher during reduction compared to the oxidation. However, the shape and relative magnitude between the bigger main peak and smaller side peak remains identical. At this point it cannot be concluded with certainty if the doublet of peaks actually represent two phase transitions (from orthorhombic to tetragonal to cubic) or if the mechanism of phase transition may involve multiple steps itself. Yet, all tested Ca-Mn-based perovskite compositions except $CaAl_{0.2}Mn_{0.8}O_{3-\delta}$ showed this behavior of a steep increase/decrease in reduction extent during heat-up/cool-down. Substituting $CaMnO_{3-\delta}$ with either Sr on

the A-site or Ti/Cr on the B-site does impact the temperature at which the phase transition occurs as well as the shape of the peaks. Baseline substracted (isolated) DSC-peaks of all compositions are shown in fig. 4.6. Therein, all compositions that did not have any distinct peaks within their DSC-signal, exhibit a flat line after baseline subtraction.

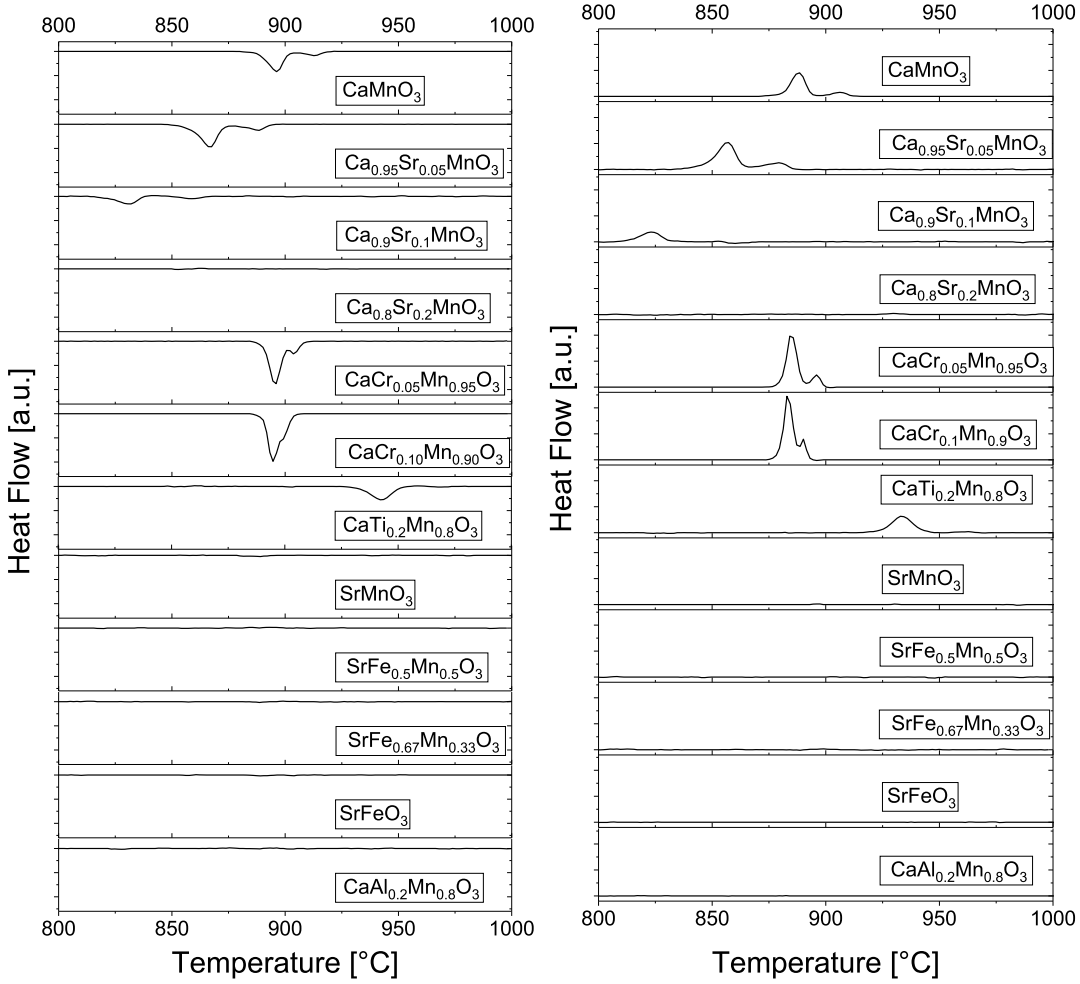

Fig. 4.6.: Baseline substracted DSC-signals for all 12 tested perovskite compositions. If present, peaks of the DSC-signal are isolated. a) Reduction (heat-up); b) Oxidation (cool-down). Data extracted from second cycle of 5 cycle measurement (see fig. 4.2). Taken from Pein et al..[17]

A-site substitution shifts the phase transition to lower temperatures and also stretches the gap between the two peaks until no DSC-peaks are visible at 20%-Sr and presumably no phase transitions takes place. B-site substitution with Ti shifts the phase transition to higher temperatures with only one peak visible. B-site substitution with Cr does not move the temperature of phase transition, but the doublet of peaks shift closer together

at 5%-Cr and merge to one peak with a small shoulder at 10%-Cr. Comparing the initial tolerance factor as well as their crystal structure (see tab. 3.2), it can be seen that only initially orthorhombic compositions exhibit a DSC-sensitive phase transition. All other compositions remain in their initial crystal structure throughout the measurement. Furthermore, compositions with a lower tolerance factor such as $CaTi_{0.2}Mn_{0.8}O_{3-\delta}$ undergo this phase transitions at higher temperatures. In contrast, compositions with higher tolerance factor such as Sr-substituted $CaMnO_{3-\delta}$ undergo the phase transition at lower temperatures. Compositions with a very similar tolerance factor such as the Cr-substituted $CaMnO_{3-\delta}$ exhibit the phase transition at temperatures close to $CaMnO_{3-\delta}$.

It can be concluded that the orthorhombic distortion from the ideal cubic phase has a major influence on the temperature of an occuring phase transition. Strongly distorted perovskites only transition to the cubic phase at higher temperatures, while the less distorted perovskites transition already at lower temperatures. The two compositions $CaAl_{0.2}Mn_{0.8}O_{3-\delta}$ and $Ca_{0.8}Sr_{0.2}MnO_{3-\delta}$ represent special cases. For $Ca_{0.8}Sr_{0.2}MnO_{3-\delta}$ it can be assumed that a transition takes place, but is smeared over a wide temperature range. It exhibits only marginal exothermal/endothermal effects and is thereby not detectable by DSC-signal. An exception of that observation is $CaAl_{0.2}Mn_{0.8}O_{3-\delta}$, which does not show any DSC-active transition to the cubic structure despite being orthorhombically distorted. With a tolerance factor between $CaTi_{0.2}Mn_{0.8}O_{3-\delta}$ and $CaCr_{0.1}Mn_{0.9}O_{3-\delta}$, a DSC-active phase transition would be expected to be visible in the temperature window between those two compositions.

In order to determine the temperature of phase transition T_{pt} through DSC analysis, three options are available. T_{pt} can be determined by the start temperature of the first peak in the DSC-signal, the peak position of one of the peaks or the end temperature of the last peak (the second peak in the case of duplet peaks). It is debatable as to which option produces the best results, but within this work the peak temperature of the biggest peak was chosen as the phase transition temperature and rendered good reproducibility over the accumulated five cycles. Determined phase transition temperatures are given in tab. 4.2.

Table 4.2.: Temperatures of phase transition T_{pt} from heat-up and cool-down of all 12 perovskite compositions. T_{pt} determined by peak temperature of biggest peak in DSC.

Composition	T_{pt} Heat-up (°C)	T_{pt} Cool-down (°C)
$Ca_{0.8}Sr_{0.2}MnO_{3-\delta}$	-	-
$Ca_{0.9}Sr_{0.1}MnO_{3-\delta}$	832	823
$Ca_{0.95}Sr_{0.05}MnO_{3-\delta}$	867	857
$CaMnO_{3-\delta}$	896	888
$CaCr_{0.05}Mn_{0.95}O_{3-\delta}$	894	883
$CaCr_{0.1}Mn_{0.9}O_{3-\delta}$	896	884
$CaAl_{0.2}Mn_{0.8}O_{3-\delta}$	-	-
$CaTi_{0.2}Mn_{0.8}O_{3-\delta}$	942	933
$SrMnO_{3-\delta}$	-	-
$SrFe_{0.5}Mn_{0.5}O_{3-\delta}$	-	-
$SrFe_{0.67}Mn_{0.33}O_{3-\delta}$	-	-
$SrFeO_{3-\delta}$	-	-

All compositions with phase transitions showed a hysteresis between heat-up (reduction) and cool-down(oxidation). During oxidation the reverse phase transition occurs between 8 °C and 11 °C lower compared to reduction. As the reduction extent and the corresponding formation of oxygen vacancies appears to influence the point where the phase transition occurs, the observed hysteresis supports the idea of slower kinetics of the oxidation reaction compared to the reduction reaction. At reasonably fast heating rates of 5 °C min^{-1}, the ever so slightly retarded oxidation results in a shift of the phase transition towards lower temperatures during cool-down.

Such observed DSC-active phase transitions can also contribute to the energy storage density of a TCES-unit. The exo- and endothermal transitions can be exploited for extra storage capacity within a certain temperature range. Additionally, knowing that the conditions under which such a transition occurs can be tuned and shifted by A- or B-site substitution of a base composition such as $CaMnO_{3-\delta}$ this offers additional benefits of utilizing perovskites in such devices. In contrast, stoichiometric oxides like Co_3O_4 will always reduce and oxidize at the same temperature, basically limiting the exploitable temperature range of a TCES-unit to a window covering this specific temperature. Perovskites provide much more flexibility in this case, allowing to store and extract thermal energy beyond the sensible heat capacity over a wide temperature range.

4.2. Oxygen Pumping Performance

As described in chapter 3.7, two different cases with respect to thermochemical oxygen pumping were tested in the material screening campaign: An isothermal (ISO) case and a temperature swing (TS) case. A detailed description of the steps involved in the procedures can be found for both cases in tab. 3.3 of chapter 3.7. In the isothermal case the PM is kept at a constant temperature of 700 °C, reduced by pressure reduction and reoxidized by oxygen released from the SM during its own reduction. In order to analyze the performance of each composition, two values can be considered: The oxygen absorbed by the SM and the resulting values of $\Delta\delta$. The latter needs to be calculated via eq. 3.17, but has the advantage to be a commonly used value for the reduction of non-stoichiometric oxides and therefore easier comparable.

Determined values of $\Delta\delta$ for the isothermal case are shown in fig. 4.7. Additionally also the background case "empty" as well as the reference case "No PM" are shown to get a better idea of the actual influence of the presence of a PM. The reference case "No PM" does exhibit small amounts of $\Delta\delta$. This residual reduction extent originates from the fact that the SF is disconnected from the PF after reduction of the CeO_2, used as the SM here. Oxygen released from CeO_2 during the reduction is trapped inside the PF and is not available for re-oxidation, resulting in small amounts of residual $\Delta\delta$. As can be seen from fig. 4.7, the presence of a PM increases this effect by not only trapping oxygen in the disconnected volume, but also binding it chemically due to oxidation of the PM.

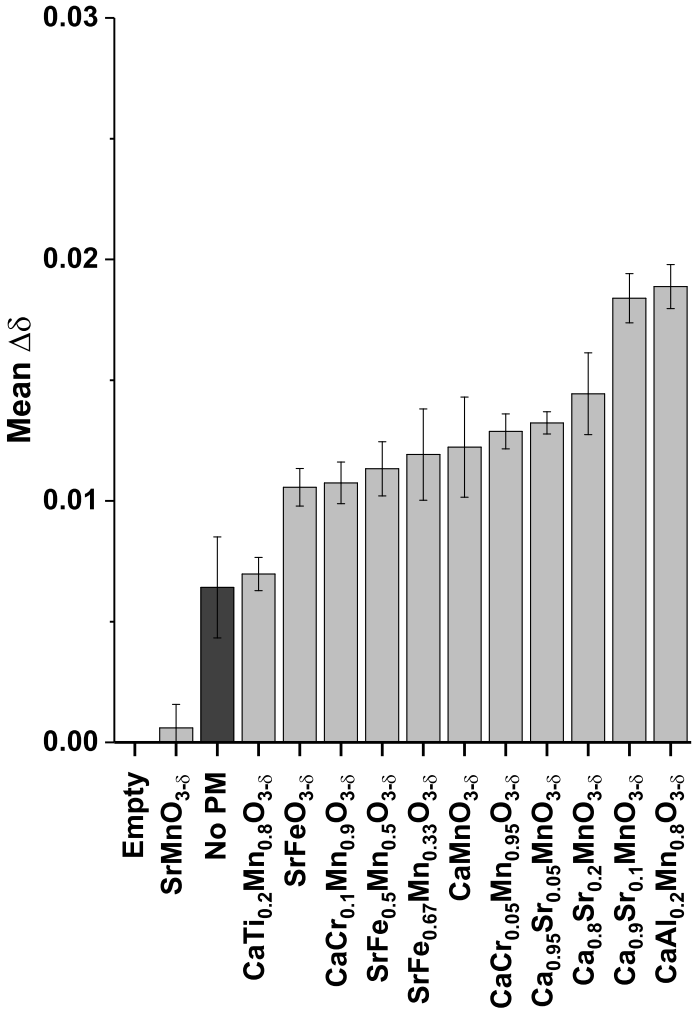

Fig. 4.7.: Values of $\Delta\delta$ obtained with different perovskite compositions as oxygen pumping material in the isothermal operation mode. "Empty"-case: no SM, no PM; "No PM"-case: only SM (CeO_2). Y-axis scale fixed for easier comparison with fig. 4.8. Taken from Pein et al..[17]

All perovskites, except $SrMnO_{3-\delta}$, have a positive impact on the reduction extent of the used CeO_2, increasing the $\Delta\delta$ in the isothermal case. Surprisingly, $SrMnO_{3-\delta}$ does actually decrease the $\Delta\delta$. This can be explained by an increased amount of oxygen present in the evacuated setup, which causes either a shift in equilibrium of CeO_2 or increases the amount of available oxygen during cool-down. That basically cancels out the effect of the disconnected PF and ultimately results in an almost fully re-oxidized CeO_2 after cool-down and before the actual re-oxidation step (compare step 4 in tab. 3.3). Since $SrMnO_{3-\delta}$ is the only hexagonal composition tested herein, there might be a correlation as hexagonal perovskites are known to have higher oxygen vacancy formation energies and are

harder to reduce compared to other perovskite structures.[189] This alone however does not explain the decrease in reduction extent. If the $SrMnO_{3-\delta}$ is only marginally reduced or not reduced at all under the applied conditions, it should not influence the process at all. A retarded reduction of the $SrMnO_{3-\delta}$, which takes place very slowly due to hindered kinetics can cause the release of oxygen in the phase where it is supposed to act as an oxygen sink.

Best performing compositions were $Ca_{0.9}Sr_{0.1}MnO_{3-\delta}$ and $CaAl_{0.2}Mn_{0.8}O_{3-\delta}$, reaching a $\Delta\delta$ of 0.0184 (±0.0010) and 0.0189 (±0.0009) respectively, compared to 0.0064 (±0.0021) in the reference case. Considering the error margins, the compositions are all very close. Still, the results demonstrate that a variety of perovskite compositions are able to function as an effective oxygen pump even under isothermal conditions. Fe-rich compositions are performing worse compared to Mn-based perovskites and their B-site doped variants. Beyond that observation no clear trends are visible.

In theory, adding a temperature swing to the operational mode of the oxygen pump will increase the oxygen affinity of the pumping material, due to a shift of the equilibrium state towards the oxidized state. The lower limit of the temperature swing, the oxidizing temperature, has been chosen to be 700 °C, identical to the isothermal case. The upper limit of the temperature swing, the reduction temperature, was chosen to be 800 °C. The rationale of using these temperatures is related to the reasonable temperature levels of waste heat from the splitting process, which can be assumed to range somewhere below the oxidation temperature of the splitting material, which is 1000 °C in this case. All twelve perovskite compositions as well as the two stoichiometric materials were employed in oxygen pumping tests following the temperature swing procedure described in tab. 3.3. Results of perovskite samples in the form of $\Delta\delta$ values are shown in fig. 4.8.

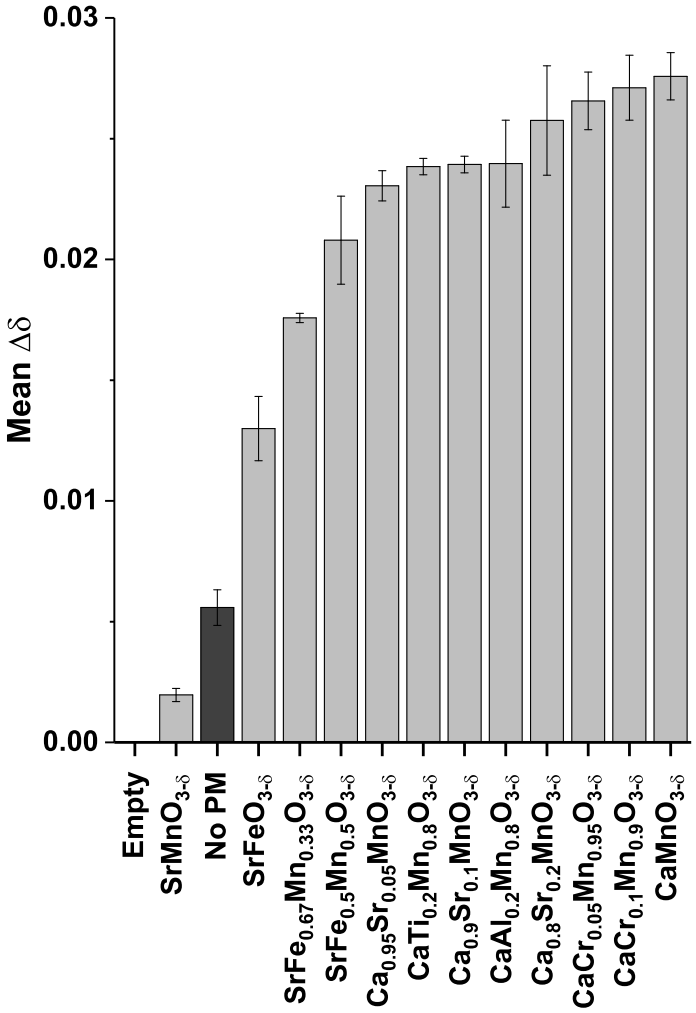

Fig. 4.8.: Values of $\Delta\delta$ obtained with different perovskite compositions as oxygen pumping material in the temperature swing operation mode. "Empty"-case: no SM, no PM; "No PM"-case: only SM (CeO_2). Taken from Pein et al..[17]

The introduction of a temperature swing significantly increased the pumping potential of most compositions. Considering the error margins, the best performing compositions can be considered equal. However, $CaMnO_{3-\delta}$ can be highlighted here among the best performing material compositions despite being a rather simple composition containing only three elements. Employment of $CaMnO_{3-\delta}$ increased the reduction extent on the reference material from $\Delta\delta = 0.0056(\pm 0.007)$ to $\Delta\delta = 0.0276(\pm 0.009)$. Thereby, $CaMnO_{3-\delta}$ increased the $\Delta\delta$ by almost 400% compared to the reference case without a PM. A clear trend can be observed, namely that Mn-rich compositions in the orthorhombic structure perform better than the Fe-rich compositions with cubic structure. The hexagonal $SrMnO_{3-\delta}$ causes negative effects on the reduction extent of the CeO_2, due to unfavorable

thermodynamics and kinetics already discussed for the isothermal case. Comparing the isothermal and temperature swing operation modes, an increase in performance of almost 30% is apparent. As intended, the applied temperature swing increased the potential of the pumping materials to pump oxygen out of the splitting furnace and increased the reduction extent of the employed CeO_2. Therefore, a temperature swing operation has also been favored for follow-up experiments discussed in chapter 7.

Representative stoichiometric oxides $(0.75)(Mn_2O_3)$*$(0.25)(Fe_2O_3)$ and Co_3O_4 were tested in adjusted temperature swing operation with T_{red}/T_{ox} = 1000 °C / 800 °C. Temperature levels were chosen in order to include their respective equilibrium temperatures of 994 °C and 915 °C. An additional run with T_{red}/T_{ox} = 900 °C / 700 °C for Co_3O_4 was performed in order to identify shifts in equillibrium temperature under reduced pressure. Measurements were carried out once and not further pursued, since only marginal or no positive impact could be identified outside of a marginal improvement of $\Delta\delta$ at 900 °C / 700 °C for Co_3O_4. The results are shown in the appendix (fig. A.1).

Furthermore, two of the best performing compositions of the temperature swing case, $CaMnO_{3-\delta}$ and $CaCr_{0.1}Mn_{0.9}O_{3-\delta}$, were also tested in the form of sintered rods. The operational mode and experimental procedure was identical to the described temperature swing case. Results are shown in fig. 4.9. Since the rods of $CaMnO_{3-\delta}$ and $CaCr_{0.1}Mn_{0.9}O_{3-\delta}$ weighed significantly more than the powders, 4.05 g and 3.76 g respectively, samples are compared with their powdered counterparts in additionally absorbed oxygen in mol per gram of pumping material.

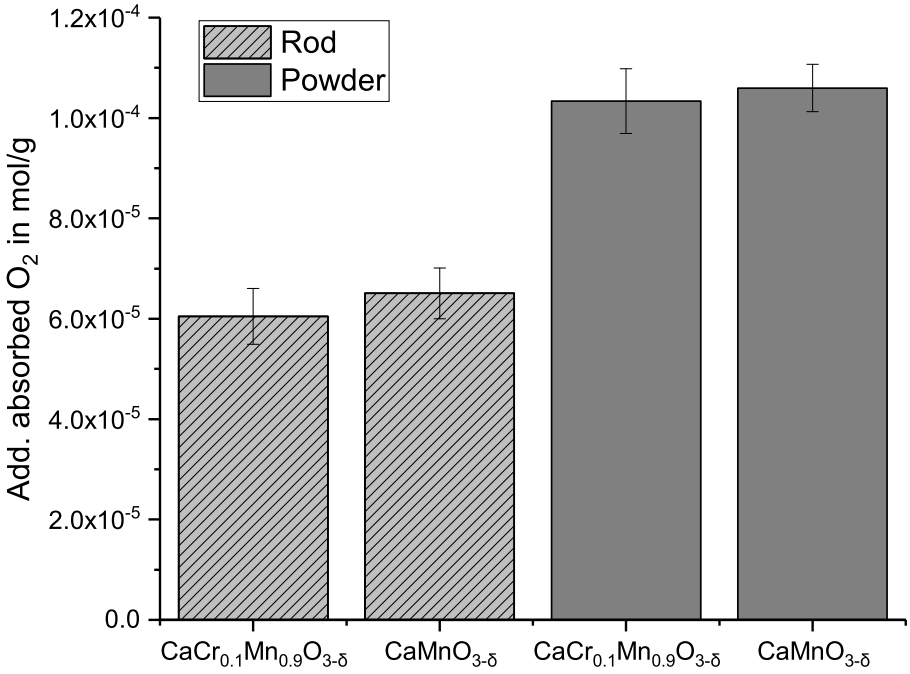

Fig. 4.9.: Comparison of rods and powders of $CaMnO_{3-\delta}$ and $CaCr_{0.1}Mn_{0.9}O_{3-\delta}$ as oxygen pumping materials in a temperature swing case. Taken from Pein et al..[17]

The tested rods were significantly underperforming compared to the respective powders. Taking $CaMnO_{3-\delta}$ as an example, the additionally absorbed oxygen increased by over 60% when using powders instead of sintered rods. It indicates that the available surface area and the reaction kinetics play a major role in the oxygen pumping process employed within this work.

4.3. Thermal and Thermochemical Expansion and Contraction

Sintered bar specimens of all 12 perovskite compositions were analyzed with a contact dilatometer as described in chapter 3.6. All samples exhibited a gradual increase in the thermal expansion coefficient within a temperature window between 700 °C to 900 °C. Therefore, two temperature regimes were defined to determine the thermal expansion coefficient α according to eq. 3.13.
300 °C to 600 °C and 1000 °C to 1200 °C were chosen as the low temperature and high temperature regimes wherein the thermal expansion occurs quasi-linear. An exemplary measurement of the heat-up of $CaMnO_{3-\delta}$ and the linear fits are shown in fig. 4.10.

Therein, also the phase-transition temperature, as determined by DSC (see tab. 4.2), is highlighted. It demonstrates that the visible point of inflection where the thermal expansion coefficient increases significantly over a small temperature range correlated well with the temperature of phase transition as determined by DSC.

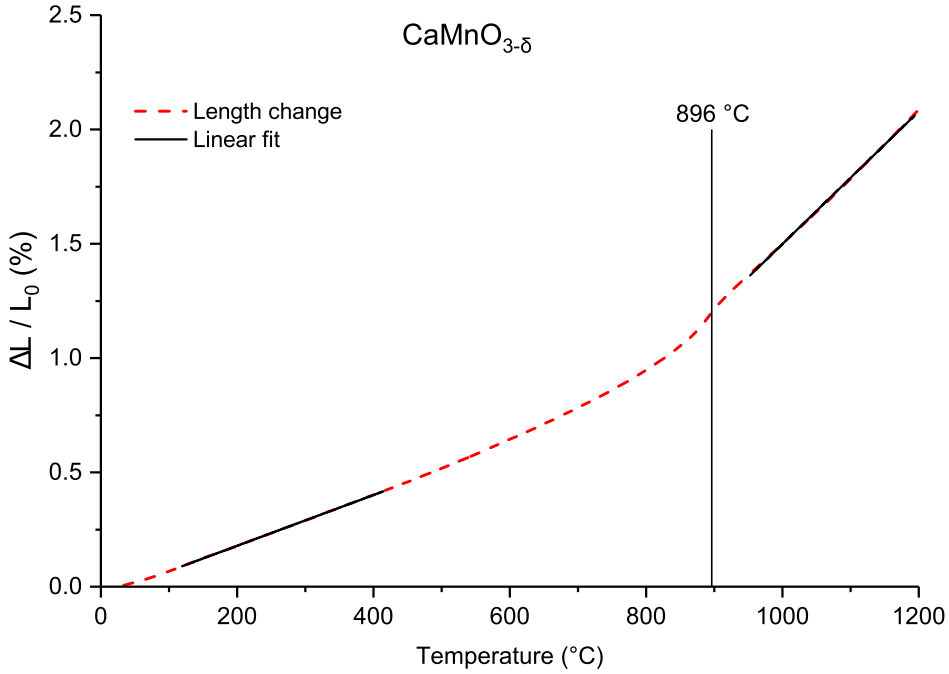

Fig. 4.10.: Exemplary depiction of thermal expansion for the two temperature regimes (300 °C to 600 °C and 1000 °C to 1200 °C). Phase transition temperature T_{pt} as determined via DSC indicated by black vertical line.

The analysis shown exemplarily in fig. 4.10 was performed for all 12 perovskite compositions for Heat-up and Cool-down. As stated before there was a 1 h isothermal step at 1200 °C between the Heat-up and Cool-down. Results of this analysis are given in tab. 4.3 together with the maximum expansion ΔL_{max}, measured after terminating the heat-up process, and the residual expansion measured by a caliper. Negative values of residual expansion respresent shrinkage of the sample. The accuracy of the device is given with $0.03 \cdot 10^{-6}/K$ by the manufacturer.

Table 4.3.: Length changes and determined thermal expansion coefficients α for all 12 perovskite compositions. α_1 for 300 °C< T <600 °C. α_2 for 1000 °C< T <1200 °C

Composition	α_1 in $10^{-6}/K$	α_2 in $10^{-6}/K$	ΔL_{max} in %	ΔL_{res} in %
		Heat-up		
$Ca_{0.8}Sr_{0.2}MnO_{3-\delta}$	13.4	30.8	2.394	−0.01
$Ca_{0.9}Sr_{0.1}MnO_{3-\delta}$	14.1	31.9	2.395	0
$Ca_{0.95}Sr_{0.05}MnO_{3-\delta}$	14.5	31.9	2.440	0
$CaMnO_{3-\delta}$	11.1	29.0	2.080	−0.01
$CaCr_{0.05}Mn_{0.95}O_{3-\delta}$	14.4	33.2	2.540	−0.32
$CaCr_{0.1}Mn_{0.9}O_{3-\delta}$	15.0	36.7	2.701	0.02
$CaAl_{0.2}Mn_{0.8}O_{3-\delta}$	11.7	24.0	1.967	0
$CaTi_{0.2}Mn_{0.8}O_{3-\delta}$	13.7	29.8	2.211	0
$SrMnO_{3-\delta}$	13.5	20.8	1.841	−0.34
$SrFe_{0.5}Mn_{0.5}O_{3-\delta}$	16.2	28.1	2.459	−0.02
$SrFe_{0.67}Mn_{0.33}O_{3-\delta}$	14.8	26.8	2.370	0.16
$SrFeO_{3-\delta}$	14.1	22.5	1.895	−0.08
		Cool-down		
$Ca_{0.8}Sr_{0.2}MnO_{3-\delta}$	13.2	30.1	2.394	−0.01
$Ca_{0.9}Sr_{0.1}MnO_{3-\delta}$	13.8	29.9	2.395	0
$Ca_{0.95}Sr_{0.05}MnO_{3-\delta}$	13.9	30.4	2.440	0
$CaMnO_{3-\delta}$	7.9	30.0	2.080	−0.01
$CaCr_{0.05}Mn_{0.95}O_{3-\delta}$	14.3	32.3	2.540	−0.32
$CaCr_{0.1}Mn_{0.9}O_{3-\delta}$	15.0	34.4	2.701	0.02
$CaAl_{0.2}Mn_{0.8}O_{3-\delta}$	9.5	27.7	1.967	0
$CaTi_{0.2}Mn_{0.8}O_{3-\delta}$	13.4	29.7	2.211	0
$SrMnO_{3-\delta}$	13.6	27.1	1.841	−0.34
$SrFe_{0.5}Mn_{0.5}O_{3-\delta}$	16.2	29.0	2.459	−0.02
$SrFe_{0.67}Mn_{0.33}O_{3-\delta}$	11.0	30.2	2.370	0.16
$SrFeO_{3-\delta}$	6.8	23.7	1.895	−0.08

All 12 perovskite compositions exhibit a significant increase in the thermal expansion coefficient from low to high temperatures. While below 600 °C α ranges from 7.9 to 16.2 $10^{-6}/K$, which is approximately in the range of steel. It increases to values of 22.5 to 36.7 $10^{-6}/K$ at temperatures above 1000 °C. This effect can be correlated to the formation of oxygen vacancies at elevated temperatures, which led to an expansion of the crystal lattice. As can be seen from a comparison of heat-up and cool-down values of α of all specimens tested (summarized in tab. 4.3), the expansion was followed by a contraction of similar magnitude. Most samples regained their original length after completion of the measurement with minor variation of 0.01 to 0.02 %.

Exceptions are $CaCr_{0.05}Mn_{0.95}O_{3-\delta}$, $SrMnO_{3-\delta}$ and $SrFeO_{3-\delta}$, which suffered from significant sintering at the isothermal step at 1200 °C. They exhibited residual shrinkage after the measurement. Additionally, $SrFe_{0.67}Mn_{0.33}O_{3-\delta}$ exhibited irreversible expansion. Compositions that transitioned into a stable cubic form at high temperatures appear to have slightly higher expansion coefficients compared to the compositions that were already cubic (or hexagonal in the case of $SrMnO_{3-\delta}$) at room temperature. Beyond that, no clear trends of a correlation of composition and thermal expansion has been identified.

The formation of oxygen vacancies could lead to an increase of the crystal lattice constants, but comparing the maximum $\Delta\delta$ values of each sample vs. the maximum expansion ΔL_{max} in fig. 4.11 do not support this conclusion. No correlation was identified.

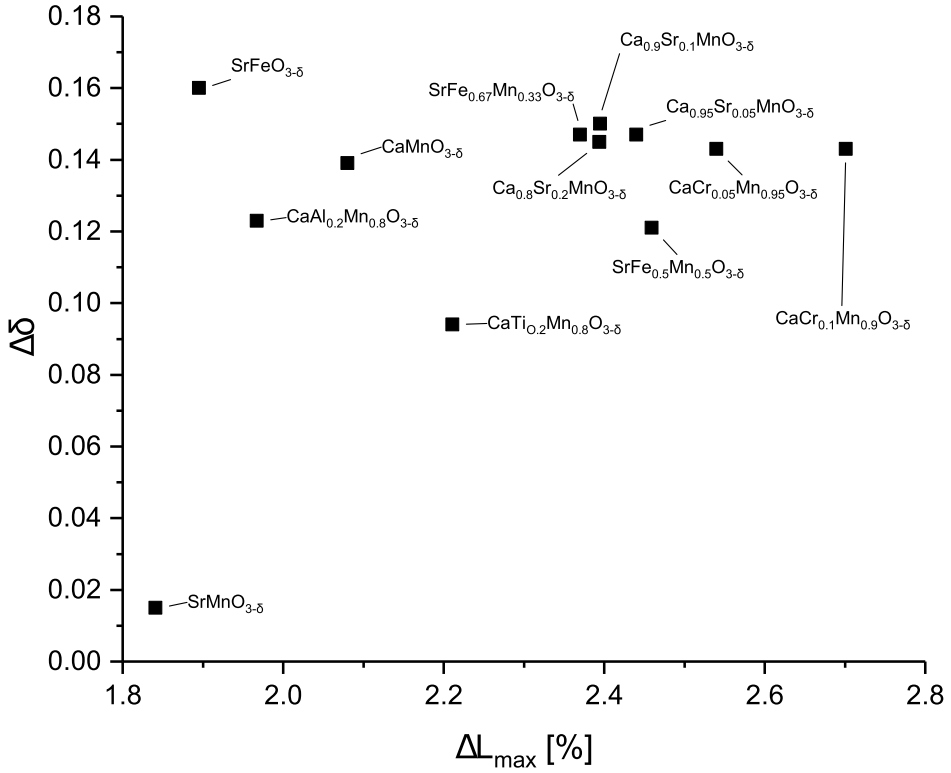

Fig. 4.11.: Reached $\Delta\delta$ values from TGA experiments plotted vs. the maximum expansion $\Delta L_{\max}$, obtained by dilatometry, for all 12 perovskite samples.

While it has to be kept in mind that the TGA measurements only reached maximum temperatures of 1100 °C compared to the 1200 °C of the dilatometer measurements, it can be concluded that the formation of oxygen vacancies most likely has an impact on the expansion. Yet, it was not the only factor determining the overal expansion of a composition over the whole temperature range up to 1200 °C. Out of all tested perovskite compositions $CaMnO_{3-\delta}$ was chosen to be compared to the stoichiometric oxides Co_3O_4 and $(0.75)(Mn_2O_3)$*$(0.25)(Fe_2O_3)$ in multicycle dilatometry experiments under air. Among the compositions that showed good performance in the oxygen pumping experiments, $CaMnO_{3-\delta}$ exhibited the lowest fully reversible thermal expansion in the investigated temperature range.

Since the employed DIL 803 contact dilatometer was not capable of multicycle measurements, the optical dilatometer L74/HS/1600 and pre-cut pieces from bar specimens (fig. 3.6) were used for multicycle experiments. Five consecutive cycles between 300 °C and 1100 °C were run under air with heating rates of 5 °C min^{-1}. Results of these 5-cycle runs are shown in fig. 4.12.

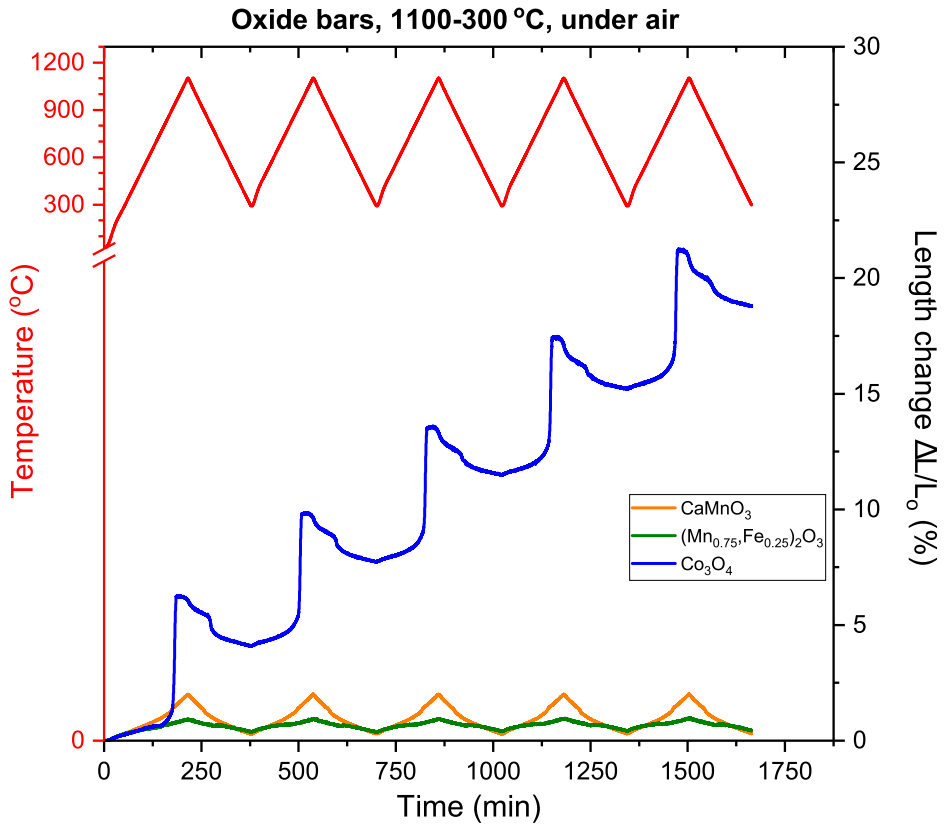

Fig. 4.12.: Thermal expansion from 5 consecutive cycles between 300 °C to 1100 °C of $CaMnO_{3-\delta}$, Co_3O_4 and $(0.75)(Mn_2O_3)$*$(0.25)(Fe_2O_3)$ under air.

Co_3O_4 exhibits the biggest expansion per cycle and also does not regain its original length at the end of a cycle. Co_3O_4 suffers from irreversible expansion in each cycle, adding up to 18.78% expansion after the fifth cycle. The mixed Mn- and Fe-Oxide $(0.75)(Mn_2O_3)$*$(0.25)(Fe_2O_3)$ exhibited the smallest maximum expansion per cycle, but a small, yet significant, residual expansion of 0.05% after 5 cycles. A significant fraction of the expansion is irreversible. $CaMnO_{3-\delta}$ showed maximum expansion of 2 %, which is in good agreement with results from the contact dilatometer. This value is much smaller than the maximum expansion of Co_3O_4, but almost double than that of $(0.75)(Mn_2O_3)$*$(0.25)(Fe_2O_3)$. However, in contrast to both these stoichiometric systems, expansion and contraction of $CaMnO_{3-\delta}$ proved to be fully reversible. Fig. 4.13 shows the isolated 5 cycles of $CaMnO_{3-\delta}$ and reveals full reversibility of the thermal expansion and contraction. Also in these experiments the inflection point where the thermal expansion coefficient increases is visible. This fact is further discussed in the following chapter 5. Full reversibility of expansion and contraction of the $CaMnO_{3-\delta}$ perovskite material can be very beneficial for applications where structural integrity of the

used material is favorable, such as reactor systems that utilize foams, honeycombs or other monolithic structures of the active material.

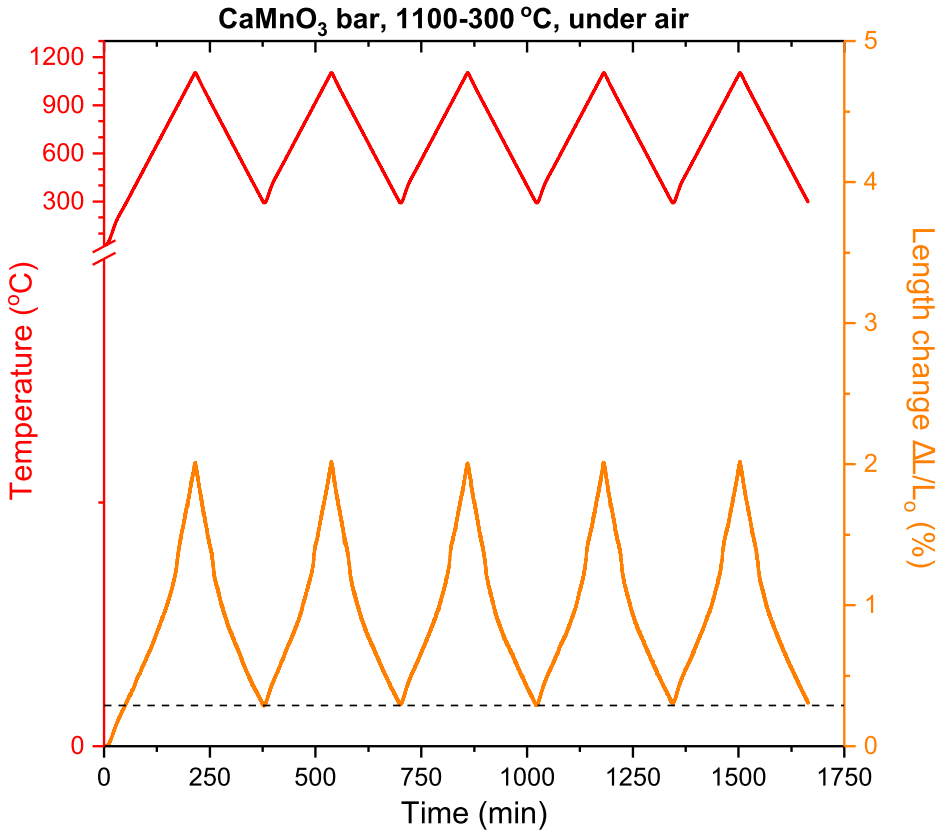

Fig. 4.13.: Thermal expansion of $CaMnO_{3-\delta}$ extracted from fig. 4.12. Horizontal dashed line represents expansion level at 300 °C.

4.4. Choosing a Material Composition for the Fabrication of Structured Specimens

The material screening campaign laid out in this chapter pursued the goal to determine a material composition that is suitable for one or all of the main downstream application of a solar thermal receiver considered within this work: Thermochemical storage, oxygen pumping and air separation. In total, 12 perovskite compositions were synthesized, tested and compared to state-of-the-art stoichiometric oxides considered for such applications. Out of the tested perovskite compositions, $SrMnO_{3-\delta}$ exhibits the smallest yield of redox conversion with a $\Delta\delta$ of only 0.01 per cycle. Additionally, Fe-rich compositions

tend to underperform in that regard, compared to the Mn-rich compositions tested. Although the Fe-rich compositions exhibited considerable reduction even at temperatures as low as 400 °C, they were dismissed for the aimed temperature window of operation, which is located within the range of 600 °C to 1000 °C.

Out of the Mn-rich compositions the very simple composition of $CaMnO_{3-\delta}$ was among the best performing materials. It showed comparable results to their B-site Cr-substituted variants, closely followed by the A-site Sr-substituted $CaMnO_{3-\delta}$-compositions. DSC analysis revealed a reversible endothermal/exothermal reaction in the temperature range of ≈800 °C to 950 °C, which can be correlated to an orthorhombic to cubic phase transition. This observation was unique to initially orthorhombic compositions only. Such phase transition not only adds to the energy storage density of such materials as the transition is endothermal during reduction and exothermal during oxidation, but is also accompanied by significant reduction and oxidation in the temperature range of the transition. This fact can be exploited if the material is cycled around the temperature range where the transition occurs to increase the reduction/oxidation yield per temperature swing or cycle. A-site Sr-substitution was observed to influence the temperature where the phase transition occurs significantly, without limiting or even increasing the thermodynamic potential of the compositions.

Furthermore, thermal expansion and contraction was found to be reversible for most perovskite compositions and the $Ca_{1-x}Sr_xMnO_{3-\delta}$-system in particular. Over 5 thermal cycles of $CaMnO_{3-\delta}$ only negligibly small amounts of residual expansion were observed in contrast to small, but significant expansion of the Mn,Fe-Oxide of 0.05% and extensive expansion of 18.78% of Co_3O_4 after 5 cycles. The reversible expansion/contraction renders perovskites superior over stoichiometric oxides for thermally cycled monolithic structures, which eventually need to be cycled up to or even beyond a thousand thermal cycles and need to maintain their structural integrity over the course.

Considering all these findings, it was decided to proceed with the $Ca_{1-x}Sr_xMnO_{3-\delta}$-system and ultimately produce open porous structures made entirely of such material. To deepen the understanding of the influence of Sr-content in the $Ca_{1-x}Sr_xMnO_{3-\delta}$-system, further investigations were conducted and are reported in the following chapter.

5. The Ca-(Sr)-Mn-O system

In initial DSC and dilatometry experiments addressed in the previous chapter, the Sr-substituted $CaMnO_{3-\delta}$ the $Ca_{1-x}Sr_xMnO_{3-\delta}$-system revealed a distinct impact of the Sr-content on the crystal structure and occurring phase transitions at elevated temperatures. In order to better understand how this material system can be tuned by adjusting the Sr-content, further investigation was carried out in the form of DSC, multicycle dilatometry and HT-XRD of samples from $Ca_{1-x}Sr_xMnO_{3-\delta}$ with $x \in [0, 0.05, 0.1, 0.2]$. Additionally, those experiments were performed under reduced $p(O_2)$ - Air, 1% O_2 and pure Ar for DSC as well as Air and 1% O_2 for dilatometry. As was shown in the previous chapter, the observed DSC-active phase transitions exhibit a hysteresis with respect to their onset and peak temperature between heat-up and cool-down. In order to make the values determined by different analysis techniques in this chapter easier to compare, phase transition temperatures and thermal expansion coefficients presented here were solely determined during the heat-up. This also holds true for multicyclic experiments.

As a first step, HT-XRD was performed for $CaMnO_{3-\delta}$ under air to confirm that the DSC active phase transition is indeed a transition from an orthorhombic to cubic crystal structure. The results in fig. 5.1 confirm the existence of such transition. Characteristic orthorhombic peaks vanish above the transition temperature of 896 °C. These peaks reappear when the sample is cooled down and reoxidized again, proving reversibility of this transition.

This chapter is partially based on peer-reviewed publications authored and co-authored by the author of this work:

Lena Klaas, Mathias Pein, Peter Mechnich, Alexander Francke, Dimitra Giasafaki, Dorottya Kriechbaumer, Christos Agrafiotis, Martin Roeb, and Christian Sattler. "Controlling thermal expansion and phase transitions in Ca1−xSrxMnO3−δ by Sr-content". In: *Physical Chemistry Chemical Physics* 24 (45 2022), pp. 27976–27988. DOI: 10.1039/D2CP04332G

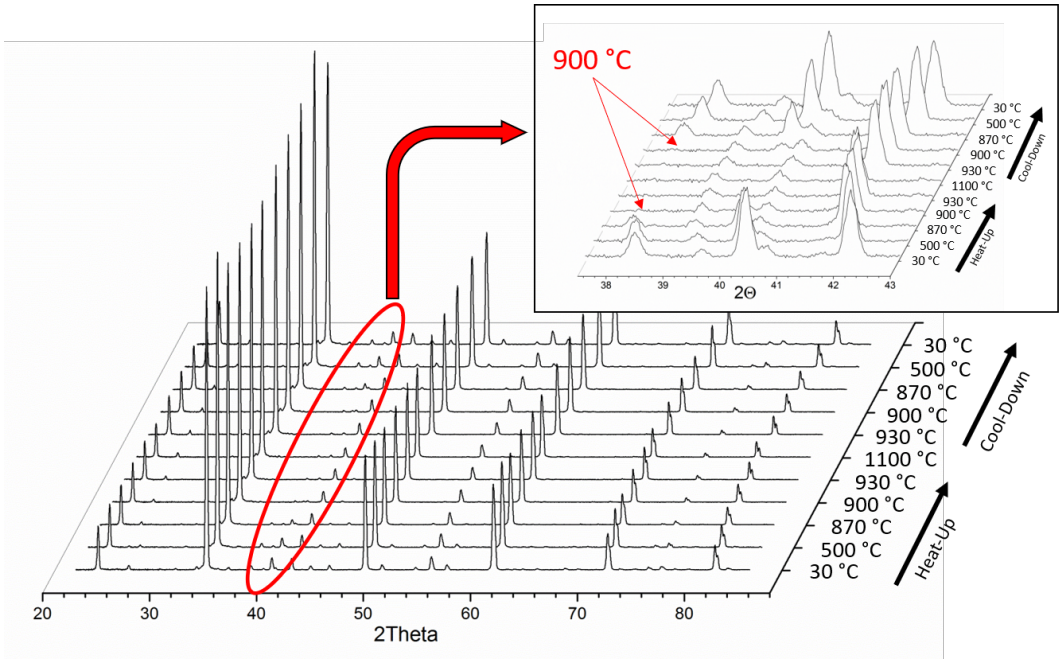

Fig. 5.1.: HT-XRD of $CaMnO_{3-\delta}$ in the temperature range from 30 °C to 1100 °C. The inlet shows an enlarged section of diffraction angles where diffraction peaks of the orthorhombic structure shrink and disappear at high temperatures and reappear during cool-down. Taken from Pein et al..[19] CC-BY

The orthorhombic $Pnma$ structure and the cubic $Pm\bar{3}m$ structure share almost all the diffraction peaks since the two crystal structures are very closely related, with the cubic $Pm\bar{3}m$ being of higher symmetry. Additionally, a tetragonal intermediate structure was reported by Leonidova et al.,[111] which can only be observed at a very narrow window of $\Delta\delta$ at elevated temperatures. The DSC results presented in chapter 4 exhibit a doublet of peaks for some compositions, which hints at an involvement of a tetragonal intermediate phase. However, this intermediate phase could not be identified in the HT-XRD experiments within this work. Therefore, the phase transition for $Ca_{1-x}Sr_xMnO_{3-\delta}$ with $x \in [0, 0.05, 0.1, 0.2]$ within this work will be labeled as orthorhombic to cubic phase transitions for simplicity. There is no evidence of the tetragonal phase largely influencing the characteristics of the tested compositions. Still, there is a chance the transition will involve at least fractional existence of a tetragonal intermediate phase, which simply cannot be resolved in the XRD.

The diffraction peaks at $\approx$ 38.5° and $\approx$ 40.5° 2Θ can be uniquely assigned to the orthorhombic $Pnma$ structure. Disappearance and reappearance of these diffraction peaks confirmed the transition from orthorhombic $Pnma$ to cubic $Pm\bar{3}m$ structure of the $CaMnO_{3-\delta}$. The temperature range where this phase transition occured correlated

well with the phase transition temperature of $CaMnO_{3-\delta}$ determined via DSC (896 °C). Furthermore, the shift of diffraction peaks towards smaller diffraction angles, best visible in the enlarged section of the inlet of fig. 5.1, could be correlated to the expansion of the crystal lattice.

5.1. Cyclic Thermal Expansion in Air and 1% O_2

As observed in previous dilatometry experiments, $CaMnO_{3-\delta}$ and Sr-substituted samples exhibited two distinct regions of a quasi-linear thermal expansion coefficient, which were consistent over the conducted five cycles. In light of the HT-XRD results above, the lower temperature thermal expansion coefficient between 300 °C and 600 °C coul be attributed to the orthorhombic phase and the thermal expansion coefficient at higher temperatures between 900 °C and 1100 °C to the cubic phase. Thereafter, they are labeled α_{ortho} and α_{cubic} respectively.

New sets of dilatometry experiments were performed to investigate the effects of Sr and $p(O_2)$ with specimens of $Ca_{1-x}Sr_xMnO_{3-\delta}$ with $x \in [0, 0.05, 0.1, 0.2]$. These dilatometry experiments were carried out with 5 cycles in the range of 300 °C to 1100 °C and a heating rate of 5 °C min^{-1}. Two distinct 5 cycle runs were performed in synthetic air and 1% O_2 diluted in N_2 respectively.
α_{ortho} was found to be in the range of $12 - 14 \cdot 10^{-6} K^{-1}$ and α_{cubic} in the range of $29 - 34 \cdot 10^{-6} K^{-1}$. No clear trends could be identified for α_{ortho} and α_{cubic} with respect to Sr-content or $p(O_2)$. Results of the 5-cycle runs in air and 1% O_2 are shown in fig. 5.2.

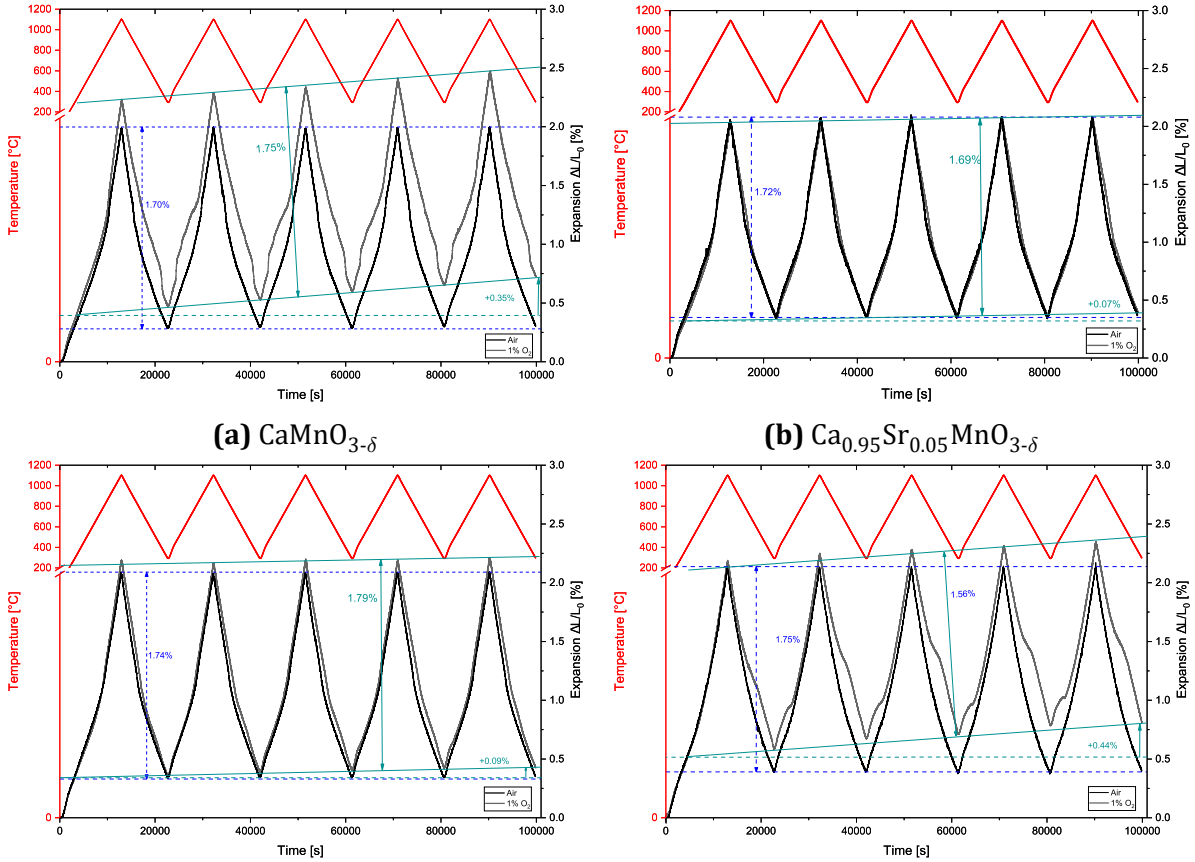

(a) $CaMnO_{3-\delta}$ **(b)** $Ca_{0.95}Sr_{0.05}MnO_{3-\delta}$

(c) $Ca_{0.9}Sr_{0.1}MnO_{3-\delta}$ **(d)** $Ca_{0.80}Sr_{0.20}MnO_{3-\delta}$

Fig. 5.2.: 5 cycle dilatometry of $Ca_{1-x}Sr_xMnO_{3-\delta}$ samples in air (black) and 1% O_2 (grey). Cycled from 300 °C to 1100 °C. Dashed blue (air) and turquoise (1% O_2) lines highlight reversible and irreversible expansion and contraction in each cycle. ΔL and L_0 represent the length change and the original, as-prepared, length at room temperature. Reproduced from Klaas and Pein et al.[20] with permission from the Royal Society of Chemistry.

All samples were found to exhibit fully reversible expansion in air between 300 °C and 1100 °C, its magnitude ranging from 1.71% to 1.75%. Reducing the oxygen concentration to 1% led to residual expansion for all samples. However, minor A-site Sr-substitution with 5% and 10% reduced this residual expansion from 0.35% for $CaMnO_{3-\delta}$ to 0.07% for $Ca_{0.95}Sr_{0.05}MnO_{3-\delta}$ and to 0.09% for $Ca_{0.9}Sr_{0.1}MnO_{3-\delta}$. The improved reversibility of thermal expansion led to a significant improvement of cyclability in oxygen depleted atmosphere. Larger Sr-contents of 20% caused an increase of the residual expansion after five cycles to 0.44% and a fluctuation of the reversible fraction of the expansion. Furthermore, $CaMnO_{3-\delta}$ showed distinctively different behavior at 1% O_2 compared to measurements in air. After the first heating cycle $CaMnO_{3-\delta}$ exhibited a sharp increase of the

expansion slope at temperatures around 450 °C and a decrease around 750 °C, resulting in a curve that resembles a peak shoulder in this temperature region. This behavior was reproduced in the following cycles. It was unique to the pure $CaMnO_{3-\delta}$ and inhibited by the addition of 5% and 10% Sr to the composition. At 20% Sr however, a shoulder-like feature reappeared in the lower temperature region.

The addition of Sr to the composition also influenced the overall maximum expansion of the samples at the upper temperature limit compared to room temperature. This becomes evident in fig. 5.3 where the heat-up phase of the third cycle of each composition is shown. With increasing Sr-content the expansion shifted to higher values. However, compositions with 5% and 10% Sr behaved very similar. This influence of Sr was expected, since the greater ionic radius of Sr^{2+} compared to Ca^{2+} leads to an expansion of the crystal lattice. Furthermore, the step like behavior of $CaMnO_{3-\delta}$ at 1% O_2 between 400 °C and 700 °C was prominent. As already discussed, this behavior was reversible and unique to $CaMnO_{3-\delta}$ with $Ca_{0.80}Sr_{0.20}MnO_{3-\delta}$ showing similar, but not identical irregularities. A possible explanation for such behavior could be kinetic limiations of the $CaMnO_{3-\delta}$ bar specimen. As this behavior only occured after the heating phase of the first cycle, incomplete re-oxidation, a reversible phase change or disproportionation of $CaMnO_{3-\delta}$ could cause the irregular expansion and contraction. If the kinetics are so slow, the material is practically frozen in a non-equilibrium state below a certain temperature threshhold (in the range of 400 °C to 700 °C). This non-equilibrium state relaxes once the adequate temperature is reached where reaction speed is sufficient.

Room temperature XRD of the $CaMnO_{3-\delta}$-sample did not reveal any changes to the crystal structure of the material. DSC-measurements of $CaMnO_{3-\delta}$ as is shown later in this chapter, also do not hint at a phase change taking place in this region. As both these techniques, XRD and DSC, were performed with powder samples, kinetic limitations of a sintered bar specimen compared to powder samples become likely as a possible explanation. The same conclusion applies for $Ca_{0.80}Sr_{0.20}MnO_{3-\delta}$, which also showed irregular, but apparently reversible behavior. Further investigation would be required to clarify the reason for the observed irregular behavior of $CaMnO_{3-\delta}$ and $Ca_{0.80}Sr_{0.20}MnO_{3-\delta}$.

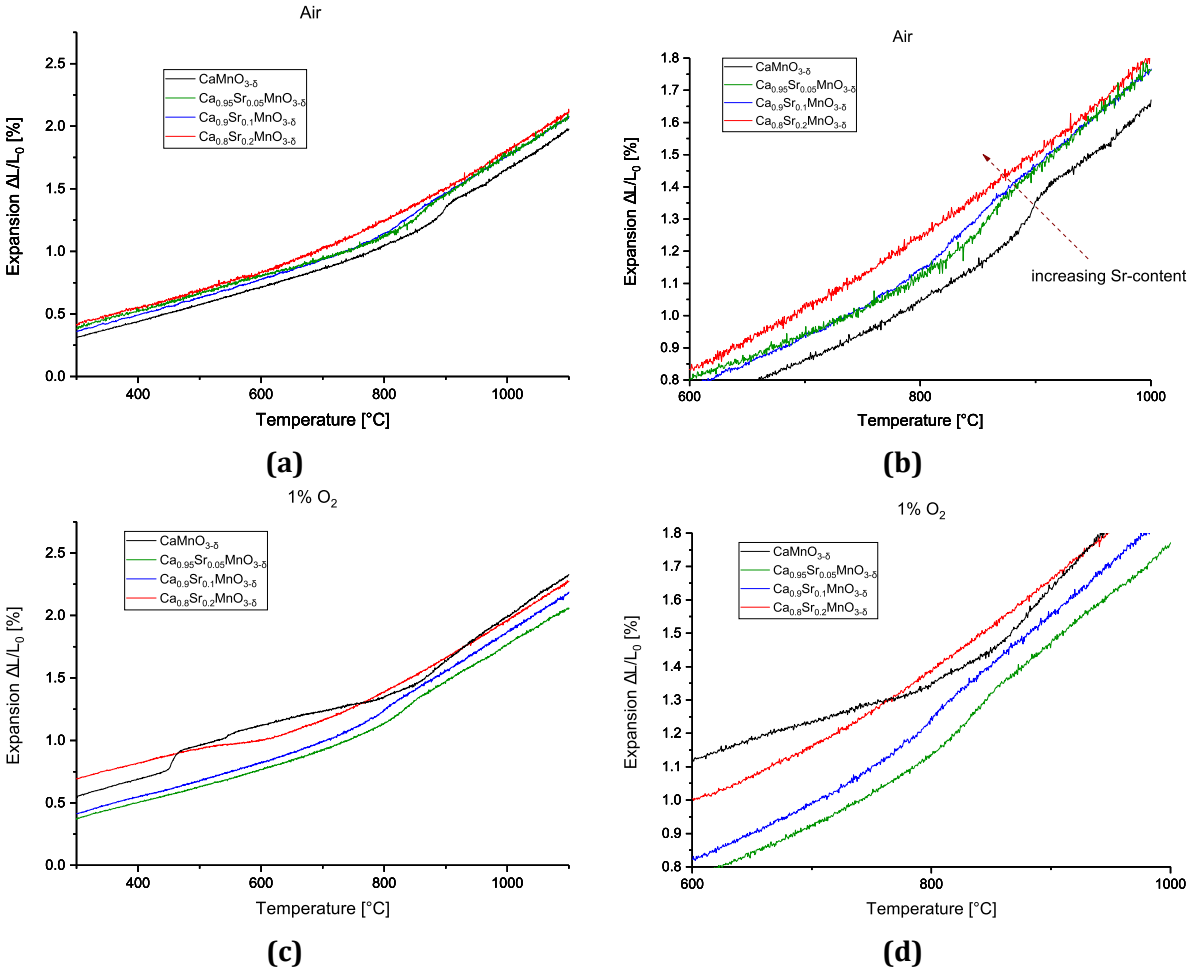

Fig. 5.3.: Thermal expansion of $Ca_{1-x}Sr_xMnO_{3-\delta}$ with $x \in [0, 0.05, 0.1, 0.2]$. a) In air. Extracted from the 3rd cycle of the dilatometry experiments. b) Zoomed in to temperatures of 600 °C to 1000 °C. c) In 1% O_2. Extracted from the 3rd cycle of each dilatometry experiment. d) In 1% O_2. Zoomed in to temperatures of 600 °C to 1000 °C. Reproduced from Klaas and Pein et al.[20] with permission from the Royal Society of Chemistry.

All determined values of expansion coefficient, reversible and residual expansion, under the two different atmospheres applied, are summarized in tab. 5.1.

Table 5.1.: Thermal expansion coefficients for $Ca_{1-x}Sr_xMnO_{3-\delta}$ with $x \in [0, 0.05, 0.1, 0.2]$ as determined by Dilatometry in air and 1% O_2. Exp_{rev} represents the reversible expansion and is given as the mean value over 5 cycles. Exp_{res} represents the residual, irreversible expansion at the end of 5 cycles compared to the initial value (determined at 400 °C). Error margins in brackets are given as the standard deviation.

Atmosphere	x	$\alpha_{ortho}[\frac{\%}{°C}]$	$\alpha_{cubic}[\frac{\%}{°C}]$	$Exp_{rev}[\%]$	$Exp_{res}[\%]$
Air	0	0.001 34(1)	0.003 10(4)	1.701(6)	-
1% O_2	0	-	0.003 48(5)	1.756(9)	0.352
Air	0.05	0.001 38(2)	0.003 08(6)	1.727(16)	-
1% O_2	0.05	0.001 29(2)	0.0029(4)	1.697(11)	0.071
Air	0.1	0.001 40(4)	0.003 09(4)	1.743(6)	-
1% O_2	0.1	0.001 31(6)	0.003 14(8)	1.797(24)	0.090
Air	0.2	0.001 39(4)	0.003 08(2)	1.753(11)	-
1% O_2	0.2	-	0.003 09(4)	1.565(29)	0.438

Determination of Phase Transition Temperatures by Cyclic Dilatometry

Previous one-cycle measurements of thermal expansion of the $Ca_{1-x}Sr_xMnO_{3-\delta}$ system in a contact dilatometer already indicated a coherence of the orthorhombic to cubic phase transitions. At the temperature of phase transition determined via DSC, a distinct macroscopic expansion was detected and the materials transitioned from one regime of linear thermal expansion to the other. In the regime at higher temperatures, now correlated to the cubic phase, thermal expansion coefficients were higher by a factor of $\approx$2 compared to the lower temperature regime of the orthorhombic phase.

With the optical dilatometer enabling multicycle measurements under different atmospheres, this feature can be analyzed with respect to its reproducibility and its influenceability by $p(O_2)$. Analogously to the peak values of the phase transition temperature regime, the inflection points of the thermal expansion curves are used here to determine the phase transition temperature through dilatometry. In order to find the inflection point, the derivative of the expansion $\frac{d\Delta L/L_0}{dt}$ is examined for local maxima. Graphs of the thermal expansion derivative are shown in fig. 5.4. It can be observed that the expansion fluctuates with time and temperature especially around the turning point from cooling to heating. Two plateaus and a steep increase with a local maximum can be identified within each cycle. This maximum sets the temperature of the inflection point in the original thermal expansion graph and was used here to determine the temperature

of phase transition.

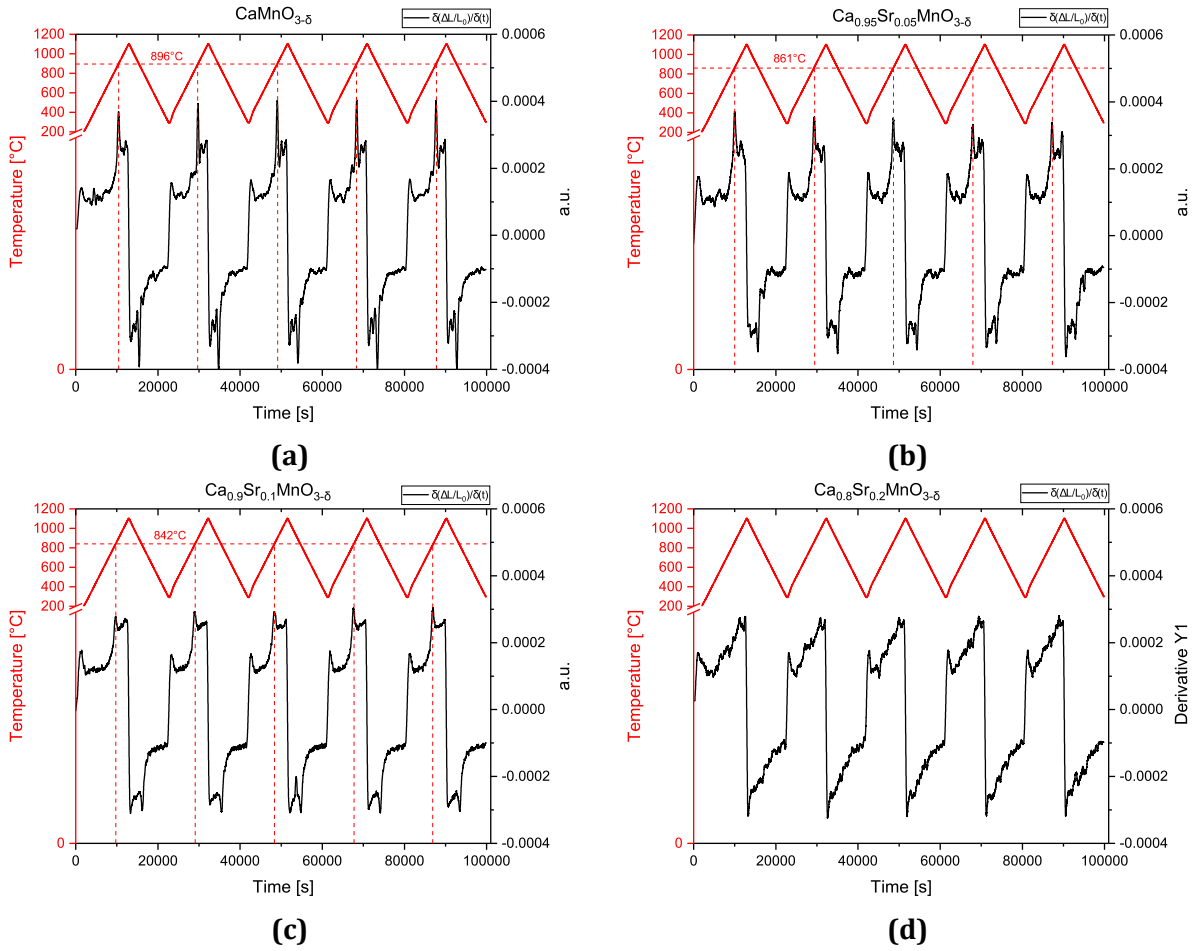

Fig. 5.4.: Derivative of thermal expansion from $Ca_{1-x}Sr_xMnO_{3-\delta}$ with $x \in [0, 0.05, 0.1, 0.2]$ in air over 5 cycles. Dashed vertical lines represent the temperature of the determined inflection point. a) was reproduced from Klaas and Pein et al.[20] with permission from the Royal Society of Chemistry.

In air, only $Ca_{0.8}Sr_{0.2}MnO_{3-\delta}$ showed a distinctively different behavior as no clear inflection point was found. In contrast, the results of $CaMnO_{3-\delta}$, $Ca_{0.95}Sr_{0.05}MnO_{3-\delta}$ and $Ca_{0.9}Sr_{0.1}MnO_{3-\delta}$ revealed clear inflection points during heat-up (local maxima highlighted in fig. 5.4) and cool-down (local minima in fig. 5.4, not highlighted). Determined temperatures are in good agreement with results from DSC (compare fig. 5.8). In contrast to the distinct increase of thermal expansion around the phase transition for the other samples, $Ca_{0.8}Sr_{0.2}MnO_{3-\delta}$ exhibited a quasi-linear increase over the whole temperature range.

For $CaMnO_{3-\delta}$ the temperature of phase transition determined by this technique was

896 °C, which is identical to the temperature determined by DSC in the previous chapter and very close to the 893 °C of the repeated DSC measurements (see section 5.2). The collected DSC-signals of all samples are given in fig. 5.6 and determined values of phase transition are reported in fig. 5.8 and tab. 5.2. In general, values determined by the described method via dilatometry matched values determined by DSC quite well. The results consolide the finding that the phase transition is accompanied by a mascroscopic expansion and contraction, which is detectable by dilatometry. $Ca_{0.8}Sr_{0.2}MnO_{3-\delta}$ did not exhibit a phase transition in air.

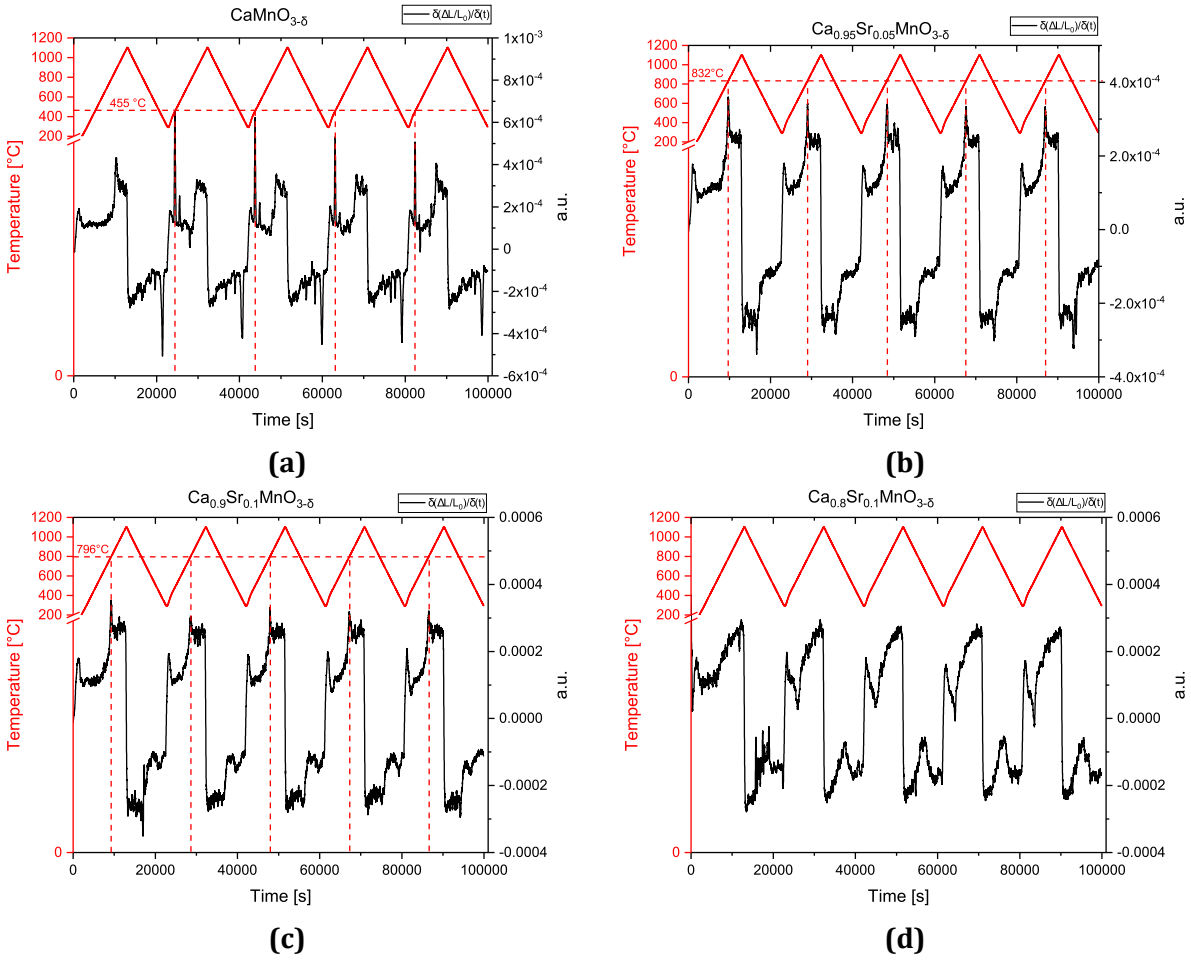

Fig. 5.5.: Thermal expansion derivative from $Ca_{1-x}Sr_xMnO_{3-\delta}$ with $x \in [0, 0.05, 0.1, 0.2]$ in 1% O_2 over 5 cycles. Dashed vertical lines represent the temperature of determined inflection points.

In reduced oxygen concentration of 1% O_2, $CaMnO_{3-\delta}$ and $Ca_{0.8}Sr_{0.2}MnO_{3-\delta}$ showed distinctively different results compared to experiments under air. $CaMnO_{3-\delta}$ exhibited a distinct shoulder-like expansion occured during the heat-up of the first cycle. This expan-

sion occured at 883 °C and was not matched by a contraction in the same temperature range during cool-down of the first cycle. Instead the contraction shifted towards much lower temperatures below 400 °C. In subsequent cycles, a distinct expansion occured at 455 °C, which was found to be reproducible over the remaining four cycles and matched with a similar contraction during cool-down that slightly shifted towards lower temperatures. This hysteresis was found for all the reversible expansion correlated with a phase transition. Although this behavior hints at a reversible reaction, DSC measurements on the same sample at 1% O_2 do not support these results. Therein, no exothermal or endothermal reaction was recorded in this temperature region. The derivative of the thermal expansion of $CaMnO_{3-\delta}$ at 1% O_2, shown in fig. 5.5a, result in the visible shoulder in fig. 5.2a.

Results of $Ca_{0.95}Sr_{0.05}MnO_{3-\delta}$ and $Ca_{0.9}Sr_{0.1}MnO_{3-\delta}$ at 1% O_2 did not reveal any shoulders or irregular behavior, but showed clear inflection points that reversibly occured at the same temperature during heating and cooling with only little deviation between cycles.$Ca_{0.8}Sr_{0.2}MnO_{3-\delta}$ did not exhibit any distinct expansion during the first cycle. In subsequent cycles however, $Ca_{0.8}Sr_{0.2}MnO_{3-\delta}$ exhibits a distinct shoulder-like contraction during heat-up, which is matched with an expansion during cool-down in approximately identical temperature windows of 545 °C to 575 °C. This behavior also leads to a shoulder-like step in the 5-cycle depiction of $Ca_{0.8}Sr_{0.2}MnO_{3-\delta}$ in fig. 5.2d. Thermogravimetric results were obtained simultaneously to the DSC measurements reported in fig. 5.6 do not hint at any reaction taking place in the above mentioned temperature regions. Considering that TGA and DSC measurements were carried out with small amounts ($\approx$ 40 mg) of powder samples compared to the sintered rods in dilatometry, the retarded expansion and contraction from $CaMnO_{3-\delta}$ and $Ca_{0.8}Sr_{0.2}MnO_{3-\delta}$ can originate from kinetic limitations at a reduced $p(O_2)$. That would lead to non-equilibrium states and re-equillibration at the observed points during thermal cycling.

5.2. Phase Stability and Redox Behavior

Simultaneously obtained results of TGA and DSC of $Ca_{1-x}Sr_xMnO_{3-\delta}$ ($x \in [0, 0.05, 0.1, 0.2]$) under various $p(O_2)$ in consecutive cycles allowed validation of the phase transition temperatures determined via DSC in this chapter. Additionally, the phase stability and redox behavior of $Ca_{1-x}Sr_xMnO_{3-\delta}$ ($x \in [0, 0.05, 0.1, 0.2]$) in correlation to Sr-content at $0.20 > p(O_2) > 10^{-4}$ and 400 °C<T<1200 °C were analyzed. Measurements were carried out as described previously in section 3.5 and are presented in fig. 5.6.

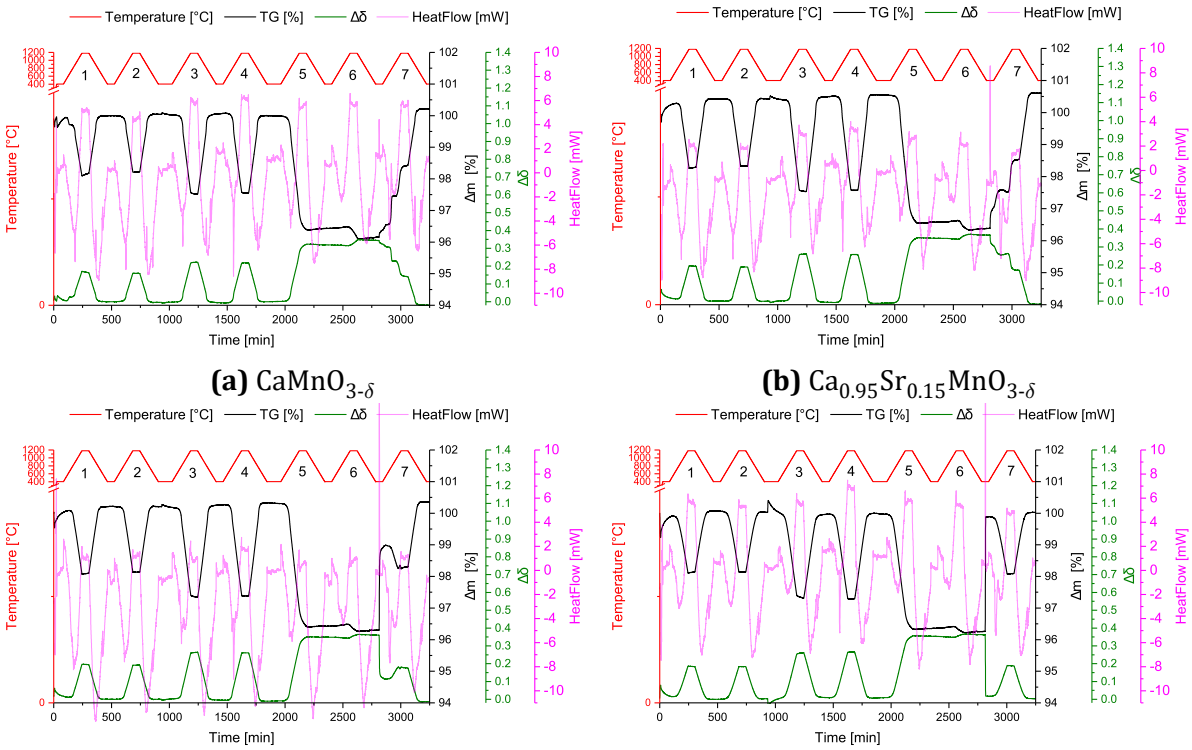

(a) $CaMnO_{3-\delta}$ **(b)** $Ca_{0.95}Sr_{0.15}MnO_{3-\delta}$

(c) $Ca_{0.9}Sr_{0.1}MnO_{3-\delta}$ **(d)** $Ca_{0.8}Sr_{0.2}MnO_{3-\delta}$

Fig. 5.6.: Simultaneously obtained TGA and DSC data of $Ca_{1-x}Sr_xMnO_{3-\delta}$ samples. Temperature was cycled between 400 °C to 1200 °C. 7 thermal cycles with varying gas flows of Ar and O_2 were performed. Cycles 1+2: 20% O_2; Cycles 3+4: 1% O_2; Cycles 5+6: pure Ar ($\approx$ 0.001% O_2); Cycle 7: 20% O_2. Δm was calculated with the initial weighed-in m_0 before the measurement, while $\Delta\delta$ was calculated from the isotherm at 400 °C after the first cycle.

First of all, some peculiarities and considerations need to be clarified and explained. The instrument used for these measurements suffers from buoyancy drift of the weight signal when gas flows are changed during the measurement, which cannot be fully eliminated by blank correction measurements. This drift is most prominent at the start of each measurement where all samples exhibit a sudden decrease in the weight signal with a following slow increase during the initial isotherm at 400 °C. Additionally, it results in a sudden change of the weight signal when the gas flows are changed in between cycles, e.g. during the isotherm between cycle two and three. As can be seen in the weight signal graphs, this buoyancy drift relaxes quickly and does not interfere with the measurement. However, especially the sharp decrease and increase at the start of measurement can lead to generally upwards or downwards shifted weight signals. It has to be carefully evaluated if the observed effect is a physical behavior of the sample or a result of the in-

strument's drift. This effect is most prominent in the initial phase of the measurement right after start of the measurement. Therefore, $\Delta\delta$ values were obtained with the sample weight at the isotherm at 400 °C after the first cycle (used as m in eq. 3.4). δ of $CaMnO_{3-\delta}$ at 400 °C and $p(O_2)$=0.20 bar in that case is approximated to zero. The %-weight change is still given with respect to the initially weighed sample mass for transparency.

The heat flow signal is influenced in a similar fashion. In addition to that, the heat effects of the samples are considerably small, which would cause quantitative analysis of absolute values be highly inaccurate. Therefore, only deviation from the pattern is used for analysis in a qualitative fashion, e.g. large endothermal or exothermal peaks, which indicate a reaction.

Furthermore, several findings can be extracted from the presented data. Independent from the Sr-content, all samples exhibit reversible reduction and oxidation at 20% and 1% O_2. Similar reduction extent is reached during heating in each of the thermal cycles carried out under identical atmosphere and samples can be considered fully oxidized after cool down. Additionally, $\Delta\delta$ at 1200 °C increases marginally with increasing Sr-content (see also fig. 5.6). This can be explained by a reduction of the oxygen vacancy formation energy, an effect of A-site Sr-substitution of $CaMnO_{3-\delta}$ that has been reported previously by Bulfin et al..[169]

Complete reoxidation at 1% O_2 also means that the residual expansion observed in dilatometry under these conditions is unlikely to originate from incomplete re-oxidation. However, kinetic limitations need to be considered as well. TGA and DSC results were obtained from small powder samples, while dilatometry results were obtained from pressed and sintered bar specimens. These bar specimens had a porosity of 10.8% as measured by Hg-porosimetry of a $CaMnO_{3-\delta}$ sintered bar sample.[19] Hence, a kinetic limitation and resulting incomplete re-oxidation cannot be ruled out as a potential source of residual expansion after cycling under reduced oxygen concentration. Complete re-oxidation was also observed in TGA for all samples of $Ca_{1-x}Sr_xMnO_{3-\delta}$ within the last cycle (7) in air after deep reduction in Ar (0.001% O_2 / $p(O_2)$=10^{-4} bar) up to reduction extents of $\Delta\delta > 0.3$. While all samples showed no re-oxidation during cooling in cycle five, they all showed additional reduction in cycle six, hinting at a non-equilibrium state after cycle five.

While all samples ultimately reached full re-oxidation at the end of cycle seven, the re-oxidation patterns during cycle seven change with increasing Sr-content in the composition. During the isotherm at 400 °C at the end of cycle six, the oxygen content in the gas flow is increased to 20%. All samples quickly reacted with re-oxidation even at these

low temperatures. However, the extent of re-oxidation, and thereby the decrease of $\Delta\delta$, is only marginally small for un-substituted $CaMnO_{3-\delta}$. $Ca_{0.95}Sr_{0.15}MnO_{3-\delta}$ reached a slightly smaller $\Delta\delta$, $Ca_{0.9}Sr_{0.1}MnO_{3-\delta}$ reached a substantially smaller $\Delta\delta$ and $Ca_{0.8}Sr_{0.2}MnO_{3-\delta}$ was already fully re-oxidized during the isothermal period of 30 minutes under air before the heating phase started. This discrepancy could be explained either by kinetic limitations in $CaMnO_{3-\delta}$ and $Ca_{0.95}Sr_{0.15}MnO_{3-\delta}$ and faster kinetics in the Sr-substituted compositions. Klaas et al. reported increasingly faster oxidation kinetics for increasing Sr-content in $Ca_{1-x}Sr_xMnO_{3-\delta}$.[187] It can also be explained by the occurrance of a dissociation reaction in the former two compositions, which is inhibited in compositions with higher Sr-content. Such dissociation reaction was reported earlier by Bakken at al.[190] for unsubstituted $CaMnO_{3-\delta}$ at high temperatures and low $p(O_2)$. Therein $CaMnO_{3-\delta}$ dissociates into non-stoichiometric $Ca_2MnO_{4-\delta'}$ and $CaMn_2O_4$ at temperatures above 1000 °C and $p(O_2) < 3 \cdot 10^{-3} bar$ and single phase $CaMnO_{3-\delta}$ is reversibly formed again in oxidizing atmosphere with increased $p(O_2)$. Although Bakken et al.[190] used differing experimental procedures in their work compared to the methods applied the presented work, it is likely that such dissociation reaction takes place for $CaMnO_{3-\delta}$.The re-oxidation patterns of $CaMnO_{3-\delta}$ and $Ca_{0.95}Sr_{0.15}MnO_{3-\delta}$ in cycle seven support this conclusion. Taking $CaMnO_{3-\delta}$ as an example, fig. 5.7 shows the zoomed in section of cycle seven from the combined TGA/DSC measurement of $CaMnO_{3-\delta}$.

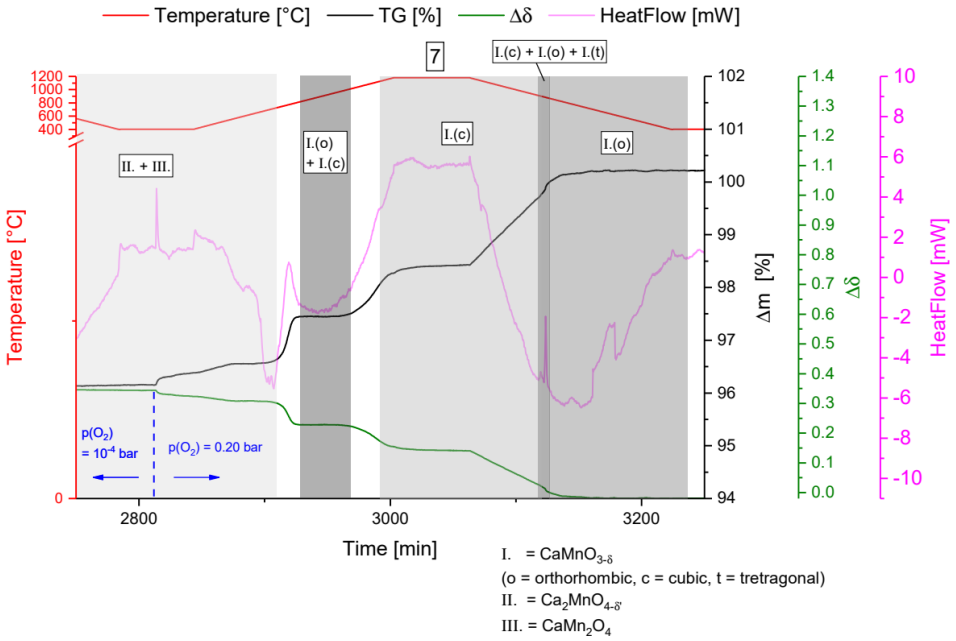

Fig. 5.7.: Zoomed in section of cycle 7 from fig. 5.6a. Crystal phases concluded to be present are indicated in each phase of the cycle.

It can be concluded that $CaMnO_{3-\delta}$ is dissociated into $Ca_2MnO_{4-\delta'}$ and $CaMn_2O_4$ to a large degree after treatment with Argon in cycles five and six. However, no information on the non-stoichiometry ranges of $Ca_2MnO_{4-\delta'}$ was found in literature. The presented results lead to the conclusion that they are small compared to $CaMnO_{3-\delta}$. Complete dissociation of $CaMnO_{3-\delta}$ into $Ca_2MnO_{4-\delta'}$ ($\delta' = 0$) and $CaMn_2O_4$ would result in a $\Delta m \approx 3.73\%$ compared to the pristine fully oxidized $CaMnO_{3-\delta}$ ($\delta = 0$). A Δm of 3.84% was observed after cycle six. Slight variation to the expected 3.73% for complete dissociation originates from additional $\delta' \neq 0$ in the $Ca_2MnO_{4-\delta'}$ compound.

After switching to an oxidizing atmosphere with higher oxygen content, the sample slowly started to gain weight. That can be related to the oxidation of either residual $CaMnO_{3-\delta}$ phase or $Ca_2MnO_{4-\delta'}$. At a temperature range of 675 °C to 800 °C a steep increase in weight was observed accompanied by an exothermal peak in the DSC-signal indicating a comparably strong reaction taking place. Previous works reporting such dissociation reaction of $CaMnO_{3-\delta}$[111,190] do not report state a lower temperature threshold where the reverse reaction back to $CaMnO_{3-\delta}$ occurs under air. The steep increase in weight and the detected exothermal heat signal however can be assigned to the reverse reaction of $Ca_2MnO_{4-\delta'}$ and $CaMn_2O_4$ back to $CaMnO_{3-\delta}$. It remains unclear if $CaMnO_{3-\delta}$ is formed in an orthorhombic or cubic phase at this stage. Due to the plateau at $\Delta\delta = 0.22$ without any further re-oxidation that followed this transition towards $CaMnO_{3-\delta}$, it is likely that the orthorhombic phase or a mixture of orthorhombic and cubic was formed. Complete transition to the cubic phase then took place above 1000 °C, where it re-equillibrated with the surrounding atmosphere leading to further re-oxidation. $\Delta\delta$ values after the isotherm in cycle seven were found to be ≈ 0.14, which is close to the observed $\Delta\delta = 0.16$ at this temperature and atmosphere during cycles one and two. During the cooling phase of cycle seven, the sample shows a typcial oxidation behavior as observed in cycles one and two, even exhibiting the phase transition back to the orthorhombic phase, determined by the well known DSC peak pattern and a steep weight gain around 885 °C.

$Ca_{0.95}Sr_{0.15}MnO_{3-\delta}$ shows a behavior almost identical to $CaMnO_{3-\delta}$, with values slightly shifted towards smaller $\Delta\delta$. That leads to the conclusion that $Ca_{0.95}Sr_{0.15}MnO_{3-\delta}$ did not completely dissociate, but a residual perovskite remains after cycles five and six. Still, a significant fraction of $Ca_{0.95}Sr_{0.15}MnO_{3-\delta}$ dissociates under the given conditions. Despite being fully reversible in oxidizing conditions, this dissociation can cause issues depending on the application's operational parameters for $CaMnO_{3-\delta}$ and $Ca_{0.95}Sr_{0.15}MnO_{3-\delta}$.
$Ca_{0.9}Sr_{0.1}MnO_{3-\delta}$ and $Ca_{0.8}Sr_{0.2}MnO_{3-\delta}$ started to gain weight rapidly after the introduction

of the oxygen rich gas stream. In conclusion, they are immediately re-oxidized. Therein, they initially gained weight rapidly. The weight gain slowed down after 10 minutes, apparently reaching a threshold at $\Delta\delta$ values of 0.12 for $Ca_{0.9}Sr_{0.1}MnO_{3-\delta}$ and 0.02 for $Ca_{0.8}Sr_{0.2}MnO_{3-\delta}$. The re-oxidation threshold during the isotherm after introducing the oxidizing gas stream appears to be connected to kinetic limitations. That leads to the conclusion that increased Sr-content speeds up the oxidation kinetics. This conclusion is also supported by recent results of Klaas et al.,[187] who reported faster oxidation kinetics with increasing Sr-content in the $Ca_{1-x}Sr_xMnO_{3-\delta}$-system, especially at lower temperatures.

Furthermore, $Ca_{0.9}Sr_{0.1}MnO_{3-\delta}$ and $Ca_{0.8}Sr_{0.2}MnO_{3-\delta}$ do not suffer from dissociation when cycled at low $p(O_2)$. The work of Imponenti[191] also reported inhibition of a dissociation reaction for small amounts of Sr-substition (5% and 10%), although only temperatures up to 1000 °C were applied. Additionally, Imponenti[191] reports an absence of any phase transition already for 10% Sr, which contradicts the findings presented in this work as the $Ca_{0.9}Sr_{0.1}MnO_{3-\delta}$ clearly exhibits a phase transition from orthorhombic to cubic. Both compositions, $Ca_{0.9}Sr_{0.1}MnO_{3-\delta}$ and $Ca_{0.8}Sr_{0.2}MnO_{3-\delta}$, are reduced again upon heating in cycle seven up to comparable reduction extents as in cycles one and two. At subsequent cooling they are fully re-oxidized again.

5.3. Conclusions for Thermochemical Cycles with $Ca_{1-x}Sr_xMnO_{3-\delta}$

An important factor to consider before bringing $CaMnO_{3-\delta}$ and its A-site Sr-substituted variants into application in thermochemical cycles, is the chemical and structural stability in the desired temperature and $p(O_2)$ range. That includes not only the occurence of crystal phase transitions on the atomic scale, but also macroscopic stability and cyclability of sintered specimens. In accordance to results reported in literature,[111,191,192] $CaMnO_{3-\delta}$ exhibits a distinct phase transition from orthorhombic to cubic. The existence of an interemediate tetragonal phase has been indicated by the doublet of peaks in the DSC signal, but could not be validated in HT-XRD experiments carried out.[20] The phase transition was found to correlate with a distinct macroscopic expansion as determined via dilatometry. In an innovative approach, the temperature of phase transition (T_{pt}) was determined via thermal expansion data. The results match well, with the exception of the 10%-Sr sample at 1% O_2, as shown in fig. 5.8.

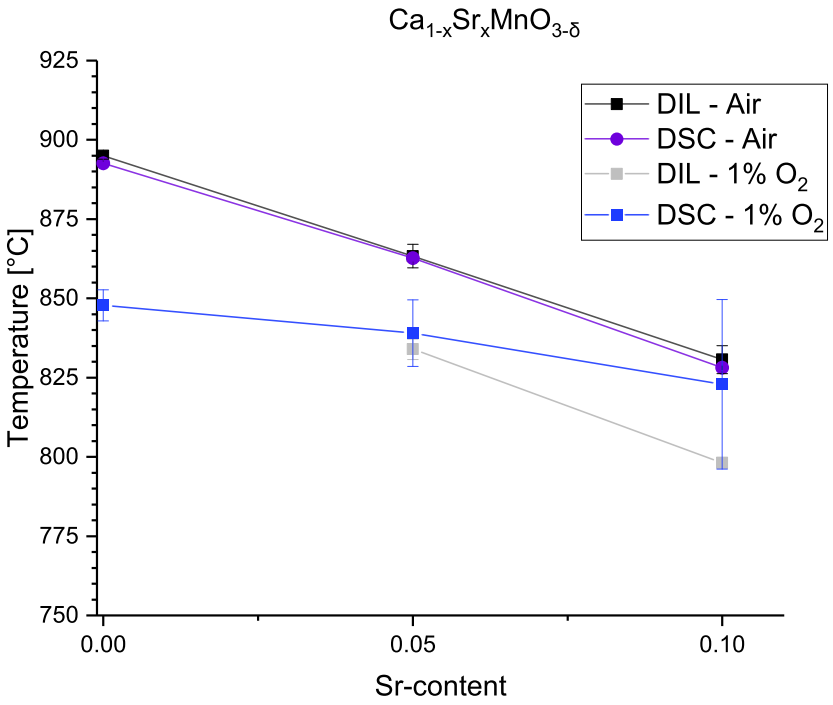

Fig. 5.8.: Temperatures of phase transition of $Ca_{1-x}Sr_xMnO_{3-\delta}$ ($x \in [0, 0.05, 0.1]$) in air and 1% O_2 as determined by DSC and dilatometry (DIL). Reproduced from Klaas and Pein et al.[20] with permission from the Royal Society of Chemistry.

The thermal expansion coefficient was found to increase, once the orthorhombic phase transitioned to a cubic phase. This is especially important to consider in applications where thermal expansion has to be kept to a minimum. In such applications it could be beneficial to avoid temperature and $p(O_2)$-ranges where the structure transitions to the much more rapidly expanding cubic phase. In air, all samples showed fully reversible expansion and contraction over 5 thermal cycles with maximum relative expansion at T_{max}=1100 °C slightly above 2%. Relative reversible expansion ranged from 1.70(6)% to 1.80(7)%. Maximum expansion tends to increase with increasing Sr-content, which can plausibly originate from a decrease in T_{pt} by the introduction of Sr on the A-site, and therefore a larger temperature range in the stronger expanding cubic phase. However, no clear trend was observed with respect to the reversible expansion.

Introducing an atmosphere with lower oxygen concentration of 1% ($p(O_2) = 10^{-2}$ bar) caused irreversible residual expansion in all samples in each cycle. Small amounts of Sr-substitution (5% and 10%) reduced this residual expansion to 0.07(1)% and 0.09(0)% respectively compared to 0.35(2)% and 0.43(8)% for $CaMnO_{3-\delta}$ and $Ca_{0.8}Sr_{0.2}MnO_{3-\delta}$ after five cycles. These results point out that small amounts of Sr-substitution can be very

beneficial for the macroscopic structural stability over multiple cycles when applying atmospheres with reduced oxygen content compared to ambient air. This is especially important to consider, when working with structured specimens where thermal stresses can lead to undesired mechanical failure.

Thermogravimetric measurements revealed a dissociation reaction of pure $CaMnO_{3-\delta}$ and $Ca_{0.95}Sr_{0.15}MnO_{3-\delta}$ at $p(O_2)$=10^{-4} bar, which limited re-oxidation at higher $p(O_2)$. This dissociation reaction was found to be reversible at $p(O_2)$=0.21 bar and elevated temperatures, but the restricted re-oxidation is a critical factor for many thermochemical applications. Such dissociation has not been reported yet for Sr-substituted $CaMnO_{3-\delta}$. At Sr-contents >10% this dissociation was not observed. Instead $Ca_{0.9}Sr_{0.1}MnO_{3-\delta}$ and $Ca_{0.8}Sr_{0.2}MnO_{3-\delta}$ exhibited fast re-oxidation at 400 °C immediately after switching to an oxygen rich atmosphere. While $Ca_{0.9}Sr_{0.1}MnO_{3-\delta}$ was not fully re-oxidized, $Ca_{0.8}Sr_{0.2}MnO_{3-\delta}$ almost reached full re-oxidation after only 30 minutes at 400 °C and $p(O_2)$=0.21 bar. Such dissociation reaction was reported to closely correlate to the reduction extent.[111] Depending on how deep the material is thought to be reduced in any given application, A-site Sr-substitution can serve as an inhibitor for undesired dissociation reactions, thereby extending the stable range of $\Delta\delta$. Key findings of this chapter are summarized in tab. 5.2.

Table 5.2.: Temperatures of phase transition T_{PT} of $Ca_{1-x}Sr_xMnO_{3-\delta}$ ($x \in [0, 0.05, 0.1]$) in air and 1% O_2 as determined by DSC, Dilatometry and XRD. Adapted from Klaas and Pein et al.

x	Atmosphere	T_{PT} [°C]		
		DSC	DIL	HT-XRD
0	Air	893	896	910
0	1% O_2	848	-	840
0.05	Air	863	863	-
0.05	1% O_2	856	834	-
0.1	Air	828	831	807.5
0.1	1% O_2	823	796	770

The results presented within this chapter highlight multiple benefits that small amounts of A-site substitution of $CaMnO_{3-\delta}$ with Sr can have. The improved cyclability at low $p(O_2)$ due to the decrease of residual expansion is beneficial. This is especially important for monolithic structured specimens in order to reduce mechanical stress during cycling. Additonally, Sr-contents of $\geq$10% were shown to inhibit a dissociation reaction at high reduction extents. It was accompanied by drastically improved re-oxidation kinetics af-

ter deep reduction at $p(O_2)$=10^{-4} bar. However, with increasing Sr-content the observed phase transition from orthorhombic to cubic is shifted towards lower temperatures, leading to larger thermal expansion at lower temperatures and increasing expansion in the temperature range around the transition. It was concluded that $Ca_{1-x}Sr_xMnO_{3-\delta}$ with $x = 0.05$ and $x = 0.10$ were the most promising compositions to be tested further in the context of open porous monolithic structures.

6. Reticulated Porous Foams from $CaMnO_{3-\delta}$

Utilizing open porous structures made from active redox material can have a multitude of benefits over the use of particles in a packed bed or fluidized bed reactor. Furthermore, it is desirable to construct such open porous structures entirely from the redox material. In comparison to coating the material onto an inert support structure, the weight load of active material with respect to the volume is reduced, which is a critical value when constructing such reactors in bigger scale.

Following the analysis of the previous chapters, $CaMnO_{3-\delta}$ and its A-site Sr-substituted variants were chosen as the redox material for the production and testing of open porous monolithic foams. As a starting point, a procedure for the production of $CaMnO_{3-\delta}$-foams, based on the replica method first reported by Schwartzwalder et al.,[152] was established. A foundation for the definition of processing parameters was established within the scope of a Bachelor thesis by Luca Matzel,[193] which was supervised by the author of this work. Foam production procedure and parameters utilized within the presented work are described in section 3.2. This procedure was also used for A-site Sr-substituted $CaMnO_{3-\delta}$ for the applicational demonstration in chapter 7. All results presented in the following were obtained from cylindrical foams produced with 30ppi polyurethane (PU) templates, and are therefore labeled as "30 ppi foams". Analysis included mechanical strength tests, microscopy (SEM and electron dispersive x-ray spectroscopy (EDX)), porosimetry, gas adsorption and thermal analysis via TGA and DSC.

This chapter is partially based on peer-reviewed publications authored and co-authored by the author of this work:

Mathias Pein, Luca Matzel, Lamark de Oliveira, Gözde Alkan, Alexander Francke, Peter Mechnich, Christos Agrafiotis, Martin Roeb, and Christian Sattler. "Reticulated Porous Perovskite Structures for Thermochemical Solar Energy Storage". In: *Advanced Energy Materials* 2102882 (2022). ISSN: 1614-6832. DOI: https://doi.org/10.1002/aenm.202102882

6.1. Sturdiness and Mechanical Strength of $Ca_{1-x}Sr_xMnO_{3-\delta}$-Foams

A multitude of foams were produced based on PU templates. Burn-off of the binder and sintering naturally leads to shrinkage of the foams, which reduced size compared to the green bodies. In order to make labeling of differently sized foams clear, as-prepared foams were labeled based on the dimensions of used green bodies. Wherever necessary, e.g. for calculation of contact area in mechanical strength tests, the actual dimensions, as measured by a caliper were used. Produced foams of various dimensions, ranging from 1.2 cm to 2 cm in diameter, are depicted in fig. 6.1. Foams of this size were reproducible in a batch-like fashion, only limited by the size of the furnace used for sintering. They were sturdy and could be handled by hand without breaking. They did however exhibit small amounts of closed pores, which did not hinder light to travel all the way through the length of the foams.

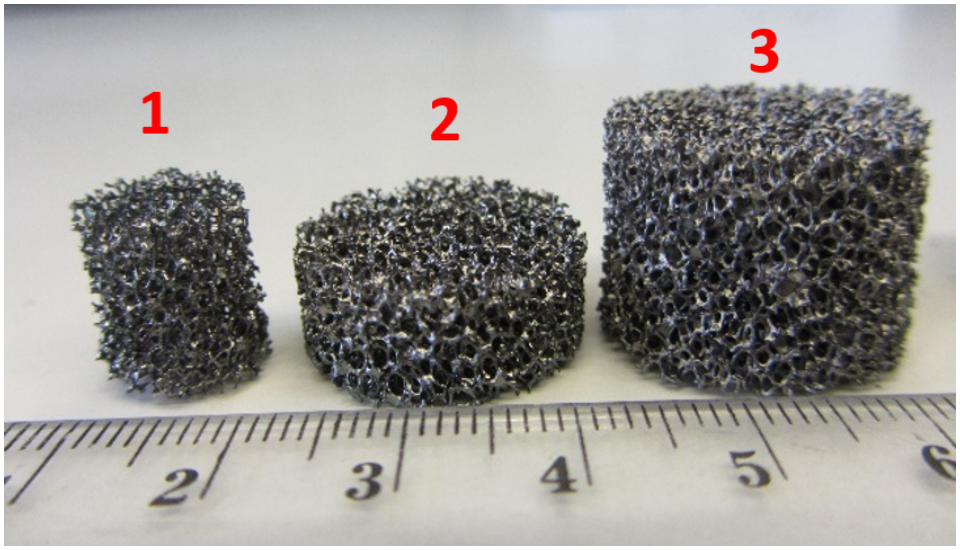

Fig. 6.1.: As-prepared cylindrical 30 ppi $CaMnO_{3-\delta}$-foams. 1) ⌀1x2 cm; 2) ⌀2x1 cm; 3) ⌀2x2 cm. Reproduced from Pein et al..[19] CC-BY.

Mechanical stress tests were carried out with two ⌀2x1 cm samples. Samples were placed between two aluminum sheets and compressed until failure. Point of failure was determined by the first significant peak of compressive force that was followed by relaxation and verified by timestamped video recording of the test. The pressure measured during the test and free frames of the recorded point of failure are depicted in fig. 6.2 and fig. 6.3.

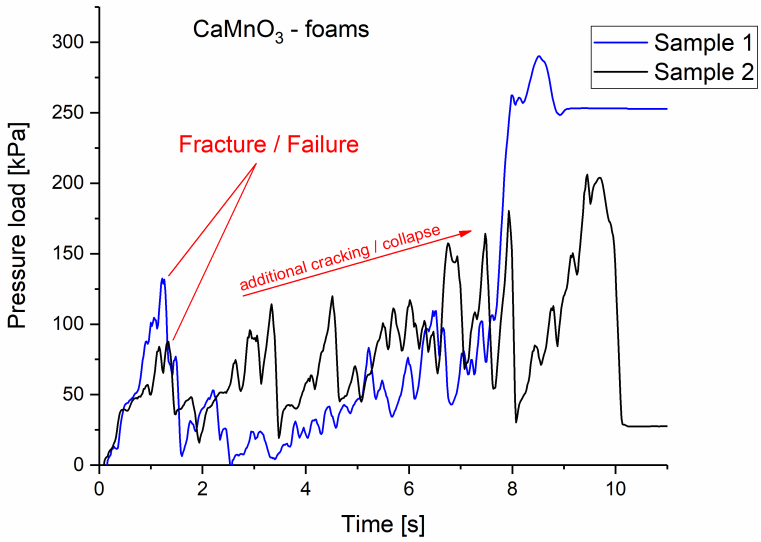

Fig. 6.2.: Measured pressure load during the strength tests of cylindrical 30 ppi $CaMnO_{3-\delta}$-foams of the dimensions ⌀2x1 cm. Point of failure is marked for each sample. Reproduced from Pein et al..[19] CC-BY.

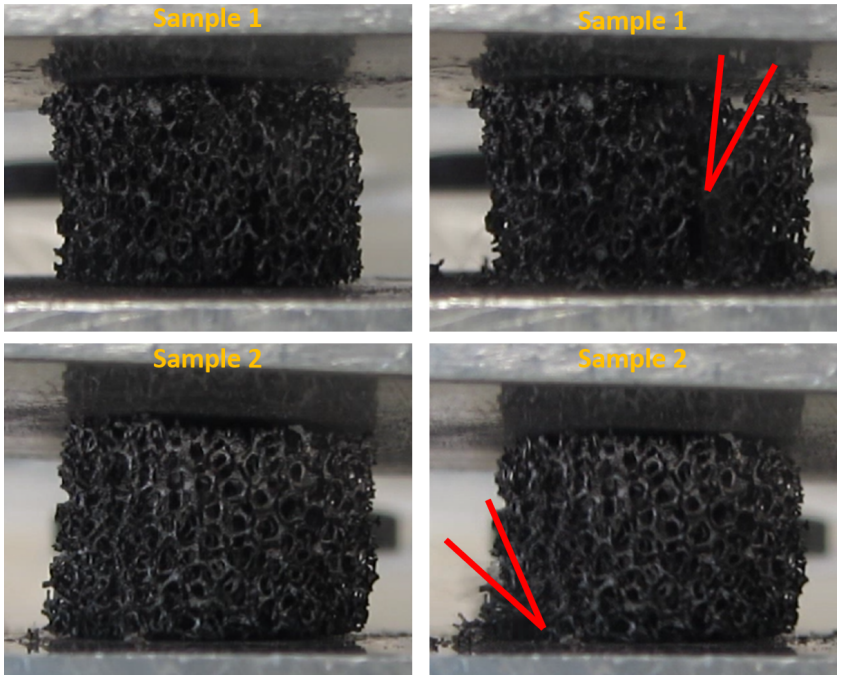

Fig. 6.3.: Freeze-frames of the video recording depicting the initial sample before the start of the strength test on the left and the point of failure with indication where the major fracture occurs in. Freeze frames of point of failure were timestamped in accordance to fig. 6.2. Reproduced from Pein et al..[19] CC-BY.

The samples were able to withstand pressure loads 132.4 and 87.5 kPa respectively, which roughly translate to 1.32 and 0.88 bar. No error margins are given for these measurements since the results are largely impacted by systematic errors, which are considered to be beyond the accuracy of the dynamometer of 0.1 N and cannot be quantified reliably. A substantial source of error, for example, is the unevenly distributed force of compression, not only originating from the available measurement setup, but also from uneven planes at the top and bottom side of the cylindrical foam specimens. However, the shown results demonstrate qualitatively that the foams are sturdy, easy to handle and generally able to withstand a multitude of their own weight ($m_{foam} \approx 2$ g for a foam of that size). In the context of upscaling and potential reactor systems consisting of modular blocks of such open porous foams, the results are promising that such foam structures can be stacked on one another in a modular fashion to fit the actual reactor size and scale without braking. Additionally, such foams are most likely suitable for pressurized operation. Yet, it is also clear that the results presented herein can only serve as a guideline and need to be validated in a sophisticated study with focus on mechanical stability of such open porous monolithic perovskite structures.

6.2. Microstructure of $Ca_{1-x}Sr_xMnO_{3-\delta}$-Foams

The microstructure of as-prepared 30 ppi foams made from $CaMnO_{3-\delta}$ were examined by means of SEM and XRD. For analysis in SEM, the foam had to be broken into very small pieces, which then could be prepared on an SEM sample holder with adhesive carbon tape. For XRD measurements, fractures of the foams were crushed entirely and ground in a mortar and pestle to a fine powder. Therefore, the applied methods are destructive with respect to the structure of specimens.

As can be seen from fig. 6.4, the as-prepared powder has a very minor marokite side phase, which is not present in the sintered foam. The marokite (Ca_2MnO_4) phase originates from a known disproportionation reaction of $CaMnO_{3-\delta}$ to Ca_2MnO_4 and $CaMn_2O_4$, which occurs at high temperatures and low $p(O_2)$.[190] Additionally, local variance in the stoichiometry that may be present during synthesis can also lead to the formation of such side phases. Because of that, the synthesis process has been adjusted to minimize the presence of these side phases (see also chapter 3.1). The disproportionation reaction is reversible and hence the material can be cured by additional sintering in oxygen rich atmosphere (e.g air). That is exactly the case during the preparation of all foam structures and is the reason why no side phases are detected anymore in the prepared $CaMnO_{3-\delta}$

foam structures.

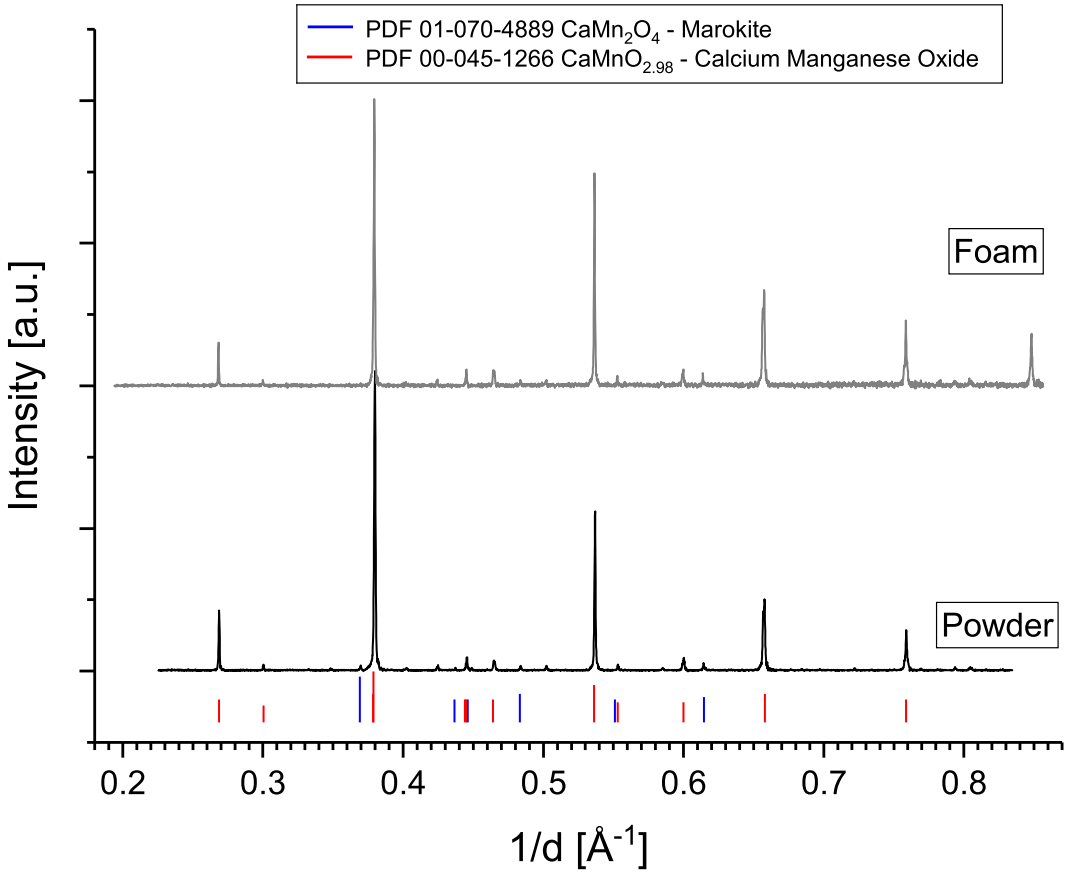

Fig. 6.4.: XRD patterns of pristine $CaMnO_{3-\delta}$ powder and a sintered foam. Minor marokite phase detected in pristine powder. Powder was measured with Cu-X-ray source, while foam was measured with Co-X-ray source. Therefore the X-scale is given in 1/d, which is independent of sources wavelength. Reproduced from Pein et al..[19] CC-BY.

SEM micrographs, given in fig. 6.5, revealed a rather smooth surface with no bigger pores in the µm-range. Interconnected struts built the network that resulted in the macroscopic open porous foam structure. These interconnected struts appeared in a triangular shape and their thickness was in the range of 100 µm. The thickness of struts increases at junction points where multiple struts meet. Foams had to be broken into small fractions to be examined in SEM. This led to broken struts at the edge of a sample, which revealed that the struts are actually hollow on the inside with inner diameters in the range of 20 µm to 40 µm and a wall thickness of about 10 µm.

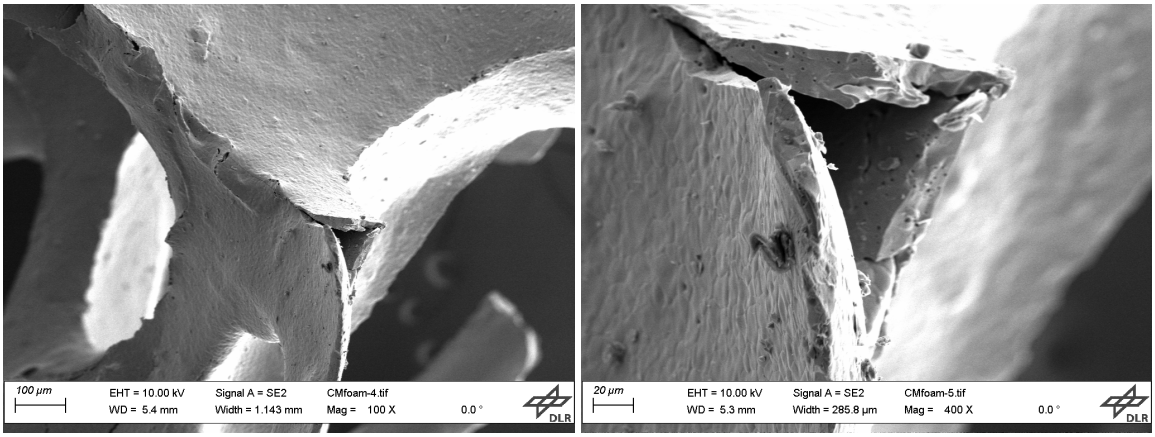

(a) **(b)**

Fig. 6.5.: SEM-micrographs of as-prepared 30 ppi $CaMnO_{3-\delta}$-foam. a) Interconnected struts with hollow opening at the edge where foam was fractured. b) Higher magnification micrograph of hollow opening on strut edge.

Porosity and Surface Area of $Ca_{1-x}Sr_xMnO_{3-\delta}$-Foams

Porosity was determined via Hg-intrusion porosimetry and N_2-adsorption porosimetry. Total porosity from pore volume was calculated to be 16.2%. Average pore size (d_{50}) in Hg-porosimetry was 38.1 µm, which is in the same range as the openings of hollow struts at the edge of foam samples as depicted in fig. 6.5. Since foam samples had to be broken into small pieces to fit into the small sample holders of the porosimeters, Hg intruded these openings into the hollow inside of the struts. This in turn could have led to a false pore detection signal to a degree that the calculated porosity is not accurate. The same holds true for N_2-adsorption measurements. Results are depicted as cumulative and differential pore volume in fig. 6.6.

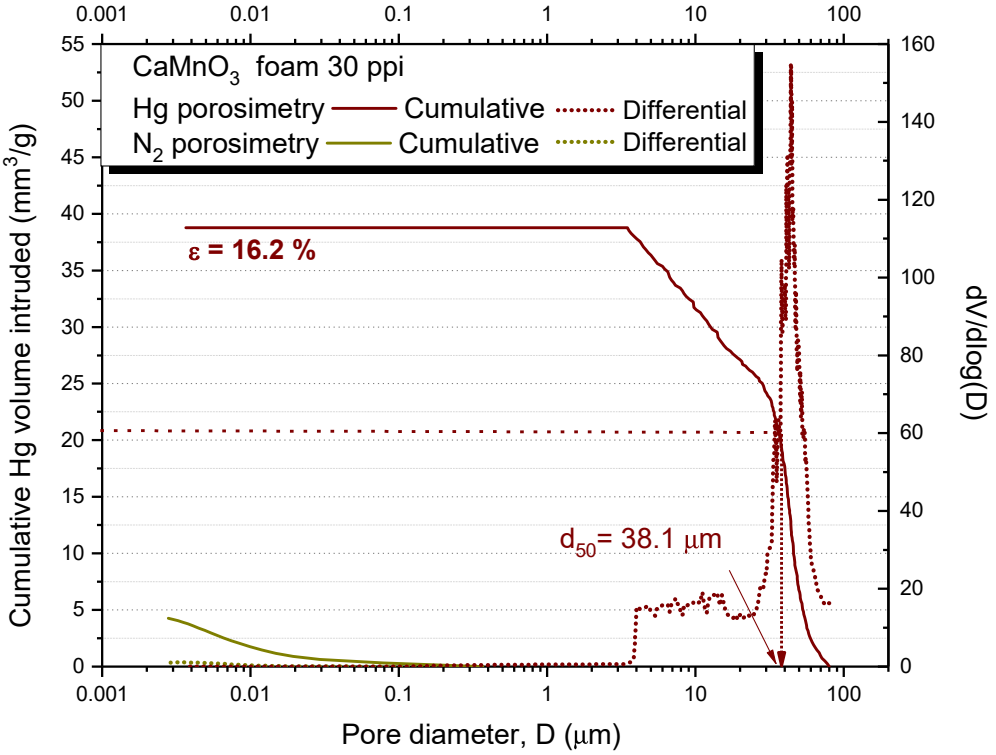

Fig. 6.6.: Cumulative and differential pore volumes of $CaMnO_{3-\delta}$-foam sample as determined via Hg-Porosimetry and N_2-porosimetry. Pore volumes add up to a total porosity $\epsilon$of 16.2%. Reproduced from Pein et al..[19] CC-BY.

Although such big pores cannot be displayed in N_2-adsorption experiments, the specific surface area of $6.59\frac{m^2}{g}$ suffered from inaccuracy due to the available access to the inner wall of the hollow struts through openings at fractured edges. In any case, this led to increased values of porosity and surface area compared to an ideal foam. However, the predominant absence of micropores, d<1 µm, is in accordance with observations made in SEM, where foam samples exhibited a smooth surface and no visible pores in this range. Additionally, specific surface area of the ball-milled powder, used to produce the foams, was determined to be $3.28\frac{m^2}{g}$. The foam exhibits comparable surface area per weight as small sized particles, an important fact when surface exchange reactions become important in a foreseen thermochemical application.

6.3. Stability of $Ca_{1-x}Sr_xMnO_{3-\delta}$-Foams during Thermal Cycling

As discussed previously in chapter 5, $CaMnO_{3-\delta}$ goes through a phase transition from orthorhombic to cubic at 895 °C in air. This phase transition is accompanied by endothermal and exothermal heat effects, distinct thermal expansion and contraction as well as weight loss and gain during reduction (heat-up) and oxidation (cool-down) respectively. The correlation of all these effects becomes evident in an overlay of the first cycles from TGA and dilatometry in fig. 6.7.

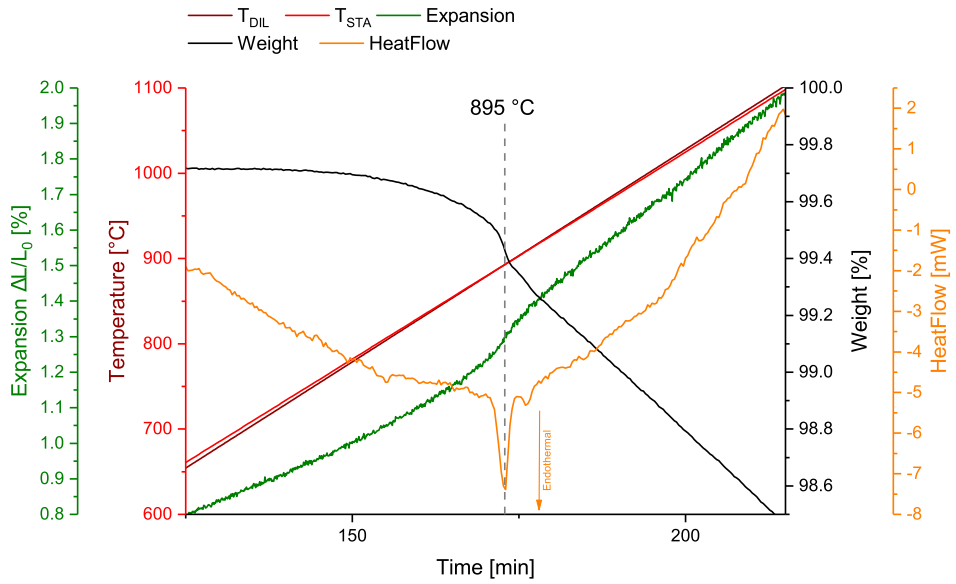

Fig. 6.7.: Overlay of heat-up phase from first cycle of figures 5.6a and 5.2a showing heat effects, weight change and expansion. T_{STA} is the recorded temperature in the simultaneous TGA and DSC measurement. T_{DIL} is the recorded temperature during dilatometry.

As fig. 6.7 includes results obtained from different sample specimens, a dense sintered bar (dilatometry) and fine milled powder (TGA/DSC), the fundamental results on thermodynamics, crystal structure and thermal expansion are independent of the type of specimen analyzed, if the concluded correlation between thermal expansion and the observed phase transition is correct. Since dilatometry experiments cannot be carried out with foam specimens with the available setup at this point, comparative TGA measurements were done with powder and foam samples in order to validate that prepared foam specimens exhibit identical behavior as the powder samples investigated.

Samples were cycled over 5 cycles between 300 and 1100 °C at considerably high $p(O_2)$.

Due to an initial miscalculation of the programmed gas flows, the oxygen concentration was not 20%, as planned originally to simulate air, but 12.3%. As can be seen in fig. 6.8, powder and foam exhibit full reversibility over the tested 5 cycles. Due to a buoyancy drift of the instruments weight signal, the plotted data in fig. 6.8 varies slightly. Therefore, maximum weight changes and corresponding reduction extents $\Delta\delta$ per cycle were calculated and averaged for better comparison of the tested samples. Results are given in tab. 6.1.

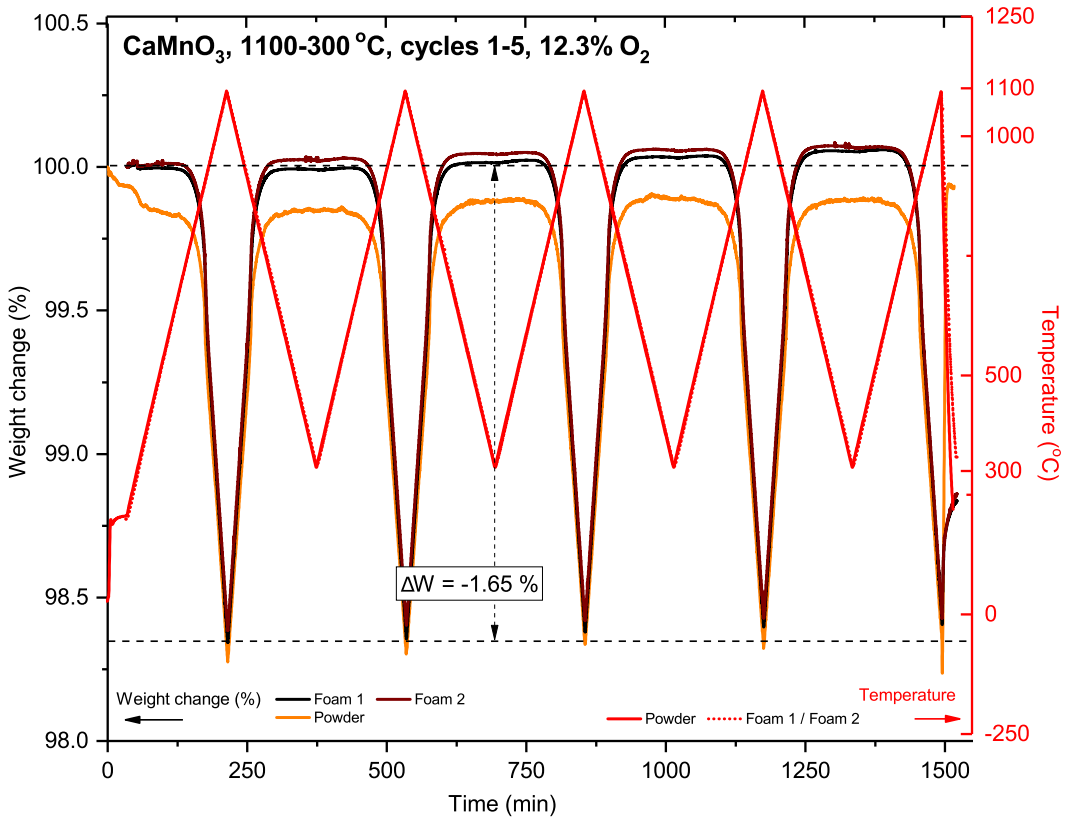

Fig. 6.8.: Cyclic TGA of $CaMnO_{3-\delta}$ powder and foam samples (30 ppi). Temperature range was 300 °C to 1100 °C with a heating rate of 5 °C min^{-1}. O_2-concentration was adjusted to 12.3% ($p(O_2)$=0.123) at total gas flow of 32 mL min^{-1}. Reproduced from Pein et al..[19] CC-BY.

Table 6.1.: Calculated values of wt.change and corresponding reduction extents $\Delta\delta$ extracted from cyclic TGA measurement (compare fig. 6.8). Δm was calculated from the minimum weight at $T_{\text{max}} = 1100\,^{\circ}\text{C}$ mid-cycle and the maximum weight at $T_{\text{min}} = 300\,^{\circ}\text{C}$ at the end of each cycle.

Cycle	Powder		Foam 1		Foam 2	
-	Δm	$\Delta\delta$	Δm	$\Delta\delta$	Δm	$\Delta\delta$
1	1.584	0.1416	1.647	0.1472	1.637	0.1463
2	1.586	0.1418	1.660	0.1484	1.643	0.1469
3	1.561	0.1395	1.651	0.1476	1.636	0.1462
4	1.586	0.1402	1.652	0.1477	1.638	0.1465
Avg.	1.575(11)	0.1208(9)	1.653(5)	0.1477(4)	1.639(3)	0.1465(2)

It can be observed in fig. 6.8 that the powder sample loses approximately 0.3wt.-% in the initial heating of cycle one at temperatures below 400 °C. This can be attributed to adsorbed water due to the hydrophilic nature of the surface[194] and has been observed previously for samples that were openly stored for extended periods. Significant weight loss due to reduction does not occur at temperatures below 700 °C. Consequently, the reversible weight loss and gain can be fully attributed to reduction and oxidation of the powder sample. The observed weight loss and gain is fully reversible over the following cycles.

Since all samples were cooled down in the last cycle with a very fast cooling rate of 30 °C min^{-1}, another observation can be made. Only the powder sample is fully reoxidized, while the two foam samples only regain $\approx 25\%$ of their lost weight in the final cool-down process. This already hints at kinetic limitations that are present in the foam samples and will be discussed further in the following section. Since the last cooling step is not comparable to the other four cycles due to the varying kinetics of the tested samples, no values for Δm and $\Delta\delta$ were calculated for the 5^{th} cycle.

In order to test the long-term stability of the $CaMnO_{3-\delta}$-foam specimens with regard to their redox activity, one of the foam samples (foam 2 from fig. 6.8) was cycled for additional cycles in the TGA up to a total number of 46 cycles. Resulting mass changes are depicted in fig. 6.9.

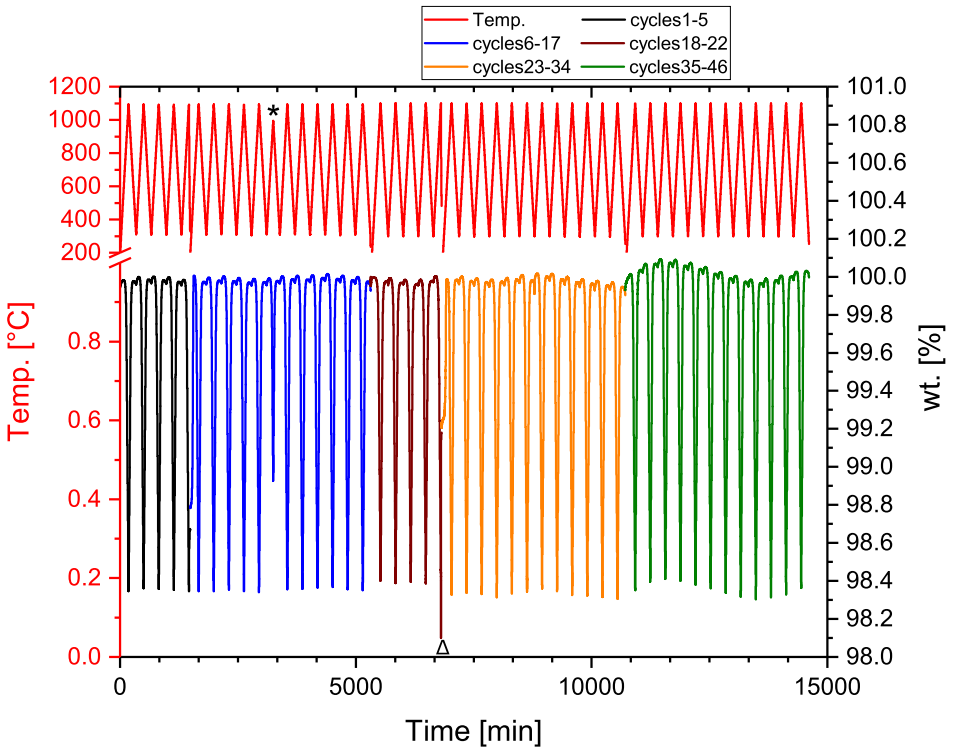

(a)

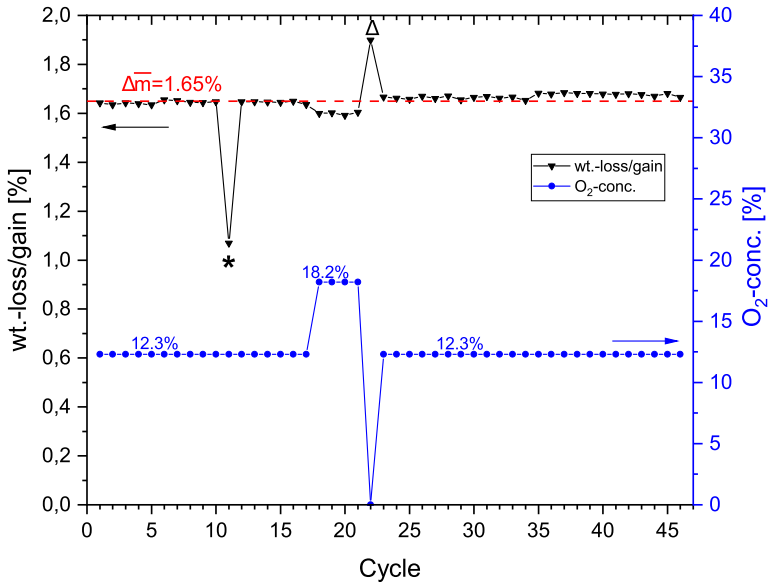

(b)

Fig. 6.9.: $CaMnO_{3-\delta}$-foam sample ("Foam 2" from fig. 6.8) cycled over 46 cycles between 300 °C and 1100 °C in 12.3% O_2. a) Mass signal recorded in TGA. b) Extracted mass changes per cycle. * represents a cycle whith $T_{max} = 1000\,°C$ instead of 1100 °C. Δ represents a single cycle under argon.

Due to erroneous programming of the TGA for some of the cycles, there are a few cycles that differ from the conditions applied in the first five cycle experiments. Therefore, applied oxygen concentrations and the resulting mass change are separately plotted in fig. 6.9b. The differing cycles allow for additional information to be gained upon the samples thermodynamic behavior. By comparing cycle 12 and cycle 22, it becomes evident that a slight reduction of the reduction temperature T_{red} by 100 °C led to much bigger changes of the resulting mass changes than reducing the $p(O_2)$ significantly. Overall, good stability with respect to repeated reduction and oxidation could be observed with an average relative mass change of 1.647($\pm$0.036)% throughout the 46 cycles at 12.3% O_2 and $T_{\text{red}} = 1100\,°C$.

Additionally, cycle 22 was carried out in Ar ($p(O_2) \approx 10^{-4}$) and demonstrates that even reduction at very low $p(O_2)$ and dissociation of $CaMnO_{3-\delta}$ under these conditions (compare fig. 5.6), neither interfers with the macroscopic structural integrity of the foam sample, nor limits the cyclic reversibility of reduction and oxidation. It can be concluded that $CaMnO_{3-\delta}$-foam samples can be thermally cycled under various conditions over multiple cycles without drastic aging with respect to its thermodynamic behavior macroscopic structure.

Determined reduction extents of $CaMnO_{3-\delta}$samples are in accordance with values reported in literature. Bulfin et al. reported values of $\Delta H = 161 \pm 6 kJmol^{-1}$ and $\Delta S = 94 \pm 7 kJmol^{-1}$.[169] Together with the underlying equilibrium model, mass changes and correlated reduction extents can be calculated and plotted for constant $p(O_2)$(see fig. 6.10). Taking the reported error margins into account, the results presented in this work are within the range and near the calculated $\Delta m = 1.5105$ ($\Delta\delta = 0.1350$) at $p(O_2) = 0.123$ and T =1100 °C. Although the error margins reported by Bulfin et al. appear to be small, fig. 6.10 points out that even small variations in ΔH and ΔS can have significant impact on the resulting mass changes and reduction extent at high temperatures.

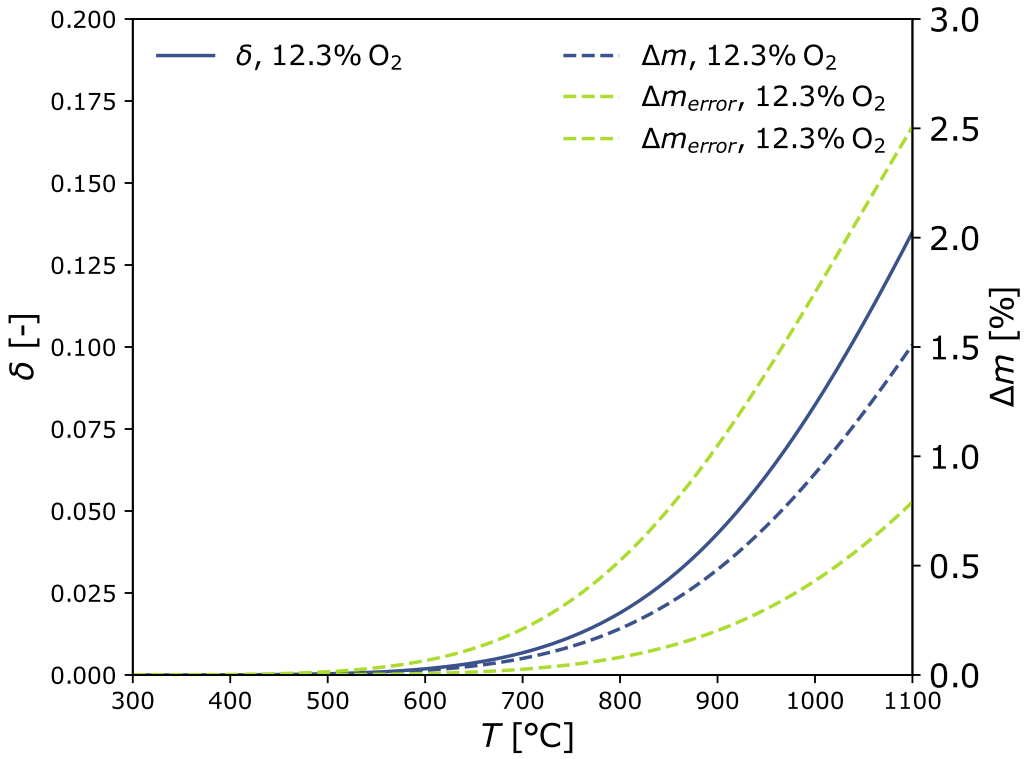

Fig. 6.10.: Mass changes Δm (dotted line) and corresponding reduction extent $\Delta\delta$ (solid line) with temperature at $p(O_2)$=0.123. Calculated using the equilibrium model and experimentally determined values of ΔH and ΔS by Bulfin et al..[169] Lower and upper limit of error margins were calculated from given error margins of ΔH and ΔS.[169]

6.4. Oxidation Kinetics of $Ca_{1-x}Sr_xMnO_{3-\delta}$ Specimen

In order to evaluate the influence of specimen structure on the oxidation kinetics, three different specimen made from $CaMnO_{3-\delta}$ were investigated: Powder, pellet and foam. Reduction was done at 1100 °C and $p(O_2) = 10^{-4}$. Re-oxidation was done at various temperatures and at $p(O_2) = 0.2$. A detailed description of the measurement can be found in section 3.5 and graphs of the measurements results are shown in fig. 6.11.

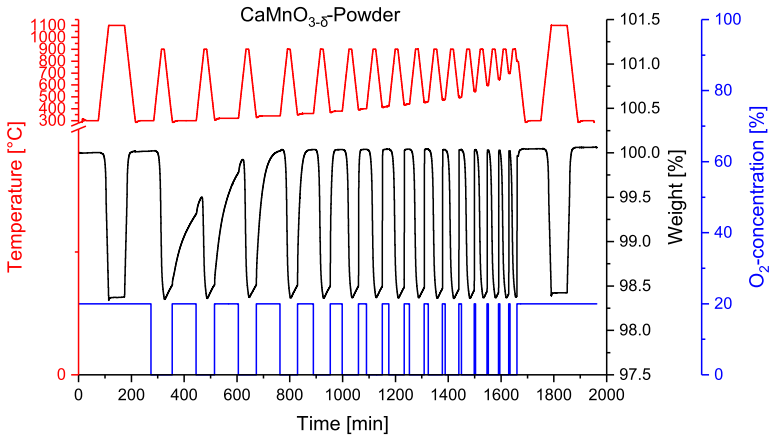

(a)

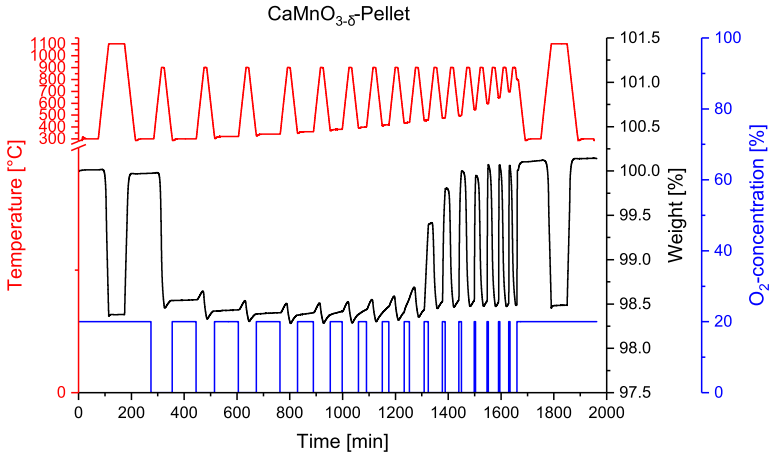

(b)

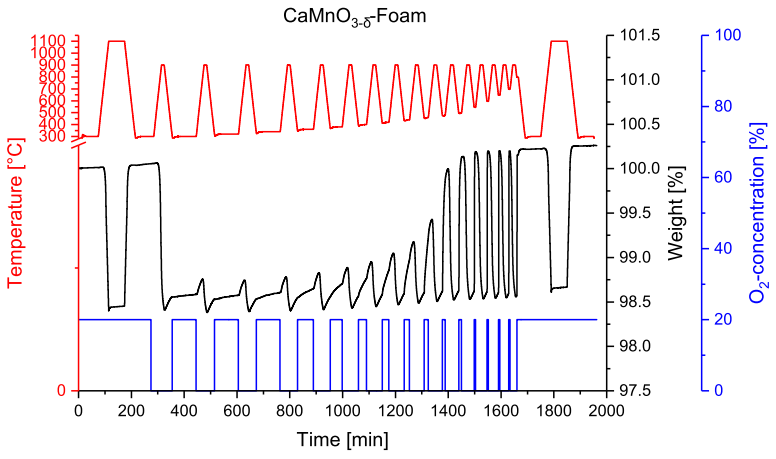

(c)

Fig. 6.11.: Oxidation kinetic measurement of $CaMnO_{3-\delta}$ samples. a) Powder; b) Pellet; c) Foam.

The powder sample was taken from ball milled $CaMnO_{3-\delta}$, which was also used to produce the foam and pellet samples. A 30 ppi cylindrical foam (⌀1.2 cm, length: 2 cm) and a pellet (⌀1.2 cm, thickness: 3 mm) were produced. Sample sizes were chosen to have similar total masses (≈350 mg), as previous experiments showed that the total mass can influence the results of thermogravimetric measurements. Determined values of $t_{1/2}$ are given in fig. 6.12. The half-time $t_{1/2}$ represents the time needed until the sample is re-oxidized up to 50%, meaning the oxidation fraction X has reached 0.5. Therein, two distinct regimes are determined for the powder sample, below and above 400 °C. For the foam and pellet samples, two distinct regimes below and above 600 °C were determined.

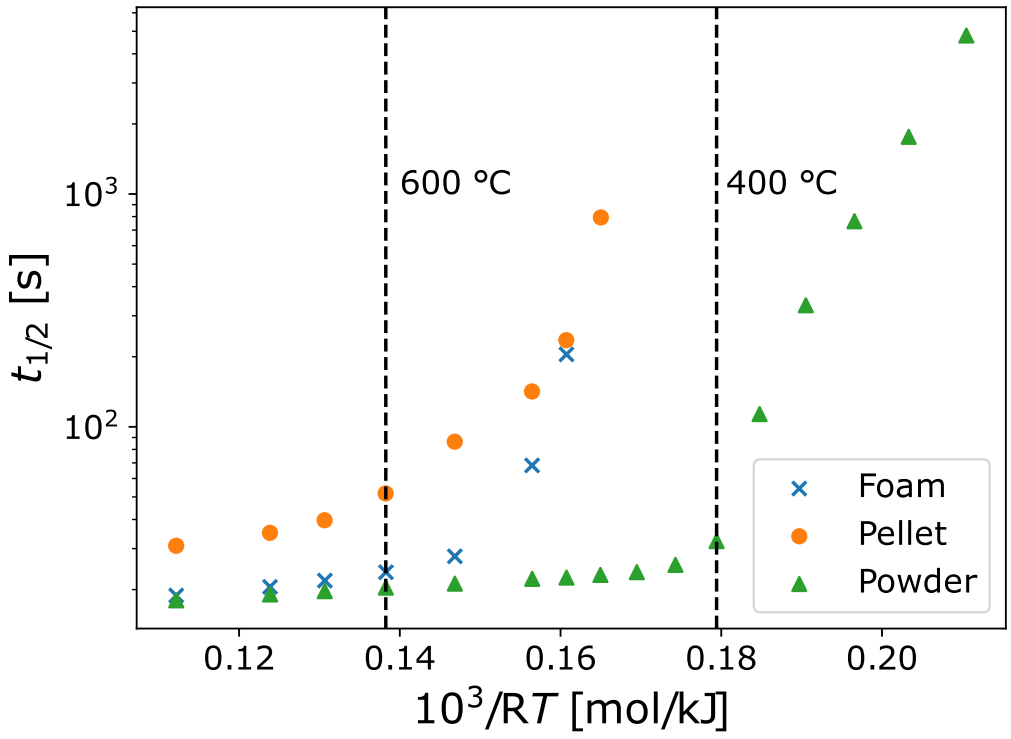

Fig. 6.12.: $t_{1/2}$ of oxidation of $CaMnO_{3-\delta}$samples (30 ppi foam, pellet, powder) in dependence on temperature as determined by kinetic TGA measurements (see also fig. 6.11).

In general the powder sample re-oxidizes faster than the foam and pellet. $t_{1/2}$ only increases very slightly from 18 s to 32 s when the oxidation temperature T_{ox} is reduced from 800 °C to 400 °C. Starting from 400 °C ($10^3/RT \geq 0.179$) the behavior changes and $t_{1/2}$ increases steeply from 32.4 seconds at 400 °C to 4796 seconds at 300 °C.

Maximum reduction extent $\Delta\delta$ was found to be 0.13(5) for all samples. For a 350 mg

sample this results in a mass change in the range of 5.2 mg or $1.65 \cdot 10^{-4}$ mol O_2, which indicates that $\approx 0.825 \cdot 10^{-4}molO_2$ are needed to oxidize the sample to $X = 0.5$. At a total mass flow 120 mL min^{-1} and an oxygen concentration of 20%, oxygen is supplied at a rate of $9.8 \cdot 10^{-6} \frac{\text{mol}}{\text{s}}$ of O_2 (calculated via ideal gas law). At this oxygen supply rate, it takes 8.4 s to supply enough oxygen to reach $X = 0.5$ assuming a 100% conversion rate. Additionally, the elapsed until the atmosphere inside the sample chamber has fully adjusted to changes in the supplied gas stream, was found to be in the range of 20 s[176] Conclusively, the oxidation reaction is predominantly mass transfer limited at higher temperatures (for powder: $T_{ox} \geq 420$ °C).

Pellet and foam samples also exhibit mass transfer limitation at high temperatures. However, the border between the two regimes is shifted to higher temperatures at 600 °C. Furthermore, foam samples exhibit much faster oxidation compared to the pellet and at temperatures above 600 °C the speed of reaction is comparable to that of the powder (23.75 s vs. 20.40 s at 600 °C). Foam and pellet exhibit a steep increase of $t_{1/2}$ below 600 °C and ultimately do not even reach $X = 0.5$ within the given measurement time when $T_{ox} < 480$ °C and $T_{ox} < 460$ °C respectively. This fact also becomes evident in the raw measurement data given in fig. 6.11. The mass gain during oxidation does not match the mass loss during reduction.

The oxidation reaction can be broken down into 3 major steps:

- Diffusion of gaseous reactants (e.g. oxygen) in the surrounding atmosphere
- Adsorption/Desorption of gaseous reactants on the perovskite surface
- Diffusion of oxygen ions, oxygen vacancies and electrons within the perovskite crystal lattice

The first two steps can be treated together as the surface reaction, leaving two main factors: Surface reaction and bulk diffusion. The available data does not allow any conclusions as to which factor is rate limiting outside of the mass transfer limited region. Yet, the distinct differences between powder, foam and pellet led to the conclusion that the sample structure, and most likely the available surface area, does influence the rate of reaction significantly at lower temperatures where bulk diffusion is presumably slow. Foam and powder have comparable specific surface areas. The pellet is expected to have a lower surface area, which could explain the slower oxidation even in the mass transfer limited temperature regime.

As described in section 3.5, the obtained data allows for calculation of apparent activation energies. However, these activation energies are only apparent and not actual

activation energies. The utilized method does not allow distinction between separate reaction mechanisms, and therefore depicts the overall reaction. Consistent with analysis of the half times $t_{1/2}$, two regimes can be distinguished for each of the samples.

As shown in fig. 6.13 for $CaMnO_{3-\delta}$-powder, activation energies had to be calculated separately for these two regimes as no reasonable regression could be made over the whole temperature range. Respective plots for pellet and foam samples are given in the appendix in fig. A.14 and fig. A.15. Cut-off temperatures were 400 °C for powder samples and 600 °C for pellet and foam samples. Determined activation energies, given in fig. 6.14, differ drastically between the two regimes as is expected from the obtained $t_{1/2}$ (compare fig. 6.12).

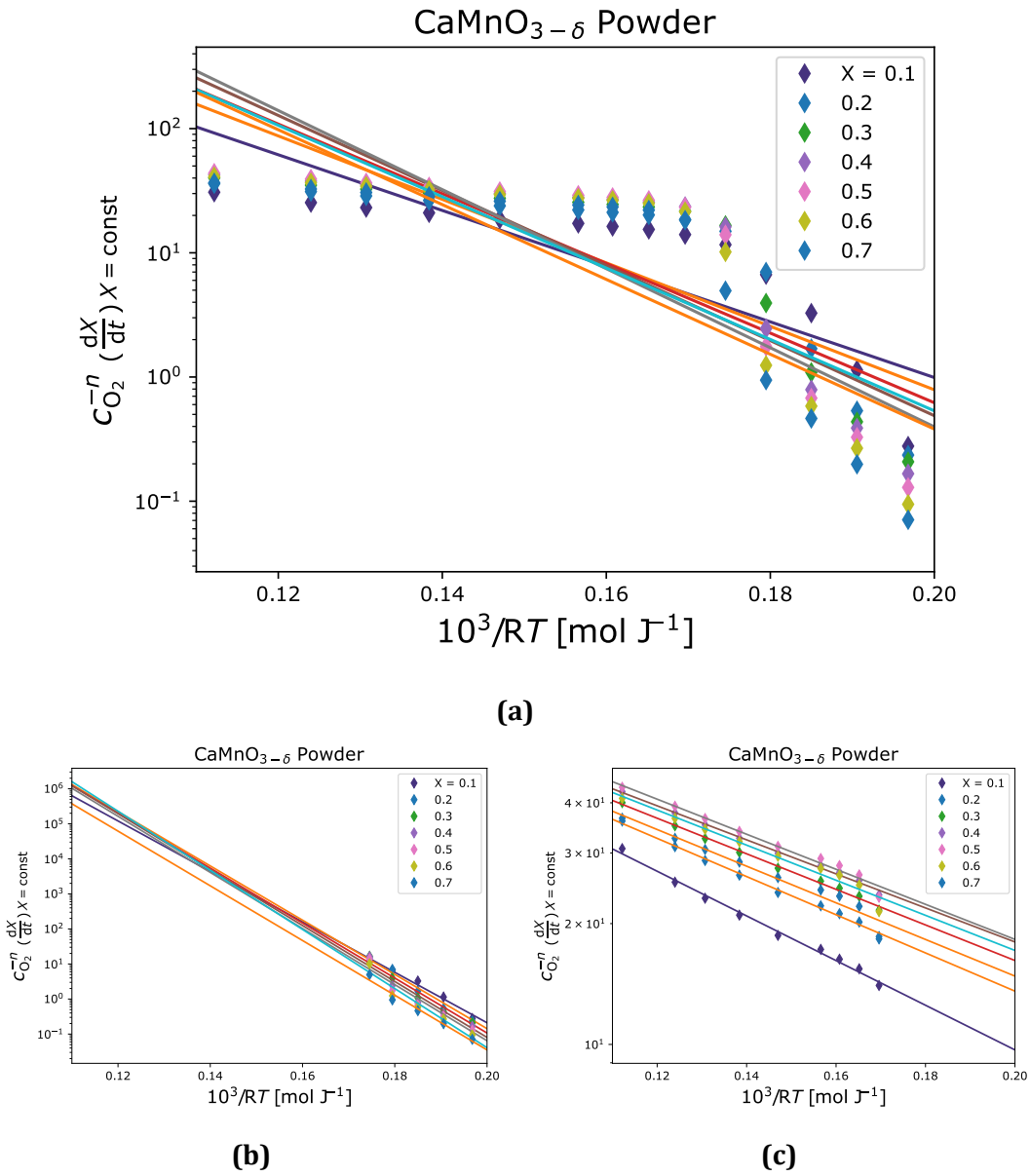

Fig. 6.13.: Log-scale plotted $c_{O_2}^{-n}\left(\frac{dX}{dt}\right)_{X=\text{const.}}$ vs. $\frac{10^3}{RT}$ for $CaMnO_{3-\delta}$ powder. Diamond marks represent determined values at constant X. The slope of each line is the activation energy -E_a. a) Plotted over complete temperature range. b) Only temperatures below 400 °C. c) Only temperatures above 400 °C. (see also fig. A.14 and fig. A.15 in the appendix for plotted graphs of the pellet and foam samples).

Since the oxidation reaction is mass transfer limited in the higher temperature regime, it can be assumed that the actual apparent activation energies E_a, at T >400 °C for the powder sample and T >600 °C for the pellet and foam samples are even lower than the found $9.6 \pm 0.8\ kJmol^{-1}$ (powder), $17.3 \pm 2.7\ kJmol^{-1}$ (Foam) and $35.8 \pm 9.0\ kJmol^{-1}$ (Pellet). As the reliability of the results suffer from the mass transfer limitation in the lower temperature region, no deeper analysis on the actual values has been conducted. Especially the substantially lower E_a of the pellet sample at T >600 °C can hardly be taken as an accountable result, due to the small amount of valid measurement points in that region. This inaccurracy also becomes evident by the intersecting lines in the log-scale plotted $c_{O_2}^{-n}\left(\frac{dX}{dt}\right)_{X=\text{const.}}$ vs. $\frac{10^3}{RT}$ for the $CaMnO_{3-\delta}$-pellet (given in fig. A.14).

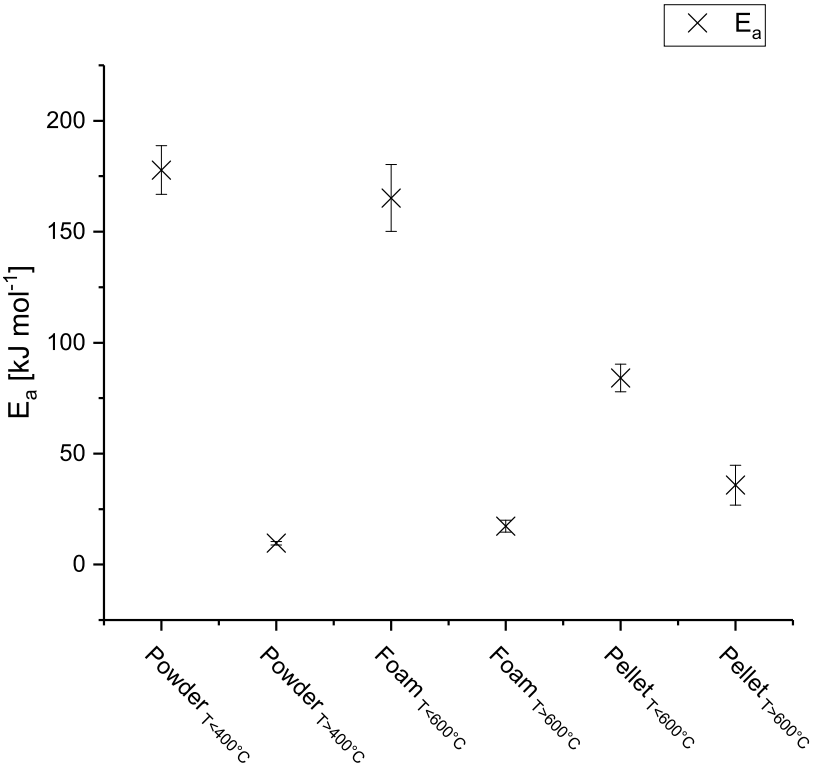

Fig. 6.14.: Determined activation energies of oxidation of $CaMnO_{3-\delta}$samples (30 ppi foam, pellet, powder) for high and low temperature regime as determined by kinetic TGA measurements (see also fig. 6.11).

While the calculated activation energies serve as an indicator for performance with respect to oxidation kinetics and redox cycles here, an extensive and designated study would be necessary to produce reliable results. Yet, the results add to the impression that at high temperatures (T >600 °C), the foams performance with respect to redox cycles is comparable to that of the powder. Desired applications such as thermochemical

heat storage and oxygen pumping are typically carried out at temperatures above 600 °C. Consequently, fast heating and cooling cycles for foam structures can be conducted without or with only minor drawbacks when it comes to the redox kinetics of the material in the actual application compared to fine powder and particles.
The results hint at the fact that the oxidation reaction is controlled by the oxygen diffusion in the bulk, since much bigger differences in E_a would be expected with respect to the surface area of the different samples if the oxidation was limited by surface reaction. The fact that $CaMnO_{3-\delta}$undergoes a phase transition from orthorhombic to cubic within the range temperature and $p(O_2)$ applied here for reduction could impact the oxidation kinetics at lower temperatures.

Due to the fast cooling, the crystal phase transition, which is supposedly reversed towards orthorhombic when cooling down the sample, does not occur or is not fully completed. Hence, the materials are be in a meta-stable, mixed phase state. Analyzing samples of $CaMnO_{3-\delta}$ powder and foam that have been quenched after reduction at 900 °C in Ar-atmosphere showed that two structural phases were found. However, both phases are orthorhombic $CaMnO_{3-\delta}$ with only the reduction extent of the two phases differing. Additionally,powder and foam exhibit identical diffraction patterns, which means it does not explain the differences observed in the oxidation kinetics.

Following up the results described in chap. 5 and the joint work by *Klaas* and the author of this work,[20] *Klaas et al.* conducted a study on the kinetics of $Ca_{1-x}Sr_xMnO_{3-\delta}$ and determined the bulk oxygen diffusion as the rate limiting step in the oxidation reaction.[187] These results are consistent with the conclusions drawn from the results presented in this work. The underlying mechanisms and the impact of makro- and microscopic structure is part of ongoing research. Most recent results indicate that higher porosity leads to faster oxidation kinetics, especially at low temperatures. It can be explained by the formation of a thin passivation layer of oxidized oxide in the surface region, which acts as a diffusion barrier for additional oxygen to be absorbed by the material.[1]

The presented results demonstrate that reticulated open porous structures made from $CaMnO_{3-\delta}$ provide a valid option for thermochemical processes aside from powder or small particles. A production pathway for mechanically sturdy and thermodynamically stable foam structures made from $CaMnO_{3-\delta}$ was established. In the following chapter such foam structures were investigated in a prototype thermochemical reactor for oxygen pumping based on the setup. The production process can also be transferred to other perovskite material systems. As chapter 5 has shown that Sr-substitution of $CaMnO_{3-\delta}$

[1] Personal communication by L. Klaas

can be beneficial for thermodynamic and phase stability, foam samples with 5% and 10% Sr were produced and tested as well.

7. Performance of $Ca_{1-x}Sr_xMnO_{3-\delta}$-Foams and -Granules in Oxygen Pumping

As shown in the previous chapters, $CaMnO_{3-\delta}$ and its Sr-substituted variants are valid material candidates for thermochemical energy storage and thermochemical oxygen pumping applications. Stable foam structures from these materials can be manufactured via the established replica method using polyurethane foams as template structure. To demonstrate the application of such perovskite foam structures, the setup already used for screening purposes in chapter 4 was rebuilt and foam structures were tested with respect to their oxygen pumping capabilities.

Based on the results of previous screening and characterisation, three compositions were tested: $CaMnO_{3-\delta}$, $Ca_{0.95}Sr_{0.05}O_{3-\delta}$ and $Ca_{0.9}Sr_{0.1}O_{3-\delta}$. Small amounts of A-site Sr-substitution in $CaMnO_{3-\delta}$ stabilized the structural stability during thermal cycling with respect to the occuring phase transitition. Furthermore, it reduced irreversible expansion during thermal cycling at lower $p(O_2)$. Two different sample types were produced for the three tested compositions, granules and foams. Specimens were produced according to the procedure described in chapter 3.2, resulting in foam structures with 30ppi and granules with a particle diameter range of 1 mm to 5 mm. As the reference H_2O/CO_2 splitting material, CeO_2 in the form of granules with a mean diameter of 200 µm were used. Similar total weights of each perovskite sample were employed within the experiment. For each sample, actual weights can be found in tab. 7.1 and exemplary sample photographs are shown in fig. 7.1.

Table 7.1.: Total weight of foam and granule samples used in oxygen pumping experiments.

Composition	Foam	Granules
$CaMnO_{3-\delta}$	4.29g	4.26g
$Ca_{0.95}Sr_{0.05}O_{3-\delta}$	4.27g	4.27g
$Ca_{0.9}Sr_{0.1}O_{3-\delta}$	4.20g	4.22g
Splitting reference		
$CeO_{2-\delta}$	-	5.02g

This chapter is partially based on peer-reviewed publications authored and co-authored by the author of this work:

Mathias Pein, Jens Keller, Christos Agrafiotis, Asmaa Eltayeb, Lena Klaas, Nicole Carina Neumann, Martin Roeb, and Christian Sattler. "Thermochemical Oxygen Pumping with Perovskite Reticulated Porous Ceramics for Enhanced Reduction of Ceria in Thermochemical Fuel Production". In: *Advanced Energy Materials* (2024), p. 2304454. DOI: https://doi.org/10.1002/aenm.202304454

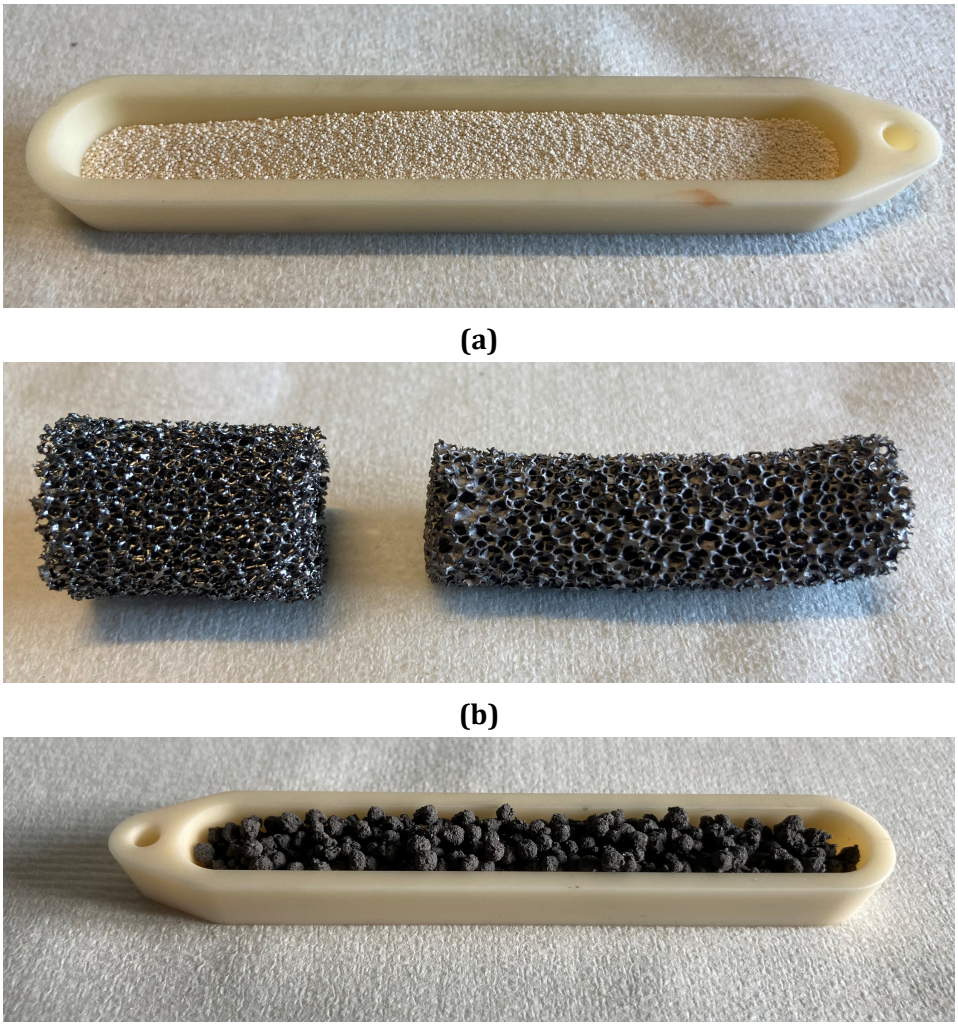

(a)

(b)

(c)

Fig. 7.1.: Exemplary photographs of specimens used for oxygen pumping experiments. a) Ceria granules. b) $Ca_{1-x}Sr_xMnO_{3-\delta}$ foams. c) $Ca_{1-x}Sr_xMnO_{3-\delta}$ granules.

In addition to the micrographic analysis of the foams in chap. 6.2, SEM micrographs were taken from the $Ca_{1-x}Sr_xMnO_{3-\delta}$ $x \in [0, 0.05, 0.10]$ granule and foam samples used in this chapter and are shown in fig. 7.2, fig. 7.3 and fig. 7.4 respectively.

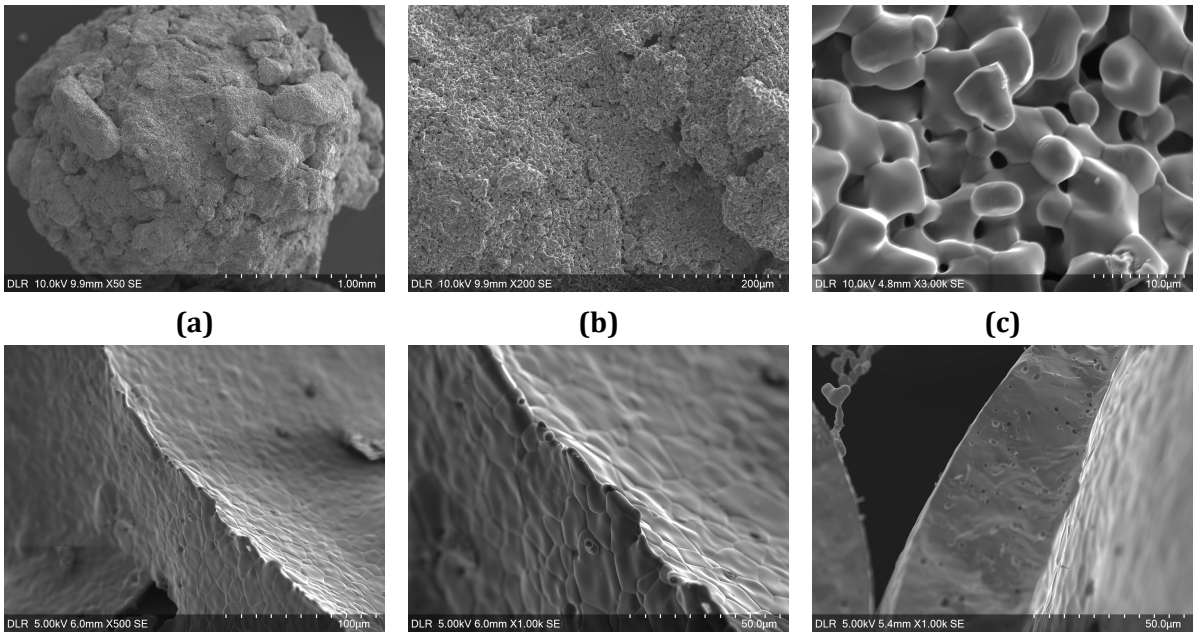

Fig. 7.2.: SEM-micrographs of $CaMnO_{3-\delta}$. Granules: a)-c). Foams: d)-f).

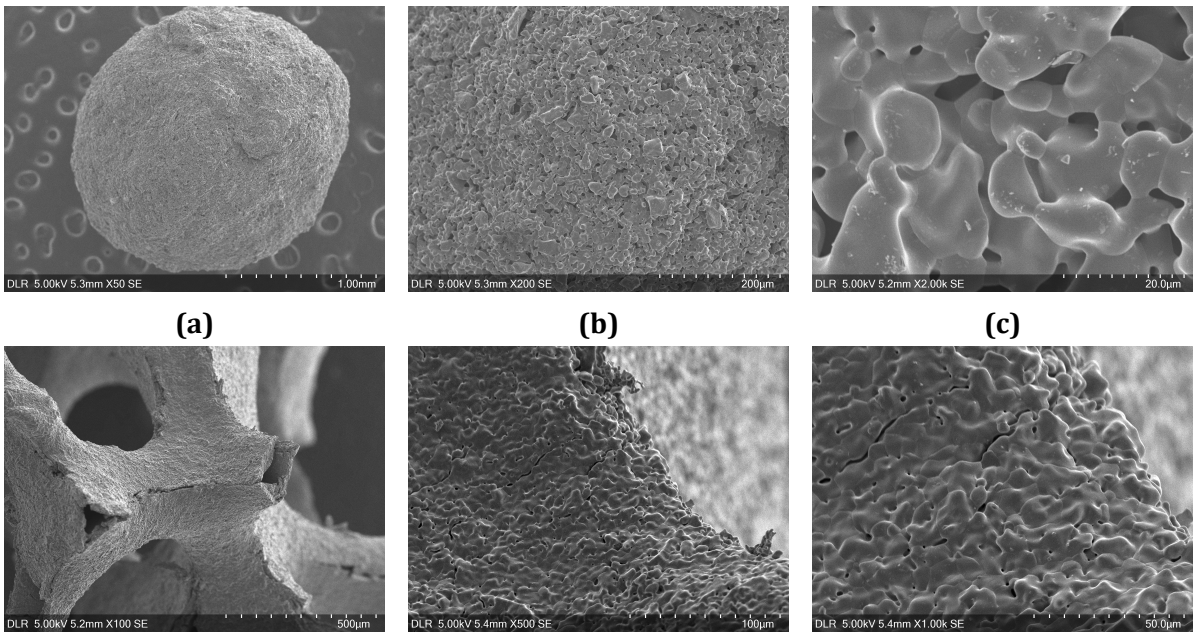

Fig. 7.3.: SEM-micrographs of $Ca_{0.95}Sr_{0.05}O_{3-\delta}$. Granules: a)-c). Foams: d)-f).

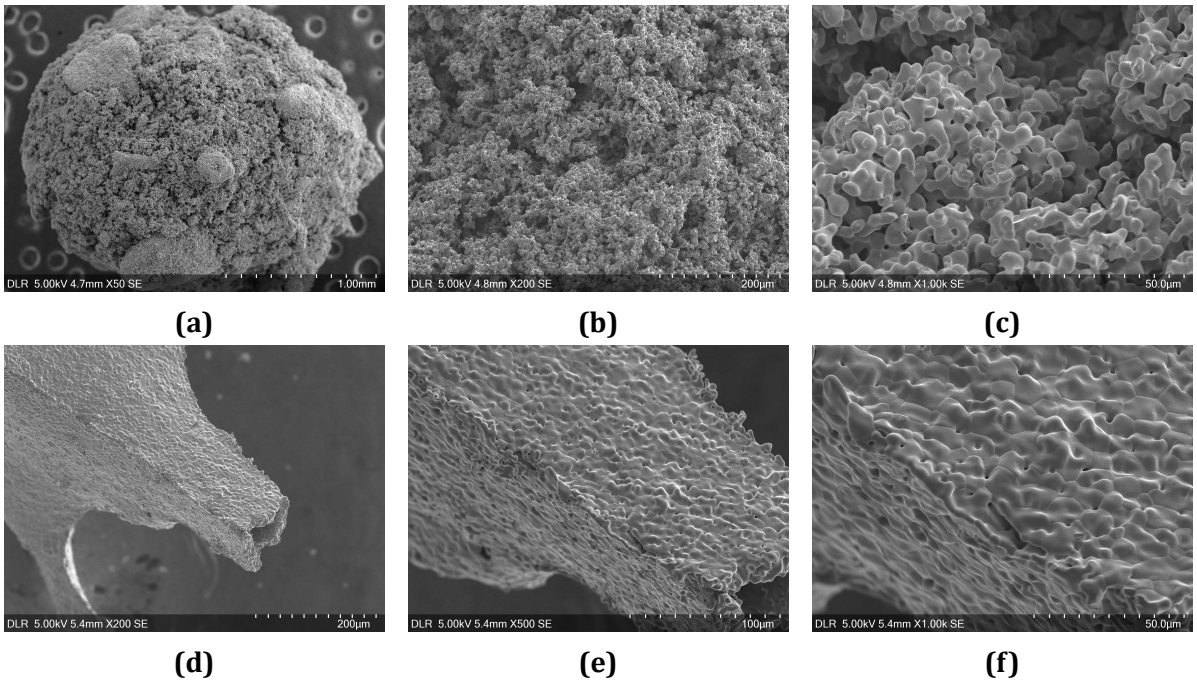

Fig. 7.4.: SEM-micrographs of $Ca_{0.9}Sr_{0.1}O_{3-\delta}$. Granules: a)-c). Foams: d)-f).

SEM-images show that the 1 mm to 5 mm granules are rather uneven with a rough surface. High magnification images (e.g. fig. 7.2c) reveal the porous nature of the granules surface. The 5 µm particles, which were used to prepare these granules, are visibly sintered together and created channels of roughly the same diameter. Porosity and surface area were determined for all used samples through Hg-intrusion porosimetry and N_2-gasadsorption with BET-analysis respectively. Results of this analysis are given in tab. 7.2. Foam samples exhibit significantly higher specific surface area compared to granule samples, although the granules appear to have higher porosity than the foams. This can be explained by the macroscopic pores of the foams, which are beyond the detection range of Hg-intrusion porosimetry, which makes the granules appear more porous than the foams in Hg-instrusion porosimetry.

Table 7.2.: Porosity and surface area of foam and granule samples used in oxygen pumping experiments as determined by Hg-intrusion and Gasadsorption respectively.

Composition	Spec. Surface Area [$\frac{m^2}{g}$]		Porosity [%]	
-	Foam	Granules	Foam	Granules
$CaMnO_{3-\delta}$	6.59	0.22	18.04	26.57
$Ca_{0.95}Sr_{0.05}O_{3-\delta}$	0.59	0.23	30.00	35.82
$Ca_{0.9}Sr_{0.1}O_{3-\delta}$	0.70	0.37	28.90	58.11

In the following, the results of the two employed process cases are discussed.

7.1. Case 1: Seperate Temperature Swings

The 5 major steps of case 1 are summarized below. A detailed description can be found in chapter 3.7. SM represents the splitting material ceria. PM represents the pumping material perovskite:

- Step 1: SM at 1500 °C, PM at 800 °C, gas phase connected
- Step 2: Evacuation for 20 minutes
- Step 3: PM cooled down to 700 °C
- Step 4: Close valve between PM and SM. Gas phases disconnected, cool down SM to 1000 °C

- Step 5: Re-oxidize SM with defined gas stream of O_2 and N_2

From the oxidizing gas stream in step 5, the reduction extent $\Delta\delta$ of the reference splitting material $CeO_{2-\delta}$ was calculated as described in detail in chapter 3.7. Furthermore, the value of additionally absorbed oxygen per gram of pumping material is defined as a figure of merit of each composition, which takes their sample weight into account. The molar weights of the three tested compositions are very close to each other. Therefore, calculations of values per mol material are waived herein as the weight plays a bigger role in industrial upscaling from a techno-econimic point of view. The value is calculated by subtracting the amount of oxygen absorbed by the splitting material during re-oxidation in the reference and pumping case respectively. Therein, "Blank CeO_2" is the reference case where no pumping material was present.
Each experiment was repeated three times for each composition and specimen. The results are represented by mean values and standard deviation of those three experimental runs in fig. 7.5 and fig. 7.6.

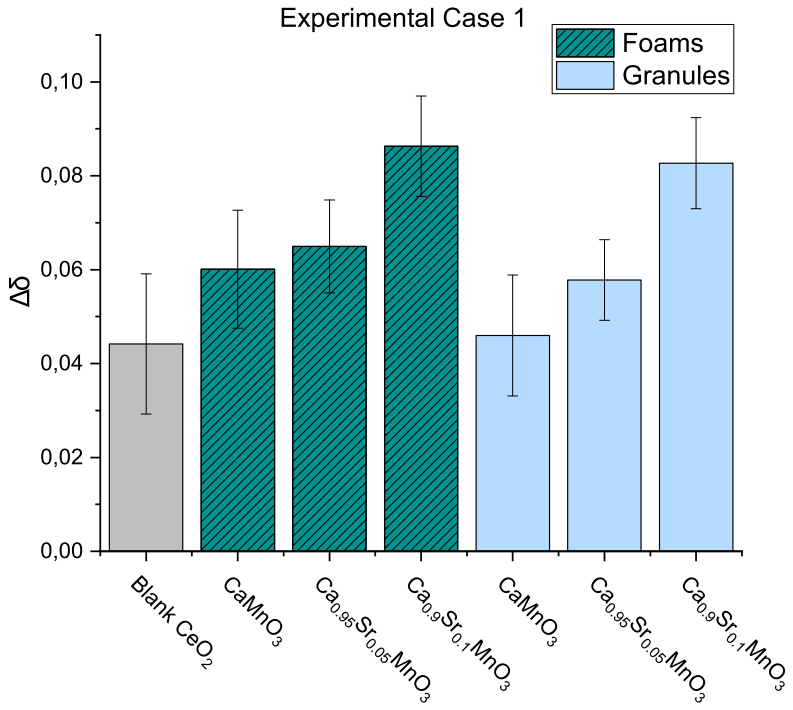

Fig. 7.5.: Resulting reduction extents $\Delta\delta$ of Case 1 oxygen pumping experiments. Labeled "Blank CeO_2" is a blank experiment that contained splitting material, but no pumping material for reference.

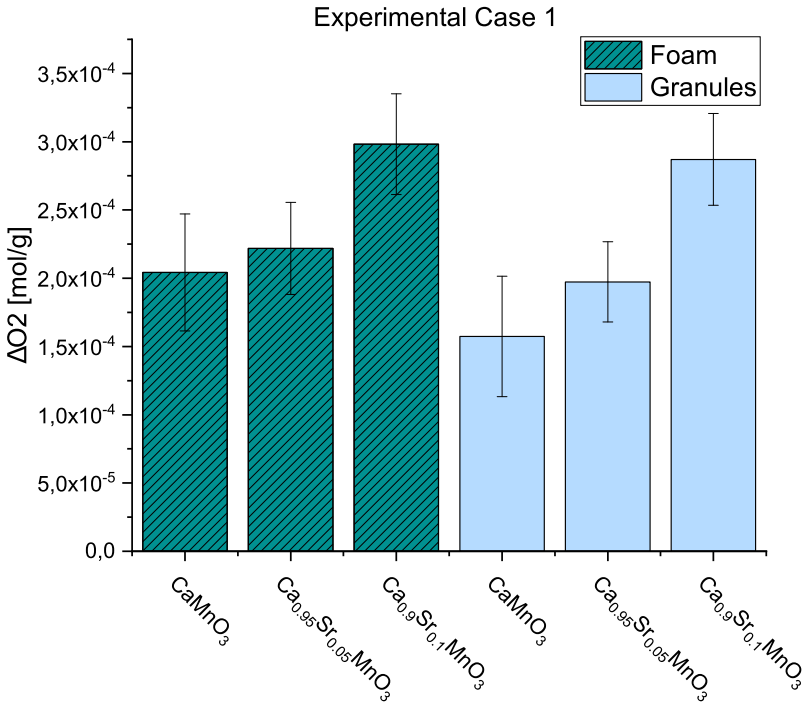

Fig. 7.6.: Resulting absorbed oxygen $\Delta\frac{o_2}{g}$ of Case 1 oxygen pumping experiments.

First of all it can be noted that all tested compositions increase the reduction extent of the reference Ceria sample. Additionally, it can be seen that error margins were comparably large, which can be explained by the relatively small sample sizes and the nature of how the experiments were carried out - with a lot of manual steps that have to be precisely timed and are prone to error. Plain reduction of the total pressure at the reduction temperature of 1500 °C led to a reduction extent $\Delta\delta = 0.0442 \pm 0.00149$ in the reference case. Introducing $Ca_{1-x}Sr_xMnO_{3-\delta}$ as pumping material increased the $\Delta\delta$, which demonstrated the working principle of a thermochemical oxygen pump. The effect did not appear significant for $CaMnO_{3-\delta}$ and $Ca_{0.95}Sr_{0.05}MnO_{3-\delta}$ considering the error margins. However, employment of $Ca_{0.9}Sr_{0.1}MnO_{3-\delta}$ boosted the reduction extent to remarkable $\Delta\delta = 0.0863 \pm 0.0107$ using foams and $\Delta\delta = 0.0827 \pm 0.0043$ using granules respectively.

Utilizing $Ca_{0.9}Sr_{0.1}MnO_{3-\delta}$ foams, thereby increased the reduction extent in this case by 95%. Taking error margins into account, no significant difference could be observed between foams and granules, although the results showed a trend in favor of foams. The same applies for the comparison inbetween the three tested compositions. A trend towards better performance with increasing Sr-content could be observed. However, only $Ca_{0.9}Sr_{0.1}MnO_{3-\delta}$ performed significantly better than the other two tested compositions

when error margins are considered.
Adjusted results with respect to the sample mass in fig. 7.6 supported the discussed results. As the sample weights were precautiously kept nearly identical, the same overall trends can be observed. $Ca_{0.9}Sr_{0.1}MnO_{3-\delta}$ significantly outperformed $CaMnO_{3-\delta}$ and $Ca_{0.95}Sr_{0.05}MnO_{3-\delta}$ with $2.98(\pm0.37)\cdot10^{-4}\frac{molO_2}{g}$ and $2.87(\pm0.34)\cdot10^{-4}\frac{molO_2}{g}$ for foams and granules respectively.

In order to gain more insights on the performance characteristics, an additional O_2-sensor by Setnag was installed in the setup. The sensor was calibrated to a gas flow of $1\,L\,min^{-1}$. However, it was stated by the manufacturer that it provides reasonable results under vacuum as well. Since the sensor was installed as a bypass on the original setup, mass flow through the sensor is restricted at atmospheric pressure. Therefore, only values of this sensor under reduced total pressure are accounted valid. Under these conditions, the mean free path of gas molecules is sufficiently large to assume fast equilibration of the gas phase in the evacuated part of the setup. That is the case during step one, two and three of the experiment. The evolution of p_{total} and $p(O_2)$ is depicted for exemplary measurements of all three pumping material compositions and the reference case in fig. 7.7.

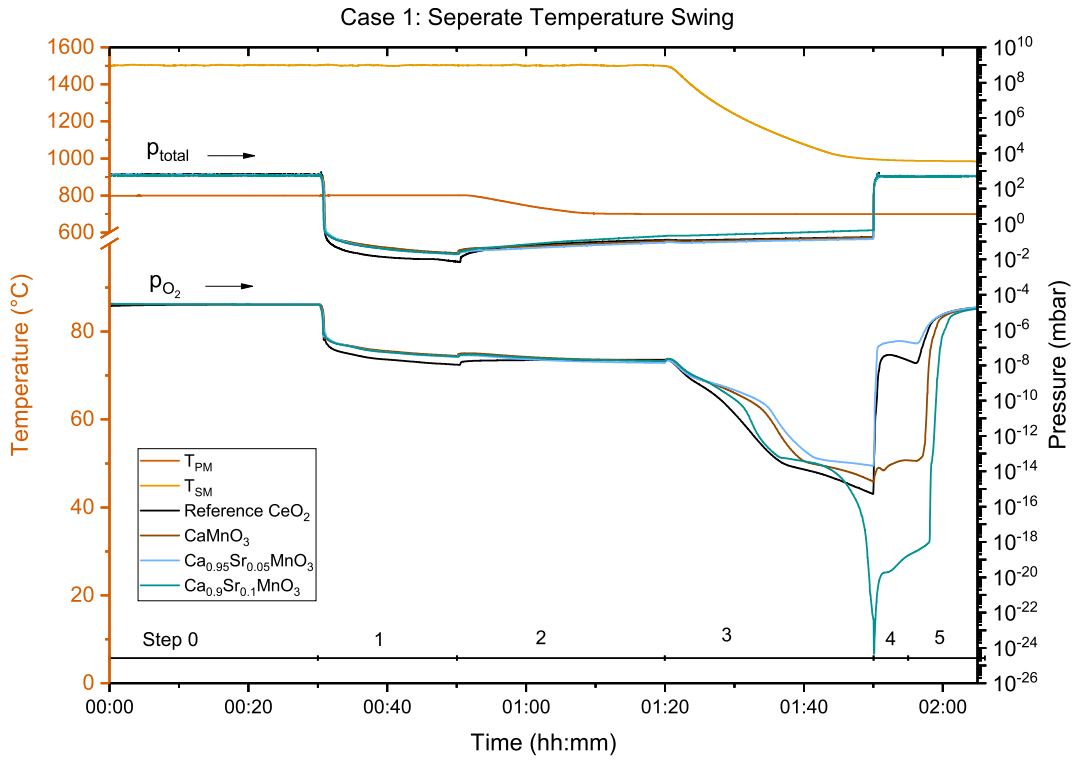

Fig. 7.7.: Evolution of p_{total} and $p(O_2)$ in Case 1 oxygen pumping experiments. Corresponding temperatures and experimental steps in accordance with tab. 3.4

The evolution of the $p(O_2)$ as recorded by the Setnag O_2-sensor did not offer any more insight to the observed differences in performance of the three tested perovskite compositions. The lower $p(O_2)$ for $Ca_{0.9}Sr_{0.1}MnO_{3-\delta}$ at the end of step three appears reasonable, considering the fact that the equilibrium $p(O_2)$ of a stronger reduced CeO_2 should be lower than that of a less reduced CeO_2. $p(O_2)$ for $CaMnO_{3-\delta}$ and $Ca_{0.95}Sr_{0.05}MnO_{3-\delta}$ were higher than in the reference case without a pumping material. This observation contradicts the increased reduction extent as shown in fig. 7.5 and fig. 7.6. Ultimately, it was concluded that the total values of the $p(O_2)$-signal cannot be used in the apparent context and only relative trends were considered for further analysis.

7.2. Case 2: Simultaneous Temperature Swings

The 5 major steps of case 2 are summarized below. A detailed description can be found in chapter 3.7. SM represents the splitting material ceria. PM represents the pumping material perovskite:

- Step 1: SM at 1000 °C, PM at 800 °C, gas phase connected

- Step 2: Evacuation for 20 minutes
- Step 3: PM cooled down to 700 °C, SM heated to 1500 °C
- Step 4: Close valve between PM and SM, Gas phases disconnected. Cool down SM to 1000 °C
- Step 5: Re-oxidize SM with defined gas stream of O_2 and N_2

A notable difference between case 1 and case 2 is the separated temperature swing of PM and SM in case 1. The SM already resides at T_{red} when the setup is evacuated in step 2 of case 1. In contrast, the SM is only heated up to T_{red} after evacuation in case 2. Thereby, the temperature swings of SM and PM are carried out simultaneously in step 3. That means the SM is only reduced during step 3. As Brendelberger et al. have shown, the reduction extent of Ceria at 1000 °C and total pressures of $10^{-2}mbar$ is negligibly small.[66] Therefore, the PM accounts for all the reduction extent of the SM, functioning as an oxygen sink during reduction. After disconnection of the two furnaces, the SM does not re-oxidize during cool-down in step 4 as the oxygen released during reduction has been absorbed by the PM.

Each experiment was repeated three times for each composition and sample specimen. The results are represented by mean values and standard deviation of three experimental runs in fig. 7.8 and fig. 7.9.

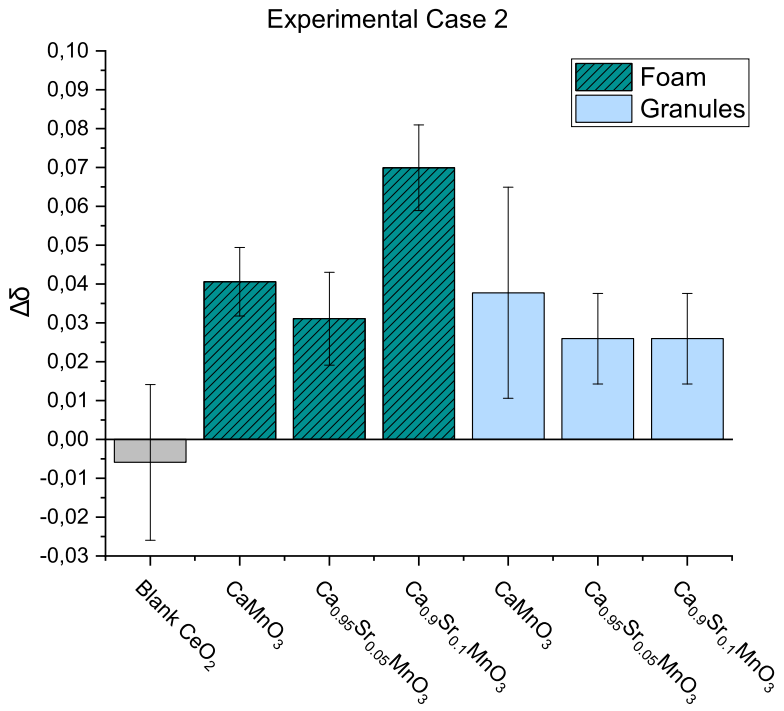

Fig. 7.8.: Resulting reduction extents $\Delta\delta$ of Case 2 oxygen pumping experiments. Labeled "Blank CeO_2" is a blank experiment that contained splitting material, but no pumping material for reference.

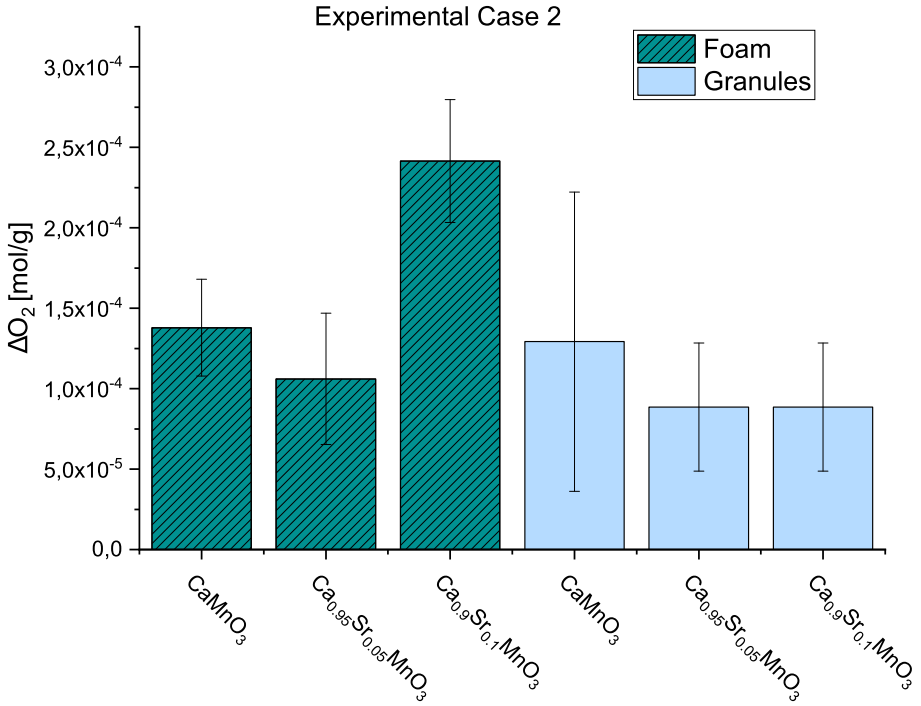

Fig. 7.9.: Resulting absorbed oxygen $\Delta\frac{o_2}{g}$ of Case 2 oxygen pumping experiments.

The blank run with only Ceria and no pumping material included in fig. 7.8 revealed the volatility of gained results, showing quite a large error margin. Error margins are larger compared to the results of case 1, which can be explained by the larger influence of leakage. All the reduction of Ceria takes place with a disconnected vacuum pump in step 3. Nonetheless, significant improvement can be achieved by the employment of a pumping material. While the reduction extent of the blank case can be considered zero, adding a perovskite pumping material led to reasonable reduction extents of the Ceria. The largest reduction extents was achieved with $Ca_{0.9}Sr_{0.1}MnO_{3-\delta}$ as PM. The foam specimen outperformed the granule sample with a $\Delta\delta = 0.0699(\pm 0.0110)$ compared to $\Delta\delta = 0.0259(\pm 0.0116)$ for the $Ca_{0.9}Sr_{0.1}MnO_{3-\delta}$ granule sample. Beyond that, no clear trends could be observed. The $CaMnO_{3-\delta}$ granule sample exhibited quite a large error margin. These results should be intepreted with care.

The results show that the employment of a pumping material like $Ca_{0.9}Sr_{0.1}MnO_{3-\delta}$ led to reasonable reduction extents. Additionally, foams appear to outperform granules in the presented experiments of case 2. This could originate from faster kinetics, due to the higher surface area and shorter diffusion pathways. Larger amounts of oxygen need to be absorbed by the PM compared to case 1, since the Ceria is not already partly reduced during evacuation of the setup. Recent results on oxidation kinetics of Sr-doped $CaMnO_{3-\delta}$ in the form powder and granules by Klaas et al. underline the correlation between surface structure, porosity of the sample and the oxidation kinetics.[187] The authors conclude that a higher porosity potentially leads to faster oxidation kinetics.[1] Investigation of the underlying fundamentals is part of ongoing research. As shown in tab. 7.2, the foam samples exhibit significantly higher surface area than the granules as determined by gasadsorption experiments.

Sample mass adjusted results confirm the observed trends, with $Ca_{0.9}Sr_{0.1}MnO_{3-\delta}$ foam being the best performing sample. Employing $Ca_{0.9}Sr_{0.1}MnO_{3-\delta}$ as the PM resulted in the highest reduction extents of the SM. The partial pressure of oxygen $p(O_2)$and total pressure p_{total} of exemplary runs with each pumping material composition and a reference run with only Ceria are shown in fig. 7.10.

[1] Personal communication with L. Klaas

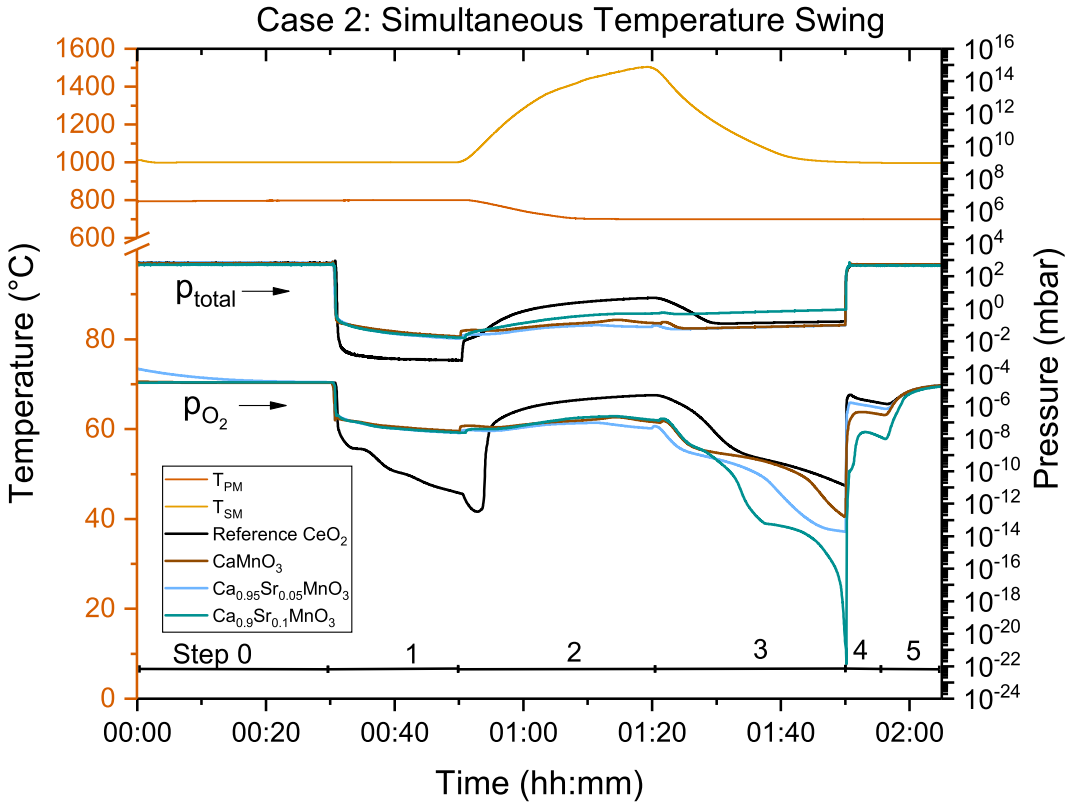

Fig. 7.10.: Evolution of p_{total} and $p(O_2)$ in Case 2 oxygen pumping experiments. Corresponding temperatures and experimental steps in accordance with tab. 3.4

In contrast to case 1, the evolution of the pressures were much more in line with the expected behavior. Nevertheless, these results should be evaluated with care with respect to the validity of absolute values. Looking at the reference case, the lower total pressures and $p(O_2)$ during step 1 (evacuation of the setup) can be explained by the fact that only Ceria was present. It was only reduced in a negligibly small extent. When a pumping material was present it got reduced during step 1, and thereby released oxygen, increasing the p_{total} and $p(O_2)$. Then, during step 2 $p(O_2)$ rised strongly in the reference case. Only a minor increase was observed in cases where a pumping material was present. The oxygen released by the Ceria SM during step 2 (temperature swing) was largely absorbed by the pumping material.

The leakage into the setup from the outside atmosphere contributed to the increase in p_{total} and $p(O_2)$ in steps 1, 2 and 3. During step 3, $p(O_2)$ dropped in all cases, but was significantly lower in all runs that employed a pumping material. Total pressure only increased due to leakage, indicating that only a small fraction of the remaining gas atmosphere inside the setup is oxygen. In contrast, in the reference case without a PM the total pressure

was reduced during step 3 since the remaining gas atmosphere contained a large fraction of oxygen. That oxygen was released by Ceria in step 2 and was now re-absorbed during cool-down of the Ceria. This re-oxidation was prohibited to a large fraction in cases where a PM was present during step 2 as most of the released oxygen is absorbed by the PM during that step. This effect led to the positive impact on the reduction extent of the SM and the values depicted previously in fig. 7.8.

Neglecting quantification of the actual $p(O_2)$ values, it was observed that lower equilibrium $p(O_2)$ values were reached at the end of step 4 in all cases a PM was employed. The best performing composition was $Ca_{0.9}Sr_{0.1}MnO_{3-\delta}$, with which the lowest $p(O_2)$ were reached. That trend supports the finding of high reduction extents when a PM is employed. Although the described results support the theoretical description of the thermochemical oxygen pumping process, findings related to the used oxygen sensor should be handled with care due to the previously described uncertainties of the sensor data.

Conclusively, the presented results in this chapter prove that the chosen perovskites function properly as thermochemical oxygen pumping materials in the tested process framework of separate and simultaneous temperature swing. Especially $Ca_{0.9}Sr_{0.1}MnO_{3-\delta}$ is promising to be an efficient material for thermochemical oxygen pumping systems. Reached reduction extents of $\Delta\delta = 0.0699(\pm 0.0110)$ were relatively high and even outperform reduction of ceria under vacuum (10^{-2} mbar) of a rotary vane pump. This offers possibilites for energy savings as no high vacuum is needed to reach sufficient reduction extents of the ceria. Energy intensive pumping systems are not required. Additionally, the parameters tuned in this study were limited. Process parameters were untouched. It is likely that adjustment of set temperatures of the pumping material and elimination of time restrictions due to feasible heating rates of the used furnaces can improve the performance even further. Increasing mass ratios of PM vs. SM could be another option to further increase performance of the oxygen pumping system.

The findings in chapter 5 pointed out that higher Sr-content led to improved kinetics and a more stable crystal structure combined with better reversibility of thermal expansion. This resulted in $Ca_{0.9}Sr_{0.1}MnO_{3-\delta}$ outperforming $CaMnO_{3-\delta}$ and $Ca_{0.95}Sr_{0.05}MnO_{3-\delta}$. Nonetheless, this can only be concluded for the used set of process parameters. For example, it is known that $Ca_{1-x}Sr_xMnO_{3-\delta}$ has a lower reduction enthalpy ΔH with increasing Sr-content. In this context that could lead to more oxygen uptake and release in the employed temperature swing window compared to pure $CaMnO_{3-\delta}$.[169]

Furthermore, the performance of the foam specimen compared to granules made from the very same composition is worth noting. Performance of foams and granules were

comparable in general. In the case of $Ca_{0.90}Sr_{0.1}MnO_{3-\delta}$ the foam even outperformed its granule counterpart. It showed that monolithic open porous structures such as foams prove to be a valid option in such thermochemical processes. as the demonstrated oxygen pumping. With $Ca_{0.90}Sr_{0.1}MnO_{3-\delta}$ foams, a $\Delta\delta = 0.0699(\pm 0.0110)$ of the ceria was reached without using high vacuum pumping or inert gas purging.

8. Summary and Conclusion

In the presented work open porous monolithic perovskite foams were demonstrated to function in thermochemical applications. The perovskite foams offer potential to be implemented in concentrated solar energy facilities in the future in context of TCES and TCOP. A complete materials development chain from material screening to synthesis and production as well as lab-scale demonstration of a representative application was carried out. Therein, $Ca_{1-x}Sr_xMnO_{3-\delta}$ perovskites were identified as the most promising perovskite material system for thermochemical oxygen pumping in the defined operational range of temperatures and pressures. The employed perovskites significantly increased the reduction extent of a reference ceria sample without the use of purge gas or high vacuum pumping. Additionally, $Ca_{1-x}Sr_xMnO_{3-\delta}$ exhibited outstanding thermal cyclability. A production process for open porous foams, made entirely from active perovskite material, was established. Perovskite foams were studied with respect to their thermodynamic properties and long-term stability. Mechanical sturdiness was demonstrated, making these foams viable to be used in a modular fashion in large-scale reactors.

Material compositions for screening tests were chosen based on the rationale that compositions should be suitable for convenient scale-up. In that sense abundance, costs and toxicity of containing elements were accounted for. Twelve compositions were identified for further screening. Thermodynamic characterisation of all compositions was carried out by means of TGA and DSC. Crystal structure and phase analysis was performed by XRD. Thermal expansion of bar samples was determined via dilatometry. All compositions were tested in an experimental lab-scale demonstrator for TCOP. Experiments revealed that the employment of a pumping material is able to increase the reduction extent of ceria significantly. $CaMnO_{3-\delta}$ was found to be the best performing composition under the chosen operational parameters, utilizing a temperature swing between 800 °C and 700 °C in the oxygen pumping reactor. $CaMnO_{3-\delta}$ increased the $\Delta\delta$ by almost 400% compared to the reference case by bringing $\Delta\delta$ from 0.0056 (±0.007) to 0.0276 (±0.009). It also showed fully reversible thermal expansion in dilatometry experiments under air, which made it suitable for foam production.

Furthermore, $CaMnO_{3-\delta}$ was among the compositions with the highest reduction extent and corresponding oxygen uptake and release in the temperature window relevant for high temperature TCES and endo- and exothermal heat effects. These heat effects were correlated to a reversible crystal phase transition from orthorhombic to cubic, which are exploitable in energy storage applications. Such chrystal phase transition generally augments the overall energy storage capacity of $CaMnO_{3-\delta}$. Hence, $CaMnO_{3-\delta}$was not only identified as a suitable composition for TCOP, but also for TCES. $CaMnO_{3-\delta}$ was chosen for the initial production and testing of monolithic open porous structures. Sr-substitution

on the A-site of $CaMnO_{3-\delta}$ was found to be beneficial to its structural stability, reducibility and cyclic thermal expansion and contraction behavior. Therefore, the compositional range of investigated foams was extended to $Ca_{1-x}Sr_xMnO_{3-\delta}$ with $x \in [0, 0.05, 0.1]$.

$CaMnO_{3-\delta}$ foam structures with a pore distribution of 30 ppi were shown to be mechanically sturdy, withstanding uniaxial pressure of up to 1 bar. Foams also did not degrade or deform with respect to their thermodynamic properties and optical appearance over the course of 46 cycles of heating and cooling between 300 °C and 1100 °C under air.

Kinetic analysis revealed that foam structures exhibit faster oxidation kinetics than pressed and sintered pellets. Beyond 600 °C, foam structures exhibited oxidation kinetics comparable to that of powdered samples, which remain superior in the temperature range between 400 °C and 600 °C. Shorter diffusion pathways and larger surface area appear to be beneficial in terms of reaction kinetics due to a rate limiting factor of involved surface reactions. The techniques applied within this work do not allow distinction between involved elementary reaction steps and the definition of a rate limiting factor. In order to examine how the macroscopic and microscopic structure impacts oxidation kinetics, further detailed studies need to be carried out. An important factor with respect to the structural integrity of foam specimens is full reversibility of thermal expansion and contraction. $CaMnO_{3-\delta}$ and its Sr-substituted variants showed fully reversible expansion and contraction over the course of 5 cycles between 300 °C and 1100 °C in air. In contrast, stoichiometric oxides, such as Co_3O_4 and mixed (Fe, Mn)-Oxides exhibited significant irreversible expansion during thermal cycling.

The fully reversible thermal expansion improves thermal cyclability of $Ca_{1-x}Sr_xMnO_{3-\delta}$, which is a great benefit over its stoichiometric competitors when monolithic structures are considered. It is especially important as such structures are foreseen to undergo a very high number of reduction-oxidation cycles during their actual large-scale cyclic operation. While under reduced $p(O_2)$, thermal expansion and contraction was not 100% reversible in $CaMnO_{3-\delta}$, small amounts of Sr-substitution (5% and 10%) were found to significantly reduce residual expansion after each cycle. Additionally, the establishment of a reliable production pathway of such structures made entirely from redox-active material is crucial to advance this technology and prove its functionality on an industrial scale level. $Ca_{1-x}Sr_xMnO_{3-\delta}$ are relatively cheap and easy to process and thereby allow fast scale-up of TCES and TCOP technology.

TCES utilizing perovskites is mostly thought to operate in air and at atmospheric or increased pressures. In contrast, TCOP requires the material to operate under reduced total pressures and $p(O_2)$. At reduced oxygen concentrations of 1%, $CaMnO_{3-\delta}$ revealed

substantial irreversible expansion as well as slow oxidation kinetics. Both effects could be correlated to an incomplete phase transition from the high temperature cubic phase to the orthorhombic phase during cool-down. Experiments showed that A-site substitution of Ca with Sr reduces the negative effects of a phase transition. That can be explained by the reduction of distortive stresses in the crystal lattice. The bigger size of the Sr^{2+}-ion compared to the Ca^{2+}-ion and correlated bond lengths cause relaxation of the stress that originates from distortion. Employing a 5% Sr-content on the A-site of the perovskite, re-oxidation characteristics were improved significantly. With 10% Sr-content, complete re-oxidation during cool-down was achieved, even at reduced $p(O_2)$. Foam structures of $Ca_{0.95}Sr_{0.05}MnO_{3-\delta}$ and $Ca_{0.9}Sr_{0.1}MnO_{3-\delta}$ were produced in order to be tested in the built TCOP demonstrator reactor. Thereby, it was proven that the established production process can be transferred to other perovskite compositions.

In an experimental demonstration of monolithic foam structures for TCOP, $CaMnO_{3-\delta}$, $Ca_{0.95}Sr_{0.05}MnO_{3-\delta}$ and $Ca_{0.9}Sr_{0.1}MnO_{3-\delta}$ were tested. Foams and granules, made from the same materials, were compared. While all compositions were able to increase the reduction extent of the reference water splitting material ceria, $Ca_{0.9}Sr_{0.1}MnO_{3-\delta}$ stood out with an almost 2-fold increase of cerias $\Delta\delta$. The reduction extent increased from 0.0442 to 0.0863 with a $Ca_{0.9}Sr_{0.1}MnO_{3-\delta}$ foam as PM compared to sole evacuation with a rotary vane pump. Results of the demonstration campaign show the potential of perovskite foams in TCOP, but need to be confirmed on a larger scale in further studies.

An experimental demonstration of monolithic structures for solar powered TCES and TCOP application has not yet been reported in literature. The presented work fills this gap by demonstrating the production utilization of sturdy and durable monolithic foam specimens made entirely from perovskites. In particular, $CaMnO_{3-\delta}$ and its Sr-substituted variants were shown to have potential for utilization in TCES and TCOP applications. Over the course of this work, insights on thermophysical properties of perovskite mixed metal oxides in the context to thermochemical applications were gained. The reported results add to the general understanding of this versatile but complex material class. The findings of this work lay out the ground to bring TCES and TCOP with monolithic open porous perovskite structures to a pre-industrial scale, further advance the technology and contribute to secure sustainable energy supply in the future.

A. Appendix

A.1. Material Screening

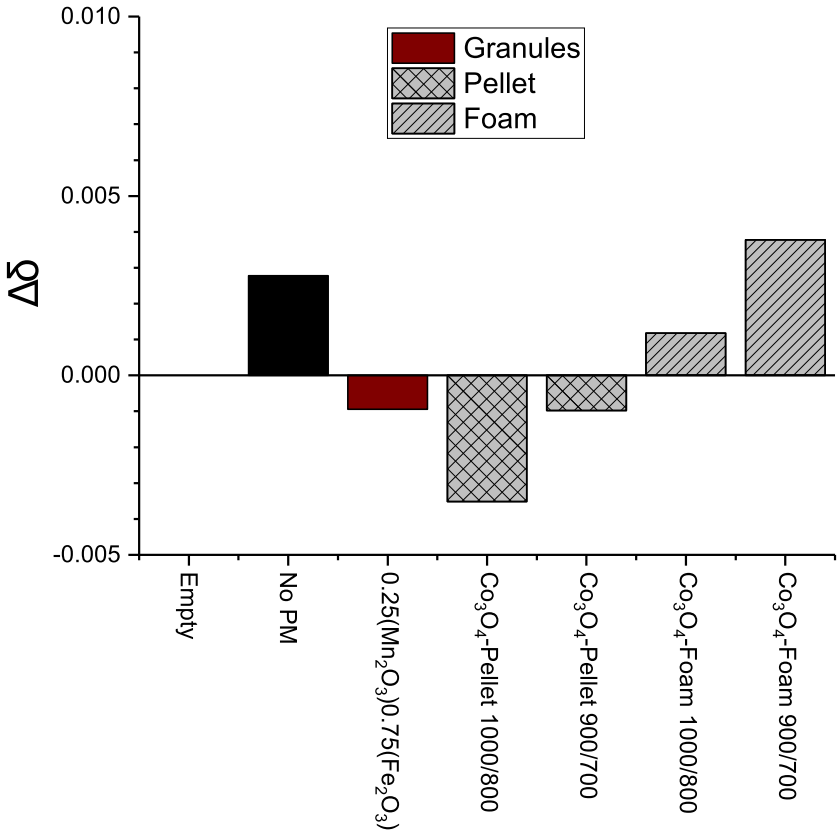

Fig. A.1.: Results of stoichiometric oxides in oxygen pumping experiments for material screening of chapter 4.

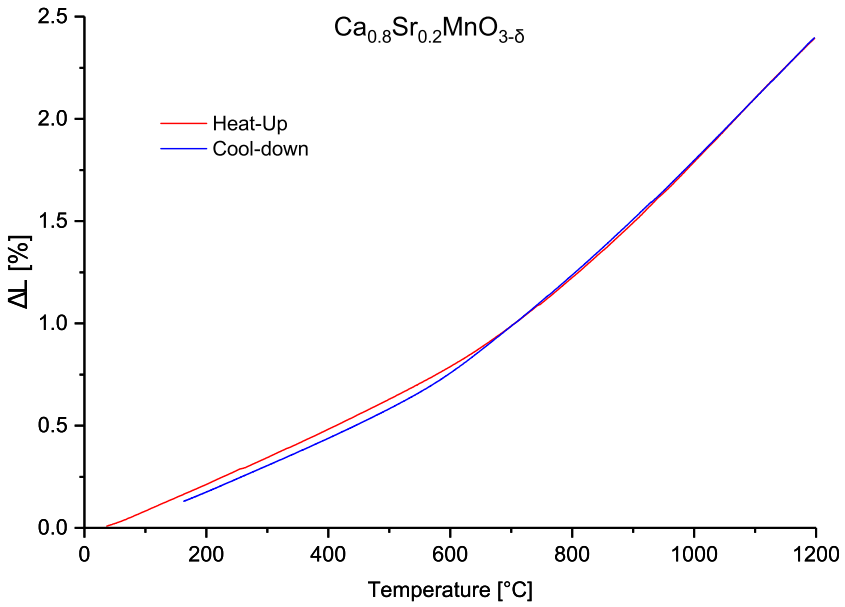

Fig. A.2.: Thermal expansion of $Ca_{0.8}Sr_{0.2}MnO_{3-\delta}$ as determined by contact dilatometry of a sintered bar specimen.

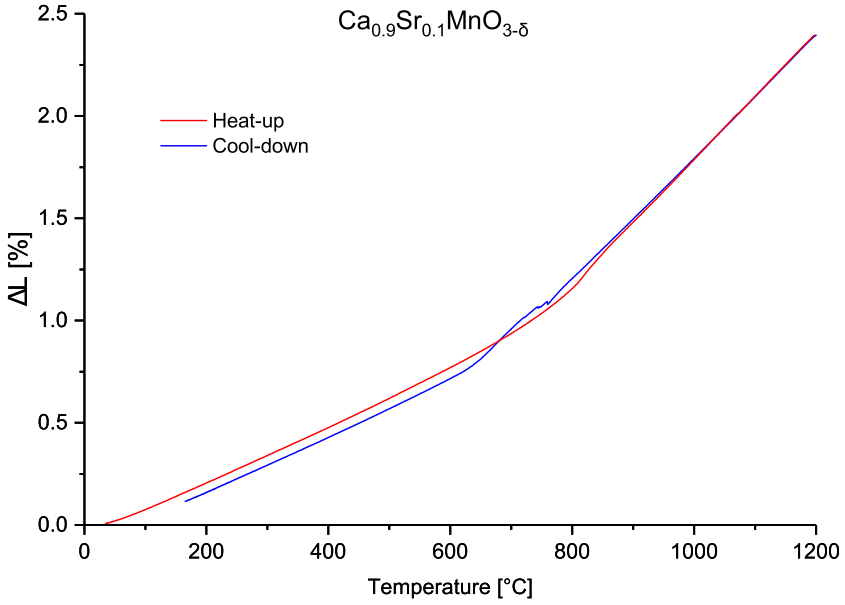

Fig. A.3.: Thermal expansion of $Ca_{0.9}Sr_{0.1}MnO_{3-\delta}$ as determined by contact dilatometry of a sintered bar specimen.

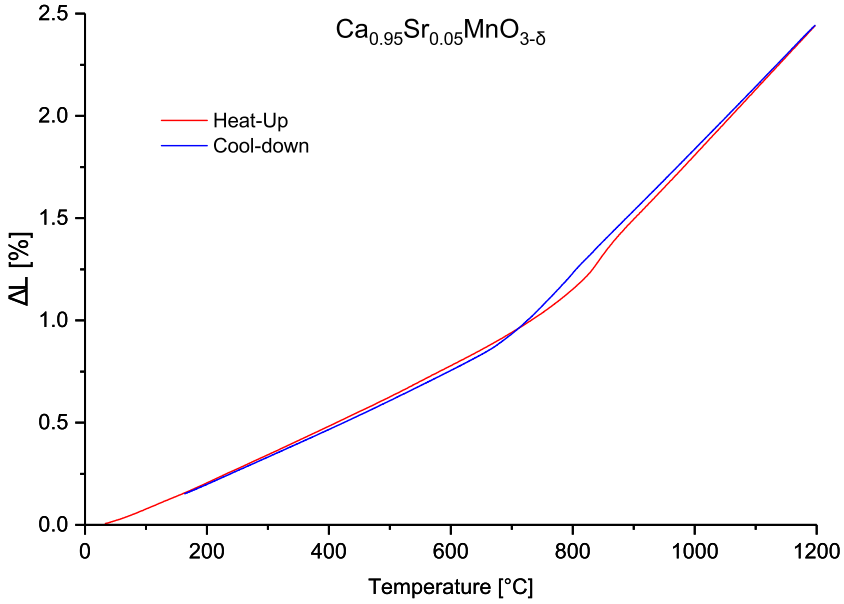

Fig. A.4.: Thermal expansion of $Ca_{0.95}Sr_{0.05}MnO_{3-\delta}$ as determined by contact dilatometry of a sintered bar specimen.

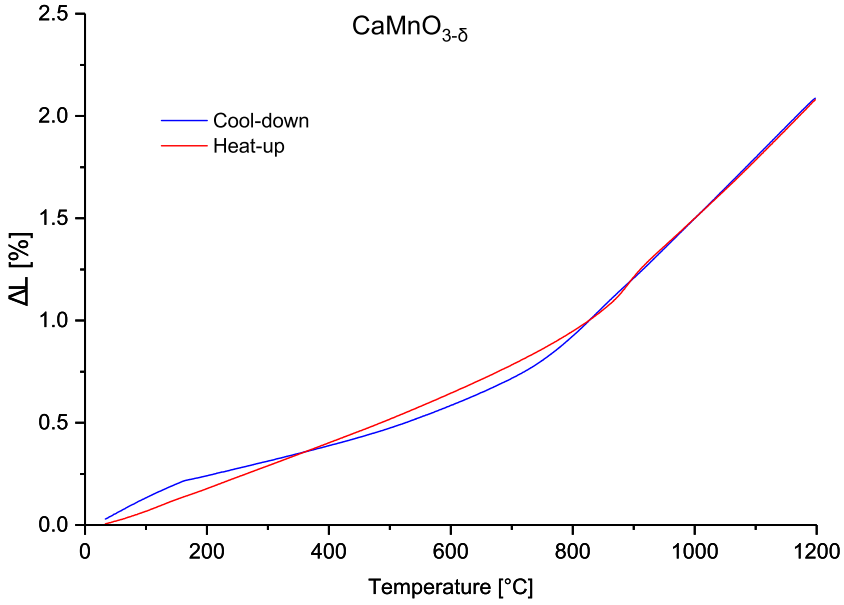

Fig. A.5.: Thermal expansion of $CaMnO_{3-\delta}$as determined by contact dilatometry of a sintered bar specimen.

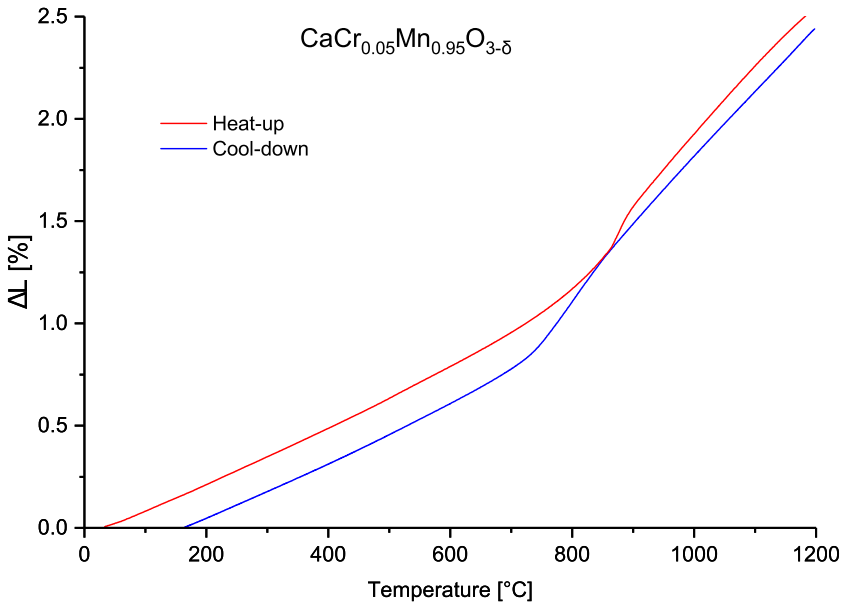

Fig. A.6.: Thermal expansion of $CaCr_{0.05}Mn_{0.95}O_{3-\delta}$ as determined by contact dilatometry of a sintered bar specimen.

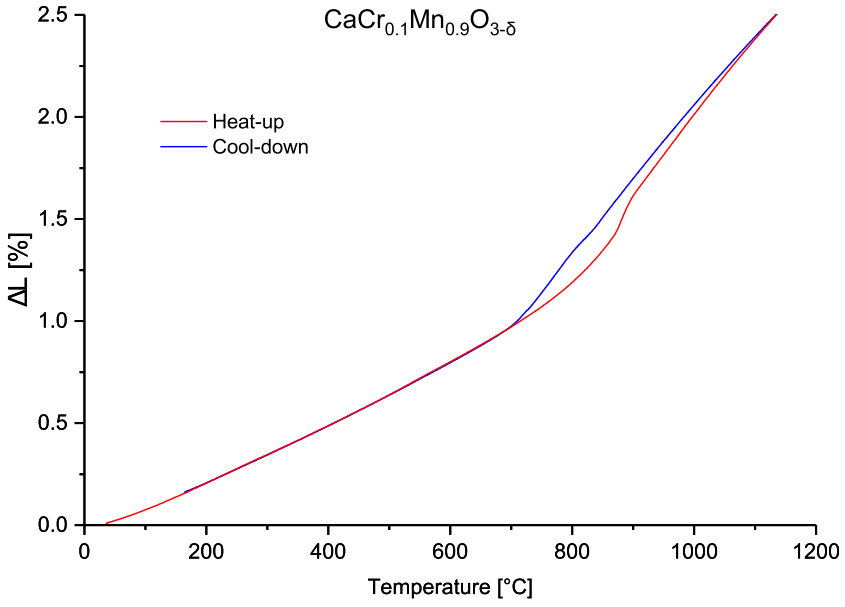

Fig. A.7.: Thermal expansion of $CaCr_{0.1}Mn_{0.9}O_{3-\delta}$ as determined by contact dilatometry of a sintered bar specimen.

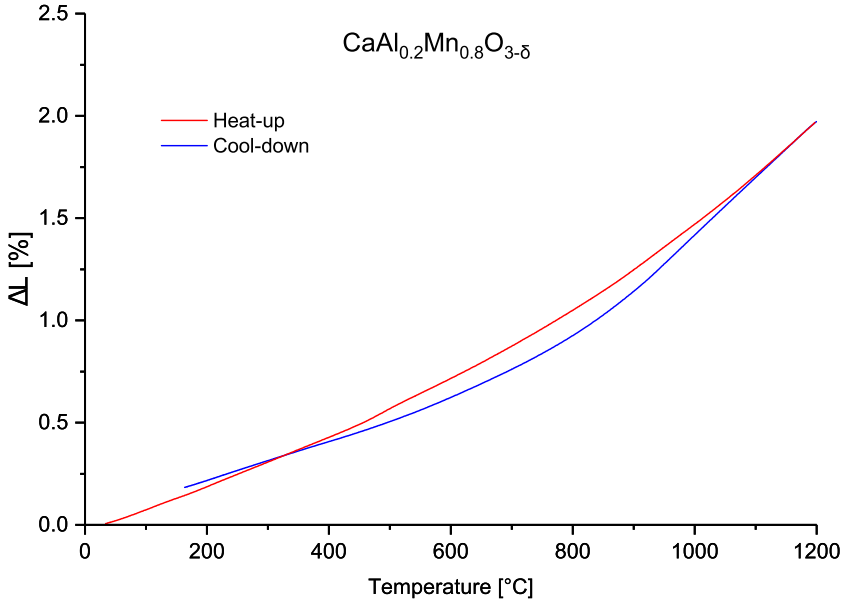

Fig. A.8.: Thermal expansion of $CaAl_{0.2}Mn_{0.8}O_{3-\delta}$ as determined by contact dilatometry of a sintered bar specimen.

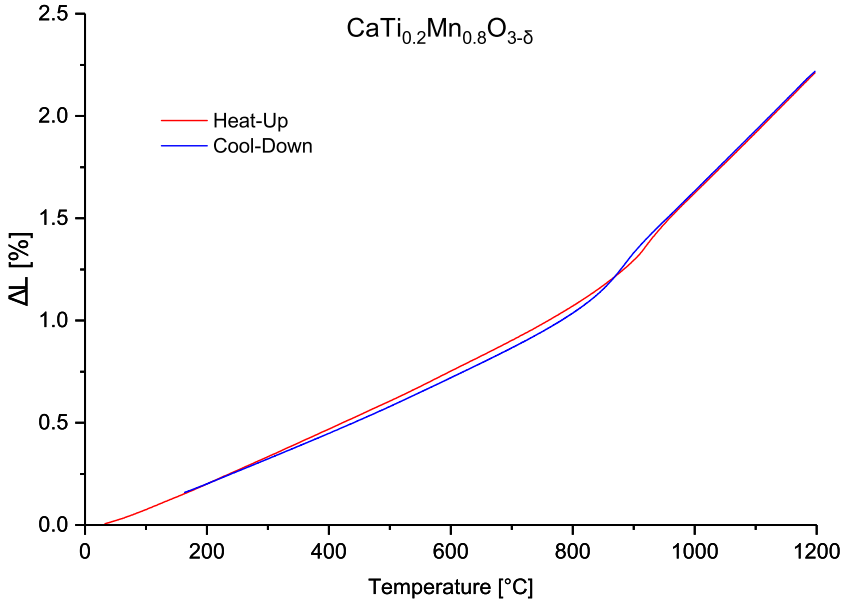

Fig. A.9.: Thermal expansion of $CaTi_{0.2}Mn_{0.8}O_{3-\delta}$ as determined by contact dilatometry of a sintered bar specimen.

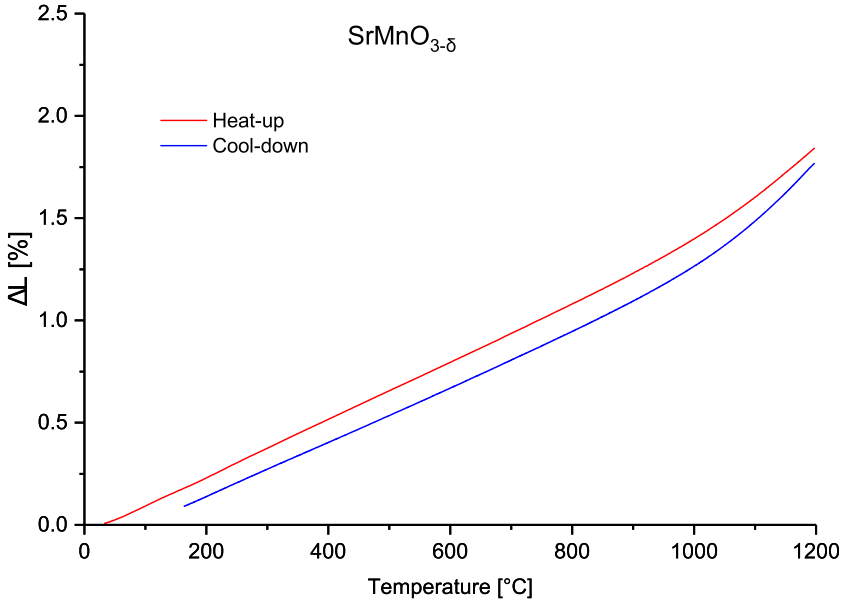

Fig. A.10.: Thermal expansion of $SrMnO_{3-\delta}$ as determined by contact dilatometry of a sintered bar specimen.

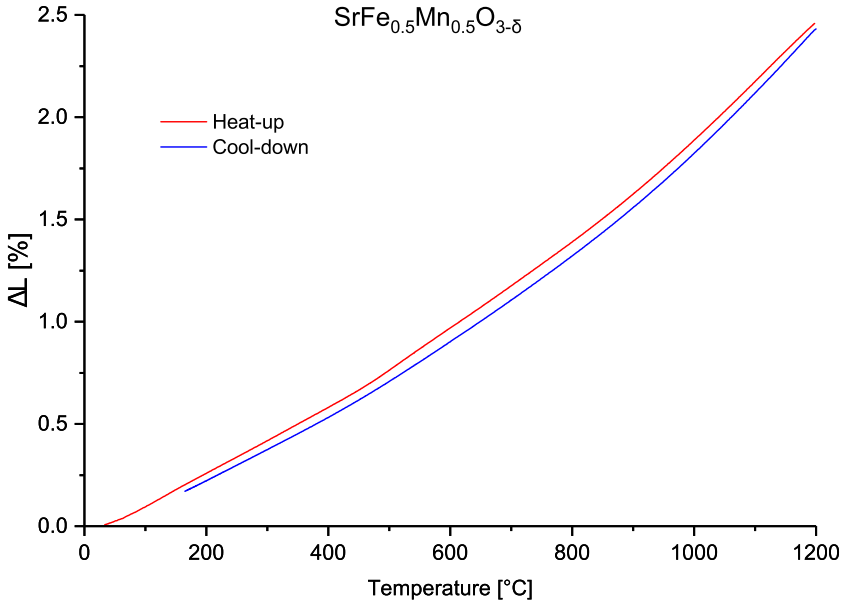

Fig. A.11.: Thermal expansion of $SrFe_{0.5}Mn_{0.5}O_{3-\delta}$ as determined by contact dilatometry of a sintered bar specimen.

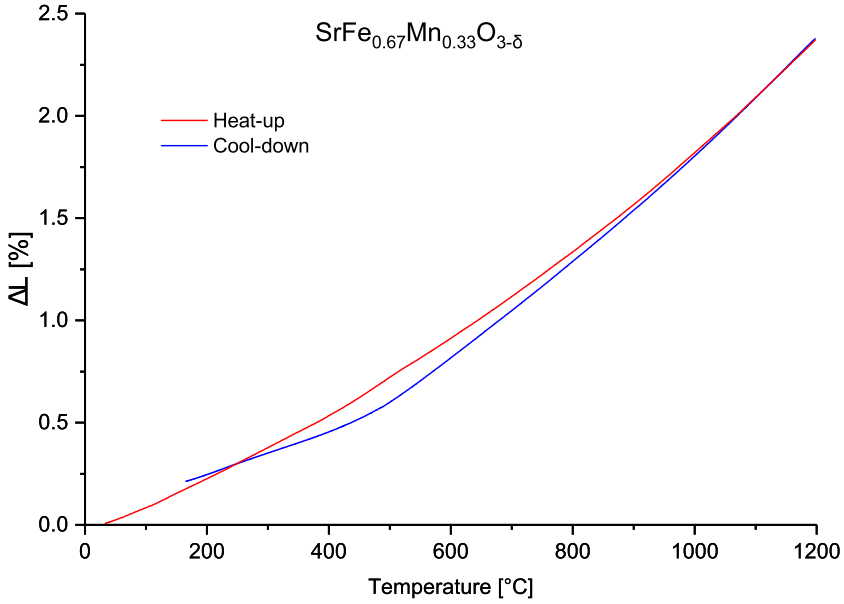

Fig. A.12.: Thermal expansion of $SrFe_{0.67}Mn_{0.33}O_{3-\delta}$ as determined by contact dilatometry of a sintered bar specimen.

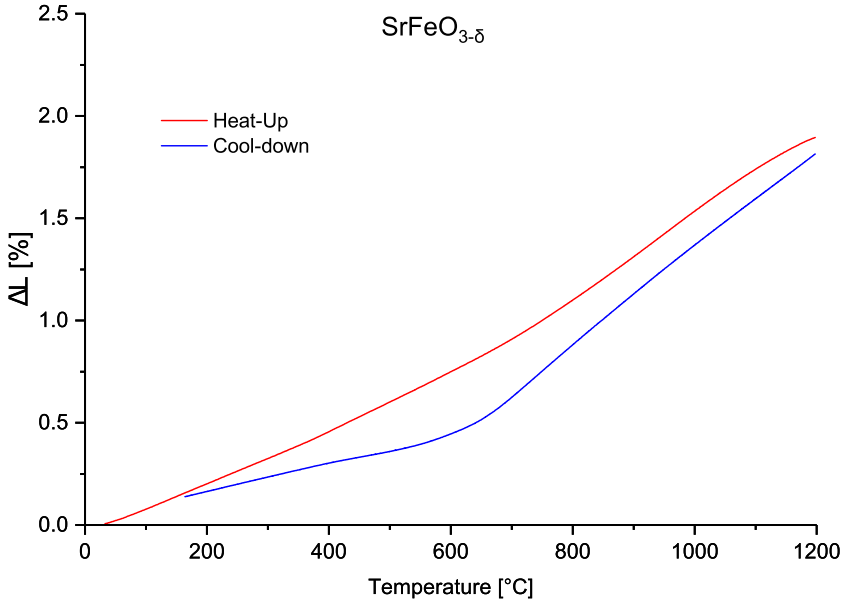

Fig. A.13.: Thermal expansion of $SrFeO_{3-\delta}$ as determined by contact dilatometry of a sintered bar specimen.

A.2. Kinetic Analysis

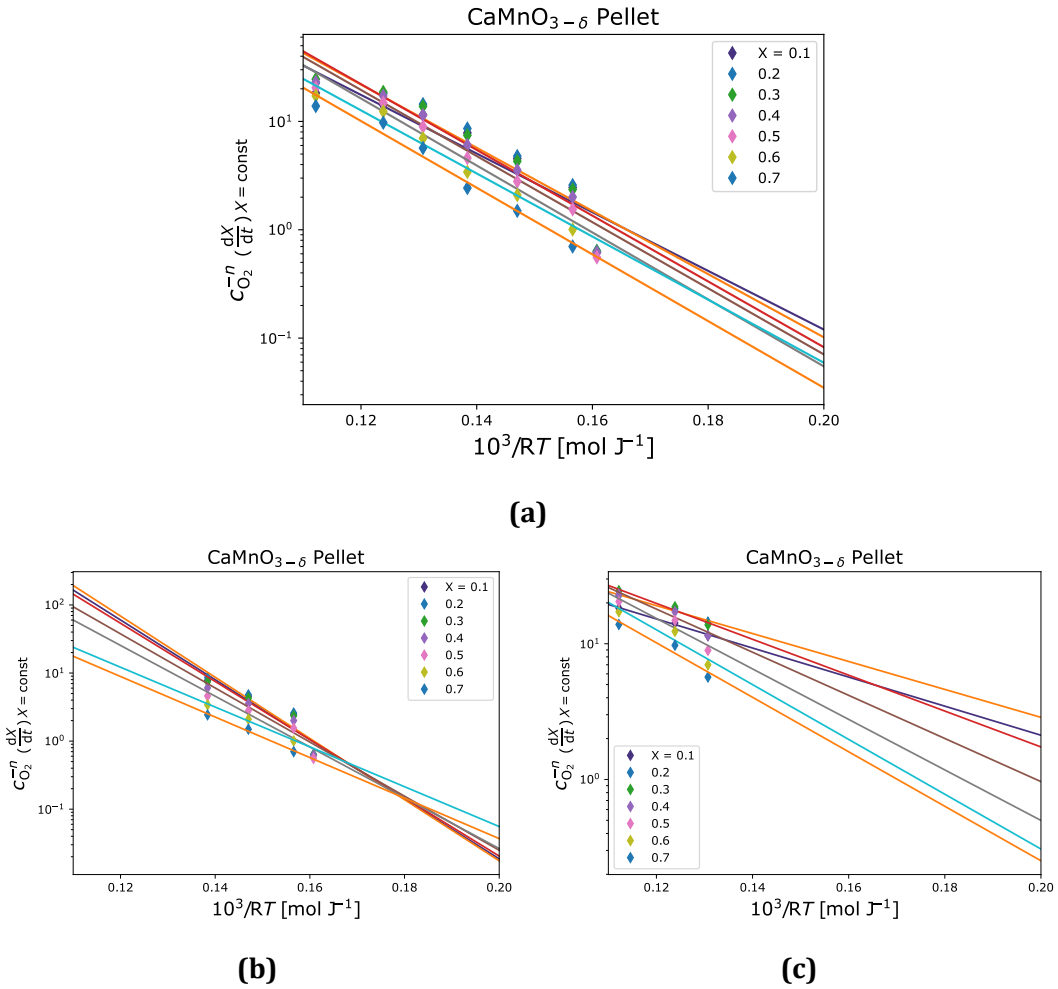

Fig. A.14.: Log-scale plotted $c_{O_2}^{-n}\left(\frac{dX}{dt}\right)_{X=\text{const.}}$ vs. $\frac{10^3}{RT}$ for $CaMnO_{3\text{-}\delta}$ pellet. The slope of each line is the activation energy -E_a. a) Plotted over complete temperature range. b) Only temperatures below 600 °C. c) Only temperatures above 600 °C.

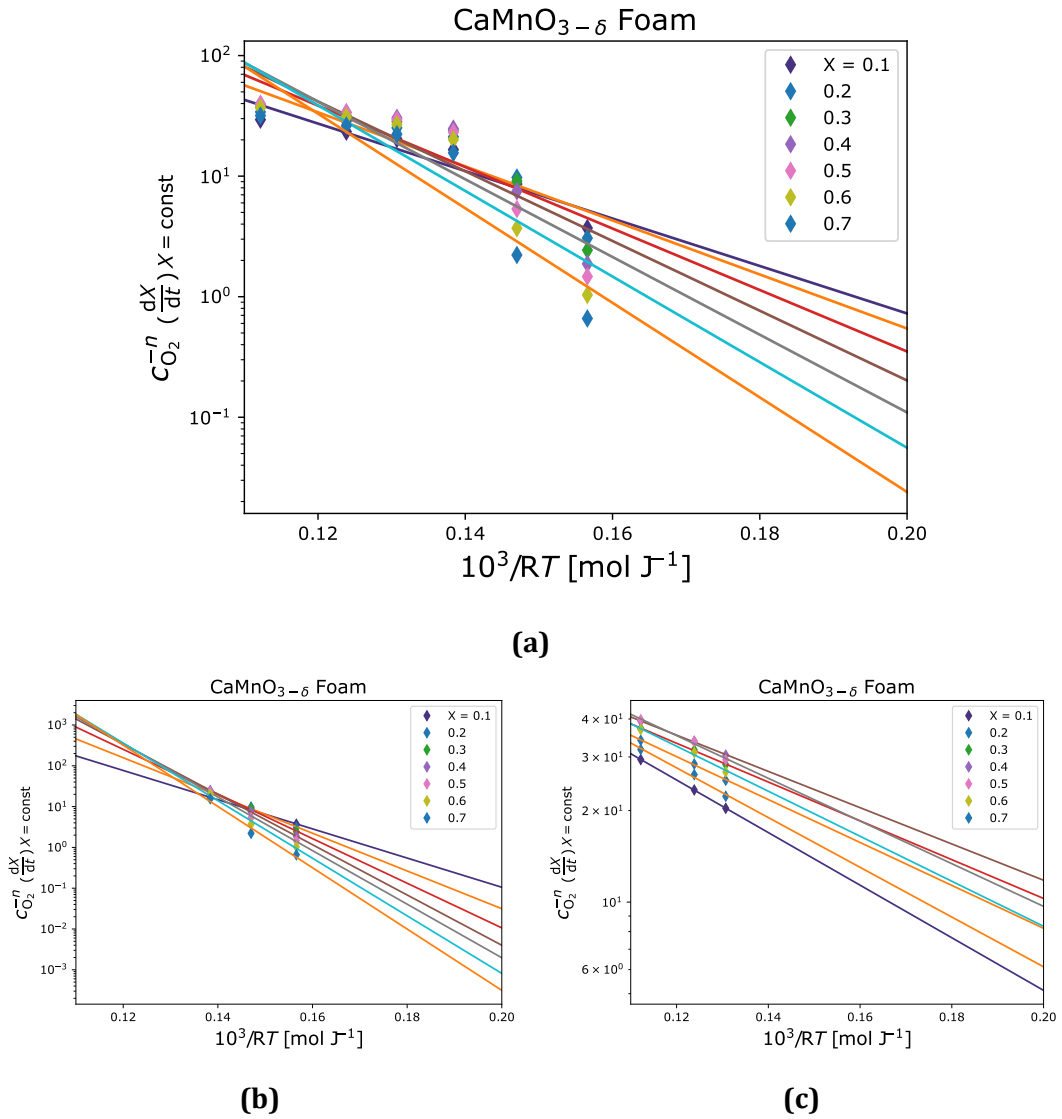

Fig. A.15.: Log-scale plotted $c_{O_2}^{-n}\left(\frac{dX}{dt}\right)_{X=\text{const.}}$ vs. $\frac{10^3}{RT}$ for $CaMnO_{3\text{-}\delta}$ 30 ppi foam. The slope of each line is the activation energy -E_a. a) Plotted over complete temperature range. b) Only temperatures below 600 °C. c) Only temperatures above 600 °C.

A.3. XRD of Quenched $CaMnO_{3-\delta}$

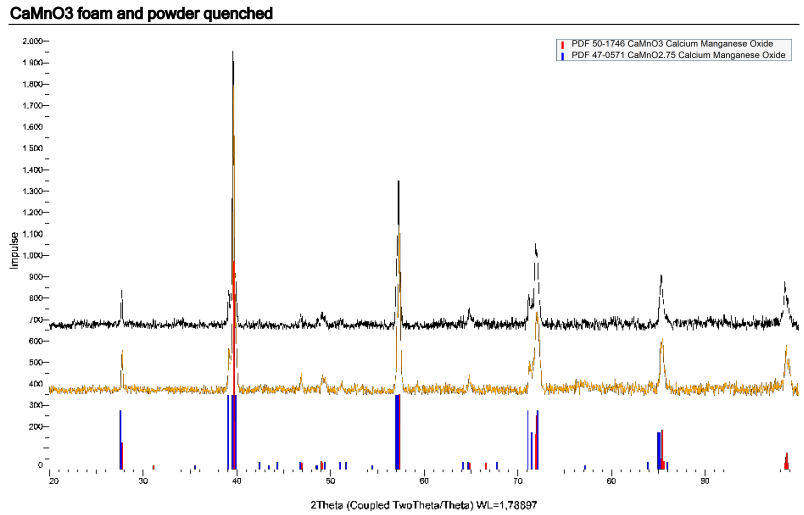

Fig. A.16.: XRD-patterns of $CaMnO_{3-\delta}$ samples quenched in Ar after reduction at 900 °C. Powder in black, foam in orange. It shows largely identical diffraction patterns for both samples with a mixture of reduced and partly oxidized orthorhombic $CaMnO_{3-\delta}$.

Bibliography

[1] Carbon Tracker Initiative. *The sky's the limit*. Apr. 21, 2021. URL: https://carbontracker.org/reports/the-skys-the-limit-solar-wind/ (visited on 07/13/2022).

[2] Navigant Energy Germany. *Energiewende in der Industrie - Potentiale und Wechselwirkungen im Energiesektor - Flexibilitätsstreckbrief der Eisen- und Stahlindustrie*. German. Bericht an das Bundesministerium für Wirtschaft und Energie. 2020. URL: https://www.bmwk.de/Redaktion/DE/Downloads/E/energiewende-in-der-industrie-ap2b-flexibilitaetssteckbrief-stahl.pdf?__blob=publicationFile&v=6 (visited on 03/01/2023).

[3] Manuel Romero and José González-Aguilar. "Solar thermal CSP technology". In: *WIREs Energy and Environment* 3.1 (2014), pp. 42–59. DOI: https://doi.org/10.1002/wene.79.

[4] Philipp Furler, Jonathan R. Scheffe, and Aldo Steinfeld. "Syngas production by simultaneous splitting of H2O and CO2via ceria redox reactions in a high-temperature solar reactor". In: *Energy Environ. Sci.* 5 (3 2012), pp. 6098–6103. DOI: 10.1039/C1EE02620H.

[5] Stefan Zoller, Erik Koepf, Dustin Nizamian, Marco Stephan, Adriano Patané, Philipp Haueter, Manuel Romero, José González-Aguilar, Dick Lieftink, Ellart de Wit, Stefan Brendelberger, Andreas Sizmann, and Aldo Steinfeld. "A solar tower fuel plant for the thermochemical production of kerosene from H2O and CO2". In: *Joule* 6.7 (2022), pp. 1606–1616. ISSN: 2542-4351. DOI: https://doi.org/10.1016/j.joule.2022.06.012.

[6] Adel A. Ismail and Detlef W. Bahnemann. "Photochemical splitting of water for hydrogen production by photocatalysis: A review". In: *Solar Energy Materials and Solar Cells* 128 (2014), pp. 85–101. ISSN: 0927-0248. DOI: https://doi.org/10.1016/j.solmat.2014.04.037.

[7] Catalina Hernández Moris, Maria Teresa Cerda Guevara, Alois Salmon, and Alvaro Lorca. "Comparison between Concentrated Solar Power and Gas-Based Generation in Terms of Economic and Flexibility-Related Aspects in Chile". In: *Energies* 14.4 (2021). ISSN: 1996-1073. DOI: 10.3390/en14041063.

[8] DLR, Institut of Technical Thermodynamics. *Trans-Mediterranean Interconnection for Concetrating Solar Power (TRANS-CSP)*. Project Report. 2006. URL: https://www.dlr.de/tt/Portaldata/41/Resources/dokumente/institut/system/projects/TRANS-CSP_Full_Report_Final.pdf (visited on 03/07/2023).

[9] IRENA. "Renewable Power Generation Costs in 2020". In: (). URL: https://irena.org/publications/2021/Jun/Renewable-Power-Costs-in-2020.

[10] https://www.energy.sener/project/central-receiver-plant-nooro-iii ; acessed 08.08.2022 SENER Energy.

[11] R.P. Merchán, M.J. Santos, A. Medina, and A. Calvo Hernández. "High temperature central tower plants for concentrated solar power: 2021 overview". In: *Renewable and Sustainable Energy Reviews* 155 (2022), p. 111828. ISSN: 1364-0321. DOI: https://doi.org/10.1016/j.rser.2021.111828.

[12] Kraftblock GmbH. Ed. by https://kraftblock.com/de/anwendungen/waste-heat.html. URL: https://kraftblock.com/de/anwendungen/waste-heat.html (visited on 03/21/2023).

[13] Daniel C. Stack, Daniel Curtis, and Charles Forsberg. "Performance of firebrick resistance-heated energy storage for industrial heat applications and round-trip electricity storage". In: *Applied Energy* 242 (2019), pp. 782–796. ISSN: 0306-2619. DOI: https://doi.org/10.1016/j.apenergy.2019.03.100.

[14] Souzana Lorentzou, Alexandra Zygogianni, Chrysoula Pagkoura, George Karagiannakis, Athanasios G. Konstandopoulos, Jan Peter Saeck, Stefan Breuer, Matthias Lange, Justin Lapp, Thomas Fend, Martin Roeb, Aurelio Jose Gonzalez, Alfonso Vidal Delgado, Jan Peter Brouwer, Robert C. Makkus, and Spyros J. Kiartzis. "HYDROSOL-PLANT: Structured redox reactors for H2 production from solar thermochemical H2O splitting". In: *AIP Conference Proceedings* 2033.1 (2018), p. 130010. DOI: 10.1063/1.5067144.

[15] Michael W. Gaultois, Taylor D. Sparks, Christopher K. H. Borg, Ram Seshadri, William D. Bonificio, and David R. Clarke. "Data-Driven Review of Thermoelectric Materials: Performance and Resource Considerations". In: *Chemistry of Materials* 25.15 (2013), pp. 2911–2920. DOI: 10.1021/cm400893e.

[16] Christos Agrafiotis, Mathias Pein, Dimitra Giasafaki, Stefania Tescari, Martin Roeb, and Christian Sattler. "Redox Oxides-Based Solar Thermochemistry and Its Materialization to Reactor/Heat Exchanger Concepts for Efficient Solar Energy Harvesting, Transformation and Storage". In: *Journal of Solar Energy Engineering* 141.2 (2019). DOI: 10.1115/1.4042226.

[17] Mathias Pein, Christos Agrafiotis, Josua Vieten, Dimitra Giasafaki, Stefan Brendelberger, Martin Roeb, and Christian Sattler. "Redox thermochemistry of Ca-Mn-based perovskites for oxygen atmosphere control in solar-thermochemical processes". In: *Solar Energy* 198 (Mar. 2020), pp. 612–622. DOI: 10.1016/j.solener.2020.01.088.

[18] Mathias Pein, Nicole Carina Neumann, Luke J. Venstrom, Josua Vieten, Martin Roeb, and Christian Sattler. "Two-step thermochemical electrolysis: An approach for green hydrogen production". In: *International Journal of Hydrogen Energy* 46.49 (2021), pp. 24909–24918. ISSN: 0360-3199. DOI: https://doi.org/10.1016/j.ijhydene.2021.05.036.

[19] Mathias Pein, Luca Matzel, Lamark de Oliveira, Gözde Alkan, Alexander Francke, Peter Mechnich, Christos Agrafiotis, Martin Roeb, and Christian Sattler. "Reticulated Porous Perovskite Structures for Thermochemical Solar Energy Storage". In: *Advanced Energy Materials* 2102882 (2022). ISSN: 1614-6832. DOI: https://doi.org/10.1002/aenm.202102882.

[20] Lena Klaas, Mathias Pein, Peter Mechnich, Alexander Francke, Dimitra Giasafaki, Dorottya Kriechbaumer, Christos Agrafiotis, Martin Roeb, and Christian Sattler. "Controlling thermal expansion and phase transitions in Ca1−xSrxMnO3−δ by Sr-content". In: *Physical Chemistry Chemical Physics* 24 (45 2022), pp. 27976–27988. DOI: 10.1039/D2CP04332G.

[21] Alfonso J. Carrillo, José González-Aguilar, Manuel Romero, and Juan M. Coronado. "Solar Energy on Demand: A Review on High Temperature Thermochemical Heat Storage Systems and Materials". In: *Chemical Reviews* 119.7 (2019), pp. 4777–4816. DOI: 10.1021/acs.chemrev.8b00315.

[22] S. Tescari, A. Singh, C. Agrafiotis, L. de Oliveira, S. Breuer, B. Schlögl-Knothe, M. Roeb, and C. Sattler. "Experimental evaluation of a pilot-scale thermochemical storage system for a concentrated solar power plant". In: *Applied Energy* 189 (2017), pp. 66–75. ISSN: 03062619. DOI: 10.1016/j.apenergy.2016.12.032.

[23] George Karagiannakis, Chrysoula Pagkoura, Eleftherios Halevas, Penelope Baltzopoulou, and Athanasios G. Konstandopoulos. "Cobalt/cobaltous oxide based honeycombs for thermochemical heat storage in future concentrated solar power installations: Multi-cyclic assessment and semi-quantitative heat effects estimations". In: *Solar Energy* 133 (2016), pp. 394–407. ISSN: 0038-092X. DOI: https://doi.org/10.1016/j.solener.2016.04.032.

[24] Chrysoula Pagkoura, George Karagiannakis, Alexandra Zygogianni, Souzana Lorentzou, Margaritis Kostoglou, Athanasios G. Konstandopoulos, Michael Rattenburry, and James W. Woodhead. "Cobalt oxide based structured bodies as redox thermochemical heat storage medium for future CSP plants". In: *Solar Energy* 108 (2014), pp. 146–163. ISSN: 0038-092X. DOI: https://doi.org/10.1016/j.solener.2014.06.034.

[25] Elisa Alonso, Alessandro Gallo, Carlos Pérez-Rábago, and Edward Fuentealba. "Thermodynamic study of CuO/Cu2O and Co3O4/CoO redox pairs for solar energy thermochemical storage". In: *AIP Conference Proceedings* 1734.1 (2016), p. 050004. DOI: 10.1063/1.4949102.

[26] A. J. Carrillo, D. Sastre, D. P. Serrano, P. Pizarro, and J. M. Coronado. "Revisiting the BaO2/BaO redox cycle for solar thermochemical energy storage". In: *Phys. Chem. Chem. Phys.* 18 (11 2016), pp. 8039–8048. DOI: 10.1039/C5CP07777J.

[27] Alfonso J. Carrillo, David P. Serrano, Patricia Pizarro, and Juan M. Coronado. "Improving the Thermochemical Energy Storage Performance of the Mn2O3/Mn3O4 Redox Couple by the Incorporation of Iron". In: *ChemSusChem* 8.11 (2015), pp. 1947–1954. DOI: https://doi.org/10.1002/cssc.201500148.

[28] B. Bulfin, J. Vieten, C. Agrafiotis, M. Roeb, and C. Sattler. "Applications and limitations of two step metal oxide thermochemical redox cycles; a review". In: *Journal of Materials Chemistry A* 5.36 (2017), pp. 18951–18966. DOI: 10.1039/c7ta05025a.

[29] R. Palumbo, J. Léde, O. Boutin, E. Elorza Ricart, A. Steinfeld, S. Möller, A. Weidenkaff, E.A. Fletcher, and J. Bielicki. "The production of Zn from ZnO in a high-temperature solar decomposition quench process—I. The scientific framework for the process". In: *Chemical Engineering Science* 53.14 (1998), pp. 2503–2517. ISSN: 0009-2509. DOI: https://doi.org/10.1016/S0009-2509(98)00063-3.

[30] A. Steinfeld. "Solar hydrogen production via a two-step water-splitting thermochemical cycle based on Zn/ZnO redox reactions". In: *International Journal of Hydrogen Energy* 27.6 (2002), pp. 611–619. ISSN: 0360-3199. DOI: https://doi.org/10.1016/S0360-3199(01)00177-X.

[31] A Weidenkaff, A.W Reller, A Wokaun, and A Steinfeld. "Thermogravimetric analysis of the ZnO/Zn water splitting cycle". In: *Thermochimica Acta* 359.1 (2000), pp. 69–75. ISSN: 0040-6031. DOI: https://doi.org/10.1016/S0040-6031(00)00508-6.

[32] F. Sibieude, M. Ducarroir, A. Tofighi, and J. Ambriz. “High temperature experiments with a solar furnace: The decomposition of Fe3O4, Mn3O4, CdO”. In: *International Journal of Hydrogen Energy* 7.1 (1982), pp. 79–88. ISSN: 0360-3199. DOI: https://doi.org/10.1016/0360-3199(82)90209-9.

[33] A. Steinfeld, S. Sanders, and R. Palumbo. “DESIGN ASPECTS OF SOLAR THERMOCHEMICAL ENGINEERING—A CASE STUDY: TWO-STEP WATER-SPLITTING CYCLE USING THE Fe3O4/FeO REDOX SYSTEM”. In: *Solar Energy* 65.1 (1999), pp. 43–53. ISSN: 0038-092X. DOI: https://doi.org/10.1016/S0038-092X(98)00092-9.

[34] Patrice Charvin, Stéphane Abanades, Gilles Flamant, and Florent Lemort. “Two-step water splitting thermochemical cycle based on iron oxide redox pair for solar hydrogen production”. In: *Energy* 32.7 (2007), pp. 1124–1133. ISSN: 0360-5442. DOI: https://doi.org/10.1016/j.energy.2006.07.023.

[35] Stéphane Abanades, Patrice Charvin, Florent Lemont, and Gilles Flamant. “Novel two-step SnO2/SnO water-splitting cycle for solar thermochemical production of hydrogen”. In: *International Journal of Hydrogen Energy* 33.21 (2008), pp. 6021–6030. ISSN: 0360-3199. DOI: https://doi.org/10.1016/j.ijhydene.2008.05.042.

[36] Tina Block and Martin Schmücker. “Metal oxides for thermochemical energy storage: A comparison of several metal oxide systems”. In: *Solar Energy* 126 (2016), pp. 195–207. ISSN: 0038-092X. DOI: https://doi.org/10.1016/j.solener.2015.12.032.

[37] William C. Chueh and Sossina M. Haile. “Ceria as a Thermochemical Reaction Medium for Selectively Generating Syngas or Methane from H2O and CO2”. In: *ChemSusChem* 2.8 (2009), pp. 735–739. DOI: https://doi.org/10.1002/cssc.200900138.

[38] Youjun Lu, Liya Zhu, Christos Agrafiotis, Josua Vieten, Martin Roeb, and Christian Sattler. “Solar fuels production: Two-step thermochemical cycles with cerium-based oxides”. In: *Progress in Energy and Combustion Science* 75 (2019), p. 100785. ISSN: 0360-1285. DOI: https://doi.org/10.1016/j.pecs.2019.100785.

[39] M. Takacs, M. Hoes, M. Caduff, T. Cooper, J.R. Scheffe, and A. Steinfeld. “Oxygen nonstoichiometry, defect equilibria, and thermodynamic characterization of LaMnO3 perovskites with Ca/Sr A-site and Al B-site doping”. In: *Acta Materialia*

103 (2016), pp. 700–710. ISSN: 1359-6454. DOI: https://doi.org/10.1016/j.actamat.2015.10.026.

[40] M. Teresa Azcondo, María Orfila, Javier Marugán, Raúl Sanz, Alvaro Muñoz-Noval, Eduardo Salas-Colera, Clemens Ritter, Flaviano García-Alvarado, and Ulises Amador. "Novel Perovskite Materials for Thermal Water Splitting at Moderate Temperature". In: *ChemSusChem* 12.17 (2019), pp. 4029–4037. DOI: https://doi.org/10.1002/cssc.201901484.

[41] Aurelio González-Pardo, Thorsten Denk, and Alfonso Vidal. "Lessons learnt during the construction and start-up of 3 cylindrical cavity-receivers facility integrated in a 750 kW solar tower plant for hydrogen production". In: *AIP Conference Proceedings* 2303.1 (2020), p. 170008. DOI: 10.1063/5.0029579.

[42] Kent J. Warren, Justin T. Tran, and Alan W. Weimer. "A thermochemical study of iron aluminate-based materials: a preferred class for isothermal water splitting". In: *Energy Environ. Sci.* (2022). DOI: 10.1039/D1EE02679H.

[43] Yogesh Manoharan, Seyed Ehsan Hosseini, Brayden Butler, Hisham Alzhahrani, Bhi Thi Fou Senior, Turaj Ashuri, and John Krohn. "Hydrogen Fuel Cell Vehicles; Current Status and Future Prospect". In: *Applied Sciences* 9.11 (2019). ISSN: 2076-3417. DOI: 10.3390/app9112296.

[44] Abhinav Bhaskar, Mohsen Assadi, and Homam Nikpey Somehsaraei. "Decarbonization of the Iron and Steel Industry with Direct Reduction of Iron Ore with Green Hydrogen". In: *Energies* 13.3 (2020). ISSN: 1996-1073. DOI: 10.3390/en13030758.

[45] Franz Fischer and Hans Tropsch. "Über die direkte Synthese von Erdöl-Kohlen/-wasserstoffen bei gewöhnlichem Druck. (Erste Mitteilung)". In: *Berichte der deutschen chemischen Gesellschaft (A and B Series)* 59.4 (1926), pp. 830–831. DOI: https://doi.org/10.1002/cber.19260590442.

[46] Mark E Dry. "The Fischer–Tropsch process: 1950–2000". In: *Catalysis Today* 71.3 (2002). Fischer-Tropsch synthesis on the eve of the XXI Century, pp. 227–241. ISSN: 0920-5861. DOI: https://doi.org/10.1016/S0920-5861(01)00453-9.

[47] Bright Appiah Adu-Gyamfi and Clara Good. "Electric aviation: A review of concepts and enabling technologies". In: *Transportation Engineering* 9 (2022), p. 100134. ISSN: 2666-691X. DOI: https://doi.org/10.1016/j.treng.2022.100134.

[48] Lilly Moua, Julio Roa, Yuanyuan Xie, and Dereck Maxwell. "Critical Review of Advancements and Challenges of All-Electric Aviation". In: *International Conference on Transportation and Development 2020*, pp. 48–59. DOI: 10.1061/9780784483138.005.

[49] Edouard González-Roubaud, David Pérez-Osorio, and Cristina Prieto. "Review of commercial thermal energy storage in concentrated solar power plants: Steam vs. molten salts". In: *Renewable and Sustainable Energy Reviews* 80 (2017), pp. 133–148. ISSN: 1364-0321. DOI: https://doi.org/10.1016/j.rser.2017.05.084.

[50] Thomas Bauer, Nicole Pfleger, Nils Breidenbach, Markus Eck, Doerte Laing, and Stefanie Kaesche. "Material aspects of Solar Salt for sensible heat storage". In: *Applied Energy* 111 (2013), pp. 1114–1119. ISSN: 0306-2619. DOI: https://doi.org/10.1016/j.apenergy.2013.04.072.

[51] T. Baumann and S. Zunft. "Properties of granular materials as heat transfer and storage medium in CSP application". In: *Solar Energy Materials and Solar Cells* 143 (2015), pp. 38–47. ISSN: 0927-0248. DOI: https://doi.org/10.1016/j.solmat.2015.06.037.

[52] R. Tiskatine, A. Eddemani, L. Gourdo, B. Abnay, A. Ihlal, A. Aharoune, and L. Bouirden. "Experimental evaluation of thermo-mechanical performances of candidate rocks for use in high temperature thermal storage". In: *Applied Energy* 171 (2016), pp. 243–255. ISSN: 0306-2619. DOI: https://doi.org/10.1016/j.apenergy.2016.03.061.

[53] N. Siegel, M. Gross, C. Ho, T. Phan, and J. Yuan. "Physical Properties of Solid Particle Thermal Energy Storage Media for Concentrating Solar Power Applications". In: *Energy Procedia* 49 (2014). Proceedings of the SolarPACES 2013 International Conference, pp. 1015–1023. ISSN: 1876-6102. DOI: https://doi.org/10.1016/j.egypro.2014.03.109.

[54] Alejandro Calderón, Anabel Palacios, Camila Barreneche, Mercè Segarra, Cristina Prieto, Alfonso Rodriguez-Sanchez, and A. Inés Fernández. "High temperature systems using solid particles as TES and HTF material: A review". In: *Applied Energy* 213 (2018), pp. 100–111. ISSN: 0306-2619. DOI: https://doi.org/10.1016/j.apenergy.2017.12.107.

[55] Christos Agrafiotis, Martin Roeb, Martin Schmücker, and Christian Sattler. "Exploitation of thermochemical cycles based on solid oxide redox systems for thermochemical storage of solar heat. Part 1: Testing of cobalt oxide-based powders". In: *Solar Energy* 102 (2014), pp. 189–211. ISSN: 0038092X. DOI: 10.1016/j.solener.2013.12.032.

[56] Christos Agrafiotis, Stefania Tescari, Martin Roeb, Martin Schmücker, and Christian Sattler. "Exploitation of thermochemical cycles based on solid oxide redox systems for thermochemical storage of solar heat. Part 3: Cobalt oxide monolithic porous structures as integrated thermochemical reactors/heat exchangers". In: *Solar Energy* 114 (2015), pp. 459–475. ISSN: 0038092X. DOI: 10.1016/j.solener.2014.12.037.

[57] Alfonso J. Carrillo, David P. Serrano, Patricia Pizarro, and Juan M. Coronado. "Understanding Redox Kinetics of Iron-Doped Manganese Oxides for High Temperature Thermochemical Energy Storage". In: *The Journal of Physical Chemistry C* 120.49 (2016), pp. 27800–27812. ISSN: 1932-7447 1932-7455. DOI: 10.1021/acs.jpcc.6b08708.

[58] Laurie André, Stéphane Abanades, and Laurent Cassayre. "Mixed Metal Oxide Systems Applied to Thermochemical Storage of Solar Energy: Benefits of Secondary Metal Addition in Co and Mn Oxides and Contribution of Thermodynamics". In: *Applied Sciences* 8.12 (2018). ISSN: 2076-3417. DOI: 10.3390/app8122618.

[59] Jarrod V. Crum, Brian J. Riley, and John D. Vienna. "Binary Phase Diagram of the Manganese Oxide–Iron Oxide System". In: *Journal of the American Ceramic Society* 92.10 (2009), pp. 2378–2384. DOI: https://doi.org/10.1111/j.1551-2916.2009.03230.x.

[60] Sean M. Babiniec, Eric N. Coker, James E. Miller, and Andrea Ambrosini. "Investigation of LaxSr1-xCoyM1-yO3-δ(M=Mn, Fe) perovskite materials as thermochemical energy storage media". In: *Solar Energy* 118 (2015), pp. 451–459. ISSN: 0038-092X. DOI: https://doi.org/10.1016/j.solener.2015.05.040.

[61] PROJECT STAFF General Atomics. "Thermochemical heat storage for concentrated solar power". In: (Oct. 2011). DOI: 10.2172/1039304.

[62] B. Bulfin, F. Call, M. Lange, O. Lübben, C. Sattler, R. Pitz-Paal, and I. V. Shvets. "Thermodynamics of CeO2 Thermochemical Fuel Production". In: *Energy & Fuels* 29.2 (2015), pp. 1001–1009. DOI: 10.1021/ef5019912.

[63] Ivan Ermanoski. "Cascading pressure thermal reduction for efficient solar fuel production". In: *International Journal of Hydrogen Energy* 39.25 (2014), pp. 13114–13117. ISSN: 0360-3199. DOI: https://doi.org/10.1016/j.ijhydene.2014.06.143.

[64] J. Lapp, J.H. Davidson, and W. Lipiński. "Efficiency of two-step solar thermochemical non-stoichiometric redox cycles with heat recovery". In: *Energy* 37.1 (2012). 7th Biennial International Workshop "Advances in Energy Studies", pp. 591–600. ISSN: 0360-5442. DOI: https://doi.org/10.1016/j.energy.2011.10.045.

[65] Stefan Brendelberger, Henrik von Storch, Brendan Bulfin, and Christian Sattler. "Vacuum pumping options for application in solar thermochemical redox cycles – Assessment of mechanical-, jet- and thermochemical pumping systems". In: *Solar Energy* 141 (2017), pp. 91–102. ISSN: 0038092X. DOI: 10.1016/j.solener.2016.11.023.

[66] Stefan Brendelberger, Josua Vieten, Muralimohan Juttu Vidyasagar, Martin Roeb, and Christian Sattler. "Demonstration of thermochemical oxygen pumping for atmosphere control in reduction reactions". In: *Solar Energy* 170 (2018), pp. 273–279. ISSN: 0038092X. DOI: 10.1016/j.solener.2018.05.063.

[67] Ivan Ermanoski and Ellen B. Stechel. "Thermally-driven adsorption/desorption cycle for oxygen pumping in thermochemical fuel production". In: *Solar Energy* 198 (2020), pp. 578–585. ISSN: 0038-092X. DOI: https://doi.org/10.1016/j.solener.2020.01.050.

[68] Brian A. Rohr, Aayush R. Singh, and Jens K. Nørskov. "A theoretical explanation of the effect of oxygen poisoning on industrial Haber-Bosch catalysts". In: *Journal of Catalysis* 372 (2019), pp. 33–38. ISSN: 0021-9517. DOI: https://doi.org/10.1016/j.jcat.2019.01.042.

[69] John Humphreys, Rong Lan, Shigang Chen, and Shanwen Tao. "Improved stability and activity of Fe-based catalysts through strong metal support interactions due to extrinsic oxygen vacancies in Ce0.8Sm0.2O2−δ for the efficient synthesis of ammonia". In: *J. Mater. Chem. A* 8 (32 2020), pp. 16676–16689. DOI: 10.1039/D0TA05238H.

[70] Francesco Baldi, Alain Azzi, and François Maréchal. "From renewable energy to ship fuel: ammonia as an energy vector and mean for energy storage". In: *29th European Symposium on Computer Aided Process Engineering*. Ed. by Anton A. Kiss,

Edwin Zondervan, Richard Lakerveld, and Leyla Özkan. Vol. 46. Computer Aided Chemical Engineering. Elsevier, 2019, pp. 1747–1752. DOI: https://doi.org/10.1016/B978-0-12-818634-3.50292-7.

[71] Kyunghwa Kim, Gilltae Roh, Wook Kim, and Kangwoo Chun. "A Preliminary Study on an Alternative Ship Propulsion System Fueled by Ammonia: Environmental and Economic Assessments". In: *Journal of Marine Science and Engineering* 8.3 (2020). ISSN: 2077-1312. DOI: 10.3390/jmse8030183.

[72] Jan Willem Erisman, Mark A. Sutton, James Galloway, Zbigniew Klimont, and Wilfried Winiwarter. "How a century of ammonia synthesis changed the world". In: *Nature Geoscience* 1.10 (Sept. 2008), pp. 636–639. DOI: 10.1038/ngeo325.

[73] Dorottya Guban, Brendan Bulfin, Josua Vieten, Martin Roeb, and Christian Sattler. "Sustainable production of ammonia using solar-thermochemical redox cycles". In: *22. Kölner Sonnenkolloquium (poster presentation) at DLR* (2018). DLR. Cologne, Germany, 2018. URL: https://elib.dlr.de/132721/.

[74] Miriam Ezbiri, Kyle M. Allen, Maria E. Gàlvez, Ronald Michalsky, and Aldo Steinfeld. "Design Principles of Perovskites for Thermochemical Oxygen Separation". In: *ChemSusChem* 8.11 (2015), pp. 1966–1971. DOI: https://doi.org/10.1002/cssc.201500239.

[75] J. Vieten, B. Bulfin, F. Call, M. Lange, M. Schmücker, A. Francke, M. Roeb, and C. Sattler. "Perovskite oxides for application in thermochemical air separation and oxygen storage". In: *Journal of Materials Chemistry A* 4.35 (2016), pp. 13652–13659. DOI: 10.1039/c6ta04867f.

[76] Josua Vieten, Brendan Bulfin, David E. Starr, Atsushi Hariki, Frank M. F. de Groot, Anahita Azarpira, Carolin Zachäus, Michael Hävecker, Katarzyna Skorupska, Nicole Knoblauch, Martin Schmücker, Martin Roeb, and Christian Sattler. "Redox Behavior of Solid Solutions in the SrFe1-x Cux O3-δ System for Application in Thermochemical Oxygen Storage and Air Separation". In: *Energy Technology* 7.1 (Dec. 2018), pp. 131–139. DOI: 10.1002/ente.201800554.

[77] Josua Vieten, Brendan Bulfin, Patrick Huck, Matthew Horton, Dorottya Guban, Liya Zhu, Youjun Lu, Kristin A. Persson, Martin Roeb, and Christian Sattler. "Materials design of perovskite solid solutions for thermochemical applications". In: *Energy Environ. Sci.* 12 (4 2019), pp. 1369–1384. DOI: 10.1039/C9EE00085B.

[78] Josua Vieten. "Perovskite Materials Design for Two-Step SolarThermochemical Redox Cycles". PhD thesis. Technische Universität Dresden, May 2019. URL: https://elib.dlr.de/127377/.

[79] Josua Vieten, Luke Venstrom, Mathias Pein, Martin Roeb, and Christian Sattler. "Verfahren und Apparatur zur elektrochemisch unterstützten thermochemischen Spaltung von Wasser und Kohlendioxid". DE102020110633A1. 2021.

[80] A. Lidor, T. Fend, M. Roeb, and C. Sattler. "High performance solar receiver–reactor for hydrogen generation". In: *Renewable Energy* 179 (2021), pp. 1217–1232. ISSN: 0960-1481. DOI: https://doi.org/10.1016/j.renene.2021.07.089.

[81] C. Agrafiotis, M. Roeb, A.G. Konstandopoulos, L. Nalbandian, V.T. Zaspalis, C. Sattler, P. Stobbe, and A.M. Steele. "Solar water splitting for hydrogen production with monolithic reactors". In: *Solar Energy* 79.4 (2005). Environmental Applications of Solar Energy, pp. 409–421. ISSN: 0038-092X. DOI: https://doi.org/10.1016/j.solener.2005.02.026.

[82] Stefan Brendelberger, Philipp Holzemer-Zerhusen, Estefania Vega Puga, Martin Roeb, and Christian Sattler. "Study of a new receiver-reactor cavity system with multiple mobile redox units for solar thermochemical water splitting". In: *Solar Energy* (2021). URL: https://elib.dlr.de/146072/.

[83] Alfonso Vidal, Aurelio Gonzalez, and Thorsten Denk. "A 100 kW cavity-receiver reactor with an integrated two-step thermochemical cycle: Thermal performance under solar transients". In: *Renewable Energy* 153 (2020), pp. 270–279. ISSN: 0960-1481. DOI: https://doi.org/10.1016/j.renene.2020.01.146.

[84] M. Neises, S. Tescari, L. de Oliveira, M. Roeb, C. Sattler, and B. Wong. "Solar-heated rotary kiln for thermochemical energy storage". In: *Solar Energy* 86.10 (2012), pp. 3040–3048. ISSN: 0038-092X. DOI: https://doi.org/10.1016/j.solener.2012.07.012.

[85] Gkiokchan Moumin. "Solar treatment of cohesive particles in a rotary kiln and role of mixing". PhD thesis. TU Dresden, 2021. URL: https://elib.dlr.de/148567/.

[86] *Upscaling, Manufacturing and Test of a Centrifugal Particle Receiver*. Vol. Volume 1: Biofuels, Hydrogen, Syngas, and Alternate Fuels; CHP and Hybrid Power and Energy Systems; Concentrating Solar Power; Energy Storage; Environmental, Economic, and Policy Considerations of Advanced Energy Systems; Geother-

mal, Ocean, and Emerging Energy Technologies; Photovoltaics; Posters; Solar Chemistry; Sustainable Building Energy Systems; Sustainable Infrastructure and Transportation; Thermodynamic Analysis of Energy Systems; Wind Energy Systems and Technologies. Energy Sustainability. V001T04A007. June 2016. DOI: 10.1115/ES2016-59252.

[87] Matti Lubkoll, Miriam Ebert, Lars Amsbeck, Alexander Hirt, Cathy Frantz, Jens Rheinländer, and Reiner Buck. "Development progress of the CentRec® particle receiver technology". In: *AIP Conference Proceedings* 2445.1 (2022), p. 110005. DOI: 10.1063/5.0086510.

[88] Martin Roeb, Christian Sattler, Ruth Klüser, Nathalie Monnerie, Lamark de Oliveira, Athanasios G. Konstandopoulos, Christos Agrafiotis, V. T. Zaspalis, L. Nalbandian, Andrew Steele, and Per Stobbe. "Solar Hydrogen Production by a Two-Step Cycle Based on Mixed Iron Oxides". In: *Journal of Solar Energy Engineering* 128.2 (2006), p. 125. ISSN: 01996231. DOI: 10.1115/1.2183804.

[89] *Simulation of a Solar Receiver-Reactor for Hydrogen Production*. Vol. ASME 2009 3rd International Conference on Energy Sustainability, Volume 1. Energy Sustainability. July 2009, pp. 295–304. DOI: 10.1115/ES2009-90273.

[90] Anis Houaijia, Christian Sattler, Martin Roeb, Matthias Lange, Stefan Breuer, and Jan Peter Säck. "Analysis and improvement of a high-efficiency solar cavity reactor design for a two-step thermochemical cycle for solar hydrogen production from water". In: *Solar Energy* 97 (2013), pp. 26–38. ISSN: 0038-092X. DOI: https://doi.org/10.1016/j.solener.2013.07.032.

[91] Alberto de la Calle, Lidia Roca, Luis J. Yebra, and Sebastián Dormido. "Modeling of a two-step solar hydrogen production plant". In: *International Journal of Hydrogen Energy* 37.14 (2012), pp. 10549–10556. ISSN: 0360-3199. DOI: https://doi.org/10.1016/j.ijhydene.2012.04.056.

[92] Marc Röger, Lars Amsbeck, Birgit Gobereit, and Reiner Buck. "Face-Down Solid Particle Receiver Using Recirculation". In: *Journal of Solar Energy Engineering* 133.3 (July 2011). 031009. ISSN: 0199-6231. DOI: 10.1115/1.4004269.

[93] Nathan P. Siegel, Clifford K. Ho, Siri S. Khalsa, and Gregory J. Kolb. "Development and Evaluation of a Prototype Solid Particle Receiver: On-Sun Testing and Model Validation". In: *Journal of Solar Energy Engineering* 132.2 (May 2010). 021008. ISSN: 0199-6231. DOI: 10.1115/1.4001146.

[94] Taide Tan and Yitung Chen. "Review of study on solid particle solar receivers". In: *Renewable and Sustainable Energy Reviews* 14.1 (2010), pp. 265–276. ISSN: 1364-0321. DOI: https://doi.org/10.1016/j.rser.2009.05.012.

[95] Nathan P. Siegel, Michael D. Gross, and Robert Coury. "The Development of Direct Absorption and Storage Media for Falling Particle Solar Central Receivers". In: *Journal of Solar Energy Engineering* 137.4 (Aug. 2015). 041003. ISSN: 0199-6231. DOI: 10.1115/1.4030069.

[96] Brantley H. Mills, Clifford K. Ho, Nathaniel R. Schroeder, Reid Shaeffer, Hendrik F. Laubscher, and Kevin J. Albrecht. "Design Evaluation of a Next-Generation High-Temperature Particle Receiver for Concentrating Solar Thermal Applications". In: *Energies* 15.5 (2022). ISSN: 1996-1073. DOI: 10.3390/en15051657.

[97] Tatsuya Kodama, Hyun Seok Cho, Kouske Inoue, Tatsuya Saito, Shouta Watanabe, Nobuyuki Gokon, and Selvan Bellan. "Particles fluidized bed receiver/reactor with a beam-down solar concentrating optics: First performance test on two-step water splitting with ceria using a Miyazaki solar concentrating system". In: *AIP Conference Proceedings* 2126.1 (2019), p. 180011. DOI: 10.1063/1.5117691.

[98] A. Steinfeld, A. Imhof, and D. Mischler. "Experimental Investigation of an Atmospheric-Open Cyclone Solar Reactor for Solid-Gas Thermochemical Reactions". In: *Journal of Solar Energy Engineering* 114.3 (Aug. 1992), pp. 171–174. ISSN: 0199-6231. DOI: 10.1115/1.2930001.

[99] F. Bai, Y. Zhang, X. Zhang, F. Wang, Y. Wang, and Z. Wang. "Thermal Performance of a Quartz Tube Solid Particle Air Receiver". In: *Energy Procedia* 49 (2014). Proceedings of the SolarPACES 2013 International Conference, pp. 284–294. ISSN: 1876-6102. DOI: https://doi.org/10.1016/j.egypro.2014.03.031.

[100] Fangzhou Wang, Fengwu Bai, Tianjian Wang, Qing Li, and Zhifeng Wang. "Experimental study of a single quartz tube solid particle air receiver". In: *Solar Energy* 123 (2016), pp. 185–205. ISSN: 0038-092X. DOI: https://doi.org/10.1016/j.solener.2015.10.048.

[101] Abhishek Singh, Justin Lapp, Johannes Grobbel, Stefan Brendelberger, Jan P. Reinhold, Lamark Olivera, Ivan Ermanoski, Nathan P. Siegel, Anthony McDaniel, Martin Roeb, and Christian Sattler. "Design of a pilot scale directly irradiated, high temperature, and low pressure moving particle cavity chamber for metal oxide reduction". In: *Solar Energy* 157 (2017), pp. 365–376. ISSN: 0038-092X. DOI: https://doi.org/10.1016/j.solener.2017.08.040.

[102] Antonio L. Ávila-Marín. "Volumetric receivers in Solar Thermal Power Plants with Central Receiver System technology: A review". In: *Solar Energy* 85.5 (2011), pp. 891–910. ISSN: 0038-092X. DOI: https://doi.org/10.1016/j.solener.2011.02.002.

[103] Bernhard Hoffschmidt, Fe´lix M. Te´llez, Antonio Valverde, Jesu´s Ferna´ndez, and Valerio Ferna´ndez. "Performance Evaluation of the 200-kWth HiTRec-II Open Volumetric Air Receiver ". In: *Journal of Solar Energy Engineering* 125.1 (Jan. 2003), pp. 87–94. ISSN: 0199-6231. DOI: 10.1115/1.1530627.

[104] R. Buck. "Volumetric Receiver Development at DLR Stuttgart." In: *Volumetric Receiver Workshop, DLR Koeln, 13-15 February 1990.* LIDO-Berichtsjahr=1990, 1990. URL: https://elib.dlr.de/25746/.

[105] Thomas Fend, Bernhard Hoffschmidt, Robert Pitz-Paal, Oliver Reutter, and Peter Rietbrock. "Porous materials as open volumetric solar receivers: Experimental determination of thermophysical and heat transfer properties". In: *Energy* 29.5 (2004). SolarPACES 2002, pp. 823–833. ISSN: 0360-5442. DOI: https://doi.org/10.1016/S0360-5442(03)00188-9.

[106] R. Pitz-Paal, B. Hoffschmidt, M. Böhmer, and M. Becker. "Experimental and numerical evaluation of the performance and flow stability of different types of open volumetric absorbers under non-homogeneous irradiation". In: *Solar Energy* 60.3 (1997), pp. 135–150. ISSN: 0038-092X. DOI: https://doi.org/10.1016/S0038-092X(97)00007-8.

[107] K. Hennecke, P. Schwarzbözl, G. Koll, M. Beuter, B. Hoffschmidt, J. Göttsche, and T. Hartz. "The Solar Power Tower Jülich — A Solar Thermal Power Plant for Test and Demonstration of Air Receiver Technology". In: *Proceedings of ISES World Congress 2007 (Vol. I – Vol. V)*. Ed. by D. Yogi Goswami and Yuwen Zhao. Berlin, Heidelberg: Springer Berlin Heidelberg, 2009, pp. 1749–1753. ISBN: 978-3-540-75997-3.

[108] Vikas R. Patil, Fabio Kiener, Adrian Grylka, and Aldo Steinfeld. "Experimental testing of a solar air cavity-receiver with reticulated porous ceramic absorbers for thermal processing at above 1000 °C". In: *Solar Energy* 214 (2021), pp. 72–85. ISSN: 0038-092X. DOI: https://doi.org/10.1016/j.solener.2020.11.045.

[109] Fritz Zaversky, Iñigo Les, Patxi Sorbet, Marcelino Sánchez, Benoît Valentin, Jean-Florian Brau, and Frédéric Siros. "The challenge of solar powered combined cycles – Providing dispatchability and increasing efficiency by integrating the open volumetric air receiver technology". In: *Energy* 194 (2020), p. 116796. ISSN: 0360-5442. DOI: https://doi.org/10.1016/j.energy.2019.116796.

[110] Vishwa Deepak Kumar, Vikas K. Upadhyay, Gurveer Singh, Sudipto Mukhopadhyay, and Laltu Chandra. "Open volumetric air receiver: An innovative application and a major challenge". In: *WIREs Energy and Environment* 11.1 (2022), e404. DOI: https://doi.org/10.1002/wene.404.

[111] Ekaterina I. Leonidova, Ilya A. Leonidov, Mikhail V. Patrakeev, and Victor L. Kozhevnikov. "Oxygen non-stoichiometry, high-temperature properties, and phase diagram of CaMnO3–δ". In: *J Solid State Electrochem* 15.5 (Feb. 2011), pp. 1071–1075. DOI: 10.1007/s10008-010-1288-1.

[112] Andrea Ambrosini, Sean Mx Babiniec, Eric Nicholas Coker, and James Ex Miller. *Thermochemical Energy Storage Using Redox-Active Metal Oxides.* Tech. rep. Sandia National Lab.(SNL-NM), Albuquerque, NM (United States), 2019.

[113] Emanuela Mastronardo, Xin Qian, Juan M. Coronado, and Sossina M. Haile. "The favourable thermodynamic properties of Fe-doped CaMnO3 for thermochemical heat storage". In: *J Mater Chem A* 8.17 (2020), pp. 8503–8517. DOI: 10.1039/d0ta02031a.

[114] K. Mocala, A. Navrotsky, and D.M. Sherman. "High-temperature heat capacity of Co3O4 spinel: thermally induced spin unpairing transition". In: *Physics and Chemistry of Minerals* 19.2 (1992). Cited by: 37, pp. 88–95. DOI: 10.1007/BF00198606.

[115] W.K. Chen and R.A. Jackson. "Oxygen self-diffusion in undoped and doped cobaltous oxide". In: *Journal of Physics and Chemistry of Solids* 30.6 (1969), pp. 1309–1314. ISSN: 0022-3697. DOI: https://doi.org/10.1016/0022-3697(69)90192-9.

[116] Brent Fultz. "Vibrational thermodynamics of materials". In: *Progress in Materials Science* 55.4 (2010), pp. 247–352. ISSN: 0079-6425. DOI: https://doi.org/10.1016/j.pmatsci.2009.05.002.

[117] Göran Grimvall. *Thermophysical Properties of Materials*. Amsterdam: Elsevier Science B.V., 1999, pp. 112–135. ISBN: 978-0-444-82794-4. DOI: https://doi.org/10.1016/B978-044482794-4/50008-5.

[118] Rasna Thakur, Archana Srivastava, Rajesh K. Thakur, and N. K. Gaur. "Low temperature specific heat of perovskite LaCoO3". In: *AIP Conference Proceedings* 1447.1 (2012), pp. 989–990. DOI: 10.1063/1.4710337.

[119] A Scrimshire, A Lobera, A M T Bell, A H Jones, I Sterianou, S D Forder, and P A Bingham. "Determination of Debye temperatures and Lamb–Mössbauer factors for LnFeO3orthoferrite perovskites (Ln = La, Nd, Sm, Eu, Gd)". In: *Journal of Physics: Condensed Matter* 30.10 (Feb. 2018), p. 105704. DOI: 10.1088/1361-648x/aaab7d.

[120] Camilla Haavik, Egil Bakken, Truls Norby, Svein Stølen, Tooru Atake, and Takeo Tojo. "Heat capacity of SrFeO3–δ; δ = 0.50, 0.25 and 0.15 – configurational entropy of structural entities in grossly non-stoichiometric oxides". In: *Dalton Transactions* 3 (2003), pp. 361–368. ISSN: 1477-9226. DOI: 10.1039/b209236k.

[121] Alexander H. Bork, Erwin Povoden-Karadeniz, and Jennifer L. M. Rupp. "Modeling Thermochemical Solar-to-Fuel Conversion: CALPHAD for Thermodynamic Assessment Studies of Perovskites, Exemplified for (La,Sr)MnO3". In: *Advanced Energy Materials* 7.1 (2017), p. 1601086. DOI: https://doi.org/10.1002/aenm.201601086.

[122] K. T. Jacob and Mrinalini Attaluri. "Refinement of thermodynamic data for LaMnO3". In: *J. Mater. Chem.* 13 (4 2003), pp. 934–942. DOI: 10.1039/B208550J.

[123] J. Leitner, P. Voňka, D. Sedmidubský, and P. Svoboda. "Application of Neumann–Kopp rule for the estimation of heat capacity of mixed oxides". In: *Thermochimica Acta* 497.1 (2010), pp. 7–13. ISSN: 0040-6031. DOI: https://doi.org/10.1016/j.tca.2009.08.002.

[124] Ihsan Barin. "Tables of thermochemical data of pure substances". In: *Thermochemical Data of Pure Substances*. John Wiley & Sons, Ltd, 1995. Chap. 12. ISBN: 9783527619825. DOI: https://doi.org/10.1002/9783527619825.ch12g.

[125] *Materials Project*. URL: https://materialsproject.org.

[126] Gregory S. Jackson, Luca Imponenti, Kevin J. Albrecht, Daniel C. Miller, and Robert J. Braun. "Inert and Reactive Oxide Particles for High-Temperature Thermal Energy Capture and Storage for Concentrating Solar Power". In: *Journal of Solar Energy Engineering* 141.2 (Jan. 2019). 021016. ISSN: 0199-6231. DOI: 10.1115/1.4042128.

[127] Bunji Iwasaki and Takashi Katsura. “The Thermodynamic Properties of the Non-stoichiometric Ceric Oxide at Temperatures from 900 to 1300°C”. In: *Bulletin of the Chemical Society of Japan* 44.5 (1971), pp. 1297–1301. DOI: 10.1246/bcsj.44.1297.

[128] R.J. Panlener, R.N. Blumenthal, and J.E. Garnier. “A thermodynamic study of non-stoichiometric cerium dioxide”. In: *Journal of Physics and Chemistry of Solids* 36.11 (1975), pp. 1213–1222. ISSN: 0022-3697. DOI: https://doi.org/10.1016/0022-3697(75)90192-4.

[129] D.J.M. Bevan and J. Kordis. “Mixed oxides of the type MO2 (fluorite)—M2O3—I oxygen dissociation pressures and phase relationships in the system CeO2–Ce2O3 at high temperatures”. In: *Journal of Inorganic and Nuclear Chemistry* 26.9 (1964), pp. 1509–1523. ISSN: 0022-1902. DOI: https://doi.org/10.1016/0022-1902(64)80038-5.

[130] B. Bulfin, L. Hoffmann, L. de Oliveira, N. Knoblauch, F. Call, M. Roeb, C. Sattler, and M. Schmücker. “Statistical thermodynamics of non-stoichiometric ceria and ceria zirconia solid solutions”. In: *Phys. Chem. Chem. Phys.* 18 (33 2016), pp. 23147–23154. DOI: 10.1039/C6CP03158G.

[131] *NIST, National Institute of Standards and Technology, Gas phase thermochemistry data*. URL: https://webbook.nist.gov/cgi/cbook.cgi?ID=C7782447&Mask=1.

[132] Stefan Brendelberger, Martin Roeb, Matthias Lange, and Christian Sattler. “Counter flow sweep gas demand for the ceria redox cycle”. In: *Solar Energy* 122 (2015), pp. 1011–1022. ISSN: 0038092X. DOI: 10.1016/j.solener.2015.10.036.

[133] Roy W. Rice. *Porosity of Ceramics*. CRC Press, Dec. 2017. Chap. 10. DOI: 10.1201/9781315274539.

[134] E. J. A. E. Williams and J. R. G. Evans. “Expanded ceramic foam”. In: *Journal of Materials Science* 31.3 (1996), pp. 559–563. ISSN: 1573-4803. DOI: 10.1007/BF00367869.

[135] Sarit B. Bhaduri. “Science and technology of ceramic foams”. In: *Advanced Performance Materials* 1.3 (1994), pp. 205–220. ISSN: 1572-8765. DOI: 10.1007/BF00711203.

[136] Peter Poživil, Nicolas Ettlin, Fabian Stucker, and Aldo Steinfeld. "Modular Design and Experimental Testing of a 50 kWth Pressurized-Air Solar Receiver for Gas Turbines". In: *Journal of Solar Energy Engineering* 137.3 (June 2015). 031002. ISSN: 0199-6231. DOI: 10.1115/1.4028918.

[137] F.A.C. Oliveira, J.C. Fernandes, J. Galindo, J. Rodríguez, I. Canãdas, and L.G. Rosa. "Thermal resistance of solar volumetric absorbers made of mullite, brown alumina and ceria foams under concentrated solar radiation". In: *Solar Energy Materials and Solar Cells* 194 (2019), pp. 121–129. ISSN: 0927-0248. DOI: https://doi.org/10.1016/j.solmat.2019.02.008.

[138] Philipp Furler, Jonathan Scheffe, Daniel Marxer, Michal Gorbar, Alexander Bonk, Ulrich Vogt, and Aldo Steinfeld. "Thermochemical CO2 splitting via redox cycling of ceria reticulated foam structures with dual-scale porosities". In: *Phys. Chem. Chem. Phys.* 16 (22 2014), pp. 10503–10511. DOI: 10.1039/C4CP01172D.

[139] Anita Haeussler, Stéphane Abanades, Fernando A. Costa Oliveira, M. Alexandra Barreiros, A. P. F. Caetano, Rui M. Novais, and Robert C. Pullar. "Solar Redox Cycling of Ceria Structures Based on Fiber Boards, Foams, and Biomimetic Cork-Derived Ecoceramics for Two-Step Thermochemical H2O and CO2 Splitting". In: *Energy & Fuels* 34.7 (2020), pp. 9037–9049. DOI: 10.1021/acs.energyfuels.0c01240.

[140] Christos Agrafiotis, Martin Roeb, Martin Schmücker, and Christian Sattler. "Exploitation of thermochemical cycles based on solid oxide redox systems for thermochemical storage of solar heat. Part 2: Redox oxide-coated porous ceramic structures as integrated thermochemical reactors/heat exchangers". In: *Solar Energy* 114 (2015), pp. 440–458. ISSN: 0038092X. DOI: 10.1016/j.solener.2014.12.036.

[141] Christos Agrafiotis, Martin Roeb, and Christian Sattler. "Exploitation of thermochemical cycles based on solid oxide redox systems for thermochemical storage of solar heat. Part 4: Screening of oxides for use in cascaded thermochemical storage concepts". In: *Solar Energy* 139 (2016), pp. 695–710. ISSN: 0038092X. DOI: 10.1016/j.solener.2016.04.034.

[142] Christos Agrafiotis, Andreas Becker, Martin Roeb, and Christian Sattler. "Exploitation of thermochemical cycles based on solid oxide redox systems for thermochemical storage of solar heat. Part 5: Testing of porous ceramic honeycomb and foam cascades based on cobalt and manganese oxides for hybrid sensi-

ble/thermochemical heat storage". In: *Solar Energy* 139 (2016), pp. 676–694. ISSN: 0038092X. DOI: 10.1016/j.solener.2016.09.013.

[143] Christos Agrafiotis, Tina Block, Marion Senholdt, Stefania Tescari, Martin Roeb, and Christian Sattler. "Exploitation of thermochemical cycles based on solid oxide redox systems for thermochemical storage of solar heat. Part 6: Testing of Mn-based combined oxides and porous structures". In: *Solar Energy* 149 (2017), pp. 227–244. ISSN: 0038092X. DOI: 10.1016/j.solener.2017.03.083.

[144] Bachirou Guene Lougou, Yong Shuai, RuMing Pan, Gédéon Chaffa, Clément Ahouannou, Hao Zhang, and HePing Tan. "Radiative heat transfer and thermal characteristics of Fe-based oxides coated SiC and Alumina RPC structures as integrated solar thermochemical reactor". In: *Science China Technological Sciences* 61.12 (2018), pp. 1788–1801. ISSN: 1869-1900. DOI: 10.1007/s11431-018-9294-y.

[145] Amir Masoud Parvanian, Hamidreza Salimijazi, Mehdi Shabaninejad, Ulrike Troitzsch, Peter Kreider, Wojciech Lipiński, and Mohammad Saadatfar. "Thermochemical CO2 splitting performance of perovskite coated porous ceramics". In: *RSC Adv.* 10 (39 2020), pp. 23049–23057. DOI: 10.1039/D0RA02353A.

[146] Amir Masoud Parvanian, Hamidreza Salimijazi, Mehdi Shabaninejad, Peter Kreider, and Mohammad Saadatfar. "Ca/Al doped lanthanum manganite perovskite coated porous SiC for CO2 conversion". In: *Materials Chemistry and Physics* 253 (2020), p. 123306. ISSN: 0254-0584. DOI: https://doi.org/10.1016/j.matchemphys.2020.123306.

[147] William C. Chueh, Christoph Falter, Mandy Abbott, Danien Scipio, Philipp Furler, Sossina M. Haile, and Aldo Steinfeld. "High-Flux Solar-Driven Thermochemical Dissociation of CO₂ and H₂O Using Nonstoichiometric Ceria". In: *Science* 330.6012 (2010), pp. 1797–1801. DOI: 10.1126/science.1197834.

[148] Philipp Furler, Jonathan Scheffe, Michal Gorbar, Louis Moes, Ulrich Vogt, and Aldo Steinfeld. "Solar Thermochemical CO2 Splitting Utilizing a Reticulated Porous Ceria Redox System". In: *Energy & Fuels* 26.11 (2012), pp. 7051–7059. DOI: 10.1021/ef3013757.

[149] Daniel Marxer, Philipp Furler, Michael Takacs, and Aldo Steinfeld. "Solar thermochemical splitting of CO2 into separate streams of CO and O2 with high selectivity, stability, conversion, and efficiency". In: *Energy Environ. Sci.* 10 (5 2017), pp. 1142–1149. DOI: 10.1039/C6EE03776C.

[150] Marie Hoes, Erik Koepf, Patrick Davenport, and Aldo Steinfeld. "Reticulated porous ceramic ceria structures with modified surface geometry for solar thermochemical splitting of water and carbon dioxide". In: *AIP Conference Proceedings* 2126.1 (2019), p. 180010. DOI: 10.1063/1.5117690.

[151] Marie Hoes, Simon Ackermann, David Theiler, Philipp Furler, and Aldo Steinfeld. "Additive-Manufactured Ordered Porous Structures Made of Ceria for Concentrating Solar Applications". In: *Energy Technology* 7.9 (2019), p. 1900484. DOI: https://doi.org/10.1002/ente.201900484.

[152] Karl Schwartzwalder and Arthur V Somers. "Method of making porous ceramic articles". US3090094A. May 21, 1963.

[153] Martyn V. Twigg and James T. Richardson. "Fundamentals and Applications of Structured Ceramic Foam Catalysts". In: *Industrial & Engineering Chemistry Research* 46.12 (2007), pp. 4166–4177. DOI: 10.1021/ie061122o.

[154] Hans-Rudolf Wenk and Andrei Bulakh. *Minerals: Their Constitution and Origin*. Cambridge University Press, 2004. DOI: 10.1017/CBO9780511811296.

[155] Jonas Horn and Derck Schlettwein. "Role of Interfaces and Contact Formation for the Application of Lead-Free Perovskite Materials in Photovoltaic Cells". In: *physica status solidi (RRL) – Rapid Research Letters* 15.11 (2021), p. 2100369. DOI: https://doi.org/10.1002/pssr.202100369.

[156] Mulmudi Hemant Kumar, Natalia Yantara, Sabba Dharani, Michael Graetzel, Subodh Mhaisalkar, Pablo P. Boix, and Nripan Mathews. "Flexible, low-temperature, solution processed ZnO-based perovskite solid state solar cells". In: *Chem. Commun.* 49 (94 2013), pp. 11089–11091. DOI: 10.1039/C3CC46534A.

[157] Felix Deschler, Michael Price, Sandeep Pathak, Lina E. Klintberg, David-Dominik Jarausch, Ruben Higler, Sven Hüttner, Tomas Leijtens, Samuel D. Stranks, Henry J. Snaith, Mete Atatüre, Richard T. Phillips, and Richard H. Friend. "High Photoluminescence Efficiency and Optically Pumped Lasing in Solution-Processed Mixed Halide Perovskite Semiconductors". In: *The Journal of Physical Chemistry Letters* 5.8 (2014). PMID: 26269988, pp. 1421–1426. DOI: 10.1021/jz5005285.

[158] Koichi Momma and Fujio Izumi. "*VESTA3* for three-dimensional visualization of crystal, volumetric and morphology data". In: *Journal of Applied Crystallography* 44.6 (Dec. 2011), pp. 1272–1276. DOI: 10.1107/S0021889811038970.

[159] Victor Moritz Goldschmidt. "Die Gesetze der Krystallochemie". In: *Die Naturwissenschaften* 14.21 (May 1926), pp. 477–485. DOI: 10.1007/BF01507527.

[160] XiangChun Liu, Rongzi Hong, and Changsheng Tian. "Tolerance factor and the stability discussion of ABO3-type ilmenite". In: *Journal of Materials Science: Materials in Electronics* 20.4 (2008), p. 323. ISSN: 1573-482X. DOI: 10.1007/s10854-008-9728-8.

[161] R.S. Roth. "Classification of perovskite and other ABO3-type compounds". In: *Journal of Research of the National Bureau of Standards* 58.2 (Feb. 1957), p. 75. DOI: 10.6028/jres.058.010.

[162] B. Dabrowski, O. Chmaissem, J. Mais, S. Kolesnik, J. D. Jorgensen, and S. Short. "Tolerance factor rules for Sr1−x−yCaxBayMnO3 perovskites". In: *Journal of Solid State Chemistry* 170.1 (2003), pp. 154–164. ISSN: 00224596. DOI: 10.1016/s0022-4596(02)00056-7.

[163] W. Travis, E. N. K. Glover, H. Bronstein, D. O. Scanlon, and R. G. Palgrave. "On the application of the tolerance factor to inorganic and hybrid halide perovskites: a revised system". In: *Chem. Sci.* 7 (7 2016), pp. 4548–4556. DOI: 10.1039/C5SC04845A.

[164] Christopher J. Bartel, Christopher Sutton, Bryan R. Goldsmith, Runhai Ouyang, Charles B. Musgrave, Luca M. Ghiringhelli, and Matthias Scheffler. "New tolerance factor to predict the stability of perovskite oxides and halides". In: *Science Advances* 5.2 (2019), eaav0693. DOI: 10.1126/sciadv.aav0693.

[165] Gregor Kieslich, Shijing Sun, and Anthony K. Cheetham. "An extended Tolerance Factor approach for organic–inorganic perovskites". In: *Chem. Sci.* 6 (6 2015), pp. 3430–3433. DOI: 10.1039/C5SC00961H.

[166] R. D. Shannon. "Revised effective ionic radii and systematic studies of interatomic distances in halides and chalcogenides". In: *Acta Crystallographica Section A* 32.5 (1976), pp. 751–767. ISSN: 0567-7394. DOI: doi:10.1107/S0567739476001551.

[167] Christodoulos Chatzichristodoulou, Poul Norby, Peter V. Hendriksen, and Mogens B. Mogensen. "Size of oxide vacancies in fluorite and perovskite structured oxides". In: *Journal of Electroceramics* 34.1 (2015), pp. 100–107. ISSN: 1573-8663. DOI: 10.1007/s10832-014-9916-2.

[168] Walter J. Moore, Dieter O. Hummel, Gundolf Trafara, and Kurt Holland-Moritz. *Physikalische Chemie*. Berlin/Boston, GERMANY: De Gruyter, Inc., 2011. URL: http://ebookcentral.proquest.com/lib/dlr-ebooks/detail.action?docID=3044785.

[169] B. Bulfin, J. Vieten, D. E. Starr, A. Azarpira, C. Zachäus, M. Hävecker, K. Skorupska, M. Schmücker, M. Roeb, and C. Sattler. "Redox chemistry of CaMnO3 and Ca0.8Sr0.2MnO3 oxygen storage perovskites". In: *J. Mater. Chem. A* 5 (17 2017), pp. 7912–7919. DOI: 10.1039/C7TA00822H.

[170] B. Bulfin, A. J. Lowe, K. A. Keogh, B. E. Murphy, O. Lübben, S. A. Krasnikov, and I. V. Shvets. "Analytical Model of CeO2 Oxidation and Reduction". In: *The Journal of Physical Chemistry C* 117.46 (2013), pp. 24129–24137. DOI: 10.1021/jp406578z.

[171] National Institute of Standards Chase M. W. and Technology (U.S.) *NIST-JANAF thermochemical tables*. English. [Washington, D.C.]; Woodbury, N.Y.: American Chemical Society ; American Institute of Physics for the National Institute of Standards and Technology, 1998.

[172] Shyue Ping Ong, William Davidson Richards, Anubhav Jain, Geoffroy Hautier, Michael Kocher, Shreyas Cholia, Dan Gunter, Vincent L. Chevrier, Kristin A. Persson, and Gerbrand Ceder. "Python Materials Genomics (pymatgen): A robust, open-source python library for materials analysis". In: *Computational Materials Science* 68 (2013), pp. 314–319. ISSN: 0927-0256. DOI: https://doi.org/10.1016/j.commatsci.2012.10.028.

[173] Maarten de Jong, Wei Chen, Thomas Angsten, Anubhav Jain, Randy Notestine, Anthony Gamst, Marcel Sluiter, Chaitanya Krishna Ande, Sybrand van der Zwaag, Jose J. Plata, Cormac Toher, Stefano Curtarolo, Gerbrand Ceder, Kristin A. Persson, and Mark Asta. "Charting the complete elastic properties of inorganic crystalline compounds". In: *Scientific Data* 2.1 (2015), p. 150009. ISSN: 2052-4463. DOI: 10.1038/sdata.2015.9.

[174] Sergey Vyazovkin, Alan K. Burnham, José M. Criado, Luis A. Pérez-Maqueda, Crisan Popescu, and Nicolas Sbirrazzuoli. "ICTAC Kinetics Committee recommendations for performing kinetic computations on thermal analysis data". In: *Thermochimica Acta* 520.1 (2011), pp. 1–19. ISSN: 0040-6031. DOI: https://doi.org/10.1016/j.tca.2011.03.034.

[175] Ammar Khawam and Douglas R. Flanagan. "Solid-State Kinetic Models: Basics and Mathematical Fundamentals". In: *The Journal of Physical Chemistry B* 110.35 (2006). PMID: 16942065, pp. 17315–17328. DOI: 10.1021/jp062746a.

[176] B. Bulfin, J. Vieten, S. Richter, J. M. Naik, G. R. Patzke, M. Roeb, C. Sattler, and A. Steinfeld. "Isothermal relaxation kinetics for the reduction and oxidation of SrFeO3 based perovskites". In: *Phys. Chem. Chem. Phys.* 22 (4 2020), pp. 2466–2474. DOI: 10.1039/C9CP05771D.

[177] Nora A. Merino, Bibiana P. Barbero, Pierre Eloy, and Luis E. Cadús. "La1−xCaxCoO3 perovskite-type oxides: Identification of the surface oxygen species by XPS". In: *Applied Surface Science* 253.3 (2006), pp. 1489–1493. ISSN: 0169-4332. DOI: https://doi.org/10.1016/j.apsusc.2006.02.035.

[178] Xiyang Wang, Keke Huang, Long Yuan, Shibo Xi, Wensheng Yan, Zhibin Geng, Yingge Cong, Yu Sun, Hao Tan, Xiaofeng Wu, Liping Li, and Shouhua Feng. "Activation of Surface Oxygen Sites in a Cobalt-Based Perovskite Model Catalyst for CO Oxidation". In: *The Journal of Physical Chemistry Letters* 9.15 (2018). PMID: 29966086, pp. 4146–4154. DOI: 10.1021/acs.jpclett.8b01623.

[179] J.L.G. Fierro. "Structure and composition of perovskite surface in relation to adsorption and catalytic properties". In: *Catalysis Today* 8.2 (1990), pp. 153–174. ISSN: 0920-5861. DOI: https://doi.org/10.1016/0920-5861(90)87016-V.

[180] Miriam Ezbiri, Michael Takacs, Boris Stolz, Jeffrey Lungthok, Aldo Steinfeld, and Ronald Michalsky. "Design principles of perovskites for solar-driven thermochemical splitting of CO2". In: *J. Mater. Chem. A* 5 (29 2017), pp. 15105–15115. DOI: 10.1039/C7TA02081C.

[181] N.E. Trofimenko and H. Ullmann. "Oxygen stoichiometry and mixed ionic-electronic conductivity of Sr1−aCeaFe1−bCobO3−x perovskite-type oxides". In: *Journal of the European Ceramic Society* 20.9 (2000), pp. 1241–1250. ISSN: 0955-2219. DOI: https://doi.org/10.1016/S0955-2219(99)00292-7.

[182] J. Sunarso, S. Baumann, J.M. Serra, W.A. Meulenberg, S. Liu, Y.S. Lin, and J.C. Diniz da Costa. "Mixed ionic–electronic conducting (MIEC) ceramic-based membranes for oxygen separation". In: *Journal of Membrane Science* 320.1 (2008), pp. 13–41. ISSN: 0376-7388. DOI: https://doi.org/10.1016/j.memsci.2008.03.074.

[183] Sang Bok Ma, Hyuk Jae Kwon, Mokwon Kim, Seong-Min Bak, Hyunpyo Lee, Steven N. Ehrlich, Jeong-Ju Cho, Dongmin Im, and Dong-Hwa Seo. "Mixed Ionic–Electronic Conductor of Perovskite LixLayMO3−δ toward Carbon-Free Cathode for Reversible Lithium–Air Batteries". In: *Advanced Energy Materials* 10.38 (2020), p. 2001767. DOI: https://doi.org/10.1002/aenm.202001767.

[184] Y. Teraoka, H.M. Zhang, K. Okamoto, and N. Yamazoe. "Mixed ionic-electronic conductivity of La1−xSrxCo1−yFeyO3−δ perovskite-type oxides". In: *Materials Research Bulletin* 23.1 (1988), pp. 51–58. ISSN: 0025-5408. DOI: https://doi.org/10.1016/0025-5408(88)90224-3.

[185] A. Kulkarni, F.T. Ciacchi, S. Giddey, C. Munnings, S.P.S. Badwal, J.A. Kimpton, and D. Fini. "Mixed ionic electronic conducting perovskite anode for direct carbon fuel cells". In: *International Journal of Hydrogen Energy* 37.24 (2012). 2011 International Workshop on Molten Carbonates and Related Topics, pp. 19092–19102. ISSN: 0360-3199. DOI: https://doi.org/10.1016/j.ijhydene.2012.09.141.

[186] Jacobus Henricus van't Hoff. *Studies in chemical dynamics*. Amsterdam, 1896.

[187] Lena Klaas, Brendan Bulfin, Dorottya Kriechbaumer, Martin Roeb, and Christian Sattler. "Impact of the Sr content on the redox thermodynamics and kinetics of Ca1−xSrxMnO3−δ for tailored properties". In: *Phys. Chem. Chem. Phys.* (2023). DOI: 10.1039/D3CP00267E.

[188] Andrea Ambrosini, James E. Miller, Sean Michael Babiniec, and Eric Nicholas Coker. "Calcium Manganite-Based Materials for High Temperature CSP Thermochemical Energy Storage." In: (June 2017). URL: https://www.osti.gov/biblio/1513618.

[189] Matthew T. Curnan and John R. Kitchin. "Effects of Concentration, Crystal Structure, Magnetism, and Electronic Structure Method on First-Principles Oxygen Vacancy Formation Energy Trends in Perovskites". In: *The Journal of Physical Chemistry C* 118.49 (2014), pp. 28776–28790. ISSN: 1932-7447. DOI: 10.1021/jp507957n.

[190] Egil Bakken, Truls Norby, and Svein Stølen. "Nonstoichiometry and reductive decomposition of CaMnO3-δ". In: *Solid State Ionics* 176.1 (2005), pp. 217–223. ISSN: 0167-2738. DOI: https://doi.org/10.1016/j.ssi.2004.07.001.

[191] Luca Imponenti. "Redox Cycles with doped Calcium Manganites for High-Temperature Thermochemical Energy Storage in Concentrating Solar Power". PhD thesis. Colorado School of Mines, 2018.

[192] Lisbeth Rørmark, Anne Beate Mørch, Kjell Wiik, Svein Stølen, and Tor Grande. "Enthalpies of Oxidation of CaMnO3-δ, Ca2MnO4-δ and SrMnO3-δ Deduced Redox Properties". In: *Chemistry of Materials* 13.11 (2001), pp. 4005–4013. ISSN: 0897-4756. DOI: 10.1021/cm0110501.

[193] Luca Christian Matzel. "Entwicklung offenporiger Metalloxidschäume für die Produktion solarer Brennstoffe". Research rep. Westfälische Hochschule, Oct. 2, 2020.

[194] Kelsey A. Stoerzinger, Wesley T. Hong, Gisele Azimi, Livia Giordano, Yueh-Lin Lee, Ethan J. Crumlin, Michael D. Biegalski, Hendrik Bluhm, Kripa K. Varanasi, and Yang Shao-Horn. "Reactivity of Perovskites with Water: Role of Hydroxylation in Wetting and Implications for Oxygen Electrocatalysis". In: *The Journal of Physical Chemistry C* 119.32 (2015), pp. 18504–18512. DOI: 10.1021/acs.jpcc.5b06621.

[195] Mathias Pein, Jens Keller, Christos Agrafiotis, Asmaa Eltayeb, Lena Klaas, Nicole Carina Neumann, Martin Roeb, and Christian Sattler. "Thermochemical Oxygen Pumping with Perovskite Reticulated Porous Ceramics for Enhanced Reduction of Ceria in Thermochemical Fuel Production". In: *Advanced Energy Materials* (2024), p. 2304454. DOI: https://doi.org/10.1002/aenm.202304454.